Master's thesis

NTNU
Norwegian University of Science and Technology
Faculty of Natural Sciences
Department of Chemistry

Sondre Taugbøl Lomeland

Synthesis and catalytic testing of oxazoline-NHC-gold(III) and β-hydroxyamide-NHC-gold(III) complexes

Master's thesis in Chemical Engineering and Biotechnology
Supervisor: Anne Fiksdahl
Co-supervisor: Helgi Freyr Jónsson

June 2021

NTNU
Norwegian University of
Science and Technology

Sondre Taugbøl Lomeland

Synthesis and catalytic testing of oxazoline-NHC-gold(III) and β-hydroxyamide-NHC-gold(III) complexes

Master's thesis in Chemical Engineering and Biotechnology
Supervisor: Anne Fiksdahl
Co-supervisor: Helgi Freyr Jónsson
June 2021

Norwegian University of Science and Technology
Faculty of Natural Sciences
Department of Chemistry

NTNU
Norwegian University of
Science and Technology

Preface

I would like to thank my supervisor, professor Anne Fiksdahl, and co-supervisor, PhD candidate Helgi Freyr Jonsson. Being part of a research group within such an interesting field of chemistry, and with so experienced and helpful researchers have led to the desire to continue working within academia.

Also, I would like to thank Torun M. Melø for assistance with NMR, Susana V. Gonzalez for assistance with MS, Ida-Marie Høyvik for access to the Idun computer cluster and Rogar Aarvik for supplying chemicals.

Lastly, I would like to thank my friends and colleagues, with whom I have had lunch with the previous year. The thesis was written during the corona pandemic, where social interaction is scarce. A good conversation has kept the head sane and the mood bright.

Abstract

A set of diastereomerically pure bidentate oxazoline-NHC gold(III) complexes were attempted synthesized. A range of different methods were carried out and reported, with varying results. Oxazoline-NHC-gold-Cl complexes were instable towards oxidation with $PhICl_2$. Cationic oxazoline-NHC-Au^+ complexes were prone to decomposition. Stabilization with polar solvents, nitrone and different silver salts was carried out. A synthesis by transmetalation could not be successfully carried out due to oxazoline ring opening. The methods failed to selectively prepare diastereomerically pure bidentate oxazoline-NHC gold(III) complexes, but could prove effective in other ligand systems.

Diastereomerically pure β-hydroxyamide-NHC gold(III) complexes were prepared and tested in the gold-catalyzed propanation reaction of propargyl acetate with styrene. The complexes were catalytically active, catalyzing the reaction within 15 min. Based on chiral HPLC analysis, the product was a racemic mixture of enantiomers.

Complementary to experimental work computations on DFT level were carried out. Geometries were optimized to better understand the three-dimensional nature of the compounds. A computational study of the gold-catalyzed propargyl mechanism was initiated, where the acetate rearrangement upon gold-coordination was investigated. The initial structure, transition state configuration and final structure were identified and optimized.

Sammendrag

Et sett av diastereomerisk rene bidentat oxazolin-NHC-gull(III) komplekser ble forsøkt syntesisert. En rekke ulike metoder har blitt utført og rapportert. Oxazolin-NHC-gull-Cl komplekser var ustabile ved oksidering med $PhICl_2$. Kationiske oxazolin-NHC-Au^+ komplekser var utsatt for dekomponering. Stabilisering med polare løsningsmidler, nitron og ulike sølvsalter ble forsøkt. Syntese gjennom transmetallering fungerte ikke, på grunn av oxazolin ring-åpning. Selv om syntesen av diastereomerisk rene bidentat oxazolin-NHC gull(III) komplekser mislyktes kan rapporterte metoder vise seg å være effektive på andre ligandesystemer.

Diastereomerisk rene β-hydroksiamid-NHC gull(III) komplekser ble fremstilt og testet i den gull-katalyserte syklopropaneringsreaksjonen med propargyl acetat og styren. Kompleksene var katalytisk aktive, hvor reaksjon med full omsetning var oppnådd innen 15 min. Basert på analyser med kiral HPLC viste det seg at kompleksene ikke påvirker enantioselektiviteten, da det ble observert en rasemisk blanding av enantiomerer.

Beregninger på DFT-nivå ble gjennomført komplementært til det eksperimentelle arbeidet. Geometrioptimalisering ble gjennomført for å få en bedre tredimensjonal forståelse av fremstilte stoffer. Fra den gull-katalyserte propargylacetat reaksjonen med styren ble acetat-omleiringen modellert. Startstruktur, overgangstilstand og sluttstruktur ble identifisert og optimalisert.

Contents

List of compounds

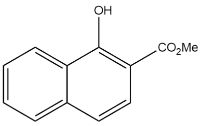

1

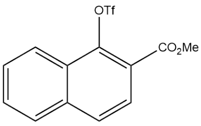

2

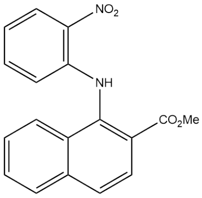

3

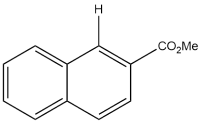

3b

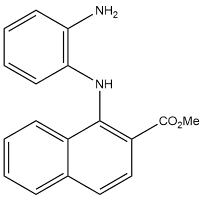

4

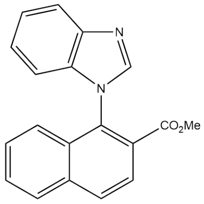

5

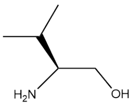

6

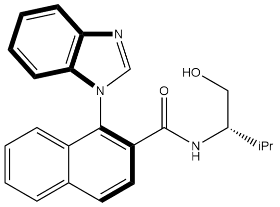

7a

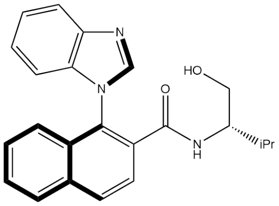

7b

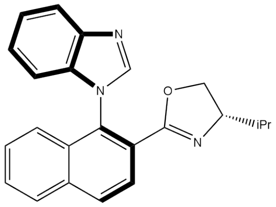

8a

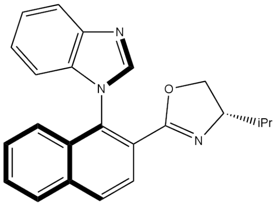

8b

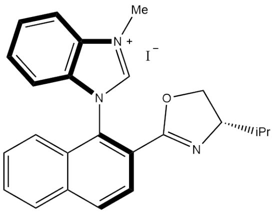

9a

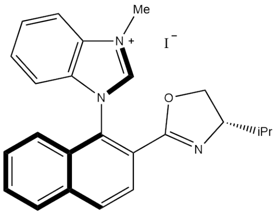

9b

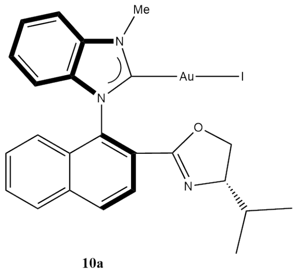

10a

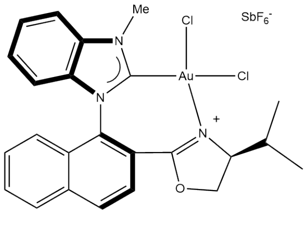

11

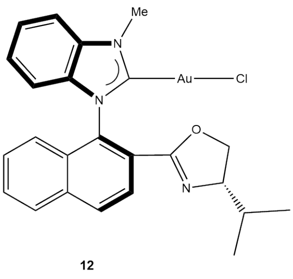

12

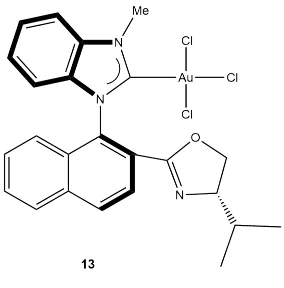

13

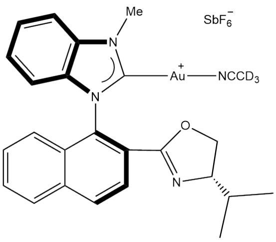

14

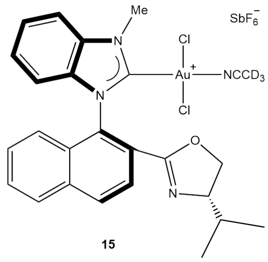

15

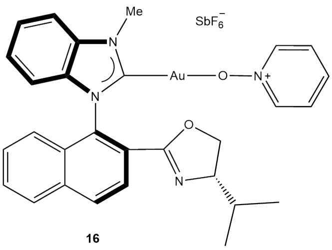

16

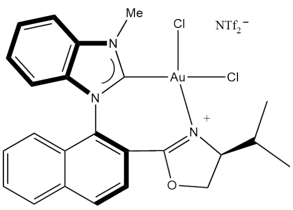

17

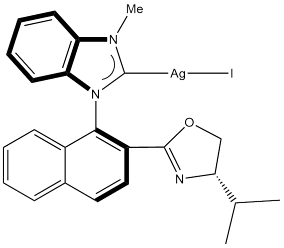

18

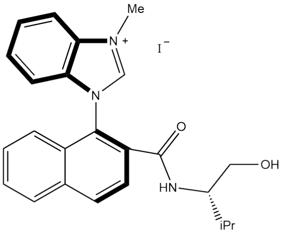

19a

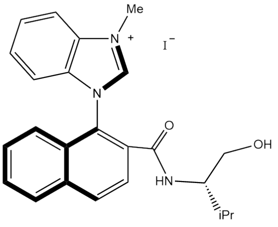

19b

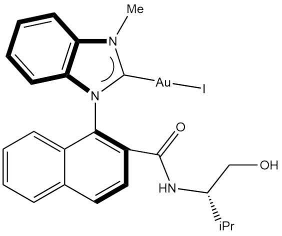

20a

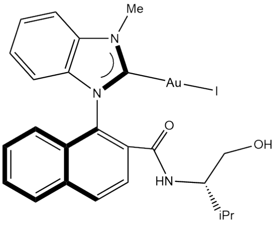

20b

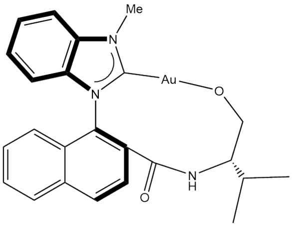

21

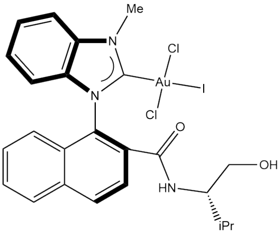

22a

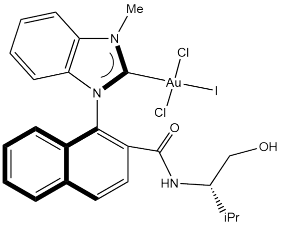

22b

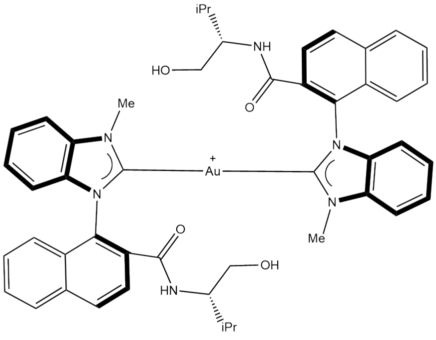

23a

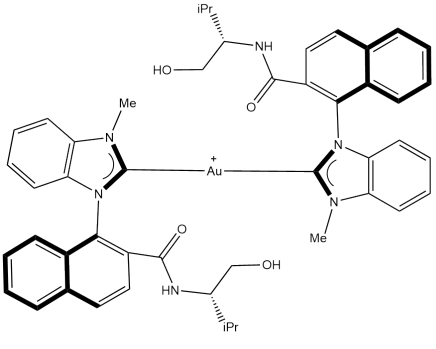

23b

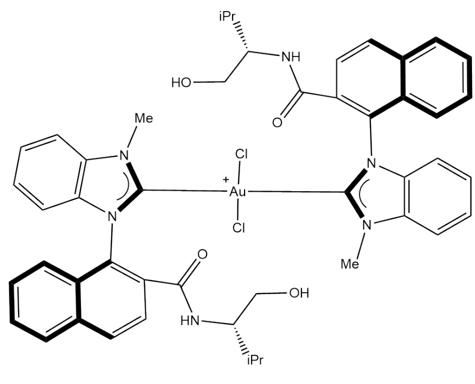

24b

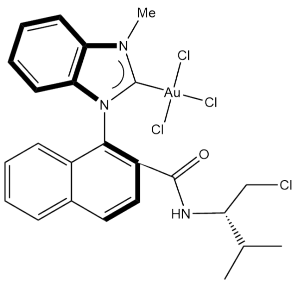

25

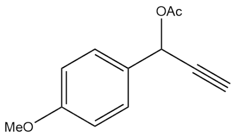

26

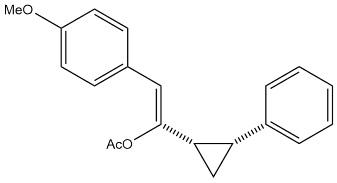

27a

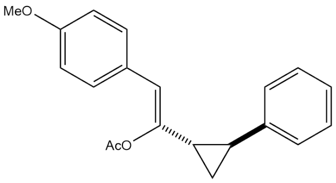

27b

1 Introduction

Gold is the rock star of chemical elements. Ask anybody on the street, and they will tell you they know about gold. It has been collected and used as a symbol of wealth throughout the history of mankind. Due to its chemical inertness, elemental gold can be found in nature as nuggets, not requiring any processing. Gold prospecting has typically been carried out from river deposits and ore mining. What makes gold so valuable, apart from its natural beauty, is the amount of work necessary to extract only a small amount of the noble metal. Despite the immense work to obtain gold, it has been extracted from every continent on the planet.[1] In ancient times Egypt was the main producer of gold. Already at 1300 BC, large networks of underground mines had been established in the Nubian desert to exploit the rocks rich in vein gold. Over 100 mines were built in the area, protected by a series of forts. With the large production of gold, Egypt established its dominance in the Middle East.[2] Gold played an important role in the evolution of the commercial revolution in medieval Europe. The first introduced high karat gold coins were minted in Florence and Genoa. A rapidly increasing demand for means of payment forced countries to develop an alternative to the existing silver denier. The higher value of the gold coins enabled large scale transactions to continue during the purchasing power boom.[3]

In its metallic form, gold is non-toxic and is even used as a food decoration in the form of gold leaves. Gold salts, however, are toxic. Gold chloride acts as a neurotoxin and lethal poisoning has been documented from ingestion of potassium gold cyanide.[4] The serum level was below the toxic threshold of cyanide. Despite its toxicity, certain gold salts are used as drugs. Auranofin, sodium aurothiomalate, and aurothioglucose have all been used to treat rheumatoid arthritis, an autoimmune disease that affects the joints.[5] The usage of gold salts in treatment of rheumatoid arthritis, also called chrysotherapy, is limited to gold salts with the oxidation state I. Gold(III) complexes have been proven to irreversibly oxidize the disulphide bonds in peptides and proteins, making them unsuitable for drug use.[6] Recent advances in gold chemistry have provided a range of gold complexes with lipophilic tunability showing promising anti-cancer activities.[7]

Compared to other transition metals, the chemistry of gold has been severely under-developed. The inert character of metallic gold has prevented an earlier development of gold as a catalytically active species. A serious interest in gold in heterogeneous catalysis followed the work by Hutchings on hydrochlorination of acetylene in 1985[8] and Haruta and Yamada on oxidation of CO at low temperatures in 1987.[9] It turned out that the hydrochlorination of acetylene correlates to the reduction potential of the metal catalyst, and gold has the highest reduction potential of all transition metals. The gold catalysts used in the oxidation of CO proved more active and were much more stable against water than the conventionally used Hopcalite catalyst. In the year 1990 the annual number of publications on gold catalysis was about 100, predominantly in the field of heterogeneous catalysis. Already in 2005, the annual number of publications was well above 700, with continuing exponential growth. Still, the majority of punlications consisted of heterogeneous catalysis. From the early 2000s the same rapid growth of number of publications occurs in the field of homogeneous gold catalysis.[10]

Even though attempts to coordinate alkynes to gold cations were documented already in the 1960s, the field of homogeneous gold catalysis did not receive much attention until the work by Teles et al. on the addition of alcohols to alkynes, using cationic phosphine gold(I) complexes, published in 1998. The replacement of mercury(II) ions provided higher total turnover numbers and turnover frequencies, using a non-toxic catalyst.[11] There are other studies which helped cast light on gold catalysis and its great potentials, such as asymmetric aldol reaction with ferrocenylphosphine-gold(I) in 1986 by Ito and Hayashi et al.[12], transformations of methyl propargyl ethers to α, β-unsaturated ketones in 1991 by Utimoto and coworkers.[13] and synthesis of substituted furans and phenols from allene and propargyl ketones in 2000 by Hashmi et al.[14] Pioneer work in the last two decades from the Nolan group[15], the Toste group[16], the Hashmi group[17] and the Zhang group[18] has been important for the continuing rapid development of homogeneous gold catalysis and its application in synthetic organic chemistry. As cleverly formulated by Nolan, we are observing a catalytic gold rush.[19]

This section will cover the most important theory of homogeneous catalysis applied to gold complexes. A basic introduction to computational chemistry will be covered, as well as the chemistry of the synthetic pathway from starting compound to ligand coordination. The theory is built upon a previous year's project, and extended where necessary.

1.1 Mechanism

The development of gold catalysis is highly sought after. The gold strongly coordinates to unsaturated carbon-carbon bonds, yet still poorly coordinates to other functional groups. The most common reaction pattern in gold catalysis to date is the addition of nucleophiles to alkynes. The gold catalyst coordinates to a π-system, activating it for nucleophilic attack. This usually occurs anti to the gold. Most nucleophiles undergo deprotonation upon addition to the multiple bonds. Reprotonation of the substrate releases the gold and the catalytic cycle is complete.[20] A general reaction mechanism of gold catalysis is shown in Scheme 1. The active species is often a gold cation. The activation of the gold catalyst usually involves the removal of a ligand, which can be carried out with either silver salts, bases or acids, depending on the ligand system. Interestingly, choice of activator may influence the regioselectivity of the reaction.[21] The ligand removal is necessary to free a coordination site for the substrate coordination.

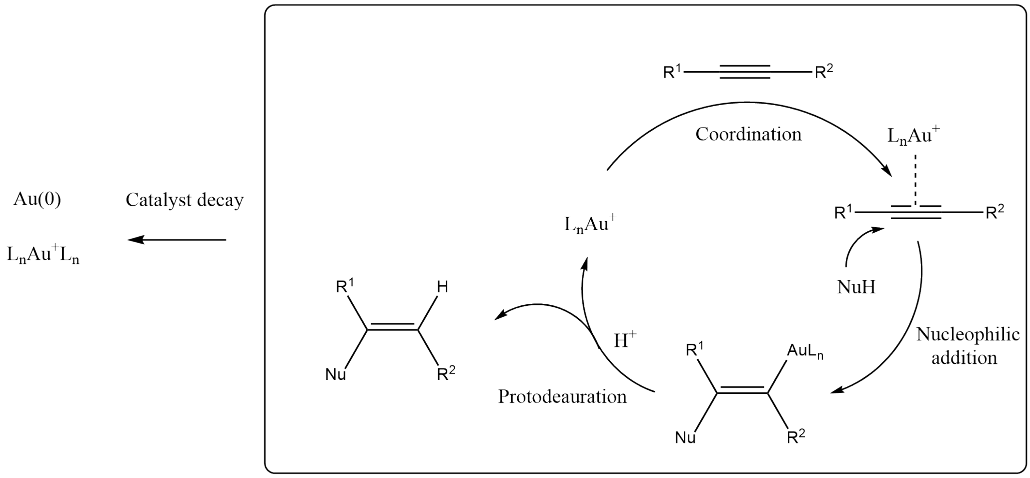

Scheme 1: The major stages of a catalytic cycle of gold-catalyzed nucleophilic addition to alkyne.[22]

Ligand effects on the reaction rate, selectivity, and turnover number (TON) is yet to be fully understood, but one might assume that electron-donating ligands will increase and electron-withdrawing ligands will decrease the rate of protodeauration. Donation of electrons promotes cleavage of gold from the substrate. Accordingly, electron-withdrawing ligands can be assumed to increase the rate of electronic activation of multiple bonds, which is determined by the electrophilic character of the gold catalyst. Ligand systems were functional groups can coordinate to the antiapproaching nucleophiles show promising results, significantly lowering needed catalytic loading. The development of catalysts with high TON is necessary to move the reactions from lab scale to large scale production.[23]

The nucleophilic attack of the activated multiple bonds is, however, not only influenced by ligand effects. The η^2-activated gold complex formation faces competition from additives and solvents, that can coordinate with the cationic gold. Studies by Lein et al. described the catalytic addition of water to propyne by $AuCl_3$, where solvent molecules and hydrogen bonds may play a significant role in the catalytic pathway.[24] Although the exact mechanism may differ, depending on substrate and catalyst, the core principle remains the same: activation of multiple bonds towards nucleophilic attack.

Gold catalysts' high affinity to π-systems is partly a consequence of the high relativistic effects. Electrons in the 6s orbital have so high velocity that relativistic mass is no longer negligible. The calculation of relativistic mass is given in equation 1.1, where m_e and v_e are the electron mass and velocity, respectively. As the electron's velocity approaches the speed of light c, the electron's mass would become infinite.

$$m_{rel} = \frac{m_e}{\sqrt{1-(v_e/c)^2}} \tag{1.1}$$

The high relativistic mass of the electrons causes the 6s orbital to contract and lower its energy. This indirectly affects the 5d orbital, increasing its energy.[25] Besides giving gold its characteristic color, the convergence of the 6s and 5d orbitals results in a metal center more acceptive towards σ-symmetric L → M donation, making it a stronger electrophile.[26] Compared to other group 11 metal-phosphine complexes, Au-phosphine complexes show significantly higher s-orbital occupancy, and M-P and M-Cl bond distances of $[MCl(PH_3)_n]$ complexes are shorter for gold complexes than similar silver analogs.[27] Because of the great extent of s-d orbital hybridization, a strong covalent character is observed in gold chemistry. Due to gold's high electronegativity, the metal-halide bond is mainly covalent. The strong covalent character is restricted to gold-halide bonds, as no other transition metal exhibits similar electronegativity.[28] The high reactivity of organocuprate with electrophiles cannot be matched by organoaurate analogs. The lower energy diffuse 5d orbital does not have a similar nucleophilic character as copper's 3d orbital. The higher valence intermediate $R_2(E)M(III)$ after coordination with the electrophile is also relatively stable for gold and does not readily decompose. The gold-carbon bond is significantly more stable than copper-carbon bonds.[29]

1.2 Ligand effects

The ligands' ability to accept or donate electrons are linked to the frontier orbital energy levels. Generally, ligands with high energy HOMO orbitals have good donating abilities. Similarly, ligands with low energy LUMO orbitals have good electron-accepting capabilities. As shown for ligands of class I, II, and III in Figure 1, there is often a correlation between strong donor effects and weak acceptor effects, and vice versa. The development of class IV ligands is wanted, as strong σ-donor and π-acceptor capabilities will contribute to metal complex stabilization.[30]

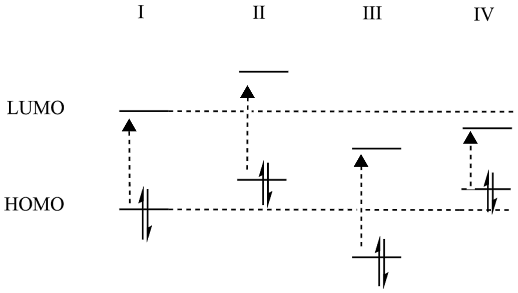

Figure 1: Visualization of different ligand classes and their frontier orbital energies

For a long time, the Tolman electronic parameter TEP has been used as a tool for describing the relative donor and acceptor strength of metal ligands by measuring the frequency of the A_1 vibrational mode of CO stretching in metal carbonyls. The idea is based on the fact that electron-donating ligands will increase the π backdonation of the metal center to the carbonyl ligand. The electrons are donated to the antibonding π^* (CO) orbital, which weakens the C≡O bond strength and a lower wavenumber is measured. Ligands with a weak donation or strong acceptor capabilities will reduce the amount of backdonation from the metal center to CO and a relatively larger wavenumber is observed.[31] TEP has later been proven to be inaccurate, as one of the main presumptions is invalid, namely that the carbonyl A_1 symmetrical mode is free of coupling with other vibrational modes in the complex. There have been studies proving significant mode-mode coupling and non-inverse relationships between the M-L and M-CO bond strengths, which can lead to larger coupling errors than the TEP variation itself.[32] Instrument improvement with terahertz spectroscopy enables direct measurement of FTIR absorption of the metal-ligand stretching frequencies. The development of the metal-ligand electronic parameter from the local metal-ligand stretching force constant gives quantitative data of metal-ligand bond strength.[33]

A study on ligand effects on homogeneous gold(I) catalysis has been carried out. As shown in Scheme 1 most gold-catalyzed reactions undergo electrophilic activation of a multiple bond (coordination), protodeauration to yield product, and regenerated cationic gold complex. From a series of isolated vinyl gold complexes, the rate of protodeauration was measured with ligands of different electronic characters. As expected, electron-donating groups like OMe promote gold cleavage and speeds up the reaction. Electron withdrawing groups like CF_3 slowed down the reaction. Activation of the multiple bond and vinyl gold formation was shown to speed up by electron-withdrawing groups and slowed down by electron-rich ligands. After protodeauration, the cationic gold species L_nAu^+ can decompose to Au^0 and L_2Au^+, which is catalytically inactive. Interestingly, it doesn't seem to be any strong correlation between electronic effects of ligand and rate of decay. The mechanism of cationic gold decay is yet to be fully understood, and seem to be highly reaction specific.[22] The group has later extended the research to include silver effects, additive effects, counterion effects, and a more thorough investigation of catalyst decay.[34]

The steric effects of the ligands are also of great interest, especially in asymmetric catalysis. The Tolman cone angle (θ) was developed in 1970 and is based on the apex angle from a zinc metal center to the outer edges of the ligand. The model assumes a constant metal-phosphine distance of 2.28 Å for monodentate, symmetric ligands.[35] The model works well for small phosphine ligands such as PH_3 and $P(CH_3)_3$, but fails for larger ligands. Ligands are folded as compact as possible and other conformations are not considered. This leads to an underestimation of the calculated cone angle.[36] Other models have been developed to better describe the wide variety of ligand classes. The solid angle descriptor has been developed, which quantifies the length of the cone and calculates an average of stable conformers.[37] The development of the SambVca program has provided a readily available tool for quantifying the steric properties of ligands, calculating the buried volume.[38] Ligand knowledge base for monodentate P-Donor ligands has proved helpful in mapping the ligand space with principal component analysis (PCA) of significant descriptors.[39]

1.2.1 Phosphine type ligands

Phosphine ligands are widely used as metal ligands, as they can serve as a large steric backbone of the catalyst and provide catalyst stability from electron donation. Gold-phosphine complexes have been intensively studied, primarily for their catalytic capabilities, but also to some extent due to their anticancer activities[40] and photophysical properties.[41] Both gold(I)- and gold(III)-complexes show promising quantum yields, and can become a key component in future organic light-emitting diodes as phosphorescents emitters.[42,43] They also show great promise as ancillary ligands in gold-catalyzed asymmetric reaction. Bimetallic gold chlorides with chiral phosphine ligands such as BINAP, BIPHEP, or SEGPHOS have been proven to catalyze certain reactions with good enantioselectivity. These phosphine ligand classes are common to use in homogeneous catalysis, and are shown in Figure 2. The ligands are classified as atropochiral biaryldiphosphines. They are C_2-symmetric but chiral due to the restricted bond rotation between the two aromatic ring systems. Tethering the phosphine with a large backbone structure ensures that the ligand will stay more coordinated with the metal center. This forces the substrate to coordinate in a certain direction, which can promote enantioselective reactions. For bidentate systems, different backbone structures alter the P-M-P angle, which in term affect the catalytic abilities of the complex.[44] The aromatic substituents on the phosphorus atoms also play a significant role in the catalytic activity. It has been documented how the more steric hindered DTBM-SEGPHOS has a weaker enantioselective control than DM-SEGPHOS in hydrative cyclization reactions.[45] Axially chiral bifunctional phosphine ligands can also be coordinated to gold. Such a ligand system has been proven to perform well in the alkyne isomerization of 2,5-hihydrofuranes, producing high diastereoselectivities. The proposed mechanism of the selectivity is shown in Scheme 2.[46].

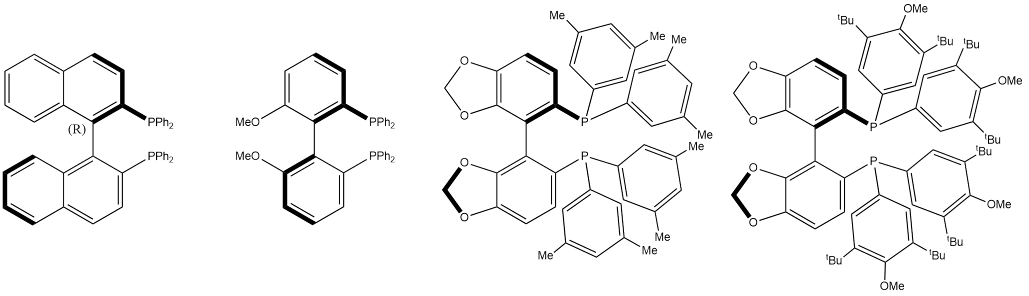

(R)-BINAP (R)-MeO-BIPHEP (R)-DM-SEGPHOS (R)-DTBM-SEGPHOS

Figure 2: Some common bisphosphines ligands used in asymmetric catalysis.

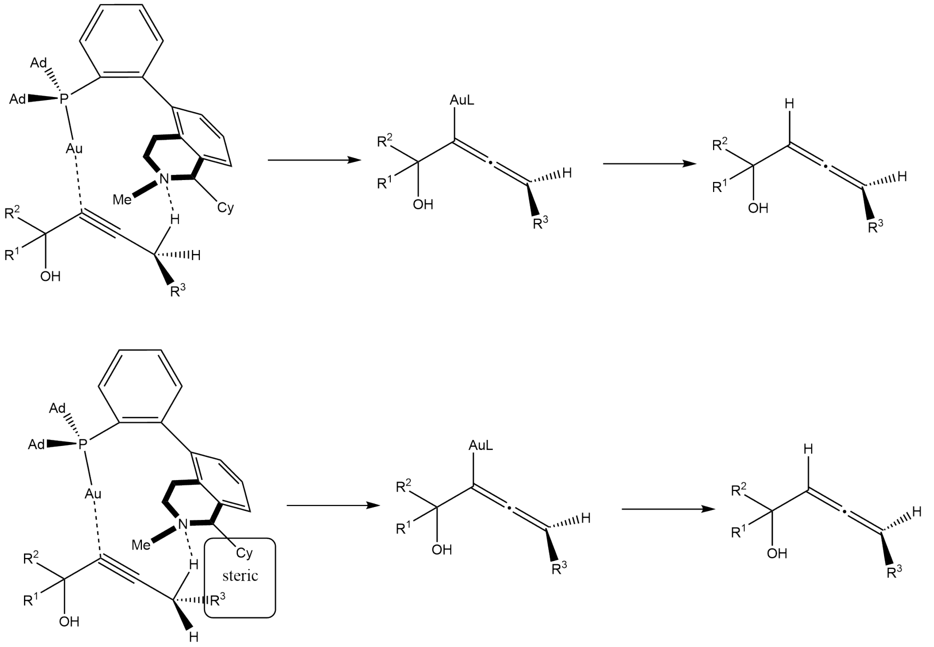

Scheme 2: Mechanism towards diastereoselective alkyne isomerization with axially chiral bisfunctional phosphine ligand.

1.2.2 N-Heterocyclic carbenes

Carbenes are often used in coordination with metal complexes. The divalent character of the carbene ligand provides complex stabilization through strong electron donation. N-Heterocyclic carbenes (NHC) were first isolated in 1991. The first crystalline compound isolated was an imidazol-2-ylidene ring with adamantyl N-substituents. The bulky substituents helped to avoid dimerization.[47] For bent carbenes there are 4 possible electron configurations for the two non-bonding electrons, namely triplet $\sigma^1 p_\pi^1$, singlet σ^2, singlet p_π^2 and the excited singlet $\sigma^1 p_\pi^1$ state (see Figure 3). The ground state configuration depends on the energy difference between the σ and p_π orbitals. In order to impose a singlet ground state, the energy difference must be above 2 eV.[48] NHC derivatives of imidazolium and imidazolinium possess the triplet ground state, due to the neighboring nitrogen atoms. Inductive effects cause the nitrogen to pull on the σ electrons, stabilizing the orbital. Electrons are also donated to the p_π orbital, further increasing the energy difference between the two orbitals.[49]

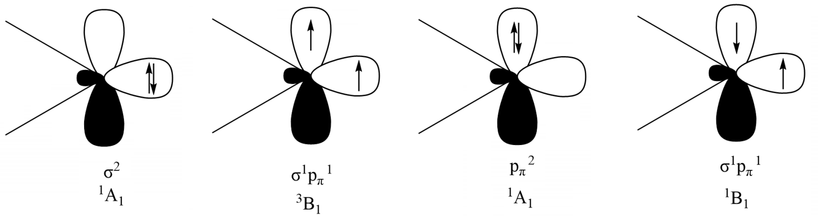

Figure 3: The 4 possible configurations of free carbenes.

The potential of the new ligand class was documented quickly after being introduced, surpassing the ubiquitous phosphine ligand in several reaction systems such as Ru-catalyzed ring opening metathesis polymerization (ROMP)[50], mildly pressurized Ir-catalyzed hydrogenation of alkene, and Pd-catalyzed Suzuki-Miyaura cross-coupling.[51]

Since many gold catalysts are activated by the generation of a cationic species upon halide removal, electron-donating ligands are desired. NHC ligands exhibit strong σ-donor and π-acceptor capacities, stabilizing the active species.[52] The possibilities to vary ring substituents and backbone structure allow fine-tuning of both electronic and steric properties. There have been developed a range of different types of NHC ligands, but some common ones are illustrated in Figure 4.[53] Unlike phosphine ligands, NHC does not dissociate and associate during a reaction and an excess of ligands is not required to avoid metal aggregation. The phosphine ligands are also prone to oxidation[54].

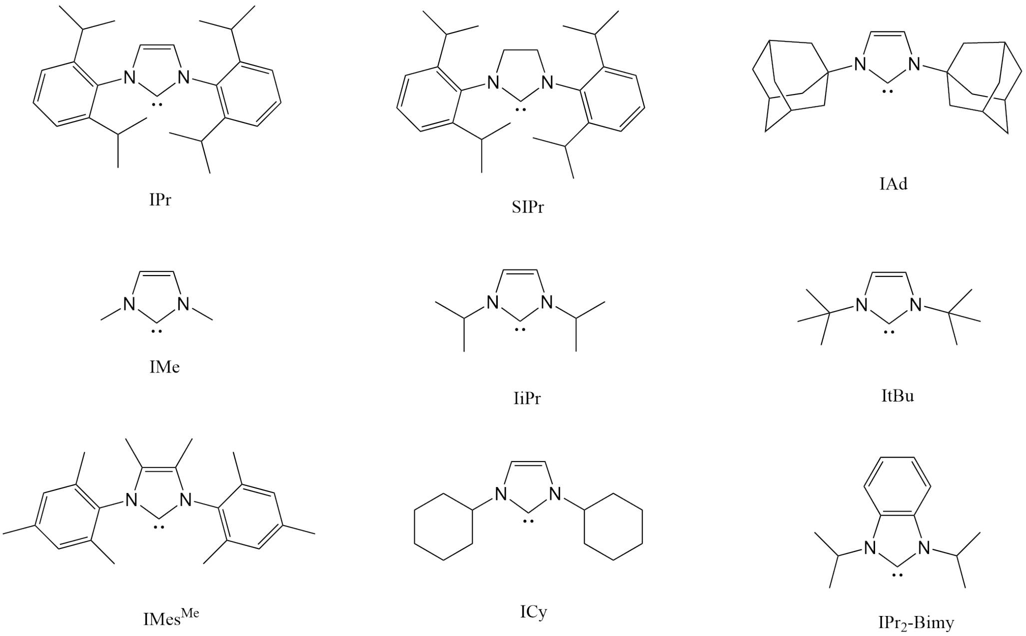

Figure 4: Some common NHC ligands often used in coordination with transition metals and their generally accepted nomenclature.

An important part of the ligand properties is the possibility to control enantioselectivity. Asymmetric catalysis with chiral N-substituents has yielded moderate results[55,56]. More successfully are certain sterically demanding N-substituents such as (-)-isopinocampheyl and bornyl.[57] It seems to be difficult to develop reliable N-substituted NHC ligands that perform well in asymmetric catalysis. Internal rotation around the N-C axis and substituent flexibility limit the steric control. NHC ligands of imidazolinium salts with a substituted backbone have been applied to asymmetric catalysis. The substituted backbone is distant from the metal center, but can influence the conformation of the N-substituents. Enantioselective ruthenium olefin metathesis has been carried out with a C_2-symmetric Grubbs catalyst. Mono-o-substituted aryl groups are arranged trans to the backbone substituents. This enables ligand stereocenters close to the metal center, as well as restriction of rotation along the N-C axis. In comparison, mesitylene N-substituents show poor enantioselectivity. This is expected, as the backbone substituents on the imidazolinium ring are too distant to provide any steric control. The structure of the mesitylen-substituted (IMes) Grubbs catalyst, and the desymmetrized catalyst are shown in Scheme 3.[58]

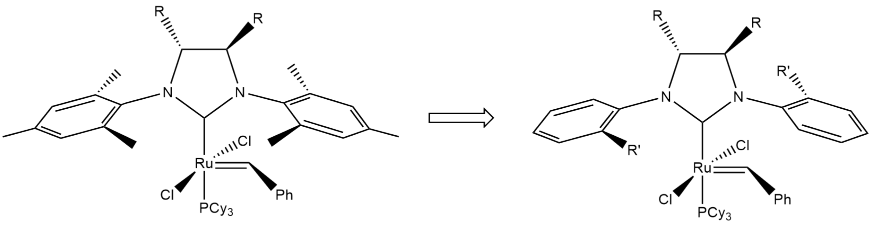

Scheme 3: Improvement in enantioselective control of the IMes/ruthenium system.

1.2.3 Oxazoline ligands

The oxazoline ring is a N-donor type ligand that has a great potential within asymmetric catalysis. The ligand class possesses properties necessary for application within coordination chemistry. It is a five-membered ring with an oxygen atom and a nitrogen atom. Different isomers can be prepared, as shown in Figure 5. There also exist a set of isomers with adjacent nitrogen and oxygen atoms, known as isoxazoline rings. However, the N-O bond is weak, and the ring structures are unstable.

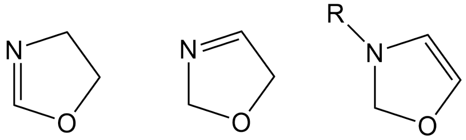

Figure 5: General structure of 2-oxazoline (left), 3-oxazoline (center) and 4-oxazoline (right)

The synthesis of the ligands is straightforward. They are versatile and can be modified for specific requirements. Chiral 4,5-dihydro-1,3-oxazoles can easily be synthesized from readily available amino alcohols. Upon coordination, the stereogenic center of the oxazoline lies close to the metal center, affecting the enantioselectivity of the reaction.[59]

The nitrogen can coordinate directly with the metal center, forming a monodentate ligand.[60] Bidentate ligand systems can be generated with N,C-donors[61] *N,N'*-donors,[62] *N,O*-donors[63,64], *N,P*-donors[65], and others. Chiral bis(oxazoline) ligands have been applied to a range of asymmetric reactions. The C_2 symmetric conformation with tunable chiral substituents near the metal center make high enantioselectivity possible. There have been synthesized a range of different bis(oxazoline) ligands, but CH_2- and pyridine-linked oxazolines are common (see Figure 6). They are abbreviated as BOX and PyBOX, respectively. Reactions such as allylic substitution[66], allylic oxidation[67], cyclopropanation[68] have been carried out with high enantioselectivity.

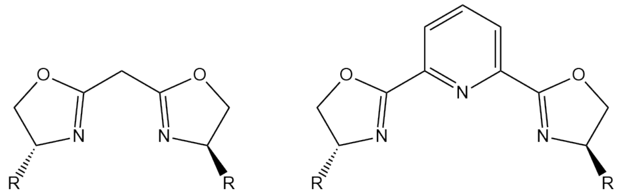

Figure 6: BOX (left) and PyBOX (right) ligands, used in asymmetric catalysis

Studies have been carried out on bidentate ligand systems containing both NHC and oxazoline moieties. The electron rich NHC provides stability to the metal center and the oxazoline provides the chirality. Both oxazoline-NHC ligands linked at the 2-position and the 4-position of the oxazoline ring have successfully been applied to asymmetric catalysis. A set of rhodium complexes has been developed and applied to hydrosilylation of ketones with high enantiomeric excess by Grade and co-workers[69], while Burgess and co-workers have synthesized iridium complexes which perform well in asymmetric hydrogenation.[70] The complexes developed by Grade and Burgess are shown in Figure 7.

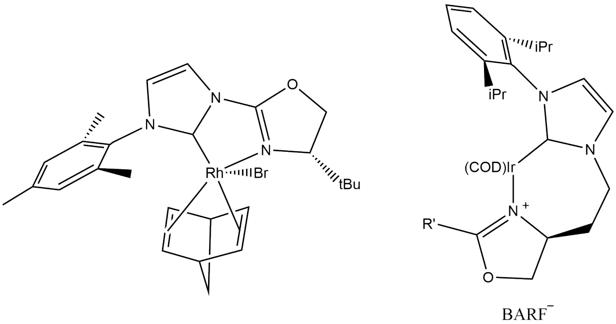

Figure 7: NHC-oxazoline ligands linked in 2-position (left) and 4-position (right) of the oxazoline

1.3 Counterion effect

In reactions proceeding through a cationic gold species, the role of the counterion may play a significant role. Weakly coordinated anions leave the gold cation with a free coordination site, more available for catalytic activation. Silver salts are commonly used as halide scavengers and a source of counterion. Parameters such as counterion choice, the equivalence of AgX, and order of addition may all influence the outcome of the reaction. Removal of chloride from phosphine gold complexes such as JohnPhosAuCl has been shown to form chloride-bridged digold complexes when reacting with silver salts with weakly coordinating anions (see Scheme 4). The digold complex is less catalytic active, and this is especially important in reactions where the substrate struggles to cleave the bridge. The difference has been documented, where [2+2] intermolecular cycloaddition could be carried out with digold complexes in the absence of silver salt, as opposed to 1,6-enyne cycloisomerization. The enyne is unable to cleave the chloride bridge and the reaction doesn't take place. In such reactions, mixing the gold catalyst and substrate prior to silver salt addition will give better results.[71]

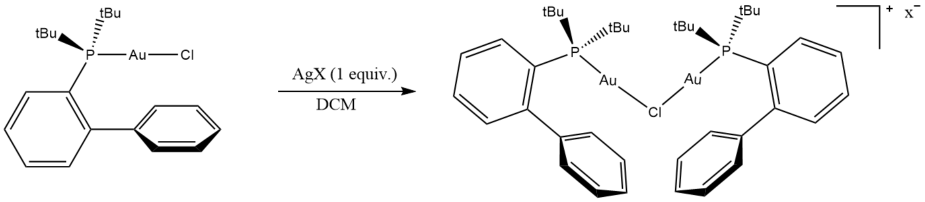

Scheme 4: Formation of chloride-bridged complex upon addition of weakly coordinating counterion to JohnPhosAuCl.

Although the mechanism of gold catalysis is proposed to go through the cationic gold species, various studies have shown interest in better describing silver effects in gold catalysis. Due to large inconsistencies in reported results from different research groups based on slightly different approaches, there has to be a more complex mechanism of gold-silver interaction that is yet to be fully understood. The silver salt might not only act as a halide scavenger in order to generate the catalytically active gold cation. In certain alkyne hydration reactions, gold cations show no activity in the absence of silver salts. (IPr)Au-Catalyzed hydration of diphenylacetylene was shown to be dependent on the loading of $AgSbF_6$. Lower silver correlated to a lower yield. An extensive overview of the silver effects on various previously reporter gold-catalyzed reactions has been documented.[72] Gold catalysis can be categorized into the following three categories: Type 1: "Genuine" Gold Catalysis (Scheme 5). Reactions such as phenol synthesis by furan-yne rearrangement[73] or oxidative coupling of gold and boronic acid[74] show little effects by the addition of silver to the cationic gold catalyst. Type 2: Au/Ag Bimetallic Catalysis (Scheme 6). Reactions such as 3,3-rearrangement of enynyl acetates[75] or 5-endo-dig carbocyclization of acetylenic dicarbonyls[76] cannot be catalyzed by gold nor silver alone. Only in a combination of cationic gold and silver salt will the reactions proceed. Type 3: Silver-Assisted Gold Catalysis (Scheme 7). In these types of reactions, the Au cation is catalytically active, but the presence of silver salt will increase the yield. The synthesis of 2-cyclopentenones by Rautenstrauch rearrangement[77] falls within this category.

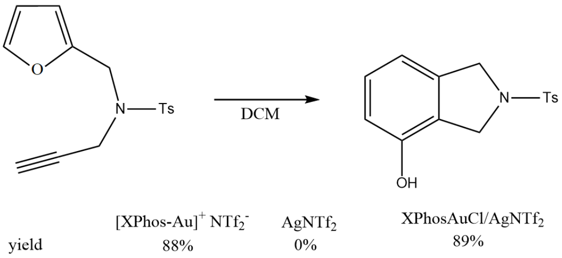

Scheme 5: Type 1 silver effect: Genuine gold catalysis. There is no difference in yield by filtration of silver salt.

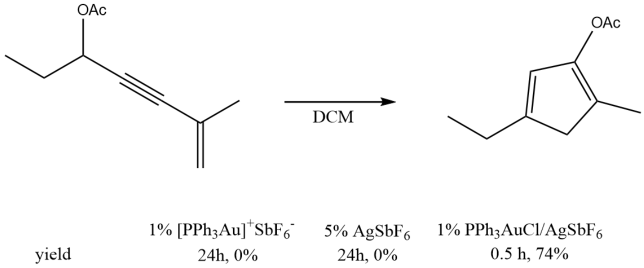

Scheme 6: Type 2 silver effect: Bimetallic catalysis. The gold complex is only active in the presence of silver salt.

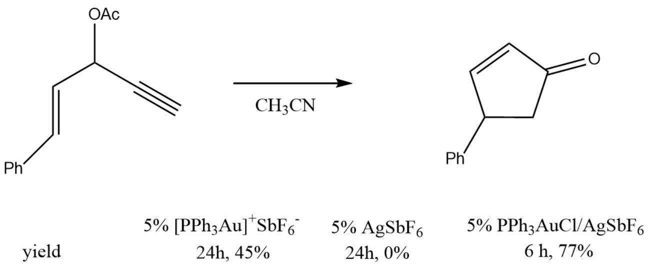

Scheme 7: Type 3 silver effect: Silver assisted catalysis. The gold complex is active alone, but higher yields are obtained in the presence of silver salt.

In the earliest stages of gold catalysis development, chloride was the predominant choice of counterion. Data from nearly 3000 references on gold(I) and gold(III) chemistry with varying counterions in the period of 2000-2013 have been collected and presented in a review article by Jia and Bandini.[78] The combined use of the weakly coordinating ions SbF_6^-, OTf^-, NTf_2^-, and BF_4^- make up 67% of all references collected.

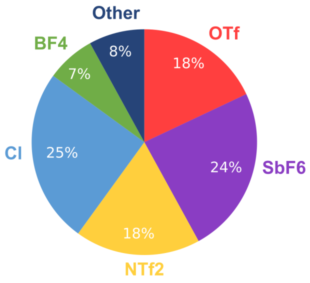

Figure 8: Usage of different counterions in gold-catalyzed reactions from 2000 to 2013.

The choice of counterion can also tune the regioselectivity. Gold-catalyzed tandem reactions of dearomative spirocarbocyclization and aza-Michael addition can be carried out with the addition of AgOTf. The final aza-Michael addition is not observed when using $AgNTf_2$. This is likely due to the NTf_2 counterion's high affinity to gold, but the low affinity to hydrogen bonding. The triflate counterion has a stronger hydrogen bonding character. This makes the amine group more nucleophilic and strengthens the π-activation of the cationic gold species. DFT calculations show that in the NTf_2 intermediate Au··N and Au··C distances are 2.162 Å and 3.208 Å, respectively, while for the OTf intermediate Au··O and Au··C distances are 2.672 and 2.322 Å.[79]

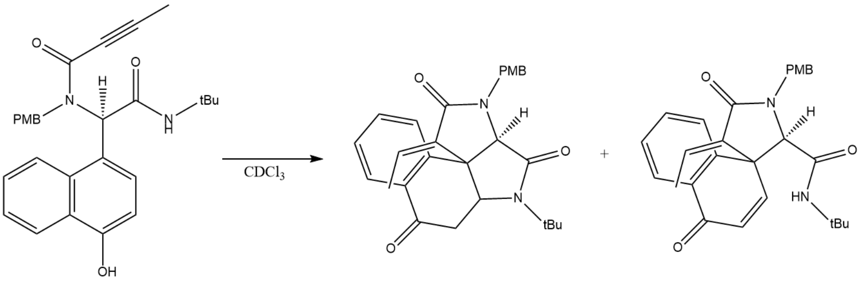

Catalyst/Counterion	Yield %	Yield%
$Au(PPh_3)Cl/AgOTf$	92	2
$Au(PPh_3)Cl/AgNTf_2$	0	93

Scheme 8: Regioselective tandem cyclization by counterion choice.

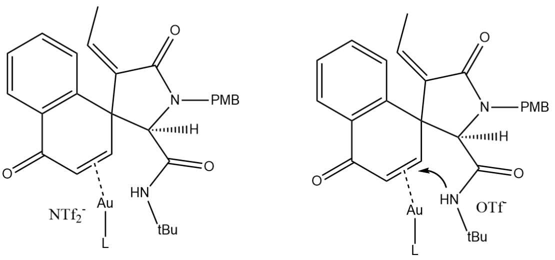

Figure 9: Mechanism for gold activated aza-Michael addition based on DFT calculated intermediates.

1.4 Gold(III) chemistry

After the realization of great potential gold(I) in homogeneous catalysis, the field continues to expand at an impressive rate. The higher valent gold(III) is lagging behind. To this day, the usage of gold(III) in catalysis is still to a large degree restricted to inorganic salts.[80] Unlike gold(I), the gold(III) metal center is less affected by relativistic effects, and the covalent radii of gold(III) complexes are similar to corresponding Ag(III) complexes.[81] Due to the high redox potential of gold(III) complexes, they are prone to undergo reductive elimination to either gold(I) or gold(0) species. The redox potential of Au(III)/Au(I) is 1.41 V and the Au(III)/Au(0) potential is 1.50 V. This is significantly higher than the M(II)/M(0) redox potential of palladium and platinum, which is 0.91 V and 1.18, respectively.[82] Since gold(III) are readily reduced, it can be difficult to determine whether the reaction mechanism involves a gold(I) or gold(III) metal center. In order to stabilize the gold(III) complexes, strongly donating ligands and chelated ligand systems are often synthesized. The metal-center stabilization may, however, reduce the catalytic activity of the gold(III) catalyst.[83] The fine balance between chemical stability and catalytic activity of gold(III) catalysts is the primary reason that most attention earlier has been dedicated to the easier-to-modify gold(I) complexes. In recent years several approaches to develop new gold(III) complexes have been documented.

A key factor to successfully develop the area seems to be the tunability of the ligands. The expanding field of NHC-type ligands has been used extensively for gold(I) complexes, but are also available as gold(III) complexes by oxidation with iodine(III), Cl_2 or Br_2 reagents. A range of Au(III) bis-NHC complexes has been documented by Nolan and his research group.[84] There has also been carried out oxidation of gold(I)-NHC complexes with aqua regia in decent yields. The synthesis is straight forward, but there is a possibility of substitution of one of the unsaturated NHC-backbone.[85]

A motivation for expanding the knowledge of gold(III) catalysts is the potential for asymmetric synthesis. Due to gold(I)'s intensive development over the last years, several ligands that are able to induce an asymmetric pathway have been synthesized. Because of the distance from the active site, the ligands need to be bulky in order to affect the enantiomeric selectivity. As opposed to the linear gold(I) complexes, gold(III) possess a square-planar geometry, and ancillary ligands will then be situated closer to the active site (see Figure 10). This in turn, should imply that the same ligand bulkiness is not required in order to achieve effective enantioselectivity.

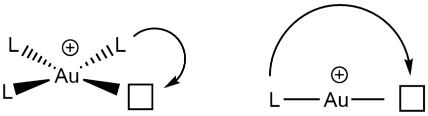

Figure 10: Visual representation of the ligand proximity of square planar gold(III) and linear gold(I) complexes to the active site.

A wide range of *C,O*-chelated[86] and *O,O*'-chelated[87] cyclometalated oxazoline complexes with gold(III) has recently been developed. The *O,O*'chelated 4,4'-biphenol cyclometalated oxazoline gold(III) complexes have been applied in asymmetric carboalkoxylation of alkynes with good yield and enantiomeric excess. The reactions were carried out in the presence of organic acids without the addition of silver salts to activate the precatalyst. Another class of catalytically active asymmetric gold(III) complexes has been developed by Bohan and Toste. Combining chiral NHC ligands with a C-C cyclometalated biphenyl ligand has proved to perform well in enantioselective 1,5-enyne cycloisomerization. The catalyst also seems stable and was able to be reisolated and still showed catalytic activity. The stability towards reductive elimination is crucial in order to be able to scale up reactions. High catalyst loading and low turnover number is not feasible on an industrial scale.[88]

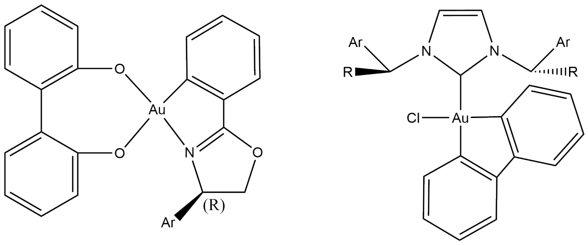

Figure 11: O,O'Chelated 4,4'-biphenol cyclometalated oxazoline and cyclometallated biphenyl NHC gold(III) complexes in enantioselective synthesis.

A better understanding of gold(III) chemistry opens up possibilities to develop cross-coupling catalytic cycles and other redox catalytic cycles which are already well explored for other transition metals. Up until now the main uses of gold catalysts have been Lewis acid activation and π-activation of alkynes and allenes. Levin and Toste were the first to report a redox-neutral cross-coupling of aryl boronic acid with allyl bromides.[89] The generally assumed mechanism of the catalytic cycle is illustrated in Scheme 9. Cross-coupling reactions with gold catalysts have been carried out earlier also, but then with the need for stoichiometric amount of an oxidant, such as Selectlfluor[90] or hypervalent iodine.[91] There has also been carried out interesting research on the usage of gold catalysts in photoredox reactions, where an aryl radical acts both as an oxidant and coupling agent.[92]

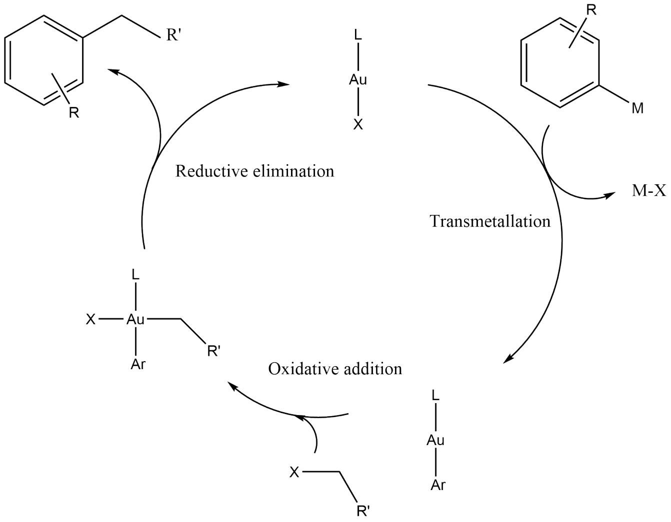

Scheme 9: Gold-catalyzed C-C coupling with oxidant-free oxidative addition.

1.5 Computational chemistry

Organic chemistry has predominantly consisted of experimental work, but in the past few decades the importance of computational organic chemistry has been rapidly growing. Now, one often has a close collaboration between theoretical and experimental chemistry. As the computer hardware continues to improve and the computational models more accurately model real chemical systems, computational chemistry will continue to strengthen its position in organic chemistry.[93] The following citation by Dirac in 1929 still holds as equally relevant, almost 100 years later:

> *The underlying physical laws necessary for the mathematical theory of a large part of physics and the whole of chemistry are thus completely known, and the difficulty is only that the exact application of these laws leads to equations much too complicated to be soluble. It therefore becomes desirable that approximate practical methods of applying quantum mechanics should be developed, which can lead to an explanation of the main features of complex atomic systems without too much computation.*[94]

The main problem one seeks to solve in computational chemistry is the ground state configuration of the electron structure. Calculations of electronic structures have become an essential tool within organometallic catalysis. Calculations can support experimental results and mechanistic proposals. They also set the foundation for rational development of new ligand systems.[95] Geometry optimizations provide visuals often necessary to predict a reaction mechanism.[96] Reaction mechanism in catalysis is difficult to know for certain, as there are many potential reaction pathways that should be explored. A combination of computational and experimental data should complement each other, and support a common proposed mechanism. Combinations of calculations with kinetic isotope effect (KIE)[97,98], mass spectrometry[99] and in situ infrared spectroscopy[100,101] can provide reliable data for confidently proposing reaction mechanisms.

A theoretical introduction to computation chemistry is given in Appendix A. Here one can find the main principles of the Hartree-Fock method, Kohn-Sham density functional theory, and the nudged elastic band method for finding transition state configurations.

1.6 Chemistry of the ligand synthesis

This section will cover the theory and important details of reactions from starting compound to oxazoline-NHC ligands, as well as coordination to gold.

1.6.1 Buchwald-Hartwig amination

Palladium-catalyzed amination has greatly improved the synthesis of carbon-nitrogen bonds. Earlier reactions consist of nucleophilic aromatic substitution and copper-catalyzed couplings, developed by Goldberg[102] and Ullmann.[103] These reactions often require high temperature, long reaction times and are limited in terms of substrate type. The palladium-catalyzed aromatic amination of aryl bromides was first documented in 1983 by Migita with $P(o\text{-}tol)_3$ ligands.[104] In 1994, Hartwig published a paper on the reaction intermediates[105] and Buchwald documented improvements on the work carried out by Migita.[106] Pioneering work through the next decade has broadened the possibilities of reactions now known as Buchwald-Hartwig amination.

$$\mathrm{ArX + HNRR'} \xrightarrow{\text{[Pd], base}} \mathrm{ArNRR'}$$

Scheme 10: Buchwald-Hartwig amination

The reaction mechanism is similar to palladium-catalyzed C-C coupling reactions. First, the aryl halide coordinates to the palladium by oxidative addition. The amine is added to the complex, followed by deprotonation by base. The product is released from the palladium complex by reductive elimination and the cycle continues[107] (see Scheme 11). Upon oxidative addition of the aryl halide to palladium with monophosphine ligands, such as the first generation tri(o-tolyl)phosphine, the complex forms a dimer.

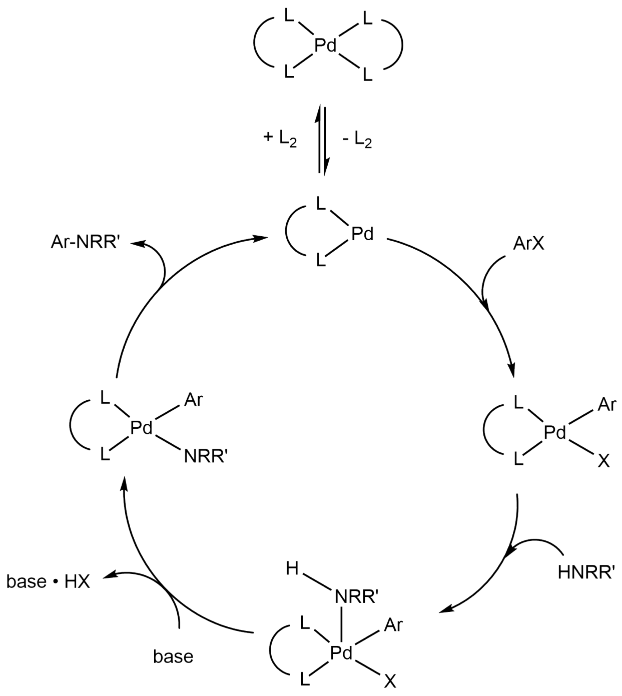

Scheme 11: Mechanism of the Buchwald-Hartwig amination

Althought the Buchwald-Hartwig amination often yields great results, the process of condition optimization can be time-consuming. The choice of nucleophile, electrophile, base and ligand type may all greatly influence the success of the reaction. Meta-analysis and plotting of the large data pool of more than 62 000 Buchwald-Hartwig coupling reactions have been carried out by Fitzner and Wuitschik and coworkers. With such data available, one can quickly design an efficient reaction system.[108]

1.6.2 Reduction of nitro compounds

Reduction of nitro groups to amines is an important part of synthetic organic chemistry. Unlike the corresponding amine, the nitro group is electron withdrawing and cannot perform nucleophilic attack. Reduction methods are to a large extent limited to aryl nitro compounds, as alkyl nitro compounds are more difficult to reduce. Alkyl nitro compounds need to undergo catalytic hydrogenation at high temperatures with transition metals, such as platinum.[109]

$$\mathrm{ArNO_2} \xrightarrow[\substack{\text{or} \\ \mathrm{Pd/C + H_2}}]{\text{metal + acid}} \mathrm{ArNH_2}$$

Scheme 12: Reduction of aryl nitro compounds.

Nitro reductions by metal dissolving reactions are well established and have been carried out with various metals. The metal act as the reducing agent by donating electrons. The reduction can be carried out with different metals in acidic conditions. The reduction of aryl nitro compounds has been carried out with different substrates by aluminium[110] or samarium[111] with ammonium chloride, zinc powder with calcium chloride[112], and indium with HCl.[113] Though being replaced by catalytic hydrogenation, the Bechamp reduction was once the staple reaction for the reduction of nitro compounds. The reduction was discovered by Bechamp in 1854, using iron with dilute acid.[114] The reaction is generally limited to nitroaryl. Reactions have been developed with iron powder in protic solvent with hydrochloric acid[115], stannous chloride[116], calcium chloride[117] or ammonium chloride.[118] The nitro group is first reduced to a nitroso group through a dihydroxylamine, hydrated to a hydroxylamino group and further reduced to the target amine.[119,120] The mechanism of the Bechamp reduction is shown in figure 13.

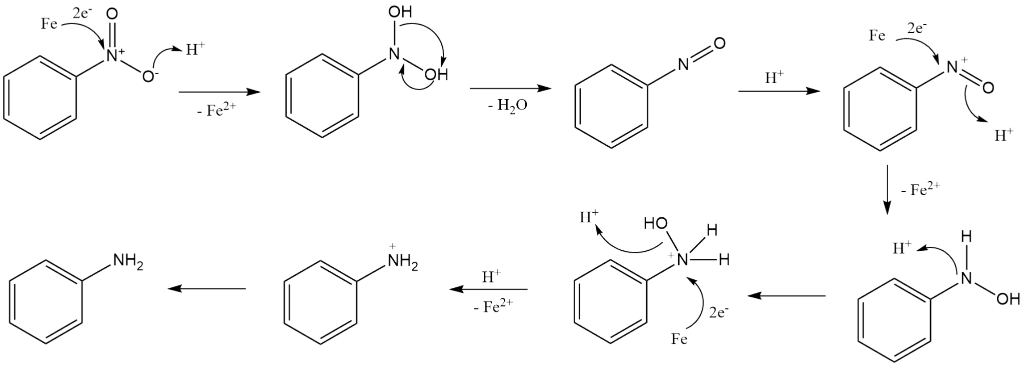

Scheme 13: Mechanism of the Bechamp reduction of nitro compounds

1.6.3 Imidazole ring formation

Formation of an imidazole ring from a diamine precursor can be carried out with an orthoester, such as trimethyl orthoformate, in the presence of a catalytic amount of acid.[121] The acid coordinates to the ester groups, which increases the electrophilicity of the orthoester. The amine groups will perform a nucleophilic attack, and the imidazole ring is complete upon elimination of hydrogen. A general mechanism scheme is proposed in figure 14. Note that protonation of the ether groups and deprotonation of the amine groups are not shown in the figure. The nucleophilic attack of the amine to the protonated orthoformate could either go through a concerted mechanism, or through a oxocarbenium ion intermediate.

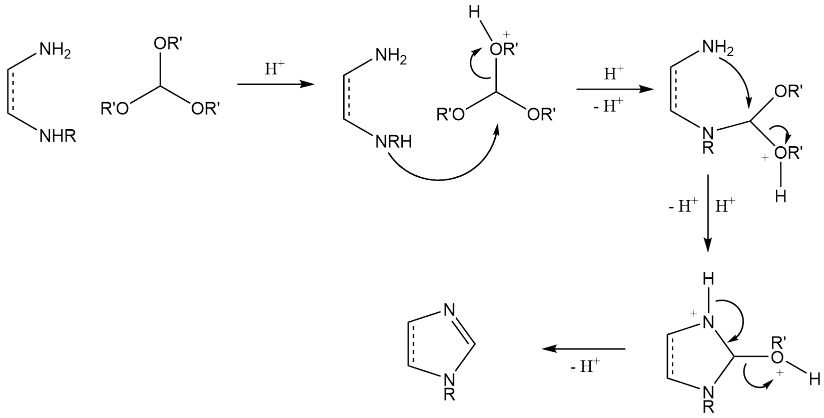

Scheme 14: Mechanism of imidazole formation

1.6.4 Ring closure of hydroxyamides to 2-oxazoline

The synthesis of 2-oxazoline compounds is relatively well explored, where the classical approach is by mixing a β-haloalkylamide in an alkaline solution.[122] Studies have shown that the reaction of thionyl chloride with a β-hydroxyalkylamide does not proceed through a nucleophilic substitution, like simple alcohols. The nucleophilic character of the carbonyl oxygen and the electrophilic character of the carbon next to the electron-withdrawing OSOCl group favors the formation of the 2-oxazolinium ion. Compared to nucleophilic attack of chloride ion, the intramolecular attack and formation of a five-membered ring is kinetically favored.[123]

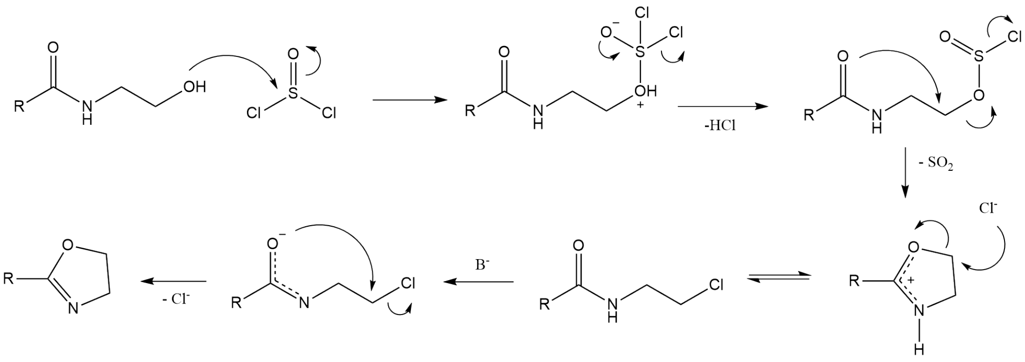

Scheme 15: Mechanism of the classic oxazoline synthesis from β-hydroxy amides.

Another synthetic pathway to yield the oxazoline ring is by using methyl N-(triethylammoniumsulphonyl)carbamate, which was developed and named after E. Burgess. The reagent was initially utilized for the preparation of alkenes from alcohols. Coordination with alcohols to form a sulfamate ester is carried out at temperatures below 30°C, and elimination occurs upon heating.[124] The mechanism is shown in figure 16. The reagent is relatively mild and selective in many reactions with substrates containing different functional groups.

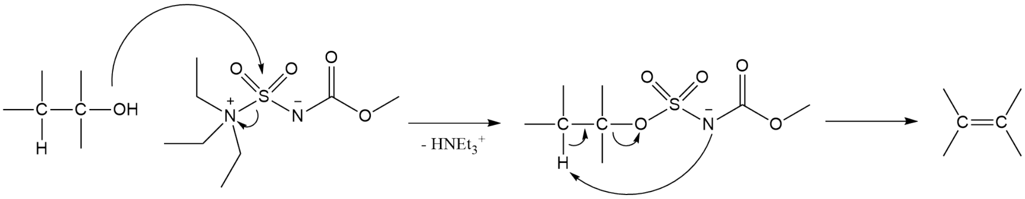

Scheme 16: Mechanism of alcohol reduction by Burgess' reagent

The usage of the Burgess' reagent to synthesize heteocyclic rings was firstly documented by P. Wipf, by cyclization of hydroxyamides. The generation of the sulfamate ester enables cyclization and elimination by increasing the leaving group ability at the alcohol position.[125]. Figure 17 illustrates the cyclization upon sulfamate ester elimination.

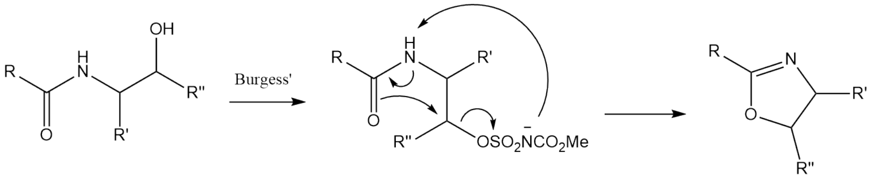

Scheme 17: Mechanism of oxazoline formation of hydroxyamide with Burgess' reagent

1.6.5 Coordination of NHC to gold

The synthesis of N-heterocyclic carbene gold(I) complexes has seen major improvements in the last decade. Earlier, the standard reactions were either with isolated carbene[126] or carried out by transmetallation with silver or copper.[127,128] Reactions with NHCs are difficult, as one needs to work in a glovebox environment to prevent degradation through carbene dimerization. Transmetallation reactions do not require the same inert atmosphere, but could be problematic if the reaction does not go to completion. If the NHC-gold complexes are to be tested for catalytic activity, traces of NHC-Ag and NHC-Cu complexes could affect the results. The earlier synthetic methods are shown in figure 18.

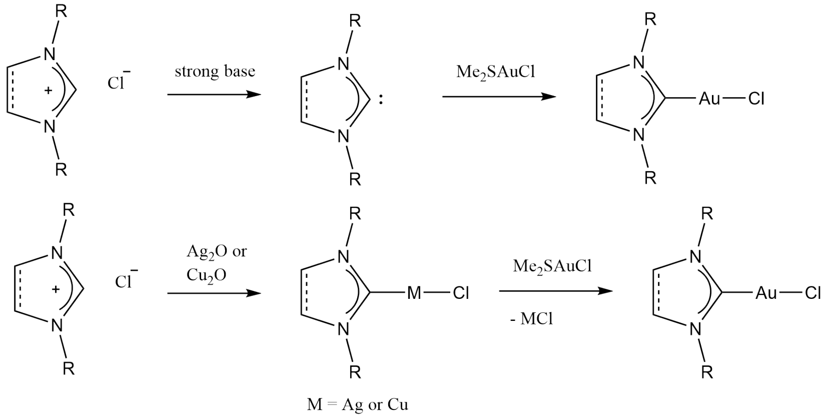

Scheme 18: Earlier standard methods for synthesis of NHC-gold(I) complexes from corresponding imidazolium chlorides

Newer methods often involve a gold chloride with a labile ligand, such as dimethylsulfide or tetrahydrothiophene. Together with the imidazolium salts and a weak base, the gold(I) complex can be generated in good yields. The weakly coordinating ligand is eliminated and the negatively charged gold intermediate is formed quickly. Deprotonation of the imidazolium is followed by coordination of gold.[129,130]

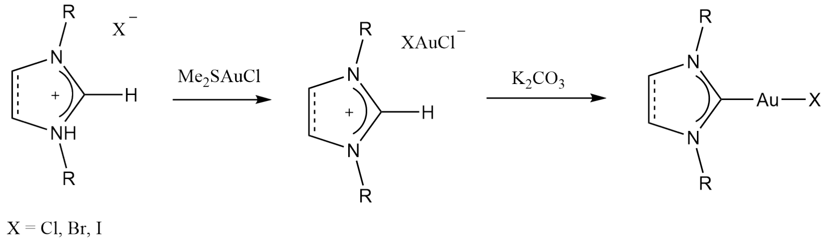

Scheme 19: The current standard method for synthesis of gold(I) complexes from imidazolium

2 Results and discussion

The project's aim was to prepare a set of diastereomerically pure bidentate oxazoline-NHC-gold(III) complexes. Axially chirality is introduced by restricted rotation around an imidazole-naphtalene bond. Strong σ-donation from the NHC ligand provides complex stabilization, which is necessary in order to prevent catalyst degradation of the cationic species upon activation with silver salts. The oxazoline ring contains a chiral center, and upon coordination to the gold center one achieves chirality close to the active site. This should contribute to a strong enantioselectivity of the catalyst. It proved difficult to fully isolate the bidentate oxazoline-NHC-gold(III) complexes, and the synthesis of the β-hydroxyamide-NHC-gold(III) complexes **22a** and **22b** was carried out as an alternative.

The following section contains the synthetic route from starting compound to the isolation of oxazoline-NHC ligands **9a** and **9b** and the β-hydroxyamide-NHC ligands **19a** and **19b**. The ligands were coordinated to gold. A set of different synthetic routes were tested towards the synthesis of the bidentate oxazoline-NHC-gold(III) complex **11**. The β-hydroxyamide-NHC ligands **19a** and **19b** were coordinated to gold and oxidized to β-hydroxyamide-NHC-gold(III) complexes **22a** and **22b**. The complexes were applied in the gold-catalyzed cyclopropanation reaction of propargyl acetate **26** with styrene.

In addition to experimental work, geometries of the gold complexes were calculated on DFT level and visualized with the ORTEP software.[131] A computational study of the mechanism of the gold-catalyzed cyclopropanation reaction with propargyl acetate and styrene was initiated. Due to the long computational times and a limited time on the project, only a portion of the full study will here be presented.

2.1 Synthetic pathway to oxazoline-NHC ligand

The synthesis of the oxazoline-NHC ligands **9a** and **9b** was carried out in accordance with the work of Shi and coworkers,[132] with a few alterations based on available chemicals (see Scheme 20).

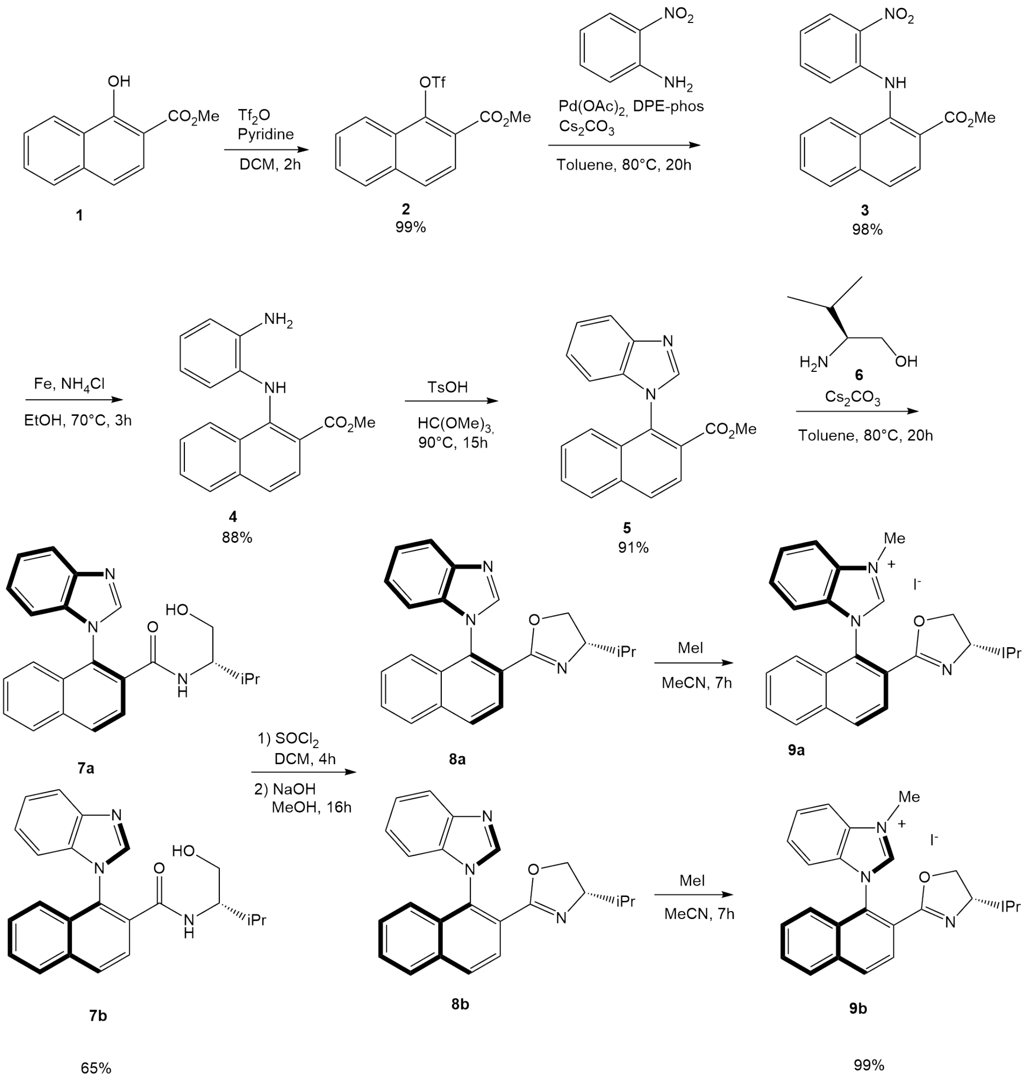

Scheme 20: Synthetic route towards oxazoline-NHC ligands **9a** and **9b**

2.1.1 Synthesis of compound 2

The triflate compound **2** was synthesized from starting compound **1** in quantitative yields (see Scheme 21). The triflic anhydride was added to a solution of reactant **1** and pyridine in DCM at 0°C dropwise to reduce boiling. Dry DCM was not necessary in order to obtain satisfactory yields. The triflate **2** was soluble in DCM and any impurities were removed with aqueous workup. Further purification was not necessary.

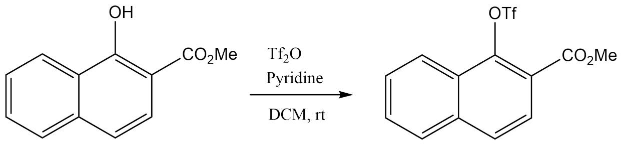

1

2
99%

Scheme 21: Synthesis of triflate **2**

2.1.2 Synthesis of compound 3

The Buchwald-Hartwig amination of triflate compound **2** with 2-nitroaniline yielded coupling product **3** with 98% yield under optimal reaction condition (see Scheme 22). The catalytic loading proved to be important to maximize the chemical yield. Too low loading resulted in a too slow reaction and full conversion was not acquired after 24 h. A too high loading also proved problematic as the amount of β-hydride elimination increased. The optimal catalytic loading was found to be 10 mol% Pd(II) acetate. The quality of the base affected the yield, and Cs_2CO_3 that was stored under dry atmosphere improved the outcome of the reaction. The reaction is oxygen sensitive and in experiments where there was oxygen present the yield of the reaction could drop by as much as 40%. The β-hydride elimination product **3b** was also isolated.

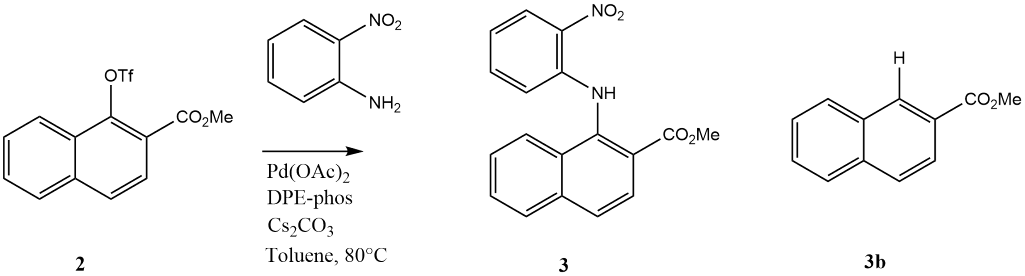

2

3
98%

3b

Scheme 22: Synthesis of compound **3**

2.1.3 Synthesis of compound 4

The Buchwald-Hartwig coupling compound **3** was reduced by iron powder under acidic conditions, similar to the Bechamp method*114* (see Scheme 23). A solvent mixture of ethanol : water (4:1) was used in order to dissolve all reagents. The ammonium chloride is poorly soluble in ethanol. The reactant **3** was not very soluble in the ethanol-water solvent, but enough to initiate the reaction. Once the reaction started, product formed quickly. Prior to extraction, the mixture was filtered through a pad of celite. The crude product was purified with flash chromatography to remove any unreacted reactant **3**. The isolated yield was 88%.

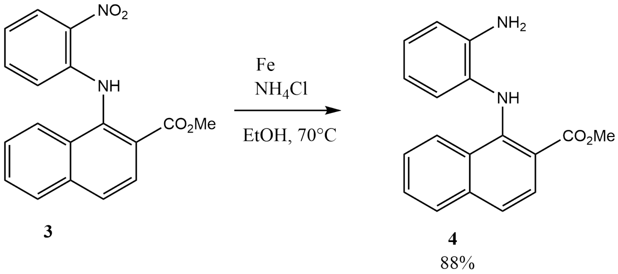

Scheme 23: Synthesis of diamine **4**

2.1.4 Synthesis of compound 5

The ring closing of the diamine **4** with trimethyl orthoformate to generate the imidazole **5** was carried out with a catalytic amount of tosylic acid (see Scheme 24). The reaction mixture was heated overnight. The diamine **4** was conveniently well soluble in trimethyl orthoformate. Most tosylic acid and solvent trimethyl orthoformate was removed with aqueous workup and evaporation under reduced pressure. The crude product was purified on a flash column to remove any remaining **4**, obtaining the product as an orange oil in 91% yield.

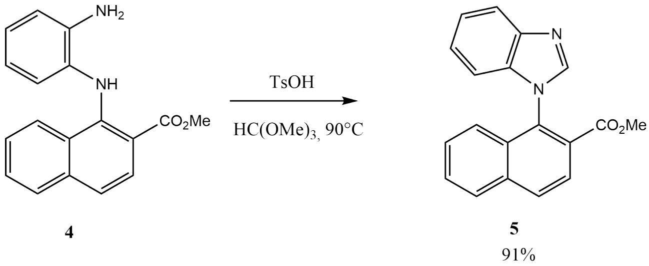

Scheme 24: Synthesis of imidazole **5**

Upon ring closing of the imidazole ring, the rotation along the imidazole-naphtalene bond is restricted, as illustrated in Figure 12. The result is a pair of enantiomers. Since they are chemically equivalent, they are not identified as two unique compounds by NMR, IR or MS. Geometry optimization of the two enantiomers was carried out, shown in Figure 13. Separation with chiral chromatography was not carried out, as further introduction of a new chiral center results in two chemically different diastereomers.

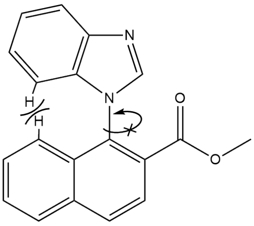

Figure 12: Axial chirality due to restricted rotation along the imidazole-naphtalene bond.

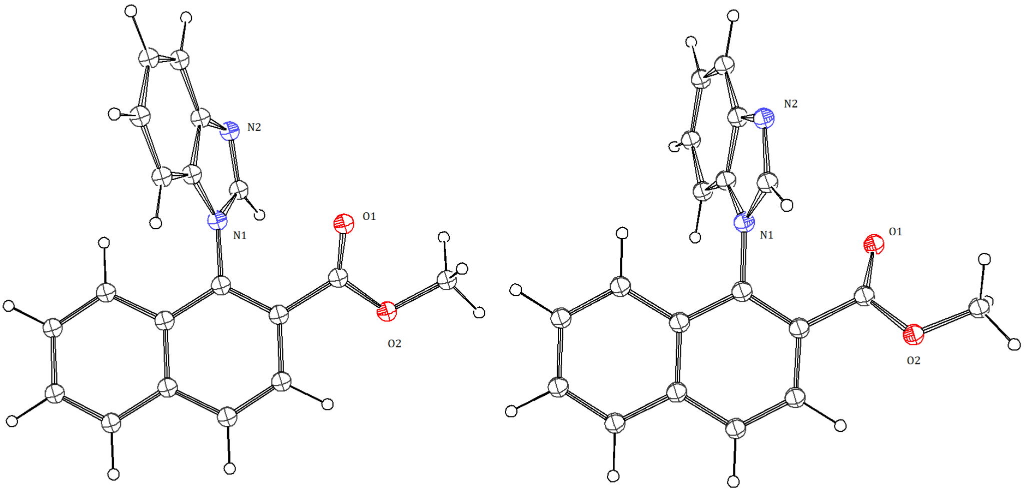

Figure 13: ORTEP view of calculated aS enantiomer (left) and aR enantiomer (right) of compound **5**

2.1.5 Synthesis of compound 7

The amide formation from naphthyl ester reactant **5** was carried out with the enantiomerically pure aminoalcohol **6** and cesium carbonate (see Scheme 25). The result is a mixture of diastereomers **7a** and **7b**. At high reactant concentrations, the solution turned into a gel-like substance. Both the amino alcohol **6** and the products **7a** and **7b** are likely contributing to a network of hydrogen bonds. More solvent and vigorous stirring eliminated this problem, and the gel formation did not seem to impact the reaction outcome. Aqueous workup was carried out to remove the amino alcohol **6** and the cesium carbonate. The product was not very well soluble in most organic solvent and the water-DCM phases proved hard to separate. This contributed to a loss of yield, and an extensive amount of DCM was required. The product was sufficiently pure to use in further synthesis and purification on flash column was not carried out, in order to limit the amount of product loss. The collected yield of diastereomers **7a** and **7b** was 65%.

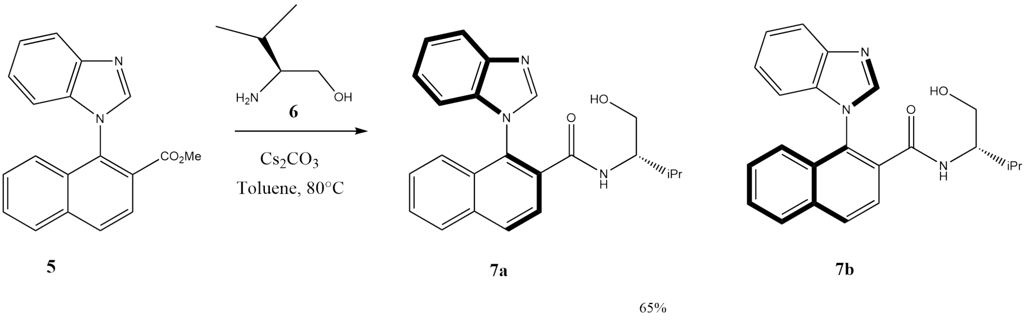

Scheme 25: Synthesis of amide compounds **7a** and **7b**

Since a new chiral center is introduced from the aminoalcohol **6**, a set of aS,S and aR,S diastereomers is obtained. The structures of the two diastereomers **7a** and **7b** were calculated, as shown in Figure 14 The diastereomers are chemically non-equivalent and carbons and protons give a unique set of chemical shifts in the NMR spectra. The amide was poorly soluble in most organic solvents, so the two diastereomers were reacted further without separation. The ratio of diastereomers was surprisingly not consistent from repeated experiments under similar reaction conditions. From the previous reaction step, upon ring closing of the imidazole **5**, one expects a racemic mixture of two enantiomers. Due to the restricted axial rotation and the amino alcohol's fixed stereocenter, one would also expect racemic mixture of diastereomers **7a** and **7b** if the reaction goes to completion. The reaction is not reversible, since the alkoxy group is a better leaving group than the amine from the tetrahedral carbonyl intermediate.

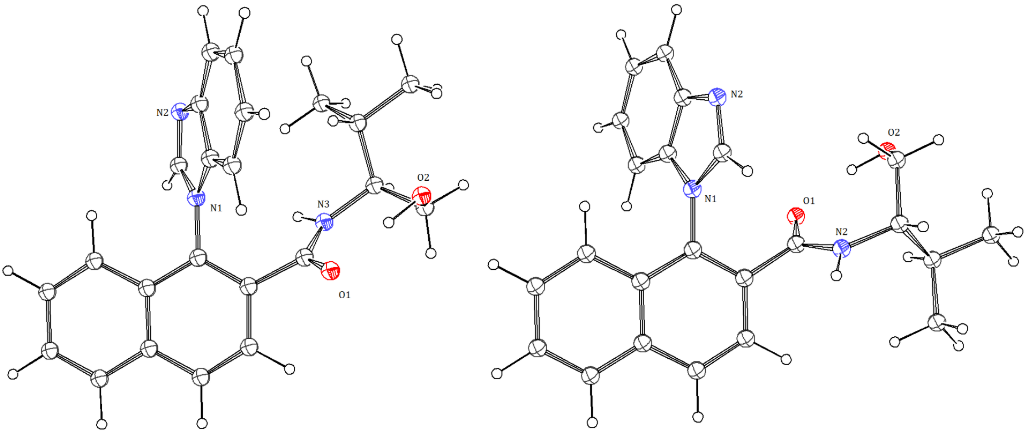

Figure 14: ORTEP view of calculated aS,S diastereomer **7a** (left) and aR,S diastereomer **7b** (right)

2.1.6 Synthesis of compounds 8a and 8b

The mixture of diastereomers **7a** and **7b** was initially reacted with Burgess' reagent in order to form the oxazoline ring. The reagent is mild and reactions could be carried out in one step. The reaction did work, but a byproduct was also formed. The byproduct formation lowers the potential yield, and it was also difficult to separate with flash chromatography. The byproduct was not identified.

Alternatively, the β-hydroxy amide was reacted with thionyl chloride to generate the β-chloro amide (see Scheme 26). Solvent was removed and the cyclization was carried out overnight in methanol with sodium hydroxide. A diastereomeric mixture of oxazolines **8a** and **8b** was obtained in high yields.

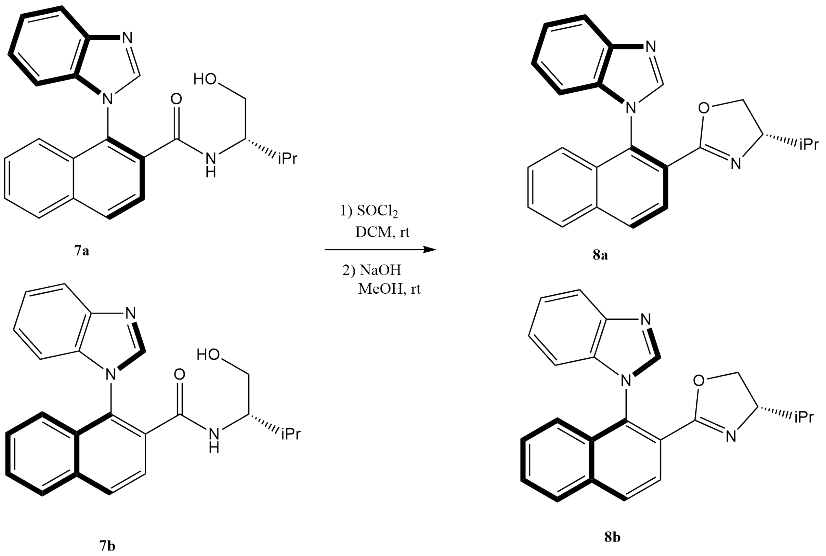

Scheme 26: Synthesis of compounds **8a** and **8b**

Separation of the two diastereomers was attempted with flash chromatography. Although the compounds are chemically different, they are retained relatively equally on silica. The aS,S diastereomer **8a** eluate first and was isolated. Unfortunately, there was a significant overlap between the two diastereomers, which means that isolated yields were low. The aR,S diastereomer **8b** was not successfully fully isolated, as the tailing of compound **8a** resulted in a mixture of diastereomers in the following fractions collected. The aR,S diastereomer **8b** was enriched by column chromatography, but as there was always some aS,S diastereomer **8a** present, further synthesis were not prioritized. In order to obtain data on enantiomeric properties in catalytic reactions, the ligands need to be enantiomerically pure. As seen from the calculated structures of the diastereomers in Figure 15, there is not much steric interactions that would significantly alter the chemical properties of the compounds.

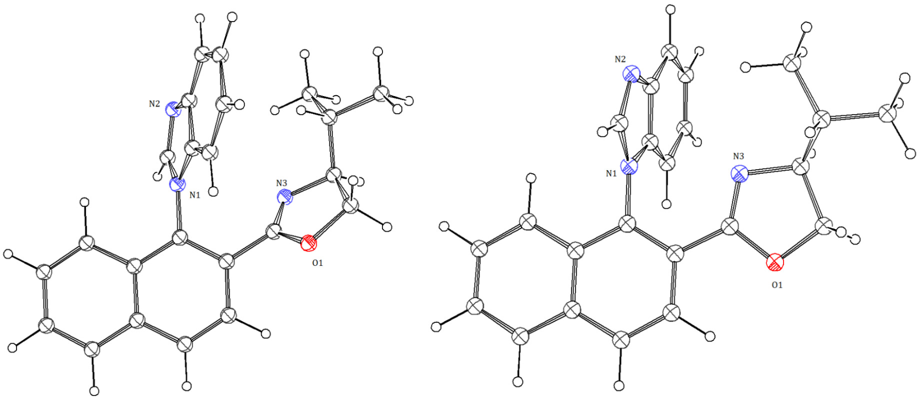

Figure 15: ORTEP view of calculated aS,S diastereomer **8a** (left) and aR,S diastereomer **8b** (right)

2.1.7 Synthesis of compound 9

The aS,S diastereomer **8a** was methylated with iodomethane (see Scheme 27). Stirred in acetonitrile at reflux, full conversion was achieved after 6.5 h. Excess iodomethane and solvent was removed under reduced pressure. However, in order to remove all traces of iodomethane, the methylated product **9a** was dissolved in DCM and precipitated with n-pentane. The iodomethane is soluble in pentane, and product **9a** needed no further purification. Similar results were obtained with the aR,S diastereomer **8b**, though the starting reactant consisted of a mixture of the diastereomers. Further synthesis with a mixture of the diastereomers was carried out to investigate if the two methylated diastereomers **9a** and **9b** were easier to separate than the diastereomers **8a** and **8b**. This proved to not be the case. Optimized geometries of diastereomers **9a** and **9b** are shown in Figure 16.

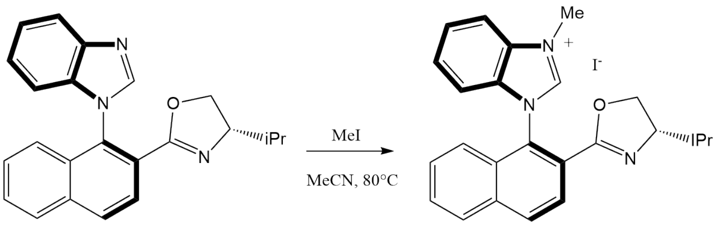

8a

9a

99%

Scheme 27: Synthesis of compounds **9a**

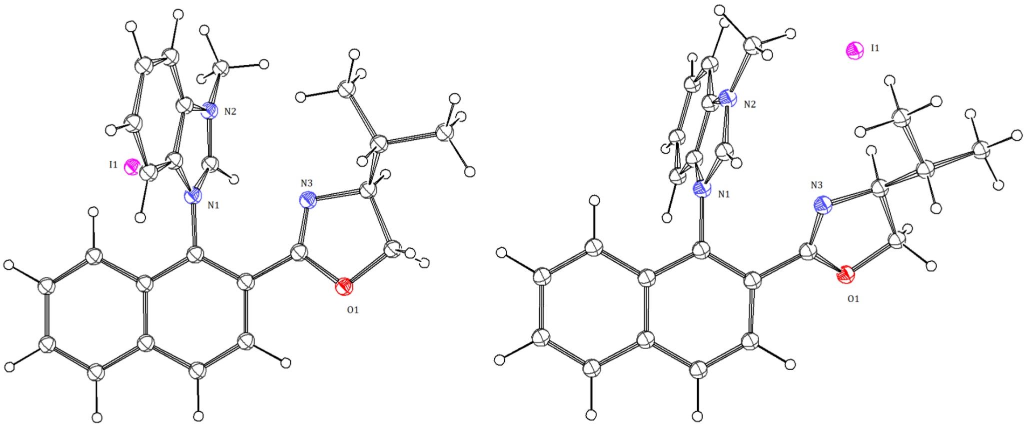

Figure 16: ORTEP view of calculated aS,S diastereomer **9a** (left) and aR,S diastereomer **9b** (right)

2.2 Coordination of NHC-oxazoline ligand to gold

2.2.1 Synthesis of NHC-oxazoline-gold(I) complex 10a

The diastereomerically pure NHC-oxazoline **9a** was coordinated to gold according to previously documented methods[129] (see Scheme 28). Reaction of imidazolium **9a** with dimethylsulfide gold(I) was carried out with an excess of potassium carbonate in acetone at reflux. Full conversion was achieved after 4 h. To remove any unreacted starting material, decomposed gold and potassium carbonate, the reaction mixture was filtered through silica. Reaction in DCM at rt for 4 h did not work, as the compound decomposed. This illustrates how the acetone better stabilizes the charged intermediate species. Decomposition could likely have been reduced by monitoring the reaction and reducing the reaction time. The potassium carbonate is more reactive in DCM than in acetone, so the deprotonation occurs quickly. Since good yields were obtained with acetone (87%), further improvements with DCM were not carried out. Methods similar to Shi and coworkers where attempted,[132] were imidazolium **9a** reacted with dimethylsulfide gold(I) and sodium acetate at rt. After 24 h the reaction had still not gone to completion. Optimized geometries of diastereomers **10a** and **10b** are shown in Figure 17.

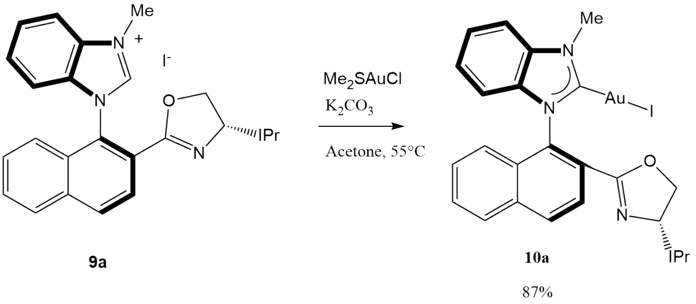

Scheme 28: Synthesis of compounds **10a**

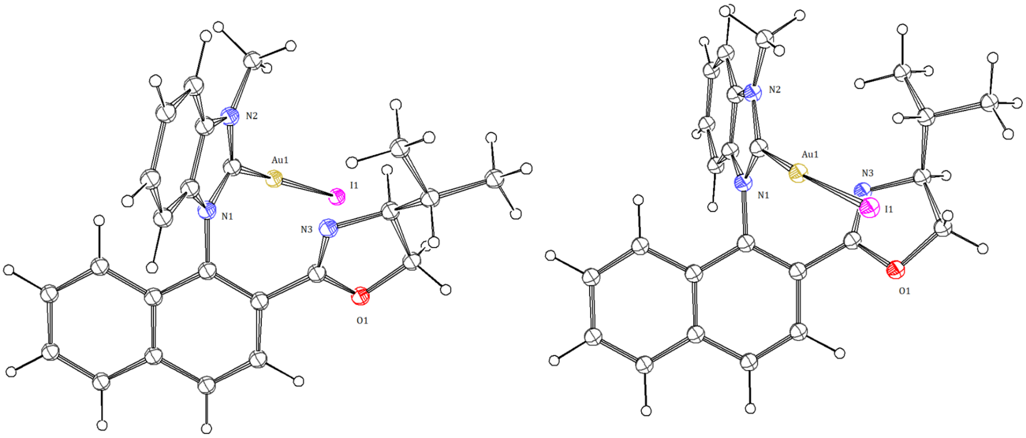

Figure 17: ORTEP view of calculated aS,S diastereomer **10a** (left) and aR,S diastereomer **10b** (right)

The weakly coordinating dimethylsulfide ligand is eliminated from the Me_2SAuCl reagent and IAuCl acts as a new counterion to the imidazolium compound. The intermediate is immediately formed, and without the addition of a base, the compound can be isolated. The ^1H NMR spectra of initial imidazolium **9a** and the intermediate are shown in Figure 18.

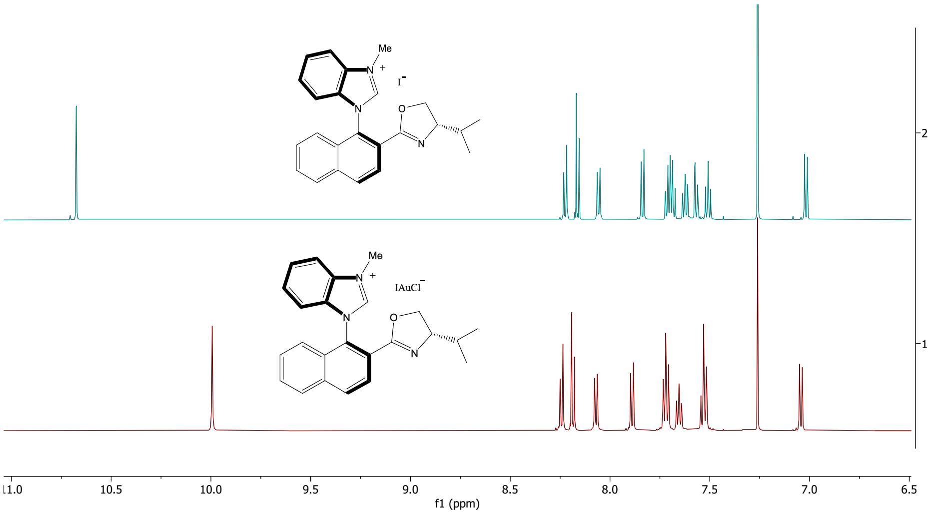

Figure 18: ^{1}H NMR spectra of the imidazolium salt **9a** and the intermediate species formed during the coordination to gold.

2.2.2 Synthesis of bidentate gold(III) complex 11

The synthesis of the NHC-oxazoline ligand was carried out with the initial plan to isolate a novel bidentate NHC-oxazoline gold(III) complex **11**, as shown in Scheme 29. The oxazoline nitrogen could coordinate to the gold center and stabilize a cationic species from decomposition. The bidentate structure would also bring the chiral center on the oxazoline ring closer to the coordination site, potentially increasing the stereoselective properties of the catalyst. As seen from the calculated optimized geometry in Figure 19, the chiral isopropyl group of the coordinated oxazoline is close in space to the gold center. This should, in turn, affect the enantioselectivity of catalyzed reactions.

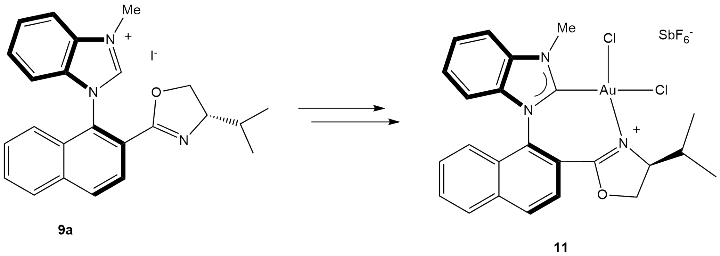

Scheme 29: Intended route to the synthesis of gold(III) compound **11** from the imidazolium **9a**

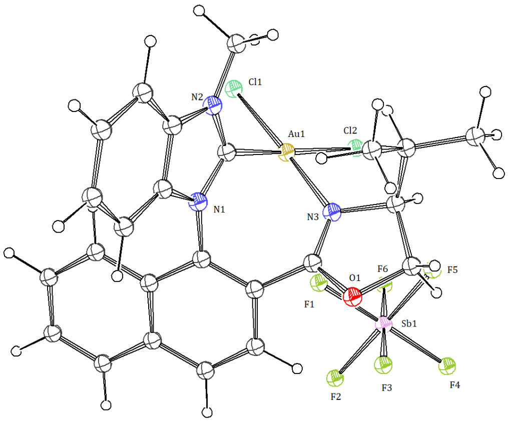

Figure 19: ORTEP veiw of the calculated structure of compound **11**

A range of different methods were tested to obtain the target bidentate gold(III) compound **11**. Unfortunately, the complex proved difficult to fully isolate. The methods represented in Table 1 show rational routes towards the synthesis of bidentate gold(III) compounds and could work better with other ligand systems. The different methods are also presented in Scheme 30.

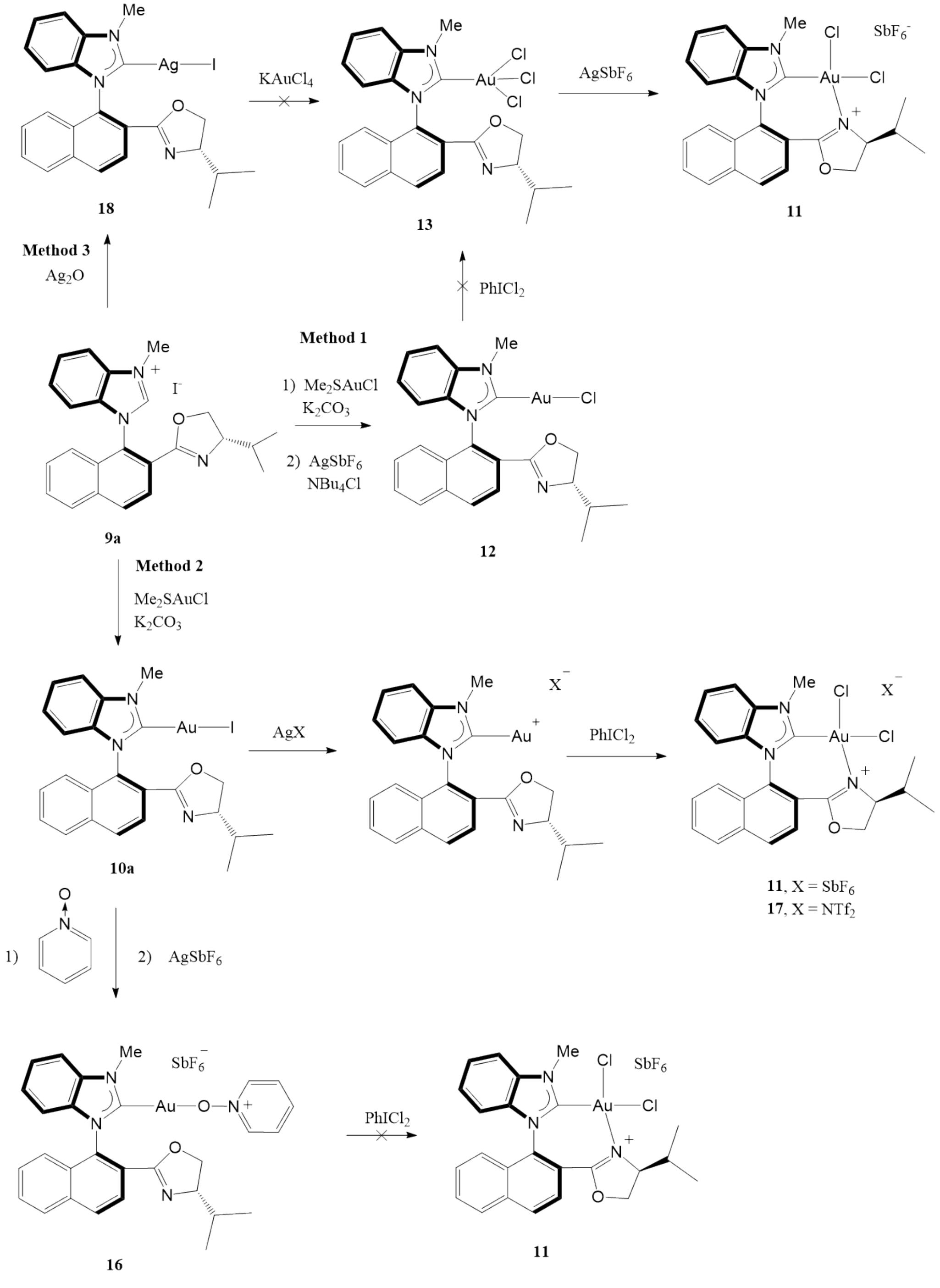

Scheme 30: The different methods explored in order to synthesize the bidentate oxazoline-NHC-gold(III) complex **11**

Table 1: Overview of different methods attempted to synthesize gold(III) complex **11**

Entry	Method	Reaction steps
1	1	i) Halide exchange of gold(I) complex **9a** ii) Oxidation with $PhICl_2$ iii) Chloride removal with $AgSbF_6$ to coordinate oxazoline
2	2.1	i) Iodide removal complex **10a** with $AgSbF_6$ in DCM ii) Oxidation with $PhICl_2$
3	2.2	i) Iodide removal of complex **10a** with $AgSbF_6$ in MeCN ii) Oxidation with $PhICl_2$
4	2.3	i) Iodide removal complex **10a** with $AgSbF_6$ in DCM in the presence of nitrone ii) Oxidation with $PhICl_2$
5	2.4	i) Iodide removal of complex **10a** with $AgNTf_2$ in DCM ii) Oxidation with $PhICl_2$
6	3	i) NHC-Ag synthesis with Ag_2O and imidazolium iodide ii) Transmetalation with $KAuCl_4$ iii) Chloride removal with $AgSbF_6$ to coordinate oxazoline

Method 1

In order to synthesize the gold(III) complex **11**, the reaction path illustrated in Scheme 31 was attempted. Firstly, ligand exchange of gold(I)-I complex **10a** was carried out to yield gold(I)-Cl compound **12**. The idea was to oxidize complex **12** to $AuCl_3$ complex **13**, followed by removal of a chloride ligand with $AgSbF_6$. The oxazoline nitrogen should be able to coordinate to the cationic gold metal center to yield the target complex **11**. The motivation for initial halide exchange was to increase the stability of the complex, as well as to avoid a mixture of gold(III) complexes with different halide ligands. Trans effects from the NHC ligand increases the halide bond length, which affects the more polarizable iodide to a greater extent.[133] The weakening of the gold-halide bond would lead to less stable complexes.[134] The iodide ligand was removed with $AgSbF_6$ and the silver iodide filtered off. The cationic gold(I) species was reacted with tetrabutylammonium chloride to yield gold-Cl complex **12**. Oxidation with iodobenzene dichloride did not yield the gold(III) complex **13**. This was surprising, as oxidation of gold-NHC species generally works well. Based on N-methyl peaks in the ^{1}H NMR spectra, it was determined that a range of different compounds were formed during the reactions. Due to gold(III)'s instability and the small reaction scale, isolation and determination of products were not carried out and other pathways were investigated to synthesize complex **11**.

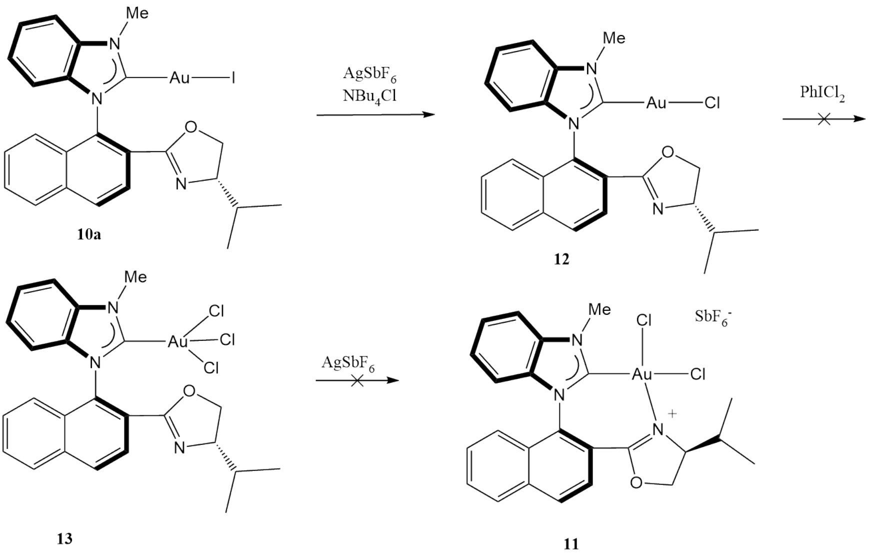

Scheme 31: Method 1: Ligand exchange of gold(I)-I complex **10a** and further intended oxidation to target gold(III) complex **11**

Method 2

Another approach to synthesize the gold(III) complex **11** is shown in Scheme 32. The NHC-Au-I complex **10a** is reacted with a silver salt, the silver iodide was filtered off and cationic species oxidized with PhICl$_2$. Oxidation of NHC-Au-Cl to NHC-Au-Cl$_3$ complex **13** proved to be a poor reaction. By first removing the halide ligand from gold(I), the oxazoline nitrogen could immediately coordinate to the gold-center after oxidation. This also eliminates the need to first perform a halide exchange reaction.

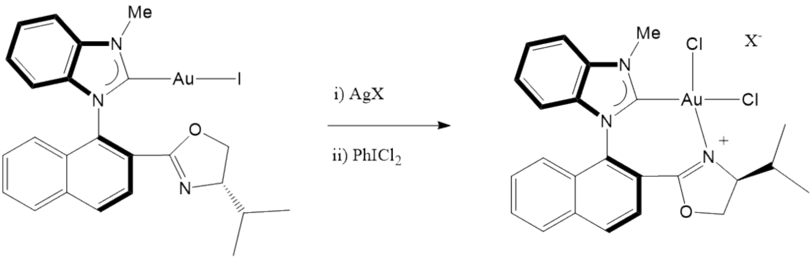

10a **11**

Scheme 32: Method 2: General synthesis of gold(III) complex **11** from gold(I)-iodide complex **10a**, by halide removal with silver salt and oxidation with PhICl$_2$.

Method 2.1

The general pathway to synthesize the bidentate oxazoline-gold(III) complex **11** was carried out with method 2, using DCM as solvent, as shown in entry 2 of Table 1. There are indications of some product beeing formed, but along with the formation of other byproducts. Unfortunately, gold(III) complexes are too unstable on silica to be purified with flash chromatography. The instability of the complexes reduced the amount of available purification methods, so finding a reaction system that works better is needed to properly isolate the compound. It is reasonable to assume that the complex is most unstable after addition of silver salt to remove the halide ligand. The instability leads to complex decomposition. The following entries of method 2 are all based on the same principle. The objective is to stabilize the cationic species, which would, hopefully, reduce the amount of unwanted side reactions. Figure 20 illustrates the objective of the following subsections.

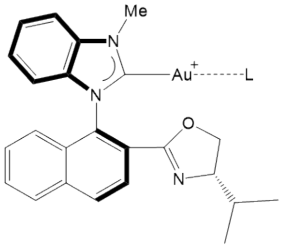

Figure 20: Coordination to the cationic gold center in order to stabilize the intermediate from undergoing unwanted side reaction and degradation.

Method 2.2

As shown in entry 3 of Table 1, the halide removal with silver salt was carried out in acetonitrile instead of DCM. The polar solvent should be better at stabilizing the cationic species, and the free electron pair of the nitrogen is able to coordinate to the metal center. The reaction was carried out in deuterated acetonitrile, so the reaction could be monitored on NMR. For reference, a ^{1}H NMR spectrum of the initial gold(I) complex **10a** was acquired. Upon addition of acetonitrile, there seem to be a mixture of two compounds in a 2:1 ratio. This has not been observed earlier from spectra in deuterated chloroform. Upon addition of acetonitrile, there seems to be a mixture of two compounds in a 2:1 ratio. This has not been observed earlier from spectra in deuterated chloroform (see Figure 21). The acetonitrile nitrogen can coordinate to the metal center of gold-NHC systems, but this would normally require a silver salt to first remove the halide.[135] There are not many other possible complexes that can be present, and the explanation could be that the gold-iodide bond is sufficiently weak, so that the acetonitrile could compete for coordination to the gold center.

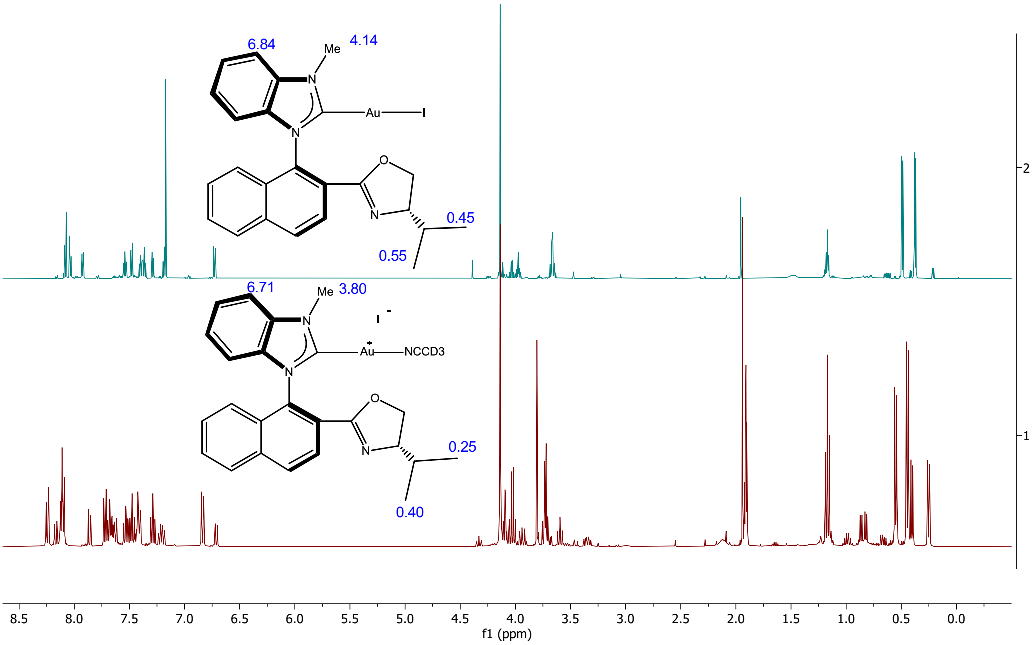

Figure 21: ^{1}H NMR spectra of gold(I) complex **10a** in acetonitrile-d$_3$ (1) and chloroform-d (2)

The mixture of iodide and acetonitrile coordination was determined not be a major issue, as the complexes were reacted with silver salt, where the AgI was filtered off. Further reactions were carried out, in accordance with entry 3 of Table 1. Both halide removal with $AgSbF_6$ and oxidation with $PhICl_2$ are quick reactions, and are done within 15 min. In contrast to DCM, there are fewer byproducts when carrying out the reaction in acetonitrile, as expected. Strong indication of oxazoline coordination and **11** formation is based on the oxazoline ^{1}H NMR signals. Upon coordination of the oxazoline ring to the gold center, the shifts all shift downfield, as shown in Figure 22.

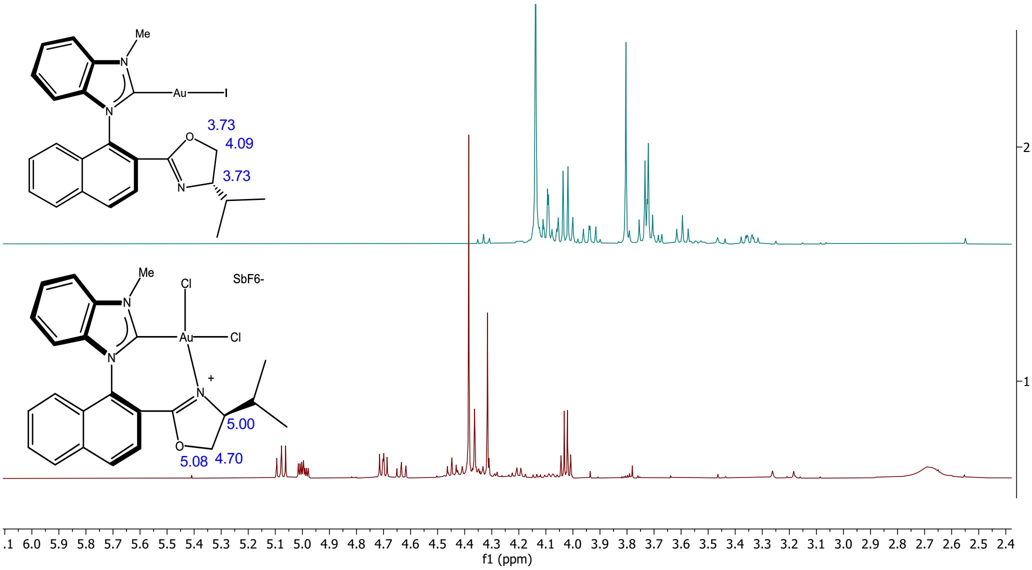

Figure 22: ^{1}H NMR spectra of gold(I) complex **10a** in acetonitrile-d_3 (1) and crude product **11**

Similarly as for the ^{1}H NMR spectrum of gold(I) complex **10a** in acetonitrile, there is a 2:1 ratio of two different complexes after the addition of silver salt and subsequent oxidation with $PhICl_2$. Since the ratio remains the same, it could be possible that the acetonitrile remain coordinated. After oxidation with $PhICl_2$ the acetonitrile is still bonded to the gold, preventing the oxazoline nitrogen from coordinating (see Scheme 33). The oxazoline is generally a better ligand, and should be able to coordinate more strongly. The coordination problems are then more likely due to the unfavorable 7-membered ring formation.

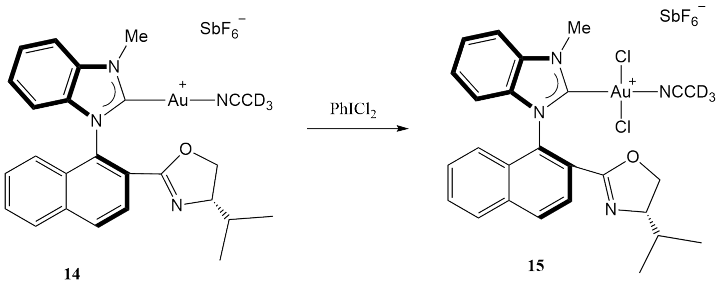

Scheme 33: Oxidation of the nitrile-coordinating gold(I) complex **14** with $PhICl_2$

As seen from the ^{1}H NMR spectrum in Figure 23, the oxazoline protons of the gold(III)-acetonitrile complex **15** are not significantly shifted downfield, which could indicate that the oxazoline is uncoordinated. The spectra of the mixture of compounds **11** and **15** are attached in the Appendix L. The isopropyl doublets also supports the claim that the oxazoline is not coordinated to the gold center in complex **15**. Compared to the bidentate gold(III) complex **11** the difference in chemical shifts between the two isopropyl doublets is significantly lower. When the oxazoline is coordinated, the isopropyl group is closer to the metal center, and the direction in space of the two methyl groups will greatly influence their chemical shifts. Based on information from the ^{13}C and HMBC NMR spectra, both the bidentate complex **11** and the acetonitrile-coordinated complex **15** have gold in oxidation state III. The C2 carbon of the imidazolium is greatly influenced by the oxidation state of the coordinated gold. NHC-gold(I) complexes have C2 carbon shifts above 180 ppm.[136] The C2 carbon shifts for complexes **11** and **15** are 148.6 ppm and 152.1 ppm, respectively. The mixture was monitored in acetonitrile-d_3, and it was observed that the ratio of complexes **11** : **15** shifted from 2:1 to 1:1 over the course of 40 h. This is interesting, as it gives valuable information about kinetic vs thermodynamic factors of the ligands. The oxazoline nitrogen has better donating abilities than the acetonitrile nitrogen, and will dominate as the kinetic product in coordination to the cationic gold(III) intermediate. Upon coordination, a seven-membered ring is formed, which seems to be rather unstable. Over time, the oxazoline-gold bond breaks and the more thermodynamically stable gold(III)-acetonitrile complex **15** is formed.

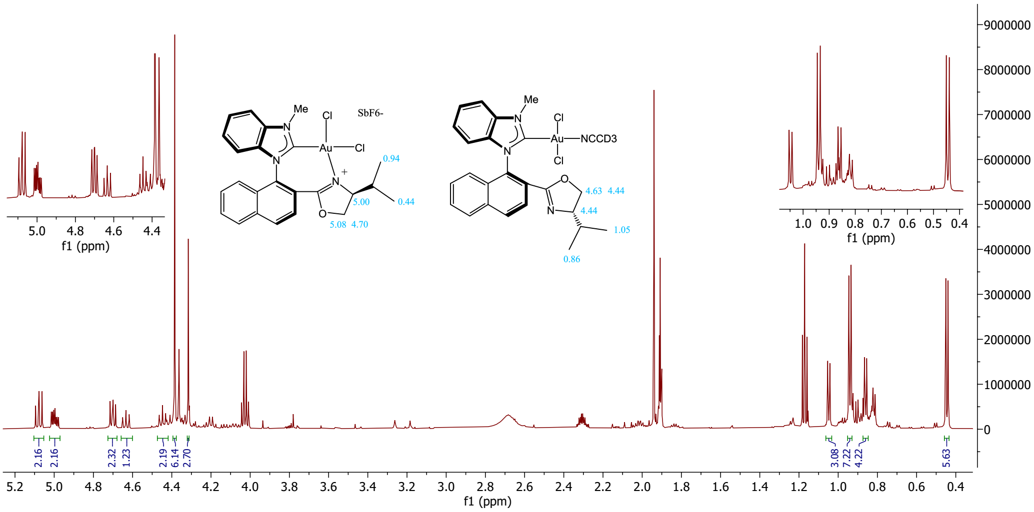

Figure 23: ^{1}H NMR spectrum of crude product **11**,

Method 2.3

Since the bidentate gold(III) complex **11** and the gold(III)-acetonitrile complex **15** could not be separated, the reaction was repeated in DCM with the addition of the nitrone pyridine-N-oxide in the reaction mixture. The reaction scheme is shown in Scheme 34 The idea is that the nitrone should coordinate to the cationic gold intermediate after silver salt addition, which has proved to be too unstable in DCM (see Method 1). Doing the reaction in DCM is important, since it ensures that no acetonitrile can occupy the coordination site. Nitrones coordinate well to gold(I) complexes, but poorly to gold(III) species.[137] Upon addition of $PhCl_2$ and oxidation of gold, the nitrone would preferably be released from the complex, as the oxazoline coordinates stronger to the gold(III) center.

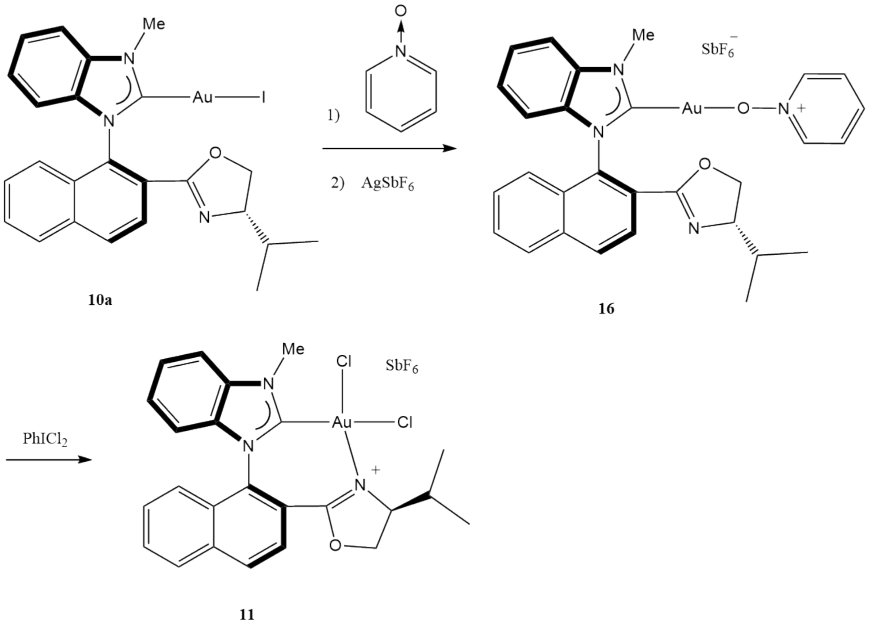

Scheme 34: Method 2.3: pyridine-N-oxide is added to the reaction mixture to stabilize the cationic species.

Based on ^{1}H NMR spectra of the crude mixture after oxidation with $PhICl_2$, it turns out that the oxazoline does not immediately displace the nitrone for the coordination site to gold. All shifts for the complex are broad, and it seems like there is a kinetic equilibrium between oxazoline and nitrone coordination, as shown in Scheme 35. Removing the pyridine-N-oxide proved to be difficult, especially since it coordinates to the gold. There was also at least one other gold-complex that was not identified, so reactions with gold-nitrone systems were discontinued.

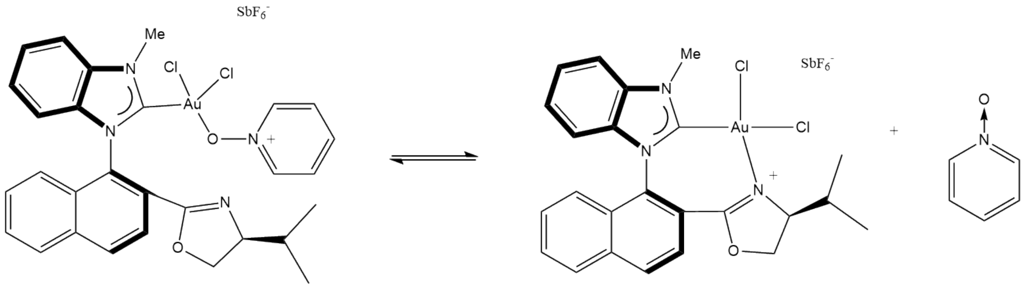

Scheme 35: Possible kinetic equilibrium of nitrone and oxazoline coordination.

Method 2.4

A final idea to improve the oxidation reaction of method 2 was to use a different silver salt (see Scheme 36). The SbF_6 anion is weakly coordinating will a realively large charge separation from the cationic gold center. The more strongly coordinating bis(trifluoromethanesulfonyl)imidate NTf_2 was used, by adding $AgNTf_2$ to remove the iodide from the gold(I) complex **10a**. The silver iodide was filtered off after addition of $AgNTf_2$ and $PhICl_2$ was added to oxidize the gold. It was expected that the oxazoline nitrogen would displace the NTf_2. The resulting bidentate gold(III) complex **17** would be similar to complex **11**, but with NTf_2 as the counterion. Based on the ^{1}H NMR spectrum, three different compounds were observed. There were indications of oxazoline coordination, based on the oxazoline proton shifts downfield, but since there were no practical way of isolating the complex, further reactions were not carried out. It seems like the seven-membered ring that is formed upon oxazoline coordination is simply too unstable and there are no good ways to oxidize the gold(I) complex **10a** to **11** in a selective manner.

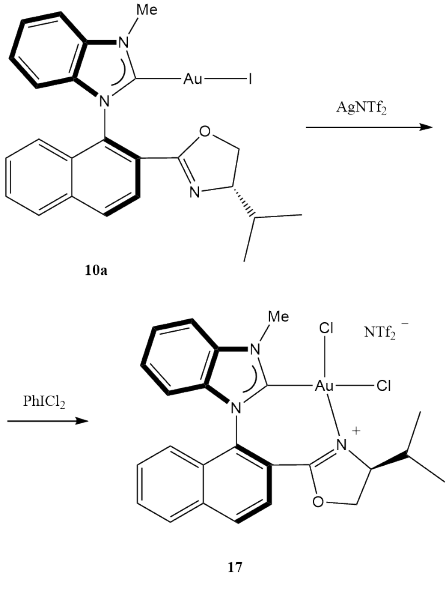

Scheme 36: Method 2 for the oxidation of gold(I) complex **10a** with $AgNTf_2$.

Method 3

The approach to synthesize bidentate-gold(III) complex **11** using method 3 is notably different than any methods described in the previous sections. As shown above, oxidation with $PhICl_2$ can be problematic. The alternative approach represented here consists of silver coordination to imidazolium, transmetalation with $KAuCl_4$ and halide removal with $AgSbF_6$ to coordinate the oxazoline ring (see Scheme 37). The method introduces the gold(III) to the ligand system in one step, without the need for further oxidation.

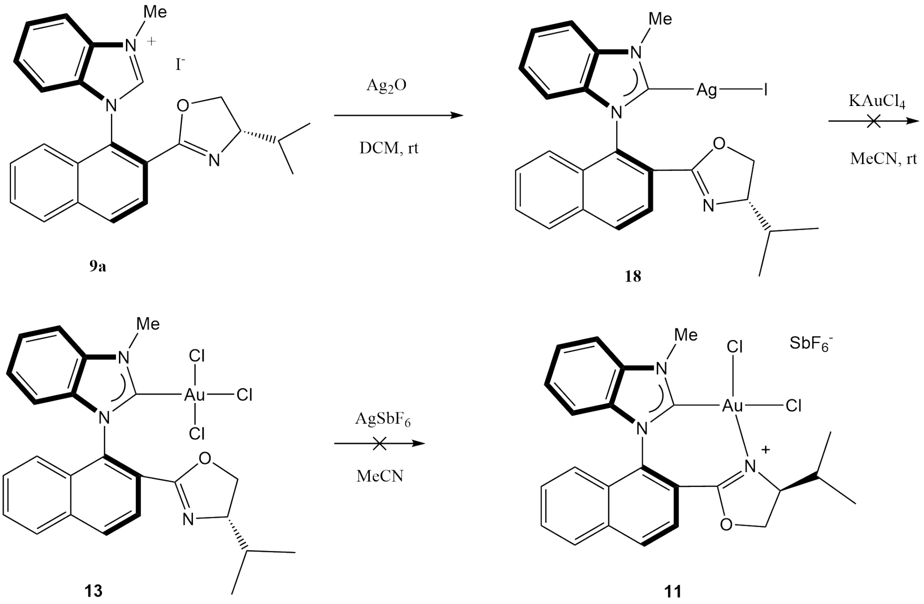

Scheme 37: Method 3 for the synthesis of gold(III) complex **11** from the corresponding imidazolium **9a** by transmetalation.

The formation of NHC-Ag complex **18** was relatively quick, and full conversion of imidazolium **9a** with Ag_2O was achieved within 30 min. The silver complex **18** was not fully characterized, but used directly in further reactions. As seen from the ^1H NMR spectra of NHC-Ag complex **18** and NHC-Au complex **10a** in Figure 24, the aromatic protons are similar, supporting the claim that the silver coordination is successfully carried out. There is also no sign of unwanted byproducts being formed.

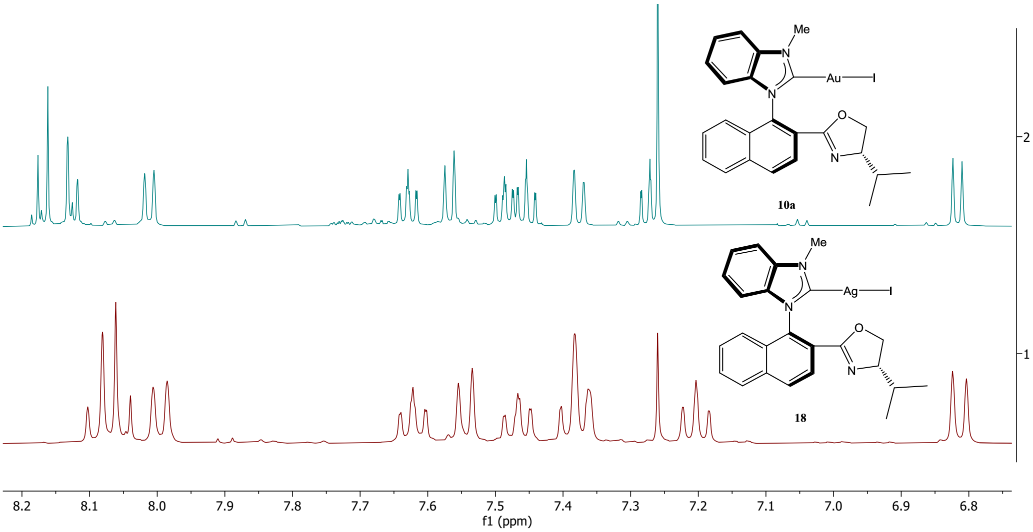

Figure 24: ^{1}H NMR spectra of NHC-Ag(I) complex **18** and NHC-gold(I) complex **10a** (2).

The reaction with $KAuCl_4$ was carried out in acetonitrile for 90 min. The result is a compound that does not correspond to the desired gold(III)Cl_3 complex **13**, since there seems to be a amide NH proton present at 5.22 ppm. Spectra of compound **25** are attached in the Appendix M. It does not couple with any carbon on the HSQC spectrum and couples to the neighboring proton on the COSY spectrum. That means that the oxazoline ring has been opened, possibly by a chloride as shown in Figure 38. ^{13}C and HMBC indicates that complex **25** is coordinated to gold(III), due to the C2 carbon shift on the imidazolium ring at 152 ppm. The shift would have been significantly higher if the complex was reduced to gold(I). The low C2 carbon shift could also indicate imidazolium protonation, but there is no acidic C2 proton in the ^{1}H NMR spectrum, which should be present around 10 ppm. Reaction with $AgSbF_6$ caused the complex to decompose, further implying that there are no oxazoline nitrogen to stabilize the cationic species. The HRMS spectrum of the decomposed complex shows strong indication of chloride atom in the compound. There is an M+2 signal caused by the ^{37}Cl isotope, and a 36 m/z fragmentation loss from HCl. The presence of chloride in complex **25** supports the mechanism shown in Scheme 38. The instability towards activation with silver salts remains a problem, and the complex will not be useful in catalysis.

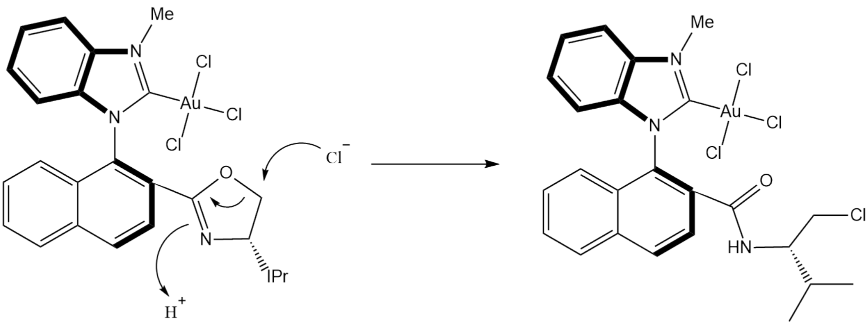

25

Scheme 38: Ring opening of oxazoline by chloride to gold(III)-amide complex **25**

2.3 The β-hydroxyamide-NHC ligand system

Synthesis of gold(III) complexes with the oxazoline ligand proved to be challenging, as described in the previous section. The oxazoline nitrogen failed to sufficiently stabilize the complex. Since a set of diastereomeric ligands **8a** and **8b** were already available, they were used to synthesize a β-hydroxyamide-NHC ligand system, coordinated with gold, and further oxidized with $PhICl_2$ to gold(III). The ligand does not provide the same steric effects as the bidentate oxazoline ligand, since the isopropyl group is situated quite far from the metal center.

2.3.1 Synthesis of compounds 19a and 19b

The methylation of the imidazole ring of was carried out in refluxing acetonitrile overnight (see Scheme 39). The yield is quantitative, and excess iodomethane is easily removed with n-pentane wash of crude product. Similarly to the oxazoline diastereomers **8a** and **8b** the two amide-imidazolium diastereomers **19a** and **19b** are difficult to separate, as they are retained similarly on silica through a flash column. The aS,S diastereomer **19a** is eluating firstly. Due to significant tailing, the rS,S diastereomer was not fully isolated.

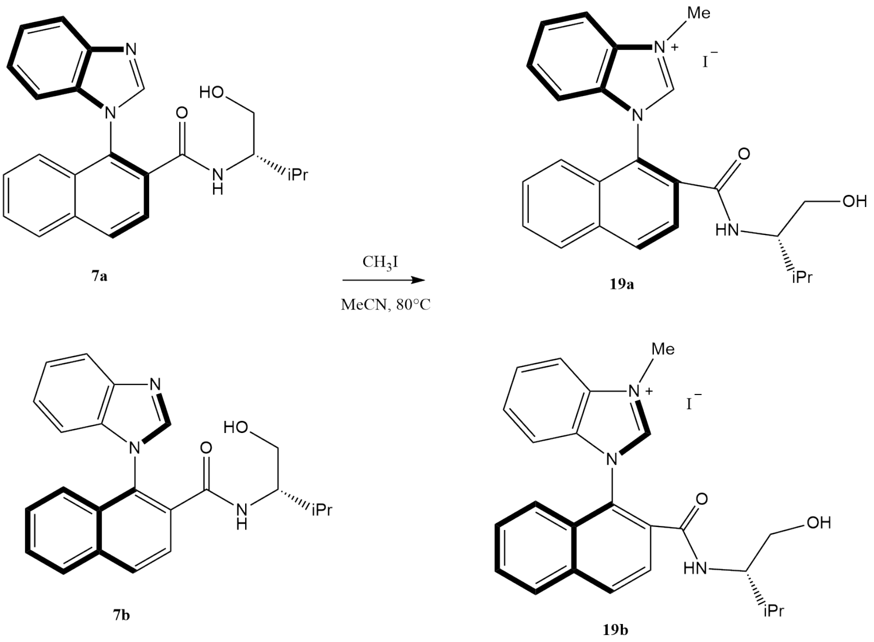

Scheme 39: Synthesis of diastereomers **19a** and **19b**

2.3.2 Synthesis of compounds 20a and 20b

The imidazolium compounds **19a** and **19b** were coordinated to gold(I) with Me$_2$SAuCl and potassium carbonate in refluxing acetone (see Scheme 40). Starting from the diastereomerically pure imidazolium **19a**, the corresponding gold(I) **20a** was synthesized in near quantitative yields on a 15 mg scale. The product was easily filtered through silica in a pipette and solvent removed under reduced pressure. On a 100 mg scale, the yield was unfortunately only 58%. The same procedure was followed, but due to the larger amount of compound, it was filtered through a longer column of silica. Decomposition on silica could be the cause of the lower chemical yield.

A diastereomeric mixture of imidazolium compounds **19a** and **19b** was also coordinated to gold. It was reason to believe that the two gold(I) diastereomers **20a** and **20b** would be more chemically different, than the corresponding imidazoliums **19a** and **19b**. The coordinated gold provides steric interactions closer to the chiral center of the amide. The diastereomers were easily separated on a flash column, and both gold complexes **20a** and **20b** were isolated and fully characterized. The yield was quite low, as a significant amount of compound decomposes on silica.

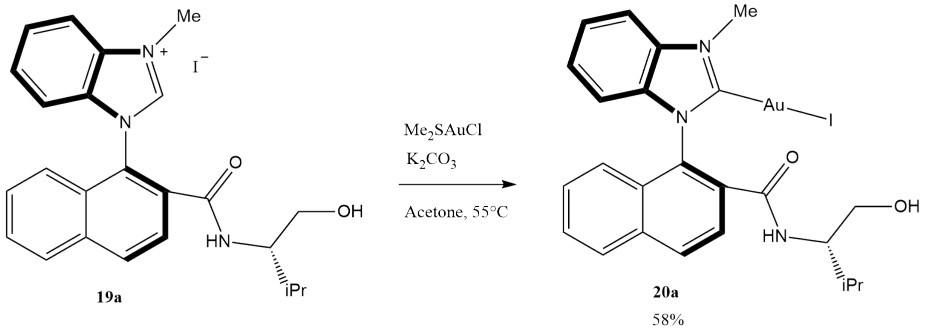

Scheme 40: Synthesis of NHC-amide-gold(I) complex **20a**

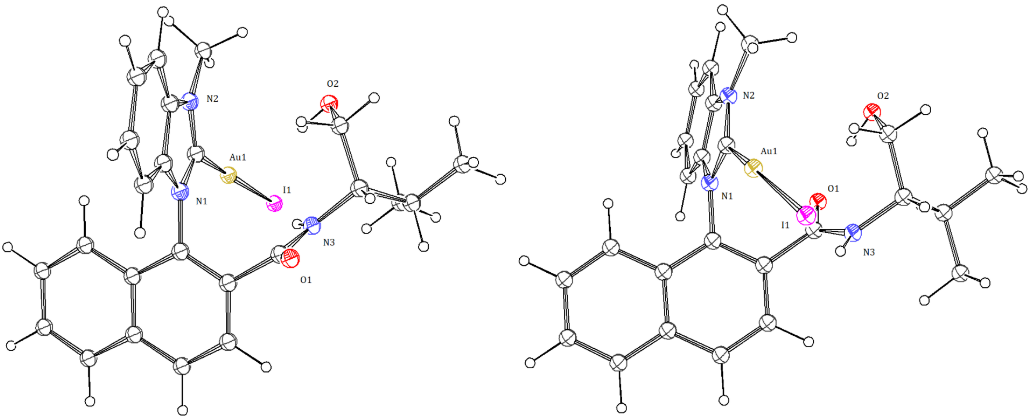

Figure 25: ORTEP view of calculated aS,S diastereomer **20a** (left) and aR,S diastereomer **20b** (right)

2.3.3 Oxygen coordination

Having an alcohol functional group in the gold(I) complex **20a**, a reaction to generate a new Au-O bond was attempted (see Scheme 41). Oxygen-coordinated gold complexes are interesting, as they can undergo silver-free activation, upon addition of an acid.[138] They can also be synthesized as intermediates for further alkylation reactions.[139,140] The reaction was carried out with cesium carbonate overnight in isopropyl alcohol. The OH proton of methanol and ethanol would likely be more acidic than the β-hydroxyamide proton, resulting in primarily solvent coordination to gold.

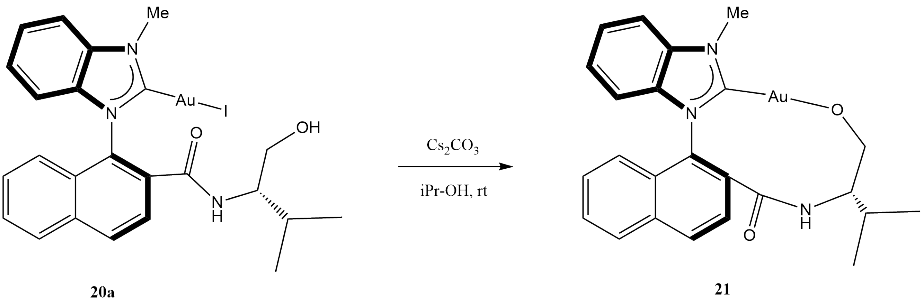

Scheme 41: O-Coordination of β-hydroxyamide-gold(I) complex **21a**

Based on NMR spectra of the product, the reaction did not work. There was selectively formed one new compound, but it does not correspond to the oxygen-coordinated complex **21**. The carbene carbon is 180 ppm suggests that it is still a NHC-gold(I) complex. However, the protons next to the coordinated oxygen should experience a shift downfield, which was not the case. The gold(I) center generally coordinates poorly to hard nucleophiles. If the complex was first oxidized to gold(III), it could possibly coordinate better.

2.3.4 Synthesis of compounds 22a and 22b

The gold(I) complexes **20a** and **20b** were reacted with $PhICl_2$ to yield the corresponding gold(III) complexes **22a** and **22b** (see Scheme 42). The gold(III) complexes are not stable on silica, and can therefore not be further purified on flash column. Recrystallization from DCM and n-pentane did improve the purity of the compounds.

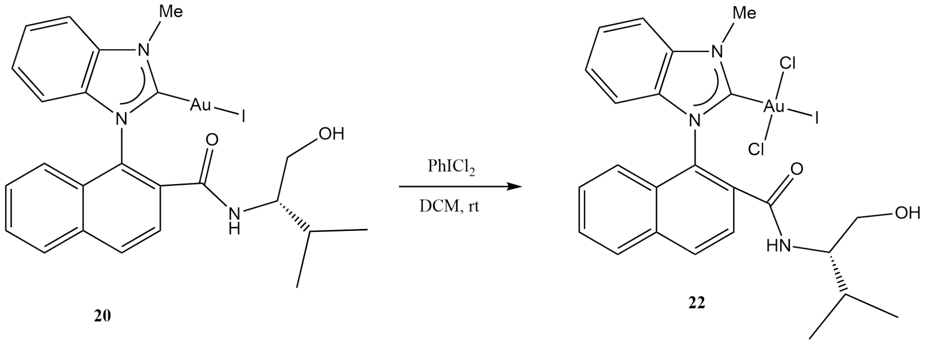

Scheme 42: Oxidation of gold(I) complexes **22a** and **22b** with $PhICl_2$

Interestingly, information from MS spectroscopy indicates that bis-NHC complexes are formed. This is likely a result of degradation during the electronspray ionization and not something that was formed over the course of the reaction with $PhICl_2$. The expected signal at 781 m/z was not detected and the dominant signal of the spectra was the 971 m/z peak, likely beeing di(NHC)-gold(I) complexes **23a** and **23b**. The MS-spectrum of R,S-diastereomer **22b** also shows a strong signal at 1041 m/z, which is likely the di(NHC)-gold(III)Cl_2 complex **24b** (see Figure 26). Interestingly, the di(NHC)-gold(III) complex was only observed for one of the diastereomers. The corresponding di(NHC)-gold(III)Cl_2 complex of the SS-diastereomer **21a** is likely too short-lived to be detected. The reduction is also prominent for the RS-diastereomer and the 971 m/z peak of compound **23b** is still the main signal of the spectrum.

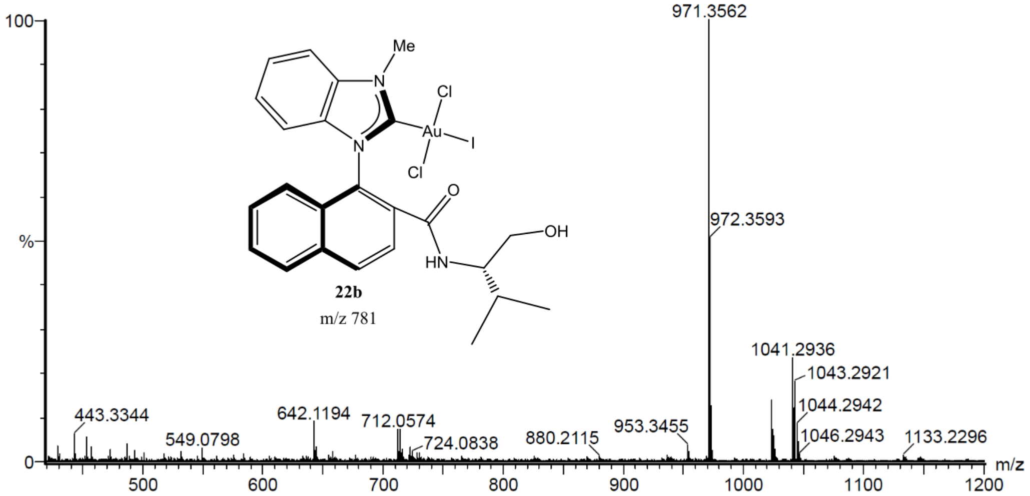

Figure 26: MS spectrum of gold(III) complex **22b**

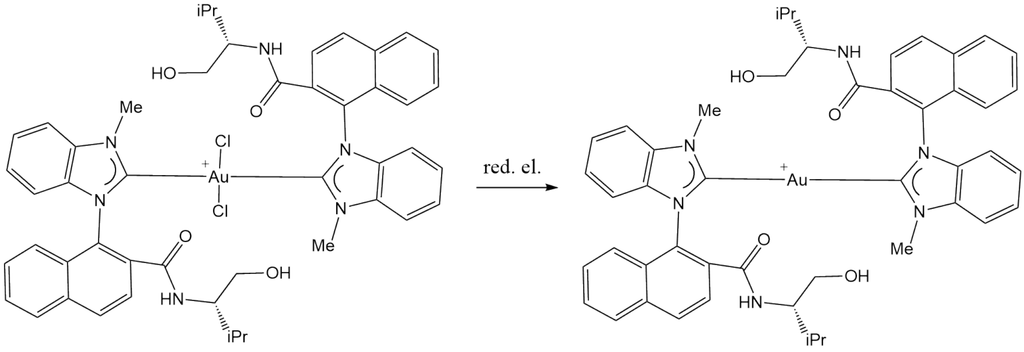

24 m/z 1041

23 m/z 971

Scheme 43: Reductive elimination of Cl_2 of the di(NHC)-gold(III)Cl_2 complex **24** to di(NHC)-gold(I) complex **23**

2.4 ^{13}C NMR shifts of C2 carbene carbons

In order to determine the oxidation state of gold coordinated to a NHC ligand, the C2 carbon of the imidazole ring provides valuable information.[136] As illustrated in Figure 27, the HMBC coupling between the N-methyl protons and the C2 carbon is detectable, even at low sample loads. This is useful in samples containing impurities or weak samples, where it can be difficult to detect the correct ^{13}C NMR signal. The quaternary C2 carbon generally gives weak signals.

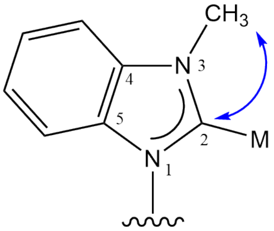

Figure 27: HMBC coupling between N-methyl protons and C2 carbon of the NHC ligand.

As shown in Table 2, the ^{13}C NMR shift of the C2 carbon can be used to determine whether the coordinated gold is in the +I or the +III oxidation state. The gold(I) complexes have C2 shifts around 190 ppm, and the gold(III) complexes have shifts around 150 ppm. Observing the significantly lowered C2 carbon shifts could therefore support the claim that an oxidation reaction has successfully been carried out. It could also indicate if a reduction has occurred in a synthetic process with gold(III) complexes.

Table 2: Chemical shifts of NHC C2 carbons of uncoordinated, gold(I)- and gold(III) coordinated NHC ligands. [a]The compound is not fully isolated and characterized.

Entry	Complex	Coordination character	C2 NMR shift [ppm]
1	**9a**	Imidazolium salt	143.27
2	**9b**	Imidazolium salt	144.41
3	**19a**	Imidazolium salt	143.39
4	**10a**	Au(I)	190.72
5	**20a**	Au(I)	188.48
6	**20b**	Au(I)	189.18
7	**11**[a]	Au(III)	148.63
8	**15**[a]	Au(III)	152.06
90	**25**[a]	Au(III)	152.44
10	**22a**	Au(III)	152.36
11	**22b**	Au(III)	153.03

2.5 Gold-catalyzed cyclopropanation

The gold-catalyzed reaction of propargyl acetate **26** with styrene was carried out according to previously described methods[141] (see Scheme 44). The results from the cyclopropanation reaction is summarized in Table 3. Ratios of *cis/trans* are approximated by ^{1}H NMR signals. Degradation and formation of colloidal gold particles decrease the resolution of the spectra, making ratio determination less accurate.

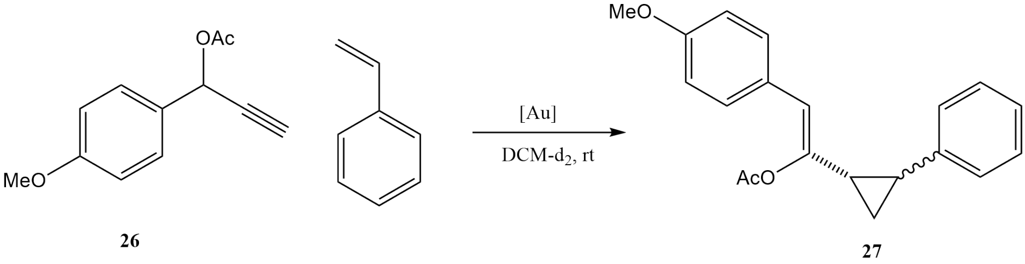

Scheme 44: Gold-catalyzed cyclopropanation of propargyl acetate **26** with styrene, to yield the *cis* cyclopropyl product **27a** or trans cyclopropyl product **27b**

Table 3: Catalyzed cyclopropanation of propargyl acetate **26** with styrene. Reactions were carried out with 5 mol% catalyst loading and 5 mol% silver salt.

Entry	Catalyst	Activation	Time	Conversion [%]	*cis/trans*
1	**10a**	$AgSbF_6$	15 min	8	99:1
2	**10a**	$AgSbF_6$	3 h	13	99:1
3	**10a**	$AgSbF_6$	16 h	15	99:1
4	**10a**	$[Ar_2I]^+BArF^-$	16 h	0	
5	**20a**	$AgSbF_6$	15 min	100	1:99
6	**22a**	$AgSbF_6$	15 min	100	1:99
7	**22b**	$AgSbF_6$	15 min	100	30:70
8	**22b**	$AgSbF_6$	2 h	100	10:90
9	**22b**	$AgSbF_6$	16 h	100	1:99

The reaction is catalyzed by the gold catalyst, which cooordinates to the propargyl triple bond. The gold-coordination promotes the rearrangement of the acetate group. The cationic intermediate species is attacked by styrene. As illustrated in Scheme 45, the conformation upon addition of styrene is controlled by steric forces. The intermediate species with gold and the large phenyl group trans to each other is more stable, resulting in the *cis*-isomer **26a** being the kinetic product of the reaction.

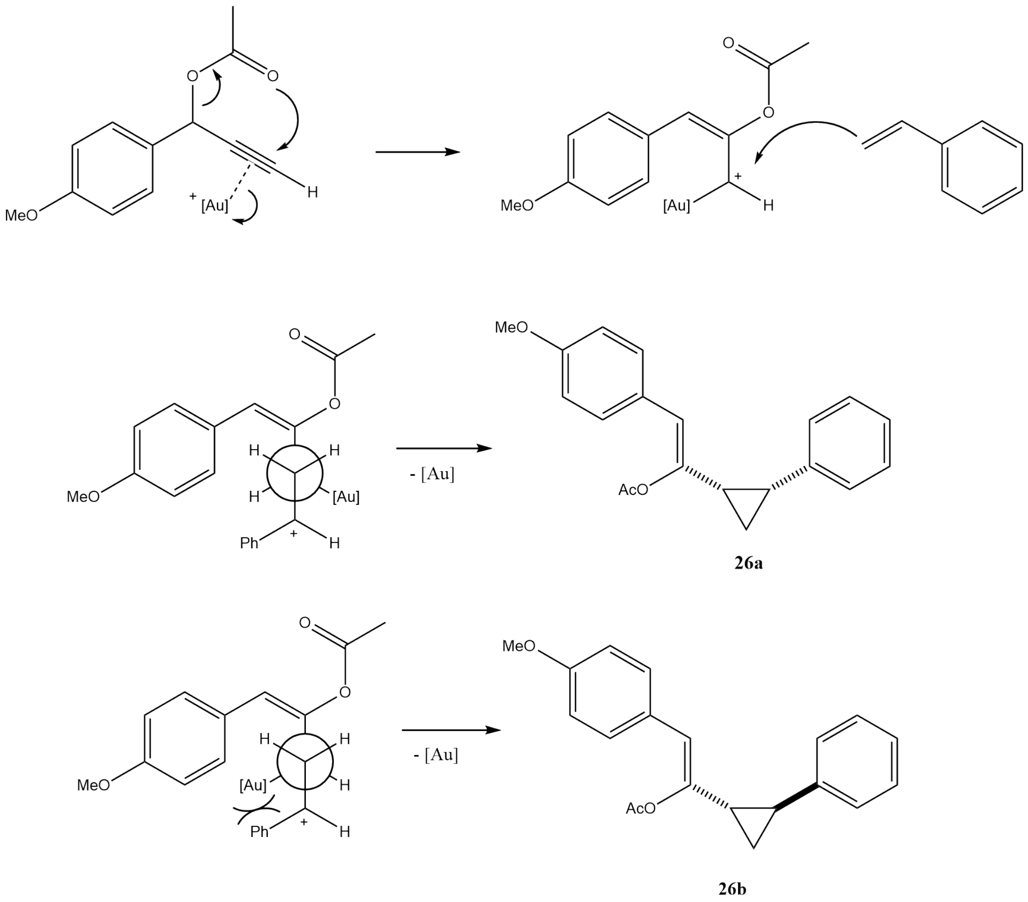

Scheme 45: Coordination of gold to propargyl triple bond, rearrangement of the acetate group, nucleophilic attack of styrene and generation of cyclopropanated product by deaureation.

The NHC-oxazoline-gold(I) catalyst **10a** failed to catalyze the reaction to full conversion. Using catalyst activation by halide removal with $AgSbF_6$, 8% conversion was achieved after 15 min. After 16 h, the conversion was still only 15 %, which indicates that the majority of the catalyst has decomposed. The cationic active species is likely too unstable, resulting in a low turnover. The activation of the gold catalyst was attempted with a halogen-bonding agent, where non-covalent bonding to the halide ligand introduces a partial positive charge at the gold center,[142] as shown in Figure 28. This should be a softer activation, reducing the rate of catalyst degradation. As shown in entry 4 of Table 3, the halogen-bonding compound failed to activate the gold catalyst. Since no conversion was achieved, the halogen-donor agent is likely weakening the gold-iodide bond enough for destabilization and degradation, without actually activating the catalyst.

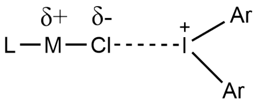

Figure 28: Halogen-bonding species for catalytic activation of metal center.

The NHC-β-hydroxyamide-gold catalysts **20a**, **22a** and **22b** catalyzed the reaction with full conversion within 15 minutes, as shown in entries 5-9 in Table 3. It is interesting to see that the NHC-amide complexes are more effective than the NHC-oxazoline complex **10a** at catalyzing the reaction. This indicates that the oxazoline ring promotes catalyst degradation. The instability of the seven-membered ring likely causes the degradation through a reductive elimination mechanism. The stability from the oxazoline donation is not enough to stabilize the complex.
Interestingly, the main product of the catalyzed reaction of propargyl acetate **26** with the amide-gold complexes was the trans product **26b**.

The cyclopropanation product **27b** from the catalyzed reactions with the NHC-β-hydroxyamide-gold catalysts **20a**, **22a** and **22b** was investigated with chiral HPLC, which consists of two enantiomers. Unfortunately, the chromatograms showed a racemic mixture of enantiomers, which means that the catalysts have no stereoselective control in the reaction.

2.5.1 Computational study on the reaction mechanism

A computational study was carried out to investigate the reaction mechanism of the gold-catalyzed cyclopropanation reaction. The computations were relatively expensive, and due to time constraints the study was not carried out to completion. The rearrangement of the acetate group, as shown in Scheme 45, was investigated and the results are presented below. In order to save computational time, the reactions were carried out with an *N,N*'-(diisopropyl)NHC-gold(I) catalyst and not an oxazoline-NHC-gold(I) complex. The mechanism should be similar, since the gold catalyst is coordinated to and stabilized by a NHC ligand. To minimize the computational cost, the reaction was modelled in gas phase. For better accuracy, one could implement a continuum solvation model and explicit solvent molecules. This can yield more accurate geometries and energies, but increases the computational time.

Since the initial images are generated by straight line interpolation between the initial and final structure, the energy path is quite far from the MEP. The initial energy path has a significantly higher energy barrier than the converged minimal path. The NEB converged after 87 iterations, and a few selected iterations are displayed in the Figure 29.

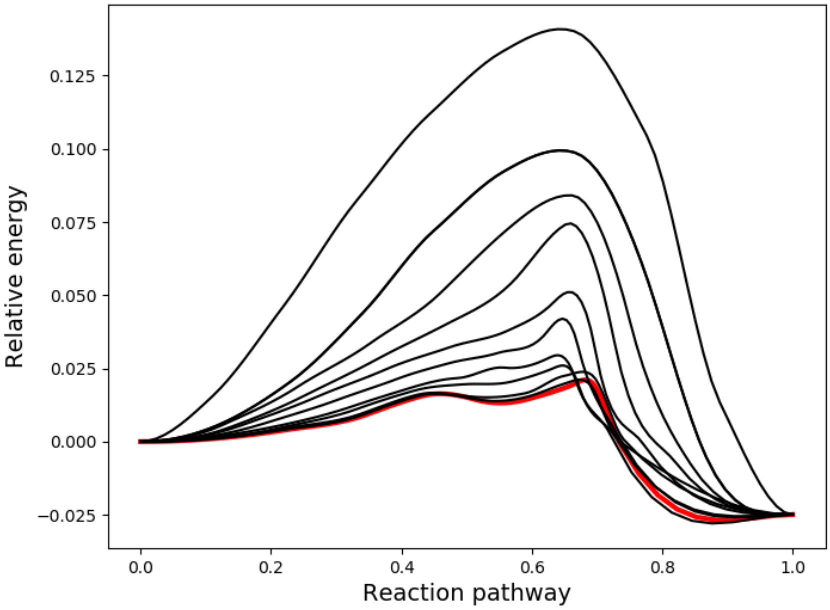

Figure 29: Iterations towards the MEP (red) of the acetate rearrangement, using the NEB method.

From the converged NEB calculation, image 6 was determined to be the climbing image. As shown in Figure 30, both image 6 and 7 are relatively close to the transition coordinate. According to the NEB calculation, there should be a second local minimum between images 4 and 5, and a transition state near image 3. The NEB computation could have been split up into two separate reactions. One computation from the reactant to the local minimum, and another one from the local minimun to the product configuration. This was not carried out.

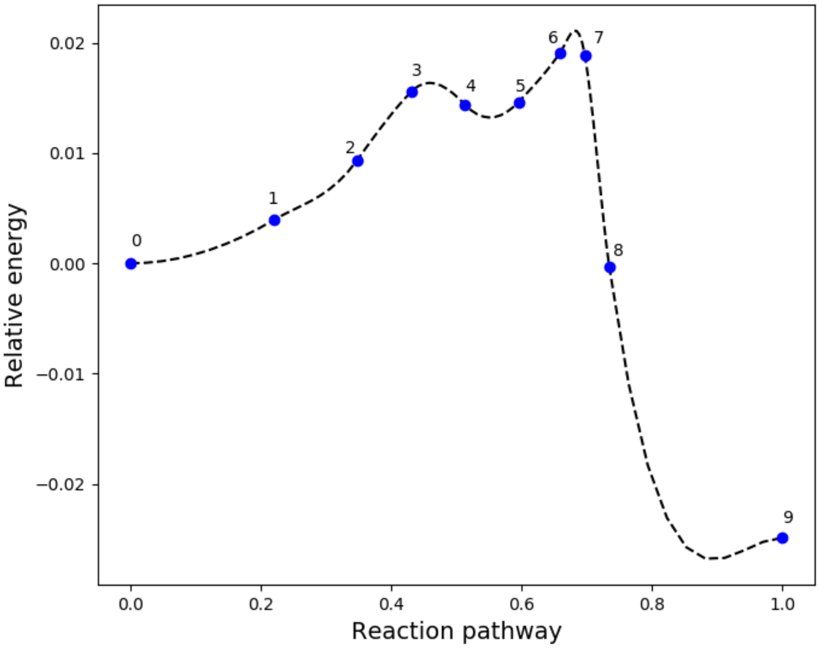

Figure 30: The MEP of the acetate rearrangement, based on interpolation between images 0 to 9.

An automatic transition state geometry optimization was carried out with the default settings of the NEB-TS method provided in the Orca package. The geometry did not converge within the maximum number of iterations. In order to obtain the optimized transition state configuration, the calculations were repeated with an initial calculation of the exact Hessian. For every five steps of the geometry optimization, the Hessian was recalculated. The Hessian describes the curvature on the potential energy surface. When searching for a transition state, one has to locate a saddle point on the potential energy surface. The calculation of the exact Hessian is computationally expensive, but proved necessary in order to converge to the transition state. Exactly one imaginary frequency showed that the transition configuration is a true saddle point. The geometries of the initial configuration, transition state and final structure are shown in Figure 31. The energy barrier of the rearrangement reaction was calculated to be 15 kJ/mol. It should be mentioned that single point energies were obtained with the relatively small basis set def2-SVP. For more accurate energies, one could redo the calculations with a triple zeta valence basis set.

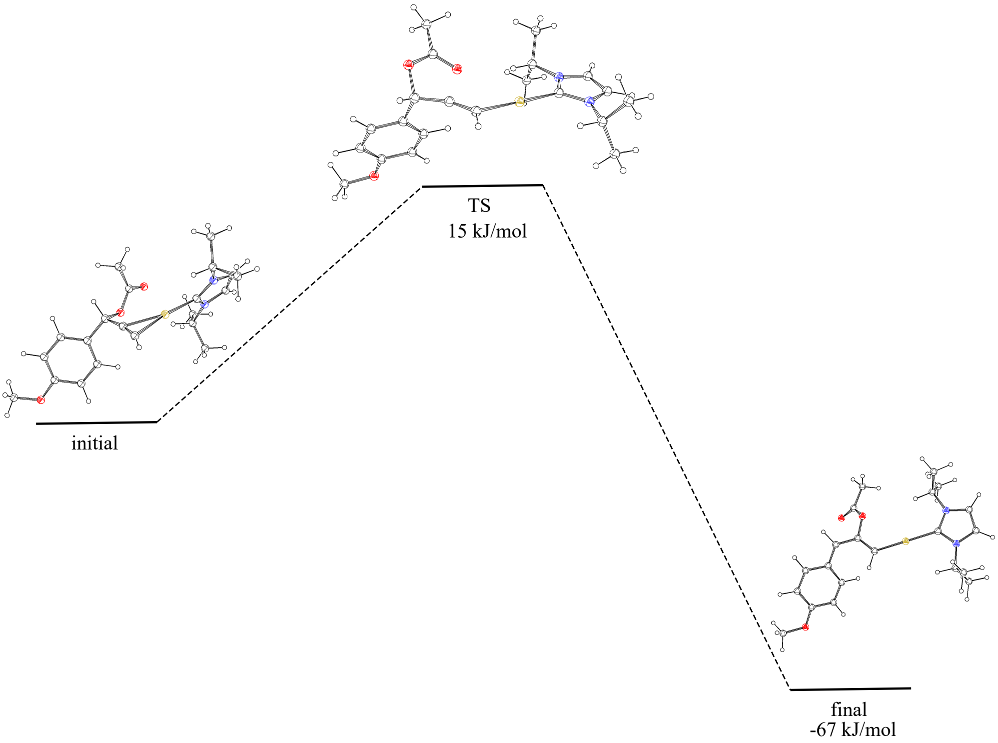

Figure 31: Geometry optimizations of the initial structure, transition state and final structure of the gold-catalyzed propargyl acetate rearrangement.

3 Conclusion

Diastereomerically pure oxazoline-NHC ligands have been synthesized and coordinated to gold. Axially chirality is introduced by restricted rotation along an imidazole-naphtalene bond and chirality is introduced upon amide synthesis with an enantiomerically pure aminoalcohol. Several methods were attempted to oxidize the gold complexes. The gold(I) complexes were firstly attempted oxidized, followed by halide removal to coordinate the oxazoline ligand, as well as the reverse order. Different solvents and silver salts were tried, addition of nitrone was carried out, and a transmetallation of the NHC-Ag complexs was attempted with $KAuCl_4$. A bidentate ligand system was concluded too unstable with a 7-membered ring system. Diastereomerically pure β-hydroxyamide-NHC ligands were prepared, coordinated to gold and oxidized with $PhICl_2$. Geometry optimalizations of synthesized compounds were carried out on DFT level. Visual representations were used to better understand compound behaviour and stability.

Prepared catalysts were applied in the cyclopropanation reaction of a propargyl acetate with styrene. The oxazoline-NHC gold complexes proved incapable of catalyzing the reaction due to rapid catalyst decomposition. β-Hydroxyamide-NHC gold complexes **20a**, **22a** and **22b** catalyzed the reaction within 15 min, resulting in only trans-cyclopropyl product. The products were analyzed by chiral HPLC, and it turned out that no catalysts could influence the enantioselectivity. The reaction mechanism was modeled on DFT level in gas phase.

4 Computational details

All computations were performed by density functional theory with the ORCA package[143]. Geometry optimizations were carried out with the BP86 functional[144]. It is a GGA functional that yields accurate geometries at low computational costs. The Karlsruhe basis set family was used with triple zeta valence quality.[145] Anions were described with minimally augmented Karlsruhe basis sets.[146] Calculations with gold complexes were carried out with relativistically contracted basis sets with an effective core potential for the inner electrons, using the zeroth-order regular approximation (ZORA).[147] Grimme's dispersion correction with BJ-damping functions were included, in order to better describe the noncovalent bonding interactions.[148] Numerical frequency calculations on optimized geometries was performed. No imaginary frequencies confirmed that the structures were true minima on the potential energy surface.

NEB computations were carried out with the B3LYP[149,150] functional and the def2-SVP Karlsruhe basis set. Transition state optimizations were carried out with calculations of the exact Hessian and numerical frequencies were computed. A single imaginary frequency was obtained and used to determine that a saddle point on the potential energy surface was successfully located.

5 Experimental

All experiments were carried out in a well ventilated fume hood. Reagents and solvents were purchased from Sigma-Aldrich and used without further purification. If necessary, dry solvents were collected from a Braun MB SPS-800 solvent purifier. TLC analysis were carried out with TLC Silica gel 60 F_{254} plates and developed using UV-light (254 nm). Silica gel (pore size 60 Å, 230-400 mesh particle size) was used for flash chromatography. Reactions were monitored, and crude product was analyzed by ^{1}H NMR with a Bruker Avance DPX 400 MHz spectrometer. Characterization of synthesized compounds were carried out by ^{1}H NMR and ^{13}C NMR with Bruker Avance III 600 MHz spectrometer, by IR spectrometry with a Bruker Alpha FTIR spectrometer with OPUS V7 software and by mass determination with a Synapt G2-S Q-TOF instrument from Waters without preliminary chromatographic separation.

5.1 Synthesis of compound 2

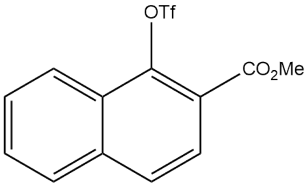

2

Triflic anhydride (2012 mg, 7.13 mmol, 1.2 ml) was added to a solution of **1** (1002 mg, 4.96 mmol) and pyridine (880.2 mg, 11.13 mmol, 0.9 ml) in DCM (4.8 ml) at 0°C and stirred at rt for 5h. The solution was diluted with water, product extracted with DCM and washed with brine and dried over anhydrous Na_2SO_4. The solvent was removed under reduced pressure to yield **2** as yellow crystals (1647.2 mg, 99%). The product was used in synthesis without further purification. The crude product was purified on flash column (1:10 EtOAc : n-Pentane) for analysis.

Spectra for compound **2** are available in Appendix B. ^{1}H NMR (600 MHz, $CDCl_3$) δ 8.20 – 8.16 (m, 1H), 7.99 (d, J = 8.5 Hz, 1H), 7.93 – 7.87 (m, 2H), 7.70 – 7.65 (m, 2H), 4.02 (s, 3H). ^{13}C NMR (151 MHz, $CDCl_3$) δ 165.3, 144.8, 136.6, 129.2, 128.3, 128.2, 128.0, 126.2, 122.2, 121.4, 119.7, 117.6, 52.8. IR (cm^{-1}) ν: 2956 (w), 1729 (s), 1426 (s), 1346 (s), 1286 (m), 1207 (s), 1138 (s), 1043 (m), 809 (m), 762 (m), 762 (w), 504 (w). HRMS (ESI, m/z): calculated for $C_{13}H_9F_3O_5SNa$ [M + Na] 357.0020; found 357.0026.

5.2 Synthesis of compound 3

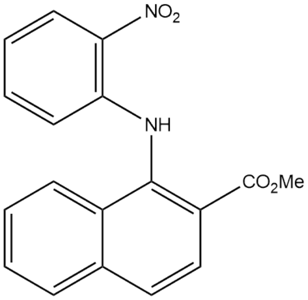

3

2 (1574 mg, 4.71 mmol), 2-nitroaniline (652 mg, 4.72 mmol), palladium(II) acetate (106 mg, 0.47 mmol), DPEphos (527 mg, 0.98 mmol), and cesium carbonate (2315 mg, 7.10 mol) were dissolved in toluene (20 mL, degassed) and stirred at 80 °C for 20 h. The solution was filtered through a pad of celite and solvent removed under pressure, extracted with DCM from water and dried over anhydrous Na_2SO_4. The crude product was purified on flash column (1:10 EtOAc : n-Pentane) to yield the product as orange crystals (1489 mg, 98%).

Spectra for compound **3** are available in Appendix C. ^1H NMR (600 MHz, $CDCl_3$) δ 10.47 (s, 1H), 8.24 (dd, J = 8.5, 1.6 Hz, 1H), 8.05 (d, J = 8.7 Hz, 1H), 7.94 – 7.88 (m, 2H), 7.81 (d, J = 8.7 Hz, 1H), 7.60 (ddd, J = 8.1, 6.8, 1.1 Hz, 1H), 7.46 (ddd, J = 8.2, 6.8, 1.2 Hz, 1H), 7.17 (dddd, J = 8.6, 7.0, 1.6, 0.6 Hz, 1H), 6.80 (ddd, J = 8.4, 7.0, 1.3 Hz, 1H), 6.34 (dd, J = 8.6, 1.2 Hz, 1H), 5.30 (s, 3H), 3.90 (s, 3H). ^{13}C NMR (151 MHz, $CDCl_3$) δ 167.1, 143.4, 138.0, 136.2, 135.1, 134.5, 129.4, 128.5, 128.5, 127.1, 126.5, 126.5, 126.3, 125.6, 122.7, 118.1, 117.5, 52.5. IR (cm^{-1}) ν: 3338 (w), 2950 (w), 1711 (m), 1612 (m), 1564 (m), 1494 (s), 1340 (s), 1269 (s), 1246 (s), 1151 (m), 767 (m), 742 (m). HRMS (ESI, m/z): calculated for $C_{18}H_{14}N_2O_4Na$ [M + Na] 345.0857; found 345.0851.

5.3 Synthesis of compound 4

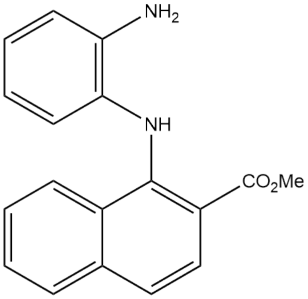

4

Compound **3** (1.253 g, 3.88 mmol), iron powder (880 mg, 15.76 mmol) and ammonium chloride (1.824 g, 34.01 mmol) were dissolved in ethanol (40 mL) and water (10 mL) and stirred at 70 °C for 3 h. The solution was filtered through a pad of celite, extracted with DCM, washed with brine, dried over Na_2SO_4 and solvent was removed under reduced pressure. The product was purified on flash column (1:10 EtOAc : n-Pentane) to yield product **4** as yellow crystals (1.000 g, 3.42 mmol, 88%).

Spectra for compound **4** are available in Appendix D. ^{1}H NMR (600 MHz, $CDCl_3$) δ 9.25 (s, 1H), 7.99 (d, J = 8.8 Hz, 1H), 7.82 – 7.75 (m, 2H), 7.47 (ddd, J = 8.1, 6.8, 1.2 Hz, 1H), 7.43 (d, J = 8.8 Hz, 1H), 7.24 (ddd, J = 8.4, 6.8, 1.3 Hz, 1H), 6.91 – 6.85 (m, 1H), 6.84 (dd, J = 7.9, 1.5 Hz, 1H), 6.50 (td, J = 7.5, 1.6 Hz, 1H), 6.42 (d, J = 7.8 Hz, 1H), 4.09 (s, 2H), 3.94 (s, 3H). ^{13}C NMR (151 MHz, $CDCl_3$) δ 169.2, 147.7, 139.3, 136.9, 133.3, 128.2, 128.2, 126.8, 126.6, 126.0, 125.2, 123.9, 121.6, 121.1, 118.7, 115.7, 113.7, 52.1. IR (cm^{-1}) ν: 3433 (w), 3350 (w), 3263 (w), 3049 (w), 2949 (w), 1682 (m), 1571 (m), 1445 (m), 1392 (m), 1271 (m), 1245 (s), 793 (m), 765 (m), 749 (m). HRMS (ESI, m/z): calculated for $C_{17}H_{13}N_2O$ [M - HOCH3 + H] 261.1028; found 261.1032.

5.4 Synthesis of compound 5

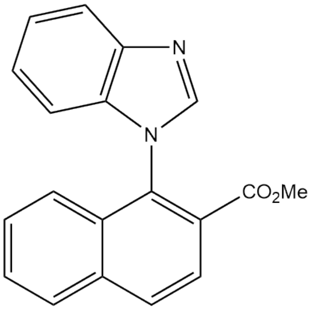

5

Diamine **4** (1.000 g, 3.42 mmol) and tosylic acid monohydrate (58.8 mg, 0.31 mmol) were dissolved in trimethyl orthoformate (10 mL) and stirred at 90°C for 20 h, diluted with water, extracted with DCM, washed with brine and dried over Na_2SO_4. Solvent was removed under reduced pressure, and the crude product was purified on flash column (1:1 EtOAc : n-Pentane) to yield product **5** as an orange oil (943 mg, 3.12 mmol, 91%).

Spectra for compound **5** are available in Appendix E. ^{1}H NMR (400 MHz, $CDCl_3$) δ 8.09 (s, 2H), 8.02 (s, 1H), 8.00 (d, J = 8.2 Hz, 1H), 7.94 (d, J = 8.1 Hz, 1H), 7.65 (ddd, J = 8.2, 6.8, 1.2 Hz, 1H), 7.47 (ddd, J = 8.2, 6.8, 1.2 Hz, 1H), 7.36 – 7.30 (m, 2H), 7.20 (ddd, J = 8.2, 7.2, 1.1 Hz, 1H), 6.91 (d, J = 8.1 Hz, 1H), 3.50 (s, 3H). ^{13}C NMR (101 MHz, $CDCl_3$) δ 165.9, 144.2, 143.1, 136.2, 135.8, 132.6, 130.9, 129.8, 128.9, 128.5, 128.3, 127.1, 126.2, 124.00, 123.7, 122.6, 120.4, 110.2, 52.6. IR (cm^{-1}) ν: 3055 (w), 2950 (w), 1724 (s), 1612 (w), 1597 (w), 1488 (s), 1454 (s), 1285 (s), 1243 (s), 1225 (m), 1134 (m), 765 (s), 744 (s). HRMS (ESI, m/z): calculated for $C_{19}H_{15}N_2O_2$ [M + H] 303.1134; found 303.1140.

5.5 Synthesis of compound 7

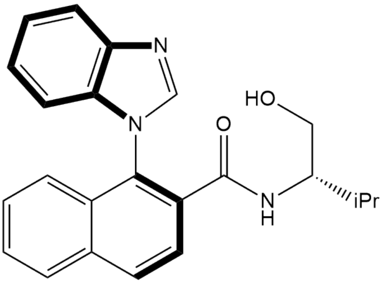

7a

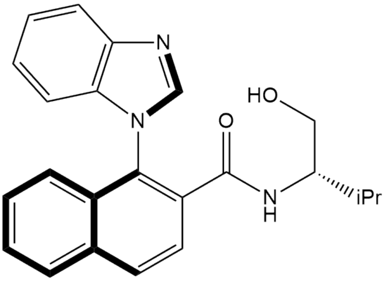

7b

Imidazole **5** (942 mg, 3.12 mmol), aminoalcohol **6** (621 mg, 6.02 mmol) and cesium carbonate (1952 mg, 5.99 mmol) were dissolved in toluene (30 mL) and stirred for 20 h. The product was diluted with water, extracted with DCM, dried over anhydrous Na_2SO_4 and solvent removed under reduced pressure to yield the two diastereomers **7a** and **7b** as white crystals (758 mg, 2.03 mmol, 65%). The diastereomers were not separated, but used as a mixture in further synthesis.

Spectra for compound **7** are available in Appendix F. ^{1}H NMR (600 MHz, $CDCl_3$) δ 8.13 - 8.08 (m, 3H), 8.02 – 7.98 (m, 1.5H), 7.96 (d, J = 8.2 Hz, 1H), 7.92 (d, J = 8.2 Hz, 0.5H), 7.87 (d, J = 8.5 Hz, 1.5H), 7.66 – 7.61 (m, 1.5H), 7.51 – 7.46 (m, 1.5H), 7.41 – 7.34 (m, 1.5H), 7.32 – 7.22 (m, 3H), 7.06 (t, J = 7.8 Hz, 1.5H), 5.74 (d, J = 8.7 Hz, 0.5H), 5.38 (d, J = 8.9 Hz, 1H), 3.65 – 3.60 (m, 1.5H), 3.31 (dd, J = 11.2, 5.2 Hz, 0.5H), 3.20 (dd, J = 11.3, 4.8 Hz, 1H), 3.11 (dd, J = 11.2, 3.5 Hz, 0.5H), 3.06 (dd, J = 11.3, 3.5 Hz, 1H), 1.49 (ddd, J = 13.6, 6.8, 2.9 Hz, 1.5H), 0.68 (d, J = 6.8 Hz, 3H), 0.61 – 0.54 (m, 6H). ^{13}C NMR (151 MHz, $CDCl_3$) δ 167.1, 166.8, 144.6, 144.1, 143.4, 143.2, 135.9, 135.8, 135.0, 134.9, 133.6, 133.4, 130.6, 130.5, 130.4, 130.2, 128.7, 128.6, 128.6, 128.5, 128.4, 128.3, 125.7, 125.6, 124.7, 124.6, 123.7, 123.5, 123.5, 123.3, 121.0, 120.8, 110.7, 110.5, 63.1, 63.0, 57.1, 57.0, 28.9, 28.7, 19.3, 19.0, 18.6, 18.4. IR (cm^{-1}) ν: 3280 (b), 2959 (m), 1639 (s), 1542 (m), 1490 (s), 1455 (m), 1228 (m), 743 (s). HRMS (ESI, m/z): calculated for $C_{23}H_{23}N_3O_2$ [M + H] 374.1869; found 374.1871.

5.6 Synthesis of compound 8

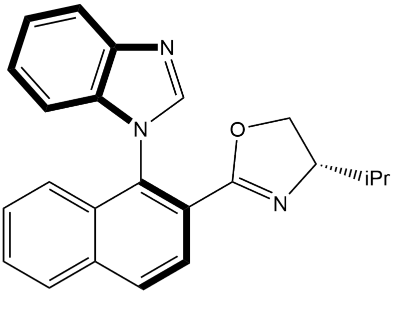
8a

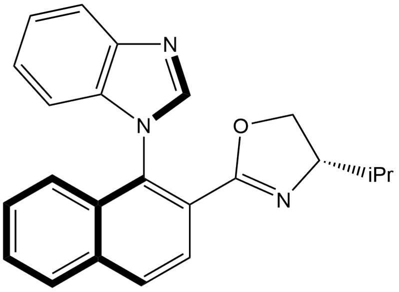
8b

The diastereomeric mixture of amides **7a** and **7b** (388 mg, 1.04 mmol) in cold DCM (12 mL, 0°C) was added thionyl chloride (636 mg, 5.35 mmol) and stirred at rt for 3 h. The solvent was removed under reduced pressure. Sodium hydroxide (424 mg, 10.60 mmol) in methanol (12 mL) was added, and the mixture was stirred for 15 h. The product was diluted with water and extracted with DCM, washed with brine and dried over anhydrous Na_2SO_4. The solvent was removed under reduced pressure to yield the two diastereomeric oxazolines **8a** and **8b** (364 mg, 1.02 mmol, 98%). The diastereomers were not easily separated. S,S-Diastereomer **8a** was isolated and R,S-diastereomer **8b** enriched by flash chromatography (2:1 n-pentane : EtOAc).

Spectra for compound **8a** are available in Appendix G. ^{1}H NMR (600 MHz, $CDCl_3$) δ 8.06 (d, J = 4.9 Hz, 3H), 8.00 (ddd, J = 8.3, 1.2, 0.7 Hz, 1H), 7.91 (dt, J = 8.1, 0.9 Hz, 1H), 7.62 (ddd, J = 8.1, 6.8, 1.2 Hz, 1H), 7.47 (ddd, J = 8.6, 6.8, 1.2 Hz, 1H), 7.37 (dd, J = 8.5, 1.0 Hz, 1H), 7.31 (ddd, J = 8.2, 7.1, 1.1 Hz, 1H), 7.19 (ddd, J = 8.2, 7.1, 1.1 Hz, 1H), 6.92 (dt, J = 8.1, 0.9 Hz, 1H), 4.12 (q, J = 7.1 Hz, 1H), 3.92 (dd, J = 9.6, 8.0 Hz, 1H), 3.81 (ddd, J = 9.6, 7.9, 6.5 Hz, 1H), 3.74 (t, J = 8.0 Hz, 1H), 1.45 – 1.36 (m, 1H), 0.70 (dd, J = 6.7, 2.2 Hz, 6H). ^{13}C NMR (151 MHz, $CDCl_3$) δ 161.4, 144.5, 143.3, 136.0, 135.2, 131.5, 130.9, 129.6, 128.3, 128.2, 126.4, 125.0, 123.6, 123.4, 122.3, 120.3, 110.3, 72.7, 70.6, 32.7, 18.4, 18.3. IR (cm^{-1}) ν: 3055 (w), 2958 (m), 1759 (m), 1649 (m), 1489 (s), 1455 (s), 1224 (m), 970 (m), 743 (s). HRMS (ESI, m/z): calculated for $C_{23}H_{22}N_3O$ [M + H] 356.1763; found 356.1768.

Spectra for compound **8b** are available in Appendix H. ^{1}H NMR (600 MHz, $CDCl_3$) δ 8.04 (d, J = 1.3 Hz, 2H), 8.02 – 7.95 (m, 2H), 7.90 (d, J = 8.2 Hz, 1H), 7.59 (t, J = 6.9 Hz, 1H), 7.34 – 7.27 (m, 2H), 6.93 (d, J = 8.1 Hz, 1H), 4.05 (dd, J = 9.8, 8.4 Hz, 1H), 3.81 (ddd, J = 9.8, 8.5, 6.6 Hz, 1H), 3.55 (t, J = 8.4 Hz, 1H), 1.51 (dt, J = 13.4, 6.7 Hz, 1H), 0.74 (d, J = 6.7 Hz, 3H), 0.67 (d, J = 6.8 Hz, 3H). ^{13}C NMR (151 MHz, $CDCl_3$) δ 161.7, 144.3, 143.1, 136.2, 135.1, 131.5, 130.8, 129.6, 128.3, 128.2, 128.2, 126.5, 125.3, 123.6, 123.5, 122.3, 120.2, 110.6, 72.6, 70.7, 32.6, 18.6, 18.1. IR (cm^{-1}) ν: 3056 (w), 2958 (m), 1646 (m), 1489 (s), 1455 (s), 1223 (s), 947 (m), 828 (m), 743 (s).

5.7 Synthesis of compound 9a

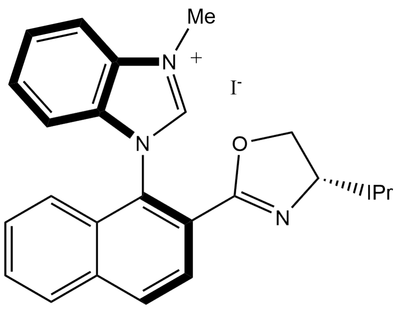

9a

The imidazole **8a** (122 mg, 343 μmol) and iodomethane (456 mg, 3.21 mmol, 200 μL) were dissolved in acetonitrile (3.6 mL) and stirred at reflux for 6.5 h. The crude product was recrystallized from DCM and n-pentane and solvent was removed under pressure to yield imidazolium **9a** as an oil (176 mg, 99%).

Spectra for compound **9a** are available in Appendix I. ^{1}H NMR (600 MHz, $CDCl_3$) δ 10.67 (s, 1H), 8.24 – 8.20 (m, 1H), 8.16 (d, J = 8.7 Hz, 1H), 8.06 (dt, J = 8.5, 1.0 Hz, 1H), 7.84 (dt, J = 8.5, 0.9 Hz, 1H), 7.72 - 7-67 (m, 2H), 7.62 (ddd, J = 8.1, 6.8, 1.2 Hz, 1H), 7.57 (dq, J = 8.6, 0.9 Hz, 1H), 7.51 (ddd, J = 8.3, 7.3, 1.0 Hz, 1H), 7.02 (dt, J = 8.3, 0.8 Hz, 1H), 4.59 (d, J = 0.7 Hz, 3H), 4.31 (dd, J = 9.8, 8.1 Hz, 1H), 3.92 (ddd, J = 9.7, 8.4, 6.4 Hz, 1H), 3.85 (t, J = 8.2 Hz, 1H), 1.18 (h, J = 6.7 Hz, 1H), 0.47 (d, J = 6.7 Hz, 3H), 0.29 (d, J = 6.7 Hz, 3H). ^{13}C NMR (151 MHz, $CDCl_3$) δ 157.1, 143.3, 133.3, 130.8, 130.3, 130.0, 127.7, 127.6, 127.3, 126.6, 125.7, 125.2, 123.8, 121.4, 121.2, 144.4, 111.3, 110.6, 71.1, 68.0, 32.8, 30.6, 16.5, 15.5. IR (cm^{-1}) ν: 2959 (m), 1642 (s), 1565 (s), 1463 (m), 1383 (m), 1245 (m), 1133 (m), 967 (m), 834 (m), 754 (s). HRMS (ESI, m/z): calculated for $C_{24}H_{24}N_3O$ [M - I] 370.1919; found 370.1924.

Spectra for compound **9b** are available in Appendix J. ^{1}H NMR (600 MHz, $CDCl_3$) δ 8.23 – 8.18 (m, 1H), 8.17 – 8.12 (m, 1H), 8.06 – 8.01 (m, 1H), 7.92 – 7.88 (m, 1H), 7.72 – 7.65 (m, 2H), 7.59 (ddd, J = 8.2, 6.8, 1.2 Hz, 1H), 7.54 – 7.48 (m, 2H), 7.00 (dd, J = 8.4, 0.9 Hz, 1H), 4.55 (s, 3H), 4.24 (dd, J = 9.8, 8.3 Hz, 1H), 3.87 (dd, J = 9.4, 8.4 Hz, 1H), 3.55 (td, J = 9.6, 7.5 Hz, 1H), 0.74 (dd, J = 8.8, 6.7 Hz, 6H). ^{13}C NMR (151 MHz, $CDCl_3$) δ 159.4, 144.4, 135.2, 132.9, 131.9, 131.9, 129.6, 129.4, 129.2, 128.5, 127.8, 127.4, 127.3, 125.8, 123.7, 123.22, 113.3, 113.0, 73.6, 70.5, 34.9, 32.8, 19.0, 18.8.

5.8 Synthesis of compound 10a

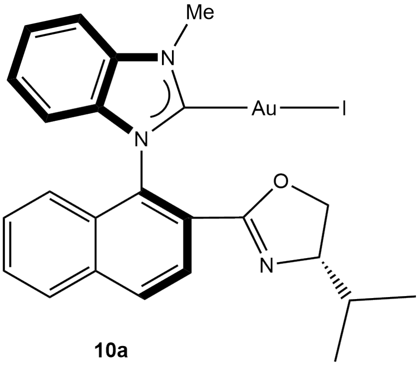

10a

The imidazolium ligand **9a** (176 mg, 282 μmol), chloro(dimethylsulfide)gold(I) (103 mg, 351 μmol) and potassium carbonate (484 mg, 3.50 mmol) were dissolved in acetone (8 mL) and stirred at reflux for 4 h. The crude product was filtered through silica to yield the gold(I) complex **10a** as a yellow solid (206 mg, 87%).

Spectra for compound **10a** are available in Appendix K. ^{1}H NMR (600 MHz, $CDCl_3$) δ 8.19 – 8.10 (m, 2H), 8.01 (dt, J = 8.3, 1.0 Hz, 1H), 7.63 (ddd, J = 8.2, 6.8, 1.2 Hz, 1H), 7.57 (dt, J = 8.3, 0.9 Hz, 1H), 7.52 – 7.43 (m, 2H), 7.38 (dd, J = 8.5, 1.0 Hz, 1H), 7.30 – 7.25 (m, 1H), 6.82 (d, J = 8.1 Hz, 1H), 4.23 (s, 3H), 4.09 – 4.04 (m, 1H), 3.79 – 3.72 (m, 2H), 1.30 – 1.23 (m, 1H), 0.58 (d, J = 6.8 Hz, 3H), 0.46 (d, J = 6.7 Hz, 3H). ^{13}C NMR

(151 MHz, $CDCl_3$) δ 190.7, 159.8, 135.3, 135.3, 133.4, 132.0, 130.5, 130.4, 128.4, 128.4, 128.3, 126.3, 124.8, 124.5, 124.2, 123.3, 112.0, 110.9, 73.0, 70.0, 35.0, 32.7, 18.7, 18.0. IR (cm^{-1}) ν: 3058 (w), 2958 (m), 2896 (m), 2870 (m), 1727 (m), 1643 (s), 1460 (s), 1440 (s), 1383 (s), 1239 (m), 745 (s). HRMS (ESI, m/z): calculated for $C_{24}H_{24}N_3OAuI$ [M + H] 694.0630; found 694.0632.

5.9 Synthesis of compound 19

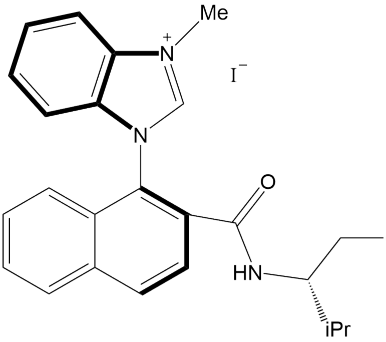

19a

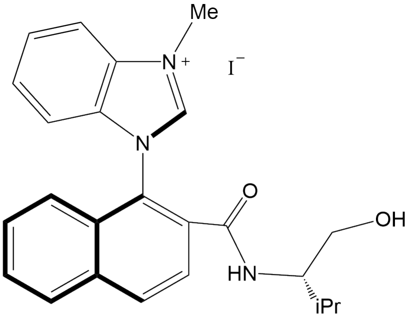

19b

A diastereomeric mixture of amides **7a** and **7b** (365 mg, 977 mmol) and iodomethane (1368 mg, 9.64 mol, 600 μL) were dissolved in acetonitrile (10 mL) and stirred at reflux for 18h. The product was recrystallized in DCM / n-pentane and solvent was removed under pressure to yield a diastereomeric mixture of imidazolium compounds **19a** and **19b** (99%). The diastereomers were not easily separated. S,S-Diastereomer **19a** was isolated and R,S-diastereomer **19b** enriched by flash chromatography (20:1 DCM : MeOH).

Spectra for compound **19a** are available in Appendix N. ^{1}H NMR (600 MHz, $CDCl_3$) δ 11.27 (s, 1H), 8.24 (dd, J = 8.6, 0.9 Hz, 1H), 8.09 (d, J = 8.5 Hz, 1H), 7.81 (dt, J = 8.5, 0.9 Hz, 1H), 7.75 (d, J = 8.4 Hz, 1H), 7.73 (ddd, J = 8.4, 7.3, 1.0 Hz, 1H), 7.69 (ddd, J = 8.2, 6.8, 1.1 Hz, 1H), 7.60 (ddd, J = 8.4, 7.3, 1.0 Hz, 1H), 7.56 (ddd, J = 8.3, 6.8, 1.2 Hz, 1H), 7.32 (d, J = 8.4 Hz, 1H), 7.26 (d, J = 5.3 Hz, 5H), 7.18 (d, J = 8.9 Hz, 1H), 4.37 (d, J = 0.7 Hz, 3H), 3.87 – 3.76 (m, 2H), 3.58 (ddd, J = 11.3, 5.5, 2.8 Hz, 1H), 3.48 (t, J = 6.0 Hz, 1H), 1.93 (h, J = 6.8 Hz, 1H), 0.99 (d, J = 6.8 Hz, 3H), 0.95 (d, J = 6.8 Hz, 3H). ^{13}C NMR (151 MHz, $CDCl_3$) δ 166.8, 143.4, 135.4, 134.6, 133.7, 132.6, 131.3, 129.3, 129.2, 128.7, 128.4, 128.2, 127.7, 125.3, 124.0, 121.7, 114.5, 112.7, 61.7, 57.8, 33.9, 29.6, 19.8, 19.2. IR (cm^{-1}) ν: 3348 (b), 3051 (w), 2962 (m), 2874 (w), 1733 (w), 1650 (s), 1564 (m), 1534 (m), 1461 (m), 1378 (m), 1258 (m), 918 (m), 751 (s), 731 (s). HRMS (ESI, m/z): calculated for $C_{24}H_{26}N_3O_2$ [M - I] 388.2025; found 388.2026. Spectra for compound **19b** are available in Appendix O. ^{1}H NMR (600 MHz, $CDCl_3$) δ 10.38 (s, 1H), 8.16 (d, J = 9.5 Hz, 1H), 8.00 (d, J = 8.4 Hz, 1H), 7.82 (dd, J = 13.6, 8.5 Hz, 2H), 7.69 – 7.61 (m, 3H), 7.55 – 7.51 (m, 2H), 7.41 – 7.34 (m, 2H), 4.31 (s, 3H), 3.55 – 3.42 (m, 2H), 3.40 (s, 1H), 3.37 – 3.32 (m, 1H), 3.03 (t, J = 6.2 Hz, 1H), 1.86-1.77 (m, 1H), 0.70 (dd, J = 6.7, 1.3 Hz, 6H).

5.10 Synthesis of compound 20

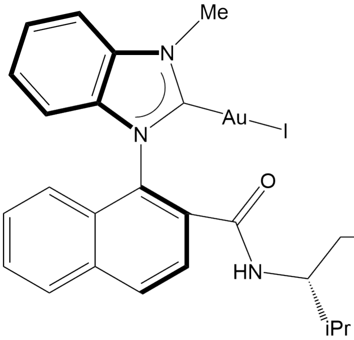

20a

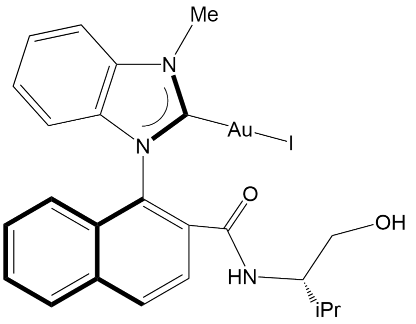

20b

Diastereomerically pure S,S-imidazolium **19a** (106 mg, 206 mmol), chloro(dimethylsulfide)gold(I) (62 mg, 210 mmol) and potassium carbonate (264 mg, 1.91 mol) were stirred in refluxing acetone (15 mL) for 2 h. The mixture was filtered through silica and solvent was removed under pressure to yield product **20a** (85 mg, 58%).

A (1:1) mixture of diastereomers **19a** and **19b** (54.2 mg, 105 mmol), chloro(dimethylsulfide)gold(I) (31 mg, 107 mmol) and potassium carbonate (146 mg, 1.05 mol) were dissolved in acetone (7 mL) and stirred at reflux for 2 h. The crude mixture was purified with flash chromatography (1:1 EtOAc : n-Pentane) to yield diastereomerically pure S,S-gold(I) complex **20a** (11.9 mg, 16%) and R,S-gold(I) complex **20b** (12.5 mg, 17%).

Spectra for compound **20a** are available in Appendix P. ^{1}H NMR (600 MHz, $CDCl_3$) δ 8.17 (d, J = 8.6, 1H), 8.08 – 8.03 (m, 1H), 7.75 (d, J = 8.5 Hz, 1H), 7.65 (ddd, J = 8.2, 6.8, 1.1 Hz, 1H), 7.59 (dt, J = 8.3, 0.9 Hz, 1H), 7.52 – 7.46 (m, 2H), 7.34 (d, J = 15.5 Hz, 1H), 7.20 (dd, J = 8.5, 1.1 Hz, 1H), 6.95 (d, J = 8.2 Hz, 1H), 6.51 (d, J = 9.2 Hz, 1H), 4.19 (s, 3H), 3.86 - 3.79 (m, 1H), 3.74 – 3.69 (m, 2H), 2.03 – 1.96 (m, 1H), 1.01 (dd, J = 14.3, 6.7 Hz, 6H). ^{13}C NMR (151 MHz, $CDCl_3$) δ 188.5, 166.9, 135.6, 134.8, 134.2, 132.8, 131.2, 130.8, 129.9, 128.8, 128.7, 128.2, 125.6, 125.0, 123.8, 122.9, 112.9, 111.5, 62.0, 56.9, 35.1, 29.4, 19.8, 19.5. IR (cm^{-1}) ν: 3348 (b), 3051 (w), 2962 (m), 2874 (w), 1733 (w), 1650 (s), 1564 (m), 1534 (m), 1461 (m), 1378 (m), 1258 (m), 918 (m), 751 (s), 731 (s). HRMS (ESI, m/z): calculated for $C_{24}H_{25}N_3O_2AuINa$ [M + Na] 734.0555; found 734.0557.

Spectra for compound **20b** are available in Appendix Q. ^{1}H NMR (600 MHz, $CDCl_3$) δ 8.15 (dd, J = 8.6, 0.9 Hz, 1H), 8.02 (dt, J = 8.3, 0.9 Hz, 1H), 7.79 (d, J = 8.5 Hz, 1H), 7.63 (ddd, J = 8.2, 6.8, 1.1 Hz, 1H), 7.59 (d, J = 8.3 Hz, 1H), 7.53 – 7.49 (m, 1H), 7.48 (ddd, J = 8.2, 6.8, 1.2 Hz, 1H), 7.36 (ddd, J = 8.3, 7.3, 1.0 Hz, 1H), 7.16 – 7.11 (m, 1H), 6.98 (dt, J = 8.3, 0.9 Hz, 1H), 6.53 (d, J = 8.2 Hz, 1H), 4.20 (s, 3H), 3.76 – 3.61 (m, 3H), 2.20 (t, J = 5.5 Hz, 1H), 1.92 – 1.83 (m, J = 6.7 Hz, 1H), 0.82 (dd, J = 6.8, 4.7 Hz, 6H). ^{13}C NMR (151 MHz, $CDCl_3$) δ 189.2, 167.5, 135.6, 134.8, 134.2, 132.8, 131.2, 130.1, 129.9, 128.7, 128.7, 128.3, 125.7, 125.3, 124.6, 122.7, 112.9, 111.3, 63.5, 58.2, 35.0, 29.0, 19.3. IR (cm^{-1}) ν: 3416 (b), 2959 (m), 2874 (w), 1651 (s), 1516 (s), 1460 (m), 1440 (m), 1388 (m), 1372 (m), 1238 (m), 911 (m), 744 (s). HRMS (ESI, m/z): calculated for $C_{24}H_{25}N_3O_2AuINa$ [M + Na] 734.0555; found 734.0557.

5.11 Synthesis of compound 22

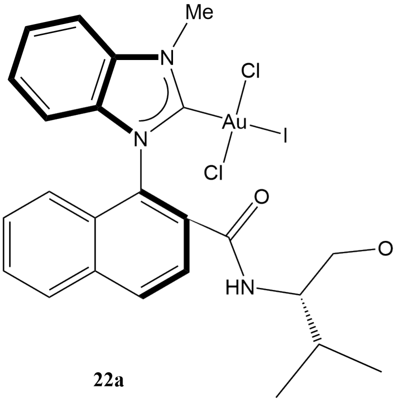

22a

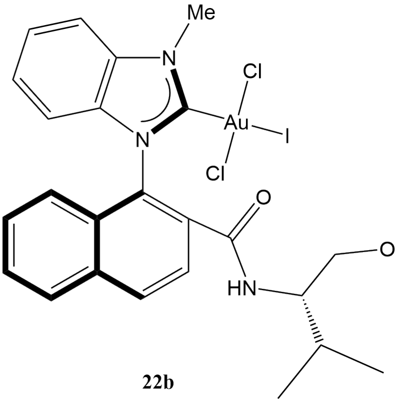

22b

Diastereomerically pure gold(I) complex **20a** (15.4 mg, 22 mmol) and $PhICl_2$ (12.4 mg, 45 mmol) were dissolved in DCM (2.5 mL) and stirred for 15 min at rt. The compound was recrystallized in n-pentane and solvent was removed under reduced pressure to yield product **22a** (5.8 mg, 34%). The diastereomer **22b** was synthesized following the same procedure.

Spectra for compound **22a** are available in Appendix R. ^{1}H NMR (600 MHz, $CDCl_3$) δ 8.23 (s, 1H), 8.05 (d, J = 8.2 Hz, 1H), 7.84 (d, J = 8.5 Hz, 1H), 7.73 - 7.66 (m, 2H), 7.61 - 7.56 (m, 2H), 7.52 - 7-49 (m, 1H), 7.45 (t, J = 8.3 Hz, 1H), 7.22 (d, J = 8.3 Hz, 1H), 7.13 - 7.08 (m, 1H), 4.36 (s, 3H), 3.61 - 3.54 (m, 1H), 3.36 - 3.29 (m, 1H), 2.97 - 2.91 (m, 1H), 1.87 - 1.77 (m, 1H), 0.93 – 0.80 (m, 6H). ^{13}C NMR (151 MHz, $CDCl_3$) δ 166.5, 152.4, 137.5, 136.2, 135.2, 133.8, 133.5, 132.4, 130.3, 129.0, 128.9, 128.6, 127.2, 126.6, 126.5, 125.1, 124.0, 114.1, 111.8, 62.5, 57.0, 35.6, 29.0, 19.2. IR (cm^{-1}) ν: 3344 (b), 3068 (w), 2962 (m), 1722 (w), 1644 (s), 1527 (m), 1504 (m), 1457 (s), 1407 (m), 1378 (m), 910 (m), 732 (s).

Spectra for compound **22b** are available in Appendix S. ^{1}H NMR (600 MHz, $CDCl_3$) δ 8.23 (d, J = 9.6 Hz, 1H), 8.08 – 8.00 (m, 1H), 7.84 (d, J = 8.5 Hz, 1H), 7.78 – 7.65 (m, 2H), 7.62 - 7.55 (m, 2H), 7.48 - 7.43 (m, 2H), 7.24 – 7.20 (m, 1H), 6.95 (d, J = 7.0 Hz, 1H), 4.37 (s, 3H), 3.62 – 3.48 (m, 3H), 1.70 – 1.63 (m, 1H), 0.69 - 0.55 (m, 6H). ^{13}C NMR (151 MHz, $CDCl_3$) δ 167.4, 153.0, 137.5, 136.2, 135.2, 133.6, 133.2, 132.5, 130.3, 129.1, 129.1, 129.0, 128.6, 127.0, 126.8, 126.6, 125.2, 124.0, 114.1, 111.7, 63.5, 58.8, 35.6, 28.9, 18.7, 18.6. IR (cm^{-1}) ν: 3339 (b), 3071 (w), 2960 (m), 1650 (s), 1522 (m), 1504 (m), 1457 (s), 1407 (m), 1377 (m), 909 (m), 730 (s).

References

1. P. L. Bernstein, *The Power of Gold (The History of an Obsession), Chapter 1 - Get Gold of All Hazards* (Wiley, 2011).
2. F. Habashi, *Gold Ore Processing (Second Edition), Chapter 1 - Gold – An Historical Introduction* (Elsevier, 2016).
3. R. S. Lopez, *Econ Hist Rev* **9**, 219 (1956).

4. E. Harmon, J. Lebin, D. Murphy, B. Watsjold, *BMJ Case Reports CP* **12** (2019).
5. P. Davis, *Can Fam Physician* **34**, 445 (1988).
6. P. L. Witkiewicz, C. F. Shaw, *J Chem Soc Chem Commun*, 1111 (1981).
7. C. M. Che, R. W. Y. Sun, *Chem Commun* **47**, 9554 (2011).
8. G. J. Hutchings, *J Catal* **96**, 292 (1985).
9. M. Haruta, T. Kobayashi, H. Sano, N. Yamada, *Chem Lett* **16**, 405 (1987).
10. A. S. K. Hashmi, G. J. Hutchings, *Angew Chem Int Ed* **45**, 7896 (2006).
11. J. Teles, S. Brode, M. Chabanas, *Angew Chem Int* **37**, 1415 (1998).
12. Y. Ito, M. Sawamura, T. Hayashi, *J Am Chem Soc* **108**, 6406 (1986).
13. K. Utimoto, Y. Fukuda, *Bull Chem Soc Jpn* **64**, 2013 (1991).
14. A. S. K. Hashmi, T. M. Frost, J. W. Bats, *J Am Chem Soc* **122**, 11553 (2000).
15. S. P. Nolan, *Nolan Group - Ghent University* (`https://www.nolan.ugent.be`).
16. F. D. Toste, *Toste Group - UC Berkeley* (`http://www.cchem.berkeley.edu/toste/index.html`).
17. A. S. K. Hashmi, *Hashmi Group - Ruprecht-Karls-Universität Heidelberg* (`https://www.uni-heidelberg.de/institute/fak12/OC/hashmi/05/english/05home.htm`).
18. L. Zhang, *Zhang Group - UC Santa Barbara* (`https://zhang.chem.ucsb.edu`).
19. S. P. Nolan, *Nature* **445**, 496 (2007).
20. S. . Hashmi, M. Rudolph, *Chem Soc Rev* **37**, 1766 (2008).
21. M. Veguillas, G. M. Rosair, M. W. Bebbington, A. L. Lee, *ACS Catal* **9**, 2552 (2019).
22. W. Wang, G. B. Hammond, B. Xu, *J Am Chem Soc* **134**, 5697 (2012).
23. Y. Wang, Z. Wang, G. Wu, G. Cao, L. Zhang, *Nat Commun* **5**, 1 (2014).
24. M. Lein, M. Rudolph, S. . Hashmi, P. Schwerdtfeger, *Organometallics* **29**, 2206 (2010).
25. P. Pyykko, J. P. Desclaux, *Acc Chem Res* **12**, 276 (1979).

26. X. G. Xiong, Y. L. Wang, C. Q. Xu, Y. H. Qiu, L. S. Wang, J. Li, *Dalton Trans* **44**, 5535 (2015).

27. P. Schwerdtfeger, H. L. Hermann, H. Schmidbaur, *Inorg. Chem.* **42**, 1334 (2003).

28. T. A. Baker, C. M. Friend, E. Kaxiras, *J Am Chem Soc* **130**, 3720 (2008).

29. W. Nakanishi, M. Yamanaka, E. Nakamura, *J Am Chem Soc* **127**, 1446 (2005).

30. H. V. Huynh, *Chem Rev* **118**, 9457 (2018).

31. C. A. Tolman, *J Am Chem Soc* **92**, 2953 (1970).

32. D. Setiawan, R. Kalescky, E. Kraka, D. Cremer, *Inorg Chem* **55**, 2332 (2016).

33. D. Cremer, E. Kraka, *Dalton Trans* **46**, 8323 (2017).

34. Z. Lu, G. B. Hammond, B. Xu, *Acc Chem Res* **52**, 1275 (2019).

35. C. A. Tolman, *J Am Chem Soc* **92**, 2956 (1970).

36. J. Jover, J. Ciera, *Dalton Trans* **48**, 15036 (2019).

37. D. White, B. C. Taverner, P. G. Leach, N. J. Coville, *J Org Comp Chem* **14**, 1042 (1993).

38. A. Poater, B. Cosenza, A. Correa, S. Guidice, F. Ragone, V. Scarano, L. Cavallo, *Eur J Inorg Chem* **13**, 1759 (2009).

39. J. Jover, N. Frey, J. N. Harvey, G. C. Lloyd-Jones, A. G. Orpen, G. J. J. Owen-Smith, *Organometallics* **29**, 6245 (2010).

40. T. S. Reddy, S. H. Privér, V. V. Rao, N. Mirzadeh, S. K. Bhargava, *Dalton Trans* **47**, 15312 (2018).

41. M. Pujadas, L. Rodríguez, *Coord Chem Rev* **408**, 213179 (2020).

42. R. Visbal, I. Ospino, J. M. López-de-Luzuriaga, A. Laguna, M. C. Gimeno, *J Am Chem Soc* **135**, 4712 (2013).

43. H. Beucher, S. Kumar, E. Merino, W. H. Hu, G. Stemmler, S. Cuesta-Galisteo, J. A. González, J. Jagielski, C. Shih, C. Nevado, *Chem Mater* **32**, 1605 (2020).

44. M. A. Birkholz, Z. Freixa, P. W. N. M. van Leeuwen, *Chem Soc Rev* **38**, 1099 (2008).

45. J. Febvay, Y. Sanogo, P. Retailleau, M. P. Gogoi, A. K. Sahoo, A. Marinetti, A. Voituriez, *Org Lett* **21**, 9281 (2019).

46. X. Cheng, Z. Wang, C. D. Quintanilla, L. Zhang, *J Am Chem Soc* **141**, 3787 (2019).

47. A. J. Arduengo, R. L. Harlow, M. Kline, *J Am Chem Soc* **113**, 361 (1991).

48. D. Bourissou, O. Guerret, F. P. Gabbai, B. G., *Chem Rev* **100**, 39 (2000).

49. C. Heinemann, W. Thiel, *Chem Phys Lett* **217**, 11 (1993).

50. T. Weskamp, W. C. Schattenmann, M. Spiegler, W. A. Herrmann, *Angew Chem Int Ed* **37**, 2490 (1998).

51. G. A. Grasa, M. S. Viciu, J. Huang, C. Zhang, M. L. Trudell, S. P. Nolan, *Organometallics* **21**, 2866 (2002).

52. N. Marion, S. P. Nolan, *Chem Soc Rev* **37**, 1776 (2008).

53. A. Collado, A. Gómez-Suárez, A. R. Martin, A. M. Slawin, S. P. Nolan, *Chem Commun* **49**, 5541 (2013).

54. S. J. Tereniak, C. R. Landis, S. S. Stahl, *ACS Catal* **8**, 3708 (2018).

55. W. A. Herrmann, L. J. Goossen, C. Köcher, G. R. Artus, *Angew Chem Int Ed* **35**, 2805 (1996).

56. H. Seo, B. Y. Kim, J. H. Lee, H. J. Park, S. U. Son, Y. K. Chung, *Organometallics* **22**, 4783 (2003).

57. S. Lee, J. F. Hartwig, *J Org Chem* **66**, 3402 (2001).

58. T. J. Seiders, D. W. Ward, R. H. Grubbs, *Org Lett* **3**, 3225 (2001).

59. M. Gómez, G. Muller, M. Rocamora, *Coord Chem Rev* **193**, 769 (1999).

60. I. Takeo, W. Hiroyuki, K. Akira, *Bull Chem Soc Jpn* **54**, 1711 (1981).

61. P. A. Bonnardel, R. V. Parish, R. G. Pritchard, *J Chem Soc Dalton Trans*, 3185 (1996).

62. H. Brunner, U. Obermann, *Chem Ber* **122**, 499 (1988).

63. H. Yang, M. A. Khan, K. M. Nicholas, *Organometallics* **12**, 3485 (1993).

64. P. G. Cozzi, C. Floriani, *Inorg Chem* **34**, 2921 (1995).

65. K. L. Bray, C. P. Butts, G. C. Lloyd-Jones, M. Murray, *J Chem Soc Dalton Trans*, 1421 (1998).

66. P. von Matt, G. C. Lloyd-Jones, A. B. E. Mindis, A. Pfaltz, L. Macko, M. Neuburger, M. Zehnder, H. Rüegger, P. S. Pregosin, *Helv Chim Acta* **78**, 265 (1995).

67. A. S. Gokhale, A. B. E. Mindis, A. Pfaltz, *Tetrahedron* **36**, 1831 (1995).

68. R. Tokunoh, H. Tomiyana, M. Sodeoka, M. Shibasaki, *Tetrahedron* **37**, 2449 (1996).

69. M. T. Powell, D. R. Hou, M. C. Perry, X. Cui, K. Burgess, *J Am Chem Soc* **123**, 8878 (2001).

70. V. César, S. Bellemin-Laponnaz, H. Wadepohl, L. H. Grade, *Chem Eur J* **11**, 2862 (2005).

71. A. Homs, I. Escofet, A. M. Echavarren, *Org Lett Vol* **15**, 5782 (2013).

72. D. Wang, R. Cai, S. Sharma, J. Jirak, S. Thummanapelli, N. Akhmedov, H. Zhang, X. Liu, J. Peteron, X. Shi, *J Am Chem Soc* **134**, 9012 (2012).

73. A. K. Hashmi, J. Hofmann, S. Shi, A. Schütz, *Chem Eur J* **19**, 382 (2013).

74. G. Zhang, Y. Peng, L. Zhang, *Angew Chem Int Ed* **48**, 3112 (2009).

75. L. Zhang, S. Wang, *J Am Chem Soc* **128**, 1442 (2006).

76. S. T. Staben, J. J. Kennedy-Smith, F. D. Toste, *Angew Chem Int Ed* **43**, 5350 (2004).

77. X. Shi, D. J. Gorin, F. D. Toste, *J Am Chem Soc* **127**, 5802 (2005).

78. M. Jia, M. Bandini, *ACS Catal* **5**, 1638 (2015).

79. Y. Li, X. Zhao, *Catal Sci Technol* **10**, 2415 (2020).

80. A. S. K. Hashmi, *Chem Rev* **107**, 3180 (2007).

81. A. Perez-Bitrian, M. Baya, J. M. Casas, D. Martin, B. Menjon, J. Orduna, *Angew Chem Int Ed* **57**, 6517 (2018).

82. S. G. Bratsch, *J Phys Chem Ref Data* **18** (1989).

83. C. Y. Wu, T. Horibe, C. B. Jacobsen, F. D. Toste, *Nature* **517**, 449 (2015).

84. A. Collado, J. Bohnenberger, M. J. Oliva-Madrid, P. Nun, D. B. Cordes, A. M. Z. Slawin, S. P. Nolan, *Eur J Inorg Chem* **25**, 4111 (2016).

85. V. Levchenko, C. Glessi, S. Ø. Ødegaard, M. Tilset, *Dalton Trans* **49**, 3473 (2020).

86. J. F. Cui, H. M. Ko, K. P. Shing, J. R. Deng, N. C. H. Lai, M. K. Wong, *Angew Chem* **129**, 3120 (2017).

87. J. J. Jiang, J. F. Cui, B. Yang, Y. Ning, N. C. H. Lai, M. K. Wong, *Org Lett* **21**, 6289 (2019).

88. P. T. Bohan, F. D. Toste, *J Am Chem Soc* **139**, 11016 (2017).

89. M. D. Levin, F. D. Toste, *Angew Chem Int Ed* **53**, 6211 (2014).

90. A. Simonneau, P. Garcia, J. P. Goddard, V. Mouries-Mansuy, M. Malacria, L. Fensterbank, *Beilstein J Org Chem* **7**, 1379 (2011).

91. A. Kar, N. Mangu, H. M. Kaiser, M. Beller, M. K. Tse, *Chem Commun* **3**, 386 (2008).

92. M. N. Hopkinson, A. Tlahuext-Aca, F. Glorius, *Acc Chem Res* **49**, 2261 (2016).

93. G. J. Cheng, X. Zhang, L. W. Chung, L. Xu, W. D. Wu, *J Am Chem Soc* **137**, 1706 (2015).

94. P. A. M. Dirac, *Proc R Soc Lond* **123**, 714 (1929).

95. K. D. Vogiatzis, M. V. Polynski, J. K. Kirkland, J. Townsend, A. Hashemi, C. Liu, E. A. Pidko, *Chem Rev* **119**, 2453 (2019).

96. Y. Minenkov, Å. Singstad, G. Occhipinti, V. R. Jensen, *Dalton Trans* **41**, 5526 (2012).

97. A. J. DelMonte, J. Haller, K. N. Houk, K. B. Sharpless, D. A. Singleton, T. Strassner, A. A. Thomas, *J Am Chem Soc* **119**, 9907 (1997).

98. D. A. Singleton, Z. Wang, *J Am Chem Soc* **127**, 6679 (2005).

99. B. Butschke, M. Schlangen, D. Schroder, H. Schwarz, *Chem Eur J* **14**, 11050 (2008).

100. J. M. Dreimann, E. Kohls, H. F. W. Warmeling, M. Stein, L. F. Guo, M. Garland, T. N. Dinh, A. J. Vorholt, *ACS Catal* **9**, 4308 (2019).

101. S. Schmidt, E. Barath, C. Larcher, T. Rosendahl, P. Hofmann, *Organometallics* **34**, 841 (2015).

102. I. Goldberg, *Chem Ber* **39**, 1691 (1906).

103. F. Ullmann, *Chem Ber* **36**, 2382 (1903).

104. M. Kosugi, M. Kameyama, T. Migita, *Chem Lett* **12**, 927 (1983).

105. F. Paul, J. Patt, J. F. Hartwig, *J Am Chem Soc* **116**, 5969 (1994).

106. A. S. Guram, S. L. Buchwald, *J Am Chem Soc* **116**, 7901 (1994).

107. S. Shekhar, P. Ryberg, J. F. Hartwig, *J Am Chem Soc* **128**, 3584 (2006).

108. M. Fitzner, G. Wuitschik, R. J. Koller, J. M. Adam, T. Schindler, J. L. Reymond, *Chem Sci* **11**, 13085 (2020).

109. M. J. Guttieri, W. F. Maier, *J Org Chem* **49**, 2877 (1983).

110. D. Nagaraja, M. A. Pasha, *Tetrahedron* **40**, 7855 (1999).

111. M. K. Basu, F. F. Becker, B. K. Banik, *Tetrahedron* **41**, 5603 (2000).

112. R. J. Sundberg, W. J. Pitts, *J Org Chem* **56**, 3048 (1991).

113. J. G. Lee, K. I. Choi, H. Y. Koh, Y. Kim, Y. Kang, Y. S. Cho, *Synthesis* **81**, 81 (2000).

114. A. J. Bechamp, *Ann Chim Phys* **42**, 186 (1854).

115. R. J. Sundberg, W. J. Pitts, *J Org Chem* **60**, 3365 (1995).

116. A. B. Gamble, J. Garner, C. P. Gordon, S. M. J. O'Conner, P. A. Keller, *Synthetic Commun* **37**, 2777 (2007).

117. S. Chandrappa, K. Vinaya, T. Ramakrishnappa, K. S. Rangappa, *Synlett* **20**, 3019 (2010).

118. K. Ramadas, N. Srinivasan, *Synthetic Commun* **22**, 3189 (1992).

119. L. Hintermann, *Angew Chem Int Ed* **49**, 2659 (2010).

120. E. Laviron, L. Roullier, *J Electroanal Chem* **288**, 165 (1990).

121. A. J. Arduengo, R. Krafczyk, R. Schutzler, *Tetrahedron* **55**, 14523 (1999).

122. R. H. Wiley, L. L. Bennett, *Chem Rev* **44**, 447 (1949).

123. M. N. Holerca, V. Percec, *Eur J Org Chem*, 2257 (2000).

124. E. M. Burgess, H. R. Penton, E. A. Taylor, *J Org Chem* **38**, 26 (1973).

125. P. Wipf, M. C. P., *J Org Chem* **58**, 1575 (1993).

126. P. de Fremont, N. M. Scott, E. D. Stevens, S. P. Nolan, *Organometallic* **24**, 2411 (2005).

127. M. R. L. Furst, C. S. J. Cazin, *Chem Commun* **46**, 6924 (2010).

128. B. Landers, O. Navarro, *Eur J Inorg Chem*, 2980 (2012).

129. A. Collado, A. Gómez-Suárez, A. R. Martin, A. M. Z. Slawin, S. P. Nolan, *Chem Commun* **49**, 5541 (2013).

130. A. Johnson, M. C. Gimeno, *Chem Commun* **52**, 9664 (2016).

131. L. J. Farrugia, *J Appl Cryst* **45**, 849 (2012).

132. F. Wang, S. Li, M. Qu, M. X. Zhao, L. J. Liu, M. Shi, *Beilstein J Org Chem* **8**, 726 (2012).

133. F. R. Hartley, *Chem Soc Rev* **2**, 163 (1973).

134. D. Curran, H. Müller-Bunz, S. I. Bär, R. Schobert, X. Zhu, M. Tacke, *Molecules* **25**, 3474 (2020).

135. P. de Fremont, E. D. Stevens, M. R. Fructos, M. M. Diaz-Requejo, P. J. Perez, S. P. Nolan, *Chem Commun*, 2045 (2006).

136. C. Hirtenlehner, C. Krims, J. Hölbling, M. List, M. Zabel, M. Fleck, R. J. F. Berger, W. Schoefberger, U. Monkowius, *Dalton Trans* **40**, 9899 (2011).

137. H. F. Jonsson, A. Fiksdahl, *Dalton Trans* **48**, 142 (2019).

138. H. Schmidbaur, A. Schier, *Chem Inform* **42** (2011).

139. I. Chambrier, D. A. Rosca, J. Fernandez-Cestau, D. L. Hughes, P. H. M. Budzelaar, M. Bochmann, *Organometallics* **36**, 1358 (2017).

140. S. Koiya, M. Iwata, T. Sone, A. Fukuoka, *J Chem Soc Chem Commun* **16**, 1109 (1992).

141. A. C. Reiersølmoen, E. Østrem, A. Fiksdahl, *Eur J Org Chem*, 3317 (2018).

142. J. Wolf, F. Huber, N. Erochok, F. Heinen, V. Guerin, C. Y. Legault, S. F. Kirsch, S. M. Huber, *Angew Chem Int Ed* **59**, 16496 (2020).

143. F. Neese, *Wiley Interdiscip Rev Comput Mol Sci* **2**, 73 (2012).

144. A. D. Becke, *Phys Rev A* **38**, 3098 (1988).

145. F. Weigend, R. Ahlrichs, *Phys Chem Chem Phys* **7**, 3297 (2005).

146. J. Zheng, X. Xu, D. G. Truhlar, *Theor Chem Acc* **128**, 295 (2011).

147. D. A. Pantazis, X. Y. Chen, C. R. Landis, F. Neese, *J Chem Theor Comput* **4**, 908 (2008).

148. S. Grimme, S. Ehrlich, L. Goerigk, *J Comp Chem* **32**, 1456 (2011).

149. A. D. Becke, *J Chem Phys* **98**, 5648 (1993).

150. C. Lee, W. Yang, R. G. Parr, *Phys Rev B* **37**, 785 (1988).

151. M. Born, R. Oppenheimer, *Ann Phys* **389**, 457 (1927).

152. S. McArdle, S. Endo, *Rev Mod Phys* **92** (2020).

153. C. Møller, S. Plesset M, *Phys Rev* **46**, 618 (1934).

154. J. C. Slater, *Phys Rev* **36**, 57 (1930).

155. S. F. Boys, *Proc R Soc Lond* **200**, 542 (1950).

156. L. H. Thomas, *Proc Camb Phil Soc* **23**, 542 (1927).

157. E. Fermi, *Rend Accad Naz Lincei* **6**, 602 (1927).

158. P. A. M. Dirac, *Proc Camb Phil Soc* **26**, 376 (1930).

159. P. Hohenberg, W. Kohn, *Phys Rev B* **136**, 864 (1964).

160. W. Kohn, L. J. Sham, *Phys Rev A* **140**, 1133 (1965).

161. J. P. Perdew, K. Schmidt, *AIP Conference Proceedings* **577**, 1 (2001).

162. O. Gunnarsson, B. I. Lundqvist, J. W. Wilkins, *Phys Rev B* **10**, 1319 (1974).

163. J. P. Perdew, J. A. Chevary, S. H. Vosko, K. A. Jackson, M. R. Pederson, D. J. Singh, C. Fiolhais, *Phys Rev B* **46**, 6671 (1992).

164. A. D. Becke, *J Chem Phys* **96**, 2155 (1992).

165. B. Hammer, K. W. Jacobsen, J. K. Nørskov, *Phys Rew Lett* **70**, 3971 (1993).

166. J. P. Perdew, K. Burke, M. Ernzerhof, *Phys Rev Lett* **7**, 3865 (1996).

167. S. Kurth, J. P. Perdew, P. Blaha, *Int J Qtm Chem* **125**, 889 (1999).

168. G. K. H. Madsen, L. Ferrighi, B. Hammer, *J Phys Chem Lett* **1**, 515 (2010).

169. J. P. Perdew, J. Tao, V. N. Staroverov, G. E. Scuseria, *J Chem Phys* **120**, 6898 (2004).

170. Y. Zhao, D. G. Truhlar, *J Chem Phys* **125**, 194101 (2006).

171. J. P. Perdew, Y. Wang, *Phys Rev B* **45**, 12344 (1992).

172. V. N. Staroverov, G. E. Scuseria, J. Tao, J. P. Perdew, *J Chem Phys* **119**, 12129 (2003).

173. F. Jensen, *J Phys Chem* **121**, 6104 (2017).

174. P. Schwerdtfeger, *Chem Phys Chem* **12**, 3143 (2011).

175. J. S. Binkley, M. S. Gordon, D. J. DeFrees, J. A. Pople, *J Chem Phys* **77**, 3654 (1982).

176. A. Schafer, C. Huber, R. Ahlrichs, *J Chem Phys* **100**, 5829 (1994).

177. F. Weigend, *Phys Chem Chem Phys* **8**, 1057 (2006).

178. S. Kristyan, P. Pulay, *Chem Phys Lett* **229**, 175 (1994).

179. A. Koide, *J Phys B* **3173**, 9 (1976).

180. S. Grimme, J. Antony, S. Ehrlich, H. Krieg, *J Chem Phys* **132**, 154104 (2010).

181. A. Tkatchenko, M. Scheffler, *J Rev Lett* **102**, 073005 (2009).

182. G. Henkelman, G. Johannesson, H. Jonsson, *Theoretical Methods in Condensed Phase Chemistry, Chapter 10 - Gold – Methods for finding saddle point and minimum energy paths* (Springer, 2002).

183. G. Henkelman, B. P. Uberuaga, H. Jonsson, *J Chem Phys* **113**, 9901 (2000).

Sondre Taugbøl Lomeland   Trondheim, Norway,

A Computational chemistry - extended

A.1 Hartree-Fock method

As for any particle described on a quantum mechanical level, one needs to consider the wave-particle duality. The electrons' positions are represented using wave functions ψ and the probability of finding an electron at a given point in space is equal to the square of the wave function. To compute the total energy of the system, we apply the Hamiltonian operator $\hat{H}$ to the wave function.

$$\hat{H}\Psi = E\Psi \tag{A.1}$$

When applying the Born-Oppenheimer approximation,[151] one can separate the wave functions of the atomic nuclei and electrons into separate functions. The nuclei are heavier than the electrons and from the electron's point of view, the nuclei are stationary and considered point charges. Therefore, for a given nuclear configuration one needs to only compute the electronic Hamiltonian. The Hamiltonian of the time-independent Schrödinger equation can be split up into a kinetic energy term $\hat{T}$, electron-nucleus interaction term $\hat{V}$ and an electron-electron interaction energy term $\hat{U}$, shown in equation A.2. The many-body wave function cannot be separated into single-particle equations because of the electron-electron interaction term.

$$\begin{aligned}\hat{H}\Psi &= \left[\hat{T} + \hat{V} + \hat{U}\right]\Psi \\ &= \left[-\frac{1}{2}\sum_{i}^{N}\nabla_i^2 - \sum_{i,I}^{N}\frac{Z_I}{|r_i - R_I|} + \frac{1}{2}\sum_{i<j}^{N}\frac{1}{|r_i - r_j|}\right]\Psi\end{aligned} \tag{A.2}$$

The Hartree-Fock method (HF) approximates the N-body wave function as a single Slater determinant. Interactions between electrons are neglected and their movement is described by using an average charge distribution of all electrons.[152] When only considering one Slater determinant for M orbitals, we assume that that N orbitals are occupied, and the remaining M - N orbitals are unoccupied. Since the HF method completely ignores the correlation energy of the system, the resulting energies are not accurate enough to be applicable to solve chemical problems.

Post-HF methods improve the accuracy of HF calculations by introducing additional determinants, improving the electron-electron correlation energies. The configuration interaction method (CI) describes a linear combination of Slater determinants, including excitation states above the HF state. Møller-Plesset perturbation theory (MP) improves the HF method by adding a term for electron pair correlation, using perturbation theory.[153] Post-HF methods can calculate accurate energies for molecules, using large basis sets. The methods are, however, often computationally expensive and are limited to smaller molecules.

The wave functions are represented as basis sets, meaning a linear combination of basis functions. For computation of chemical system the basis sets are most often composed of atomic orbitals of either Slater-type[154] or Gaussian-type[155] functions. Since chemical accuracy is most critical around molecular bonds, split-valence basis sets are composed. The valence orbitals are represented by several basis functions, which make the basis sets more flexible to different chemical systems. The number of valence basis sets is denoted by zeta ζ. In molecules, atomic orbitals will not accurately describe the true orbitals. When two neighboring orbitals move towards each other, they shift. Polarization functions are included in the basis sets, which allow orbital shifts. The inclusion of a p orbital allows an s orbital to polarize in a given direction. In order to better model anions and weak interactions, diffuse functions are added to basis sets.

A.2 Density functional theory

At the same time as the Schrödinger equation and wave functions were introduced to describe the electronic structure of many-body systems, Thomas[156] and Fermi[157] separately developed a model based on electron density in 1927. The model fails to accurately represent kinetic energy, and by neglecting the electron correlation the exchange energy is not included. In 1930 Dirac added an exchange energy term to describe the electron correlation.[158] Their work has set the foundation for density functional theory (DFT).

The development of density functional theory of Kohn led to the Nobel Prize in Chemistry 1998, along with Pople. Together with Hohenberg, Kohn proved that there exists a density funcional $F[n(\mathbf{r})]$ which can describe the exact ground state energy associated with an external potential $v(\mathbf{r})$ of an interacting electron gas.[159] The Kohn-Sham (KS) method simplifies the calculation of the ground state energy by solving the one-electron Schrödinger equation of non-interacting electrons in a Kohn-Sham potential. The external potential is defined such that the ground state density equals the one used to evaluate the density functional F[n($\mathbf{r}$)]. The strength of this approach, is that the wavefunction of non-interacting particles can be solved by Slater determinants of the orbitals. The Kohn-Sham wavefunction A.3 with a kinetic energy operator and an effective potential computes the Kohn-Sham orbitals ϕ_i that reproduce the density of the system.

$$\left[-\frac{1}{2}\nabla^2 + v_{KS}(\mathbf{r})\right]\phi_i(\mathbf{r}) = \varepsilon_i\phi_i(\mathbf{r}) \tag{A.3}$$

The Kohn-Sham potential includes the external potential, electron potential and exchange-correlation energy, as shown in equation A.4.[160]

$$v_{KS}(\mathbf{r}) = v_{ext}(\mathbf{r}) + \int \frac{\rho(\mathbf{r}')}{|\mathbf{r}-\mathbf{r}'|}d\mathbf{r}\ ' + \frac{\delta E_{XC}[\rho]}{\delta\rho(\mathbf{r})} \tag{A.4}$$

The Kohn-Sham equations are solved numerically, using the self-consistent field method (SCF). The wave functions are solved with an approximate potential, to obtain more accurate molecular orbitals. The algorithm is repeated until a convergence threshold is reached. A simplified algorithm of the SCF method is shown in Scheme 46.

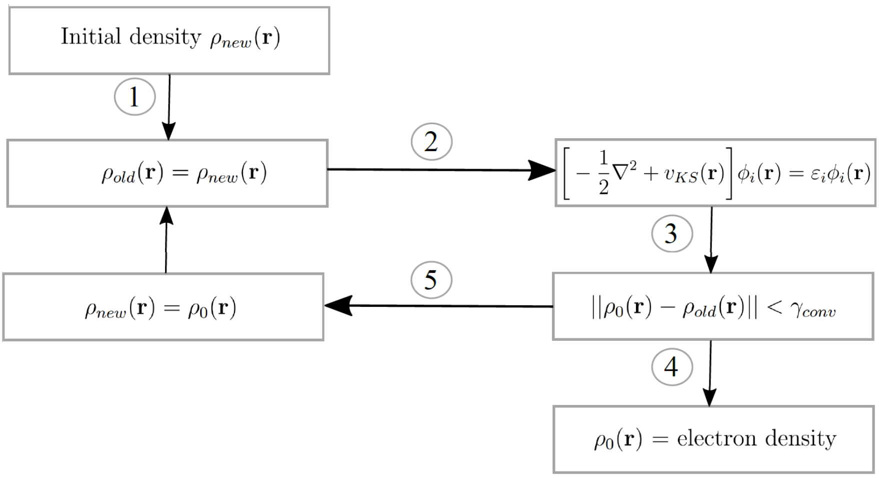

Scheme 46: SCF method to solve the Kohn-Sham wave functions. 1) Electron density from initial configuration. 2) Calculation of the Kohn-Sham equations. 3) Convergence test. 4) Final electron density, if convergence threshold is met. 5) Repeat cycle if the convergence threshold is not met.

The exchange-correlation energy is the only unknown term in the Kohn-Sham DFT method, and different functionals are implemented to approximate the correct energy. Choosing a suitable functional for depicting the exchange-correlation energy is illustrated by Perdew and Jacob's Ladder of density functional approximations. The lower rungs of the ladder represent simple models and higher rungs include increasingly complex models to reach higher chemical accuracy. Choosing the correct approximation depends on the chemical accuracy needed versus the computational cost one can afford.[161]

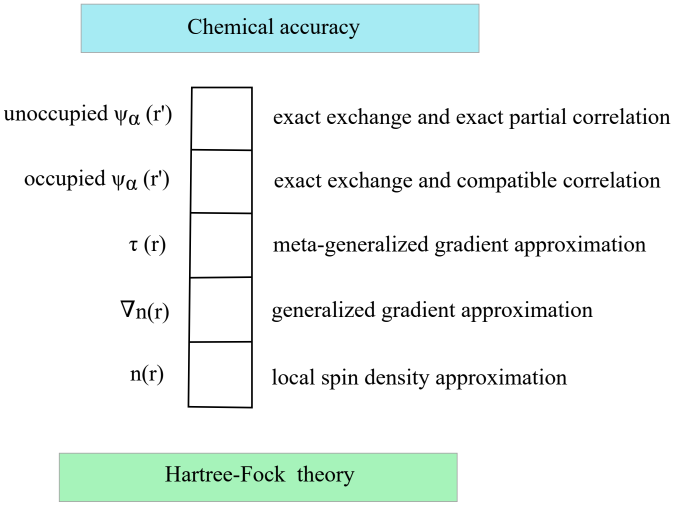

Figure A.1: Jacob's ladder of density functional approximations.

The local density approximation (LDA), developed by Kohn and Sham[160], is a simple approximation, where the energy functional depends only on the electron density at the point of evaluation, typically using a homogeneous electron gas model (HEG). LDA can be generalized to electron spin, called the local spin-density approximation (LSD). The exchange-correlation represented by equation A.5. Including the spin of the electrons in the model greatly improves the accuracy of systems with unpaired spin, such as the sodium atom.[162] LSD has been successful modeling various system where the density is slowly varying, such solids and solid surfaces, as they can be modelled as many-electron systems with external potentials. The LSD approximation, however, has a tendency to underbind core electrons and overbind atoms in molecules.

$$E_{XC}^{LSD}[n_\uparrow, n_\downarrow] = \int d\mathbf{r}\, n(\mathbf{r})\, \varepsilon_{XC}^{unif}\big(n_\uparrow(\mathbf{r}), n_\downarrow(\mathbf{r})\big) \tag{A.5}$$

Improvements on LDA, implementing generalized gradient approximations (GGA) have been developed. In order to more accurately model chemical systems, the exchange-correlation term is valued by density and its gradient, shown in equation A.6 below. The developed functionals are semi-local of the density, as it requires the density at an infinitely small area surrounding the point **r** of evaluation. GGA functionals reduce errors connected to the inhomogeneous electron density, especially when the density is varying quickly. Compared to previous methods with LSD approximations, total energies[163], atomization energies[164] and dissociation energies[165] are greatly improved when gradient corrected exchange-correlation approximations are implemented. The BLYP[144] functional developed by Becke and the PBE[166] functional developed by Perdew and co-workers are considered staple GGA functionals.

$$E_{XC}^{GGA}[n_\uparrow, n_\downarrow] = \int d\mathbf{r}\, n(\mathbf{r})\, \varepsilon_{XC}^{GGA}\big(n_\uparrow(\mathbf{r}), n_\downarrow(\mathbf{r}), \nabla n_\uparrow(\mathbf{r}), \nabla n_\downarrow(\mathbf{r})\big) \tag{A.6}$$

More complex approximations past GGA can be divided into emprical and nonempirical. The motivation to develop nonempirical functionals is their robustness to different systems. Semiempirical functionals perform well within the scope of their training sets, but can struggle to accurately model systems significantly different to their training sets. Also, it seems that accuracy does not scale linearly with the number of fit parameters.[167] Meta-generalized gradient approximations (meta-GGA) are a step up in the hierarchy on the Jacob's ladder. Built upon GGA, the meta-GGA functionals include the Kohn-Sham kinetic energy densities $\tau_\sigma(\mathbf{r})$, shown in equation A.7. The kinetic energy density is defined in terms of the Kohn-Sham orbitals $\psi_{i\sigma}(\mathbf{r})$. The meta-GGA functionals are non-local of the density, but constrained within Kohn-Sham orbitals. This results in functionals that are not significantly more computationally costly than GGA functionals. The additional information from the kinetic energy density enables meta-GGA functionals to descriminate between covalent bond and dispersion forces.[168] Further development of nonempirical functionals is important in order to obtain strong functionals that are versatile and that can model any chemical system. The most frequently used meta-GGA functionals now are the TPPS[169] and M06-L[170] functionals and their derivatives, but are generally neglected in favor of semi-empirical functionals. They are, however, useful as a foundation for expansion into hybrid functionals with empirical parameters included.

$$E_{XC}^{mGGA}[n_\uparrow, n_\downarrow] = \int d\mathbf{r}\, n(\mathbf{r})\, \varepsilon_{XC}^{mGGA}\big(n_\uparrow(\mathbf{r}), n_\downarrow(\mathbf{r}), \nabla n_\uparrow(\mathbf{r}), \nabla n_\downarrow(\mathbf{r}), \tau_\uparrow(\mathbf{r}), \tau_\downarrow(\mathbf{r})\big) \tag{A.7}$$

Hybrid functionals incorporate the exact exchange energy from Hartee Fock theory to more accurately describe the exchange-correlation. The three-parameter functional introduced by Becke in 1993 set the foundation for what is now the most frequently used DFT functional. The B3PW91 functional is shown in equation A.8 and includes the exact exchange energy E_X^{exact}, Becke's gradient correction for the exchange energy ΔE_X^{B88}[144] and the gradient correction for the correlation energy ΔE_C^{PW91} by Perdew and Wang.[171] The emprical parameters a_0, a_x and a_c were determined by linear least-squares fit of atomization energy, ionization potential, proton affinity and total atomic ennergy of selected molecules.[149] The replacement of ΔE_C^{PW91} with the LYP correlation-energy functional[150] has shown to be more accurate. The result is the B3LYP functional, which now for many researchers is considered the default functional when performing DFT calculations. As for the addition of exact exchange energy to GGA functionals, meta-GGA functionals can also be extended to hybrid functionals. The TPPSh functional performs equally well as B3LYP in many cases.[172] Since semiempirical functionals are developed by determining parameters from training sets, their performances are often inconsistent. An example is the hybrid functional B3P86, which outperforms most other functionals in describing the equilibrium bond lengths of diatomic molecules, but fails to accurately predict ionization potentials.

$$E_{XC}^{B3PW91} = E_{XC}^{LSDA} + a_0\big(E_X^{exact} - E_X^{LSDA}\big) + a_x\Delta E_X^{B88} + a_c\Delta E_C^{PW91} \tag{A.8}$$

In order to apply DFT to compute chemical system, not only the exchange-correlation functional needs to be chosen correctly. Chosing the correct basis set is necessary to yield high chemical accuracy at low computational cost. Basis sets developed for post HF computations are available, but often converge slower. Gaussian basis sets that are optimized for DFT methods generally perform better.[173] In order to speed up calculations, core electrons in large elements are often describe with a pseudopotential. This reduced the amount of basis sets needed and speeds up the calculations without losing much accuracy.[174] Some common basis set families for DFT methods are the Pople[175] and

Karlsruhe[176] basis sets. Addition of auxiliary basis sets and implementation of the resolution of identity approximation, the computational costs of two electron four-centered integrals can be greatly reduced. This applies to the Coulomb part of the Kohn-Sham equation, as well as the Hartree-Fock exchange part in hybrid functionals.[177]

Both local and hybrid functionals generally fail to correctly describe the long-range dispersion forces between molecules.[178] These attractive forces are considered weak, which is the case for a single atom pair interaction. For larger systems, the overall contribution of dispersion forces are too large to ignore to reach chemical accuracy. The dispersion forced between two atoms can be described by a convergent series, dependent on C_6/R^6.[179] R represents the distance between two atoms, and the C_6 coefficient is fitted to empirical data.[180,181] Dispersion corrected density functional theory (DFT-D) is implemented by the addition of the atom pair-wise dispersion potential to the standard KS DFT method.

A.3 Nudged elastic band

The nudged elastic band (NEB) method is a computational method for calculating transition states and the minimum energy path (MEP) between two local minima. The two local minima are given by submission of reactant and product configuration. A string of images are created from the reactant to the product, all connected by springs. The spring interaction between images is necessary to ensure continuity along the path. The initial images are created by doing a straight line interpolation between the reactant and the product. Through an iterative process the images are relaxed towards the MEP. The "nudging" part of the NEB method refers to the implementation of a force projection, so that the spring forces do not hinder MEP convergence. The force on an image contain the parallel component of the spring force and the perpendicular component of the true force. If the nudging is not implemented the band will not be able to follow a curved path (due to corner-cutting). This reduces the image density around the maxima, where accuracy is needed the most.[182]

The standard notation for a series of N+1 images of an elastic band is [$\mathbf{R}_0$, $\mathbf{R}_1$, $\mathbf{R}_2$, ..., $\mathbf{R}_N$], where $\mathbf{R}_0$ and $\mathbf{R}_N$ represent initial and final configurations, respectively. The forces acted on an image $\mathbf{R}_i$ is given as the sum of parallel spring forces and perpendicular true forces to the local tangent $\hat{\tau}_i$, as shown in equation A.9.

$$F_i = F_i^S|_{||} - \nabla E(\boldsymbol{R_i})|_{\perp} \tag{A.9}$$

To obtain only the perpendicular gradient of the true force, one simply subtracts the parallel component.

$$\nabla E(\boldsymbol{R_i})|_{\perp} = \nabla E(\boldsymbol{R_i}) - \nabla E(\boldsymbol{R_i}) \cdot \hat{\tau}_i \tag{A.10}$$

The spring force with spring constant k is shown in equation A.11. If the spring constant remains unchanged, the distance between images is evenly spaced. In order to more accurately describe the tangent near the saddle point, it would be better to implement varying spring constants. A strong spring near the saddle point ensures a higher image density. The effect on the image density is shown in Figure A.2.

$$F_i^S|_{||} = k\big(|\boldsymbol{R_{i+1}} - \boldsymbol{R_i}| - |\boldsymbol{R_i} - \boldsymbol{R_{i-1}}|\big)\hat{\tau}_i \tag{A.11}$$

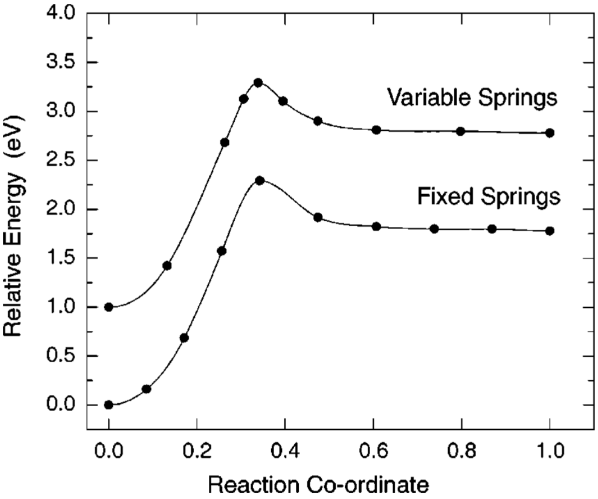

Figure A.2: Variable spring constants and its effects on the image density around the saddle point.[183]

In order to better describe the energy of the saddle point, one usually includes the climbing image (CI-NEB) modification. The image with the highest energy is turned into a climbing image, which moves up the potential energy surface along the band path, while going down the potential energy surface perpendicular to the band. All images will converge to the MEP, with an image at the saddle point. For classical NEB calculations the images rarely appears close to the saddle point and the saddle point energy is estimated by interpolation.[183]

The force on the image with the highest energy is not calculated by equation A.9, but rather with the full force as shown in equation A.12. Spring forces are not included in force calculations on the maximum energy image.

$$F_{i_{max}} = -\nabla E(\boldsymbol{R_{i_{max}}}) + 2\nabla E(\boldsymbol{R_{i_{max}}})|_{\|} \tag{A.12}$$

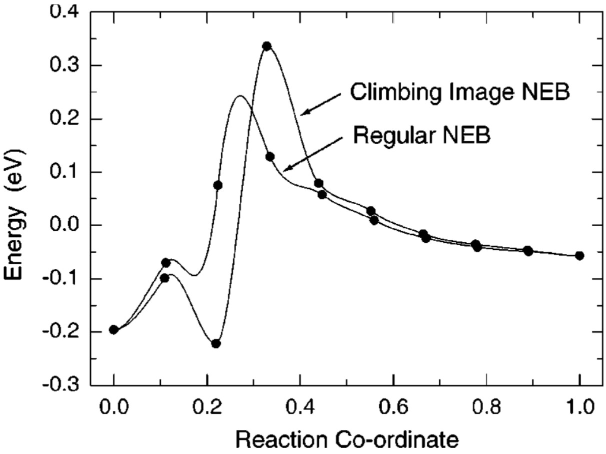

Figure A.3: MEP calculation with regular NEB and the climbing image modification.[183]

B Spectroscopic data for compound 2

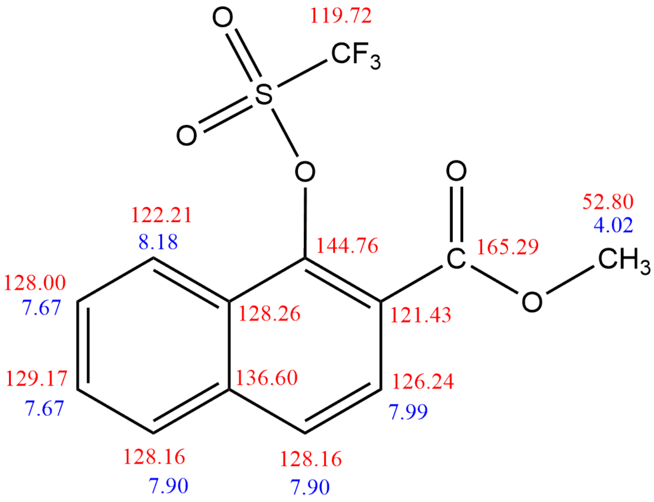

Figure B.1: Assigned ^{1}H and ^{13}C NMR signals of compound **2**

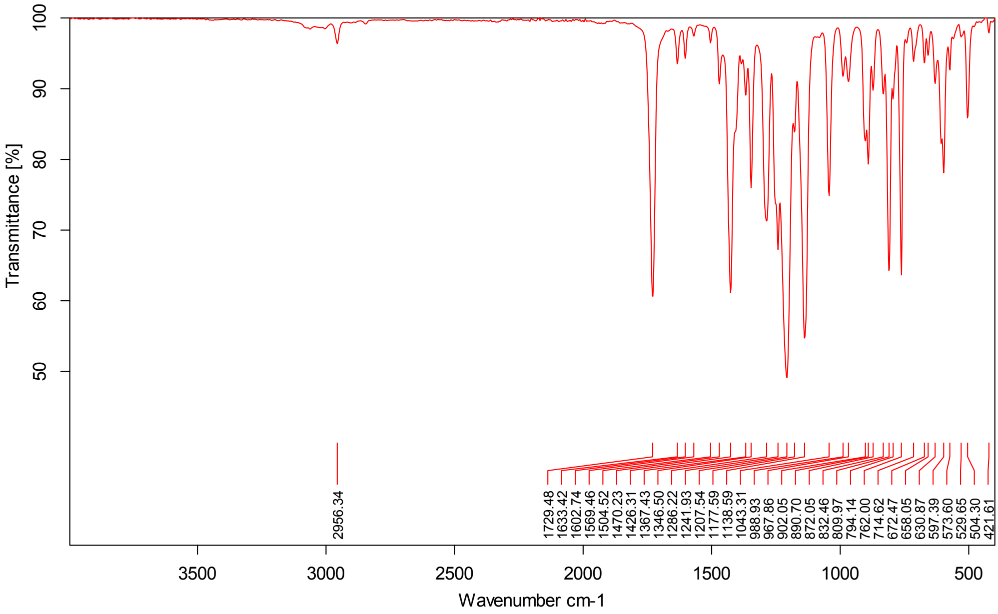

Figure B.2: IR spectrum of compound **2**

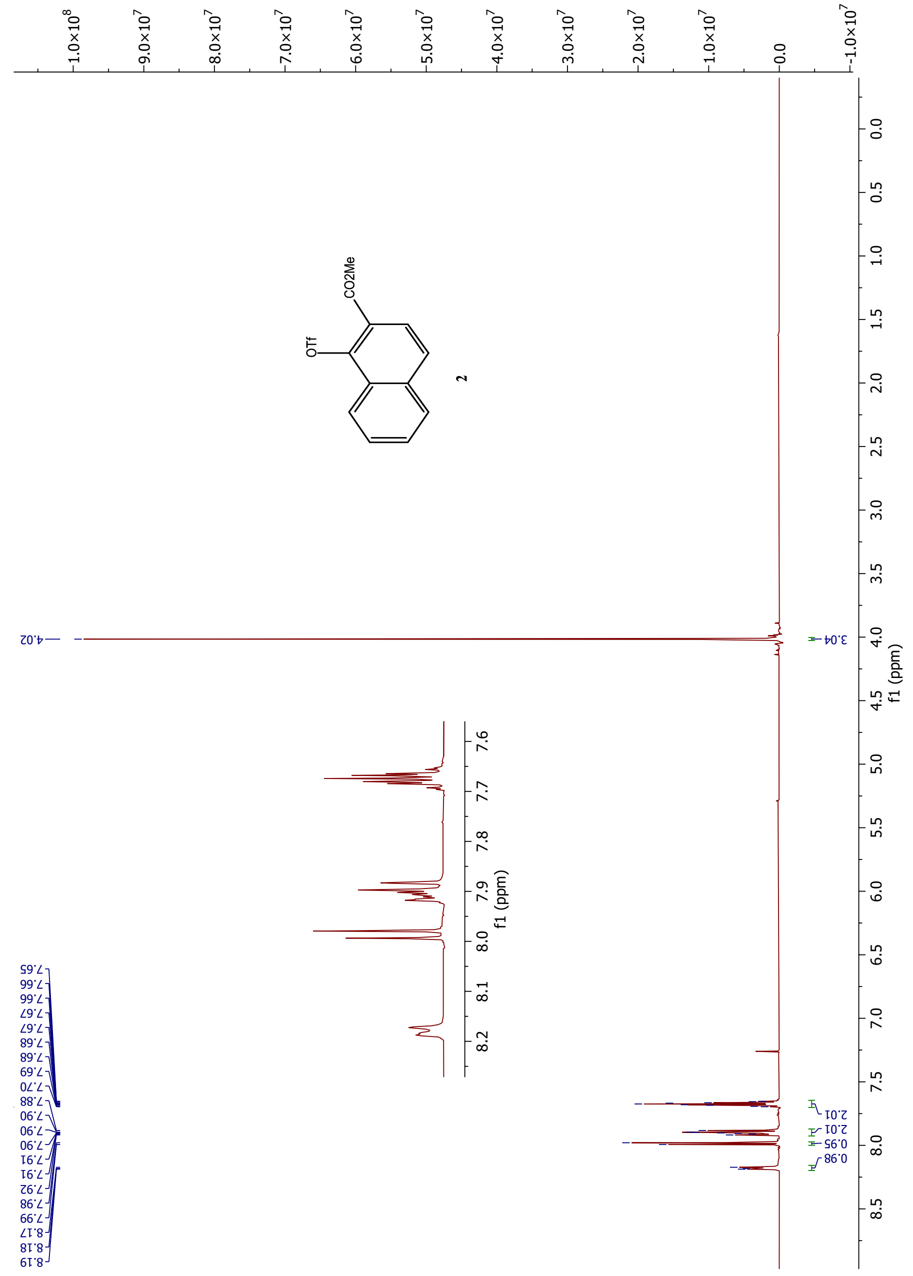

Figure B.3: ^{1}H NMR spectrum of compound **2**

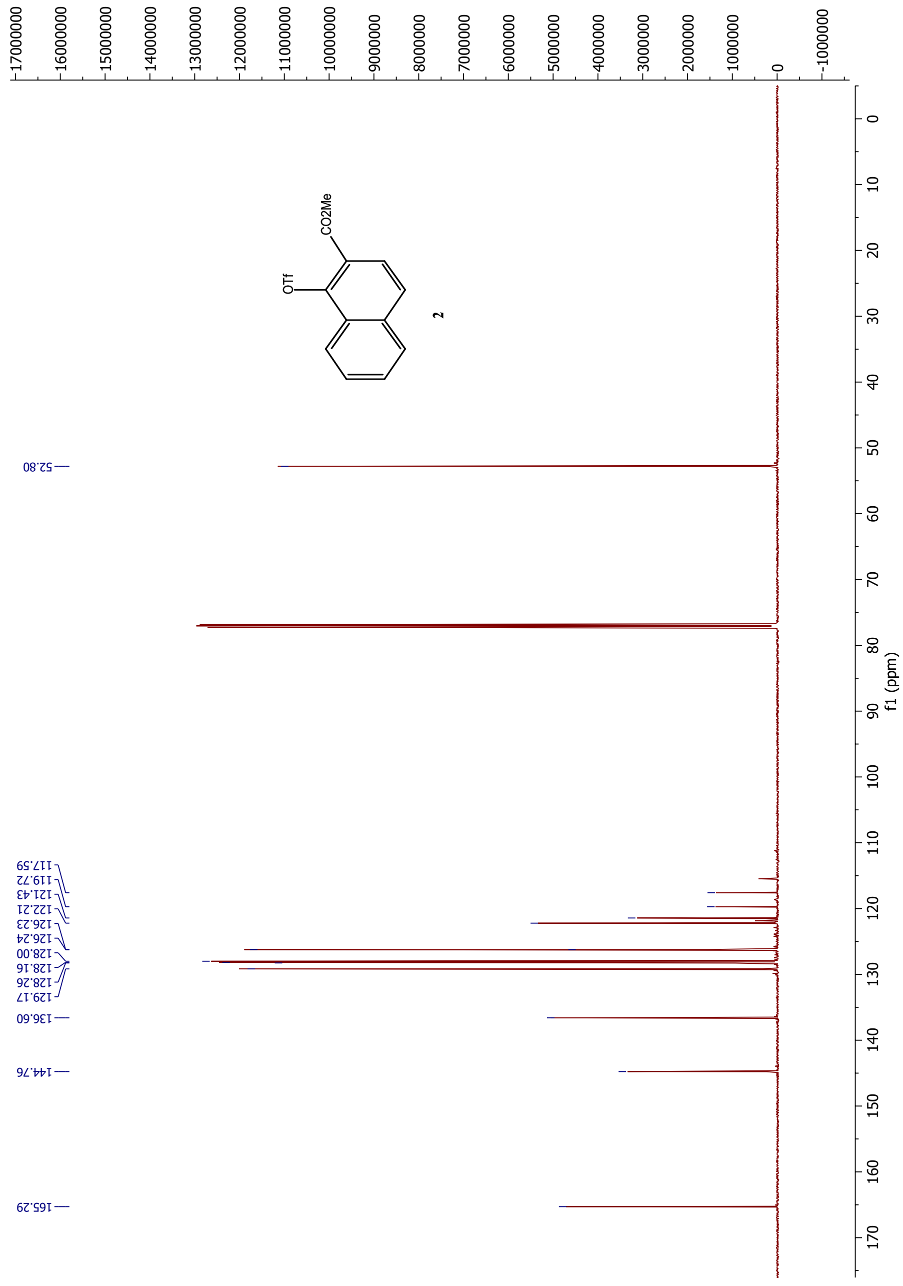

Figure B.4: ^{13}C NMR spectrum of compound **2**

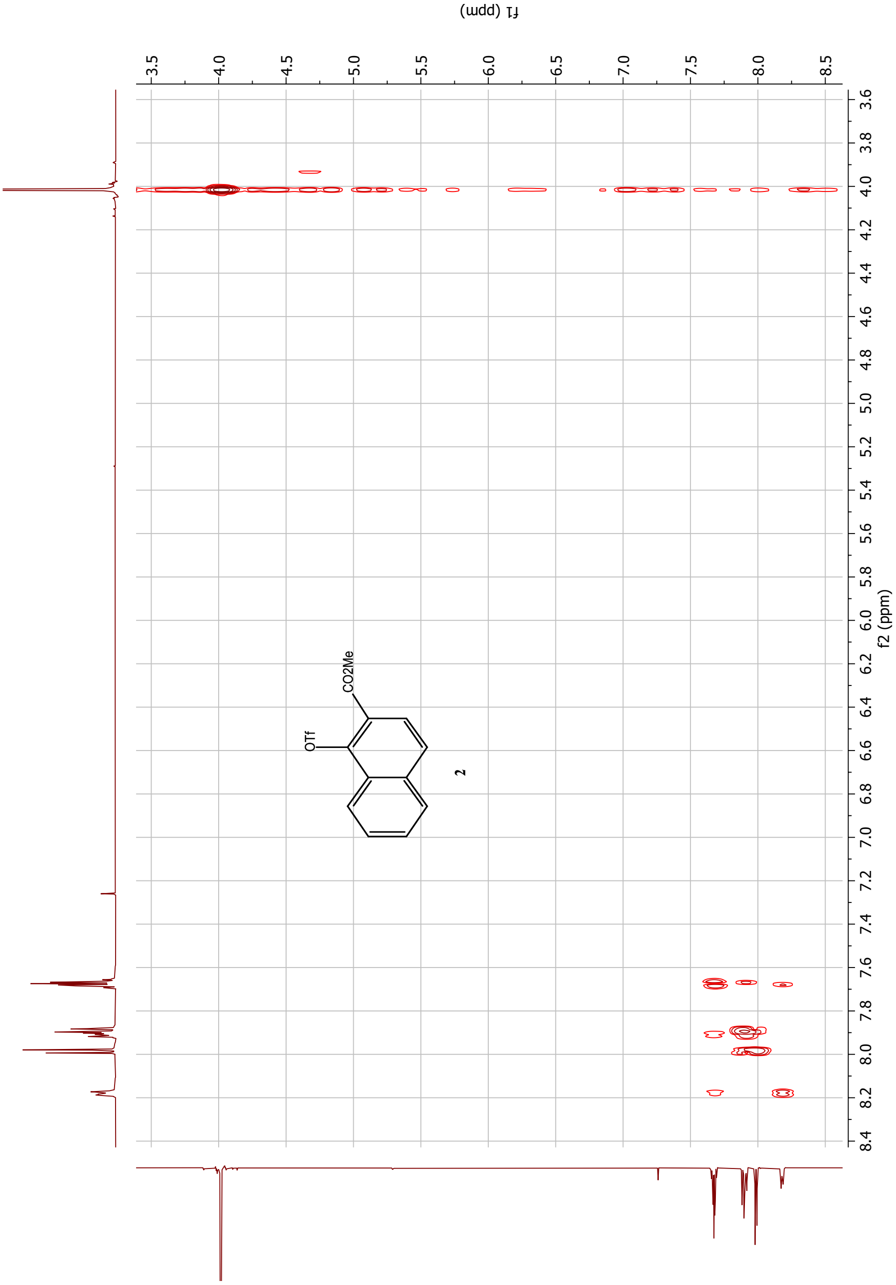

Figure B.5: COSY NMR spectrum of compound **2**

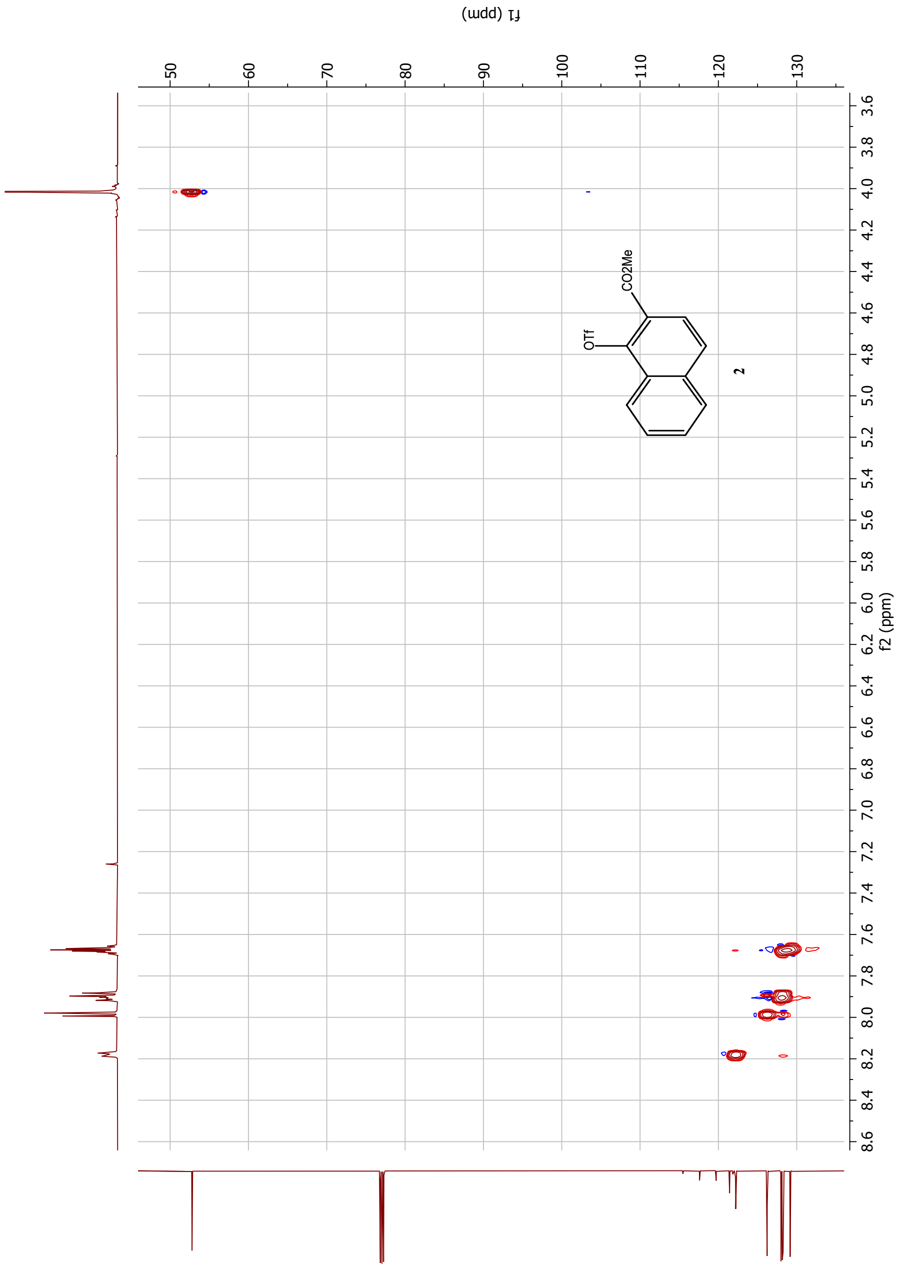

Figure B.6: HSQC NMR spectrum of compound **2**

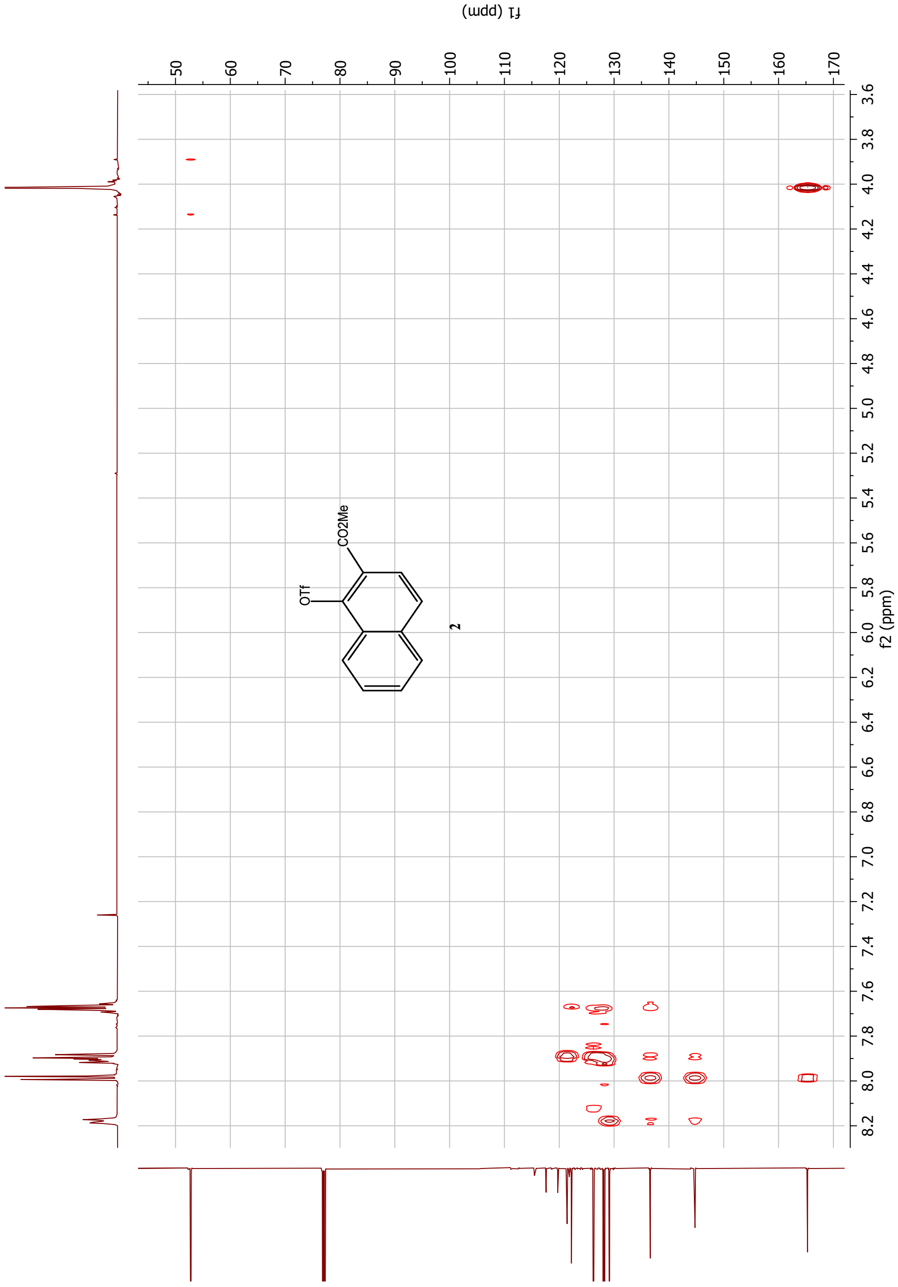

Figure B.7: HMBC NMR spectrum of compound **2**

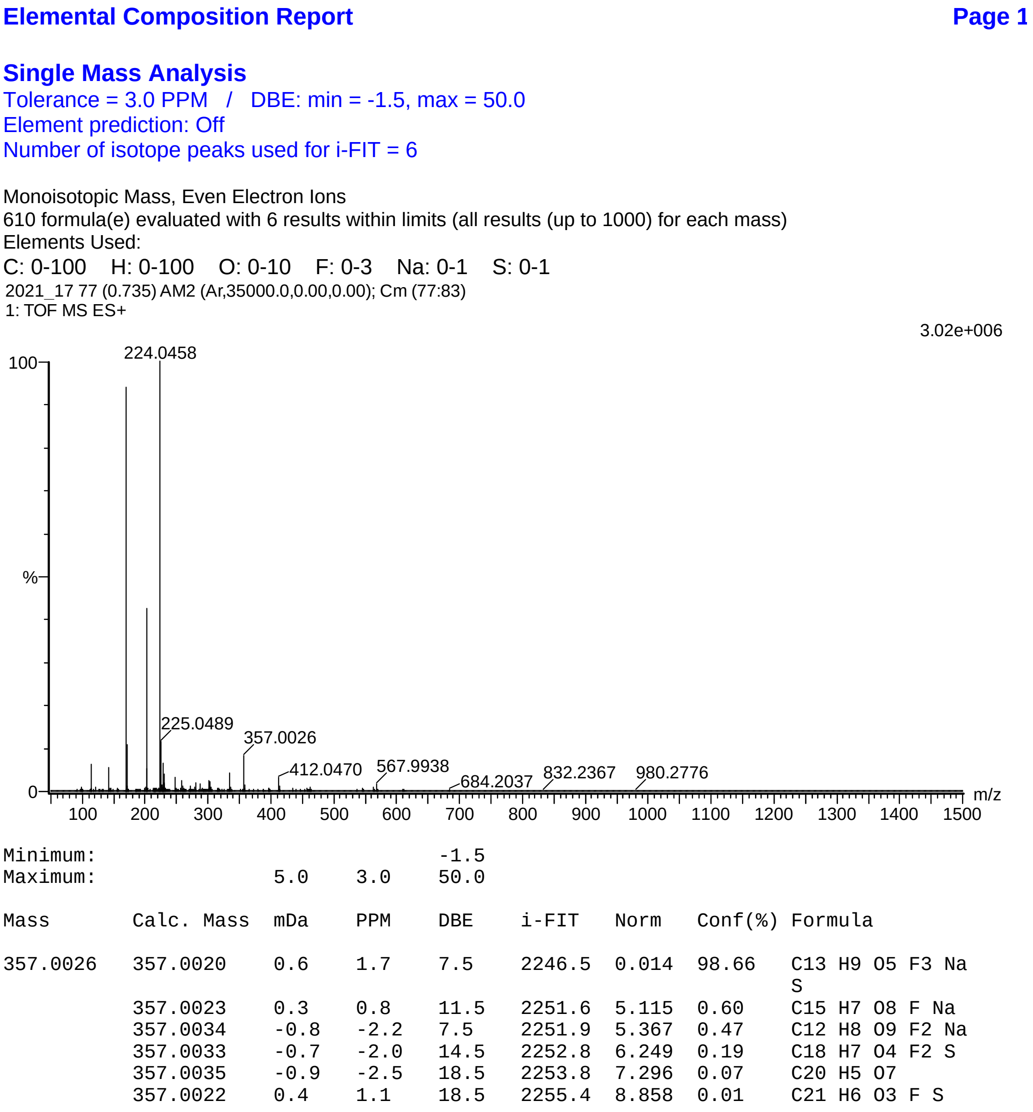

Elemental Composition Report **Page 1**

Single Mass Analysis
Tolerance = 3.0 PPM / DBE: min = -1.5, max = 50.0
Element prediction: Off
Number of isotope peaks used for i-FIT = 6

Monoisotopic Mass, Even Electron Ions
610 formula(e) evaluated with 6 results within limits (all results (up to 1000) for each mass)
Elements Used:
C: 0-100 H: 0-100 O: 0-10 F: 0-3 Na: 0-1 S: 0-1
2021_17 77 (0.735) AM2 (Ar,35000.0,0.00,0.00); Cm (77:83)
1: TOF MS ES+

```
Minimum:                                -1.5
Maximum:                5.0     3.0     50.0

Mass       Calc. Mass   mDa     PPM     DBE     i-FIT    Norm    Conf(%)  Formula

357.0026   357.0020     0.6     1.7     7.5     2246.5   0.014   98.66    C13 H9 O5 F3 Na
                                                                          S
           357.0023     0.3     0.8     11.5    2251.6   5.115   0.60     C15 H7 O8 F Na
           357.0034     -0.8    -2.2    7.5     2251.9   5.367   0.47     C12 H8 O9 F2 Na
           357.0033     -0.7    -2.0    14.5    2252.8   6.249   0.19     C18 H7 O4 F2 S
           357.0035     -0.9    -2.5    18.5    2253.8   7.296   0.07     C20 H5 O7
           357.0022     0.4     1.1     18.5    2255.4   8.858   0.01     C21 H6 O3 F S
```

Figure B.8: MS spectrum of compound **2**

C Spectroscopic data for compound 3

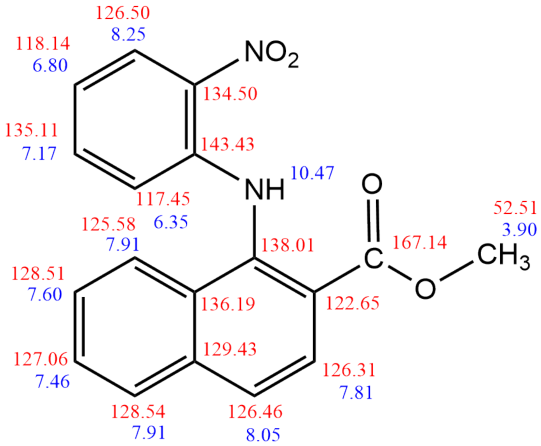

Figure C.1: Assigned ^{1}H and ^{13}C NMR signals of compound **3**

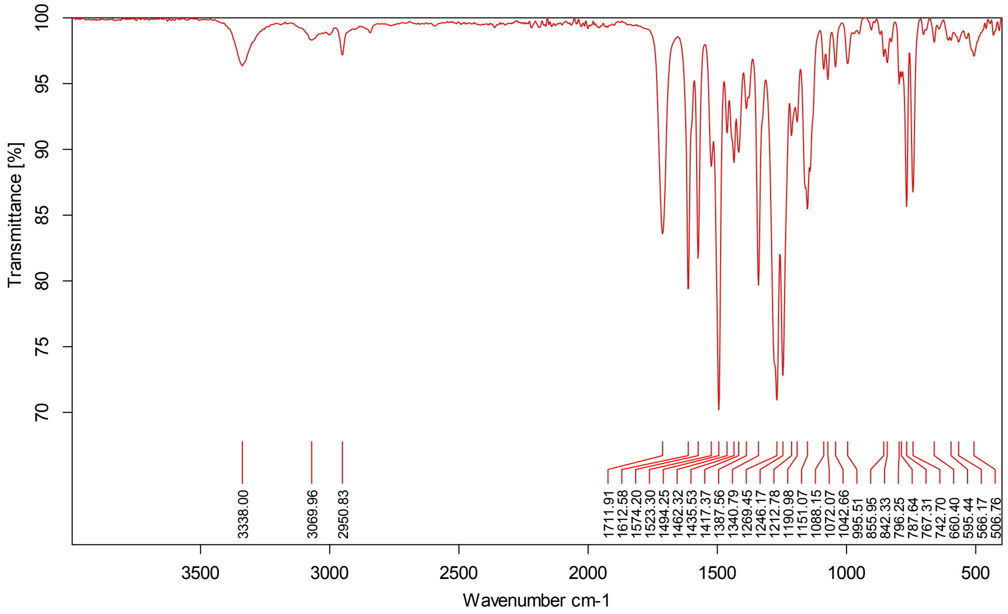

Figure C.2: IR spectrum of compound **3**

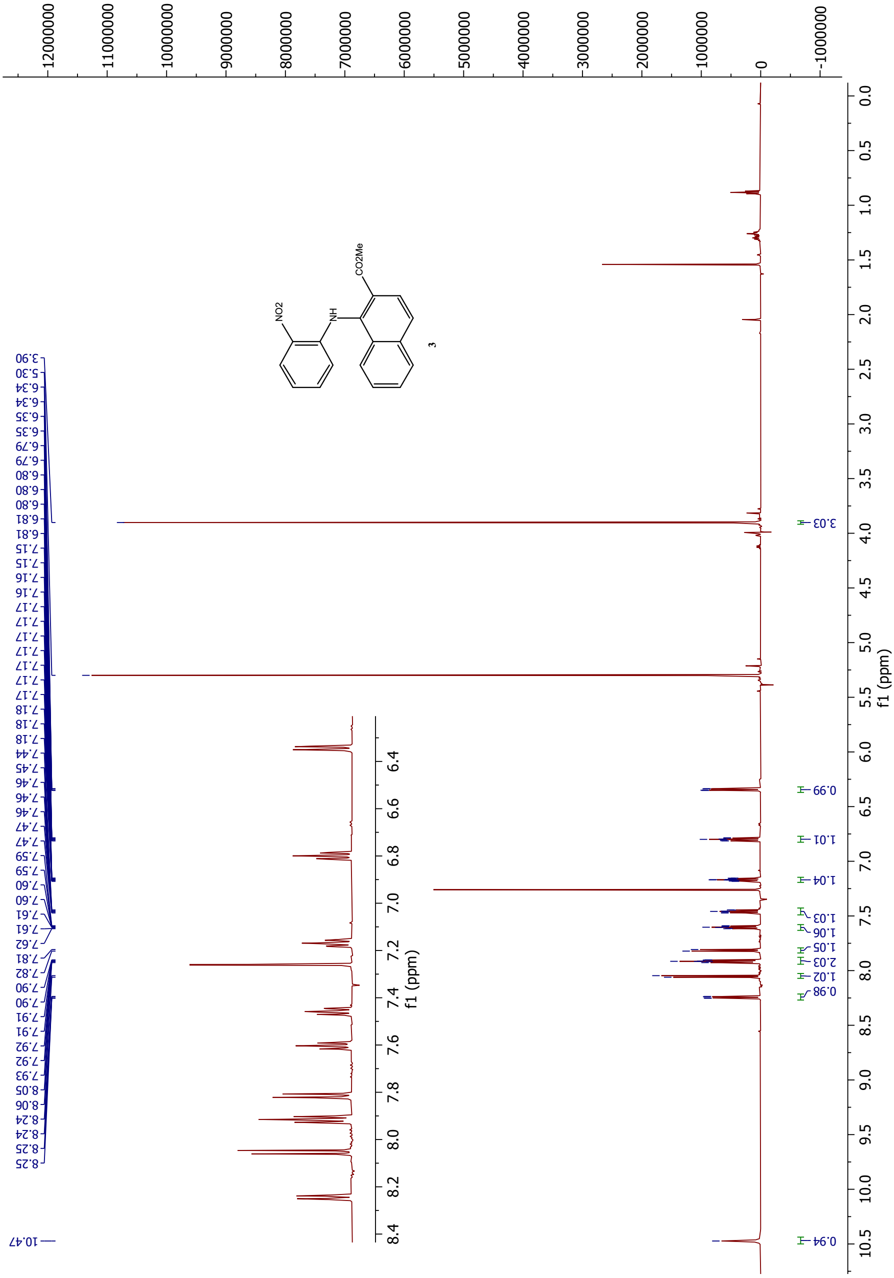

Figure C.3: ^{1}H NMR spectrum of compound **3**

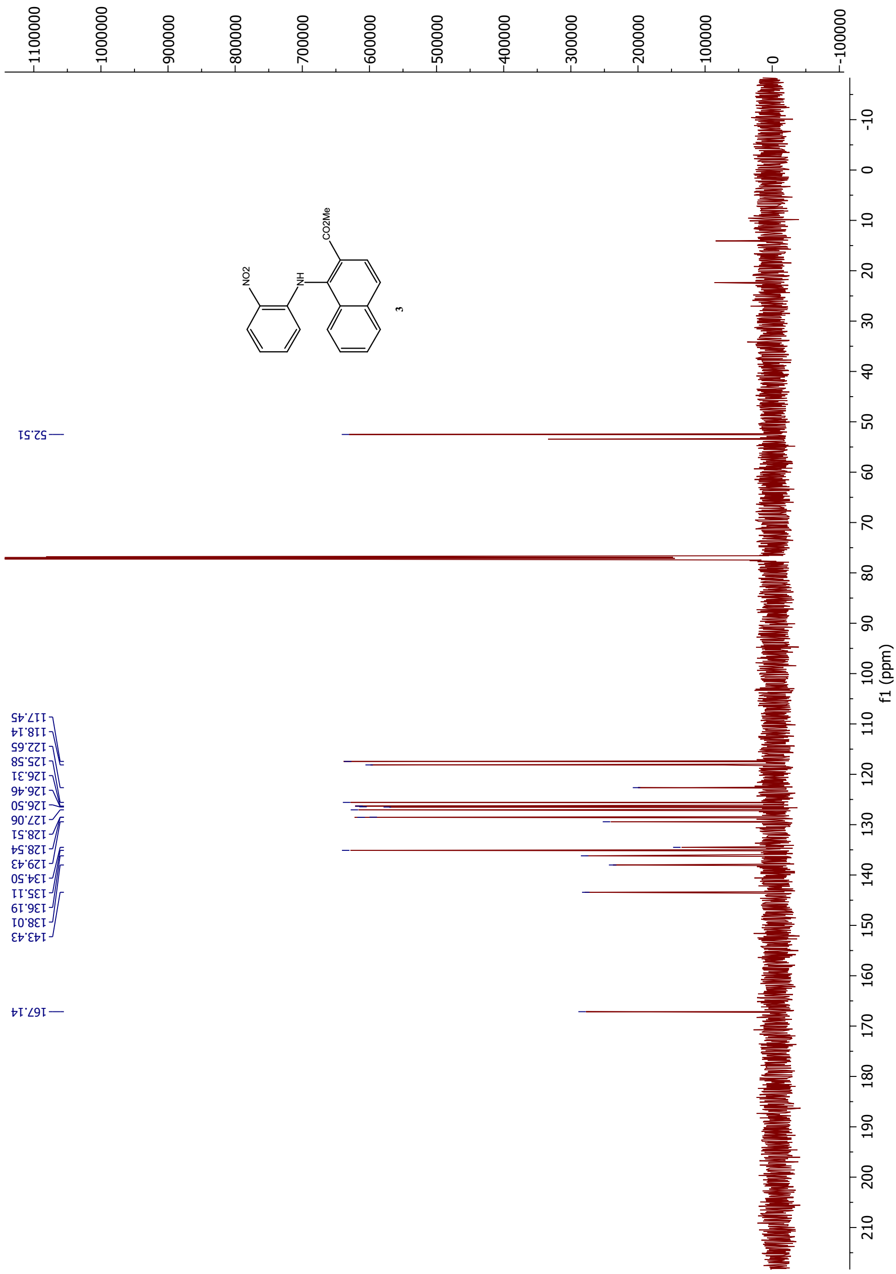

Figure C.4: ^{13}C NMR spectrum of compound **3**

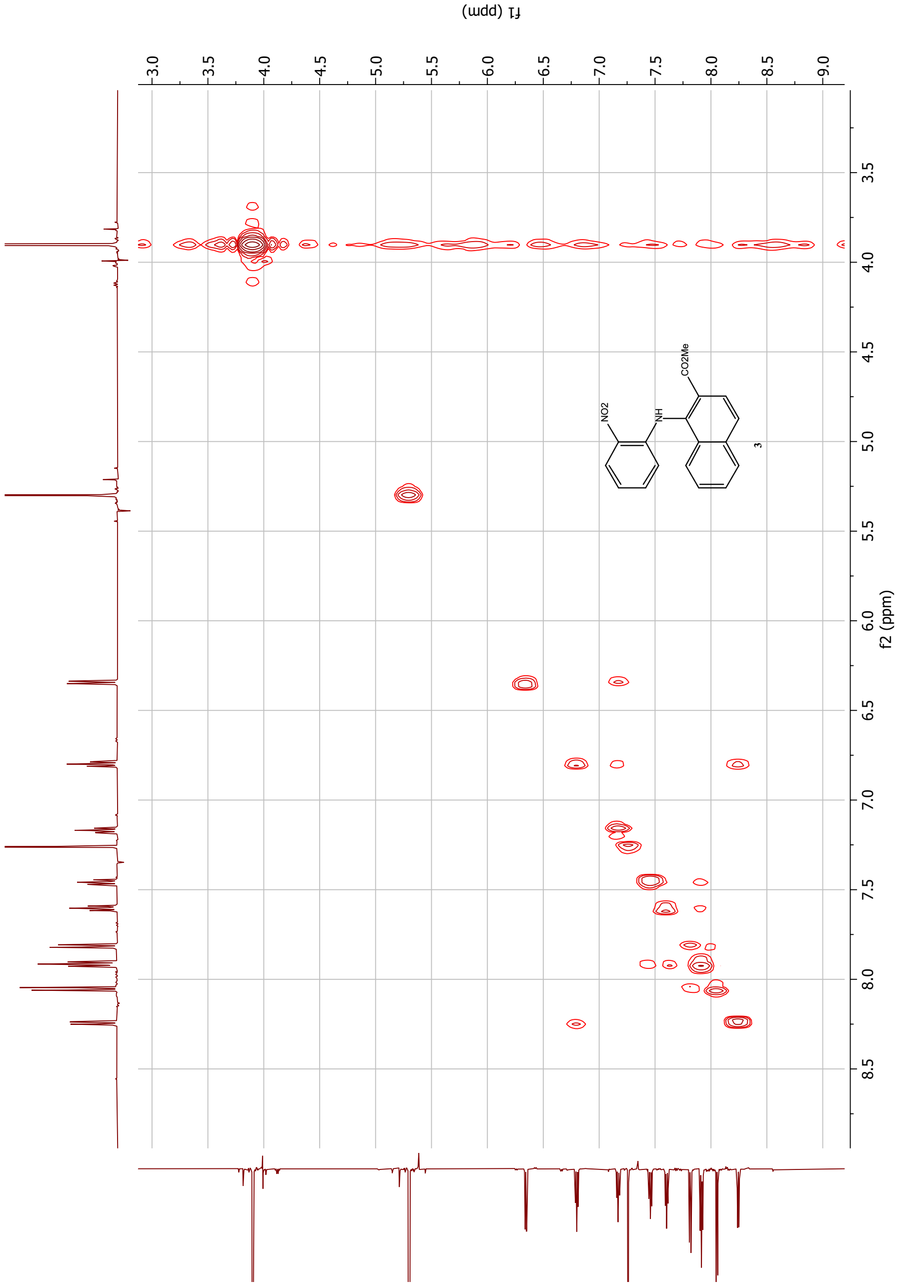

Figure C.5: COSY NMR spectrum of compound **3**

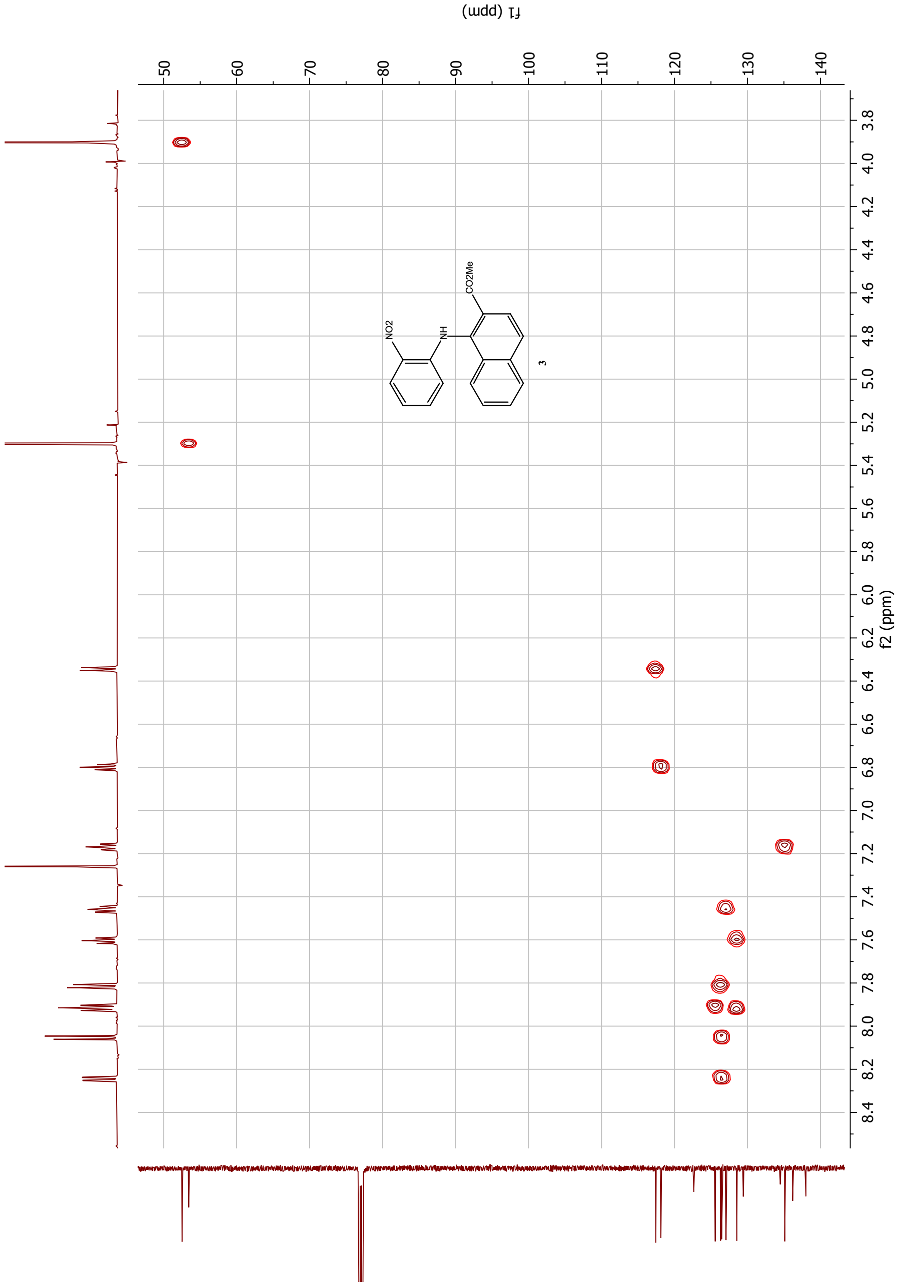

Figure C.6: HSQC NMR spectrum of compound **3**

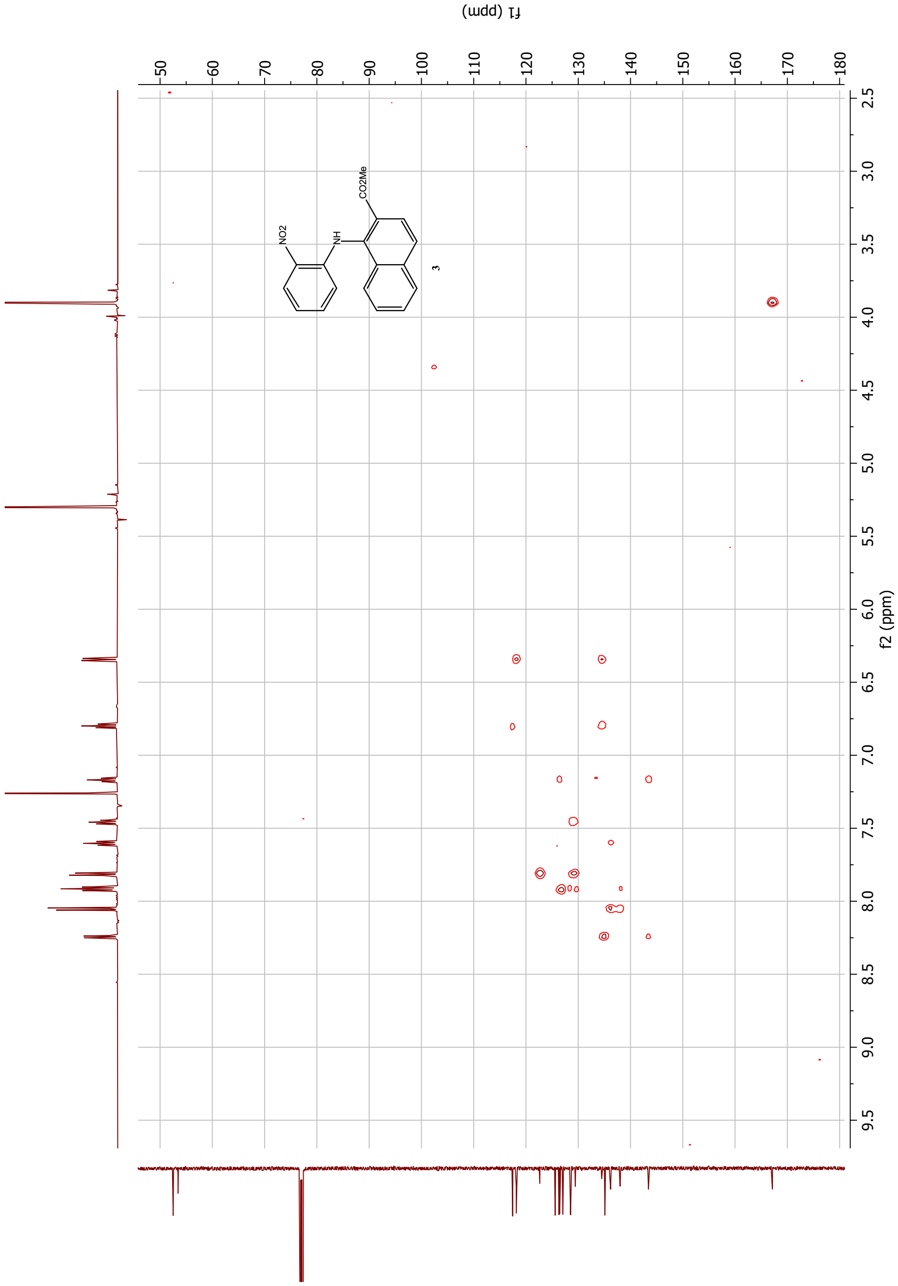

Figure C.7: HMBC NMR spectrum of compound **3**

Elemental Composition Report

Page 1

Single Mass Analysis

Tolerance = 3.0 PPM / DBE: min = -1.5, max = 50.0
Element prediction: Off
Number of isotope peaks used for i-FIT = 6

Monoisotopic Mass, Even Electron Ions
713 formula(e) evaluated with 3 results within limits (all results (up to 1000) for each mass)
Elements Used:
C: 0-100 H: 0-100 N: 0-8 O: 0-10 Na: 0-1

2021_19 70 (0.665) AM2 (Ar,35000.0,0.00,0.00); Cm (64:72)
1: TOF MS ES+

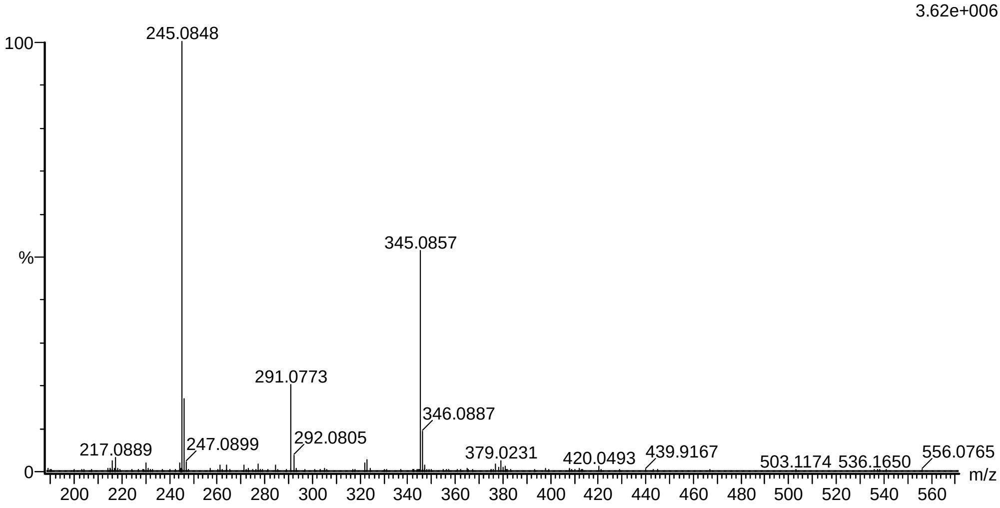

```
Minimum:                                -1.5
Maximum:                 5.0     3.0    50.0

Mass        Calc. Mass   mDa     PPM     DBE     i-FIT    Norm    Conf(%)  Formula

345.0857    345.0851     0.6     1.7     12.5    2551.7   1.386   25.02    C18 H14 N2 O4
                                                                           Na
            345.0865     -0.8    -2.3    17.5    2556.5   6.281   0.19     C19 H10 N6 Na
            345.0848     0.9     2.6     16.5    2550.6   0.290   74.80    C16 H9 N8 O2
```

Figure C.8: MS spectrum of compound **3**

D Spectroscopic data for compound 4

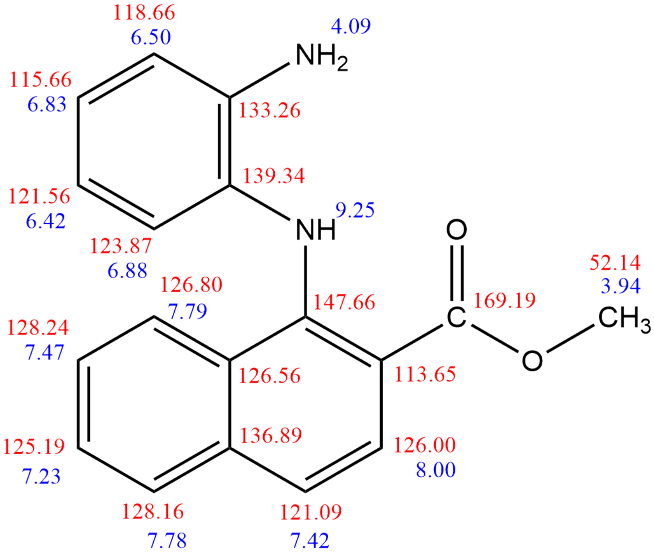

Figure D.1: Assigned ^{1}H and ^{13}C NMR signals of compound **4**

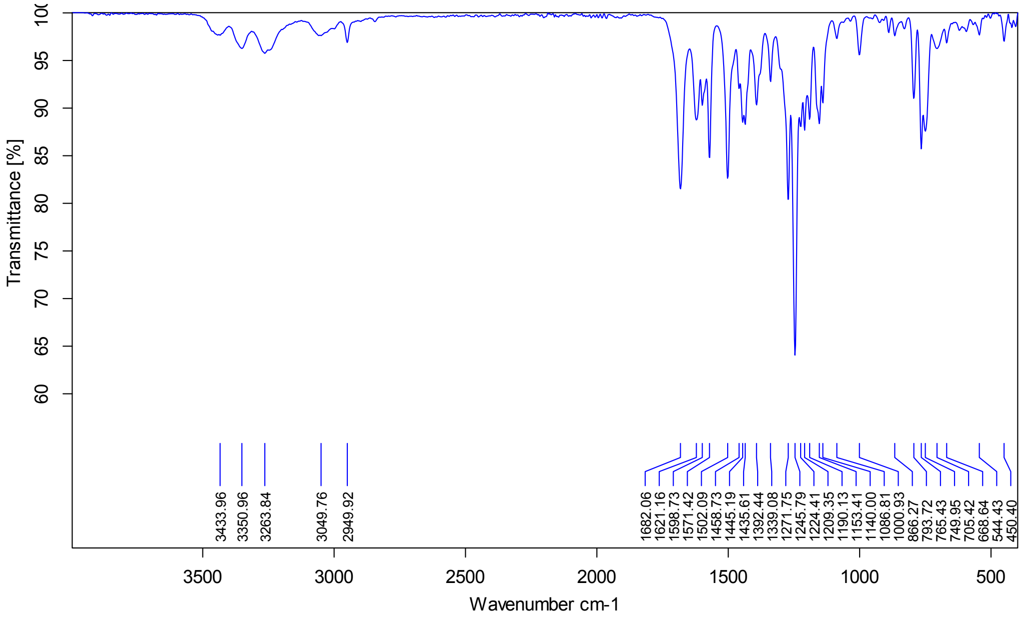

Figure D.2: IR spectrum of compound **4**

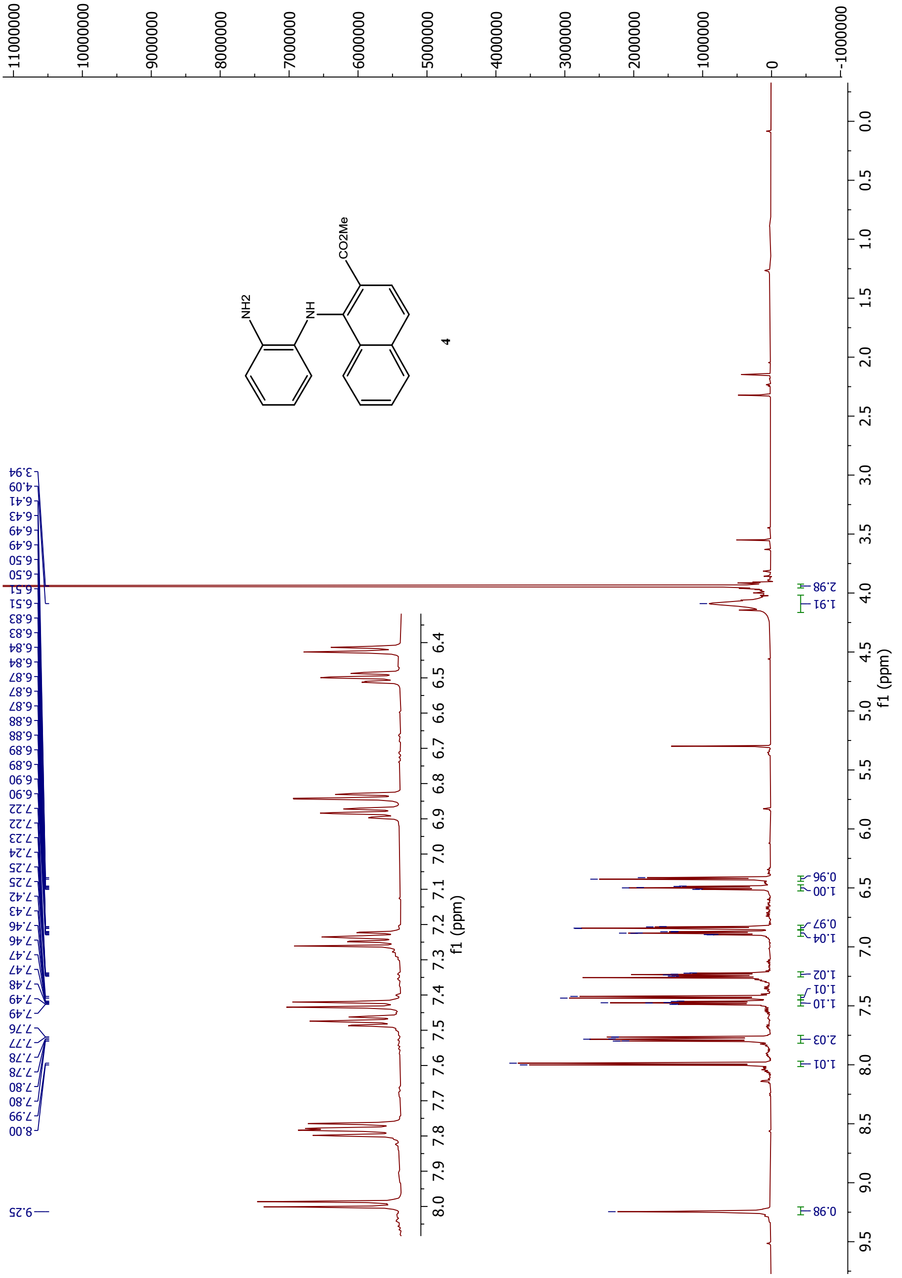

Figure D.3: ^{1}H NMR spectrum of compound **4**

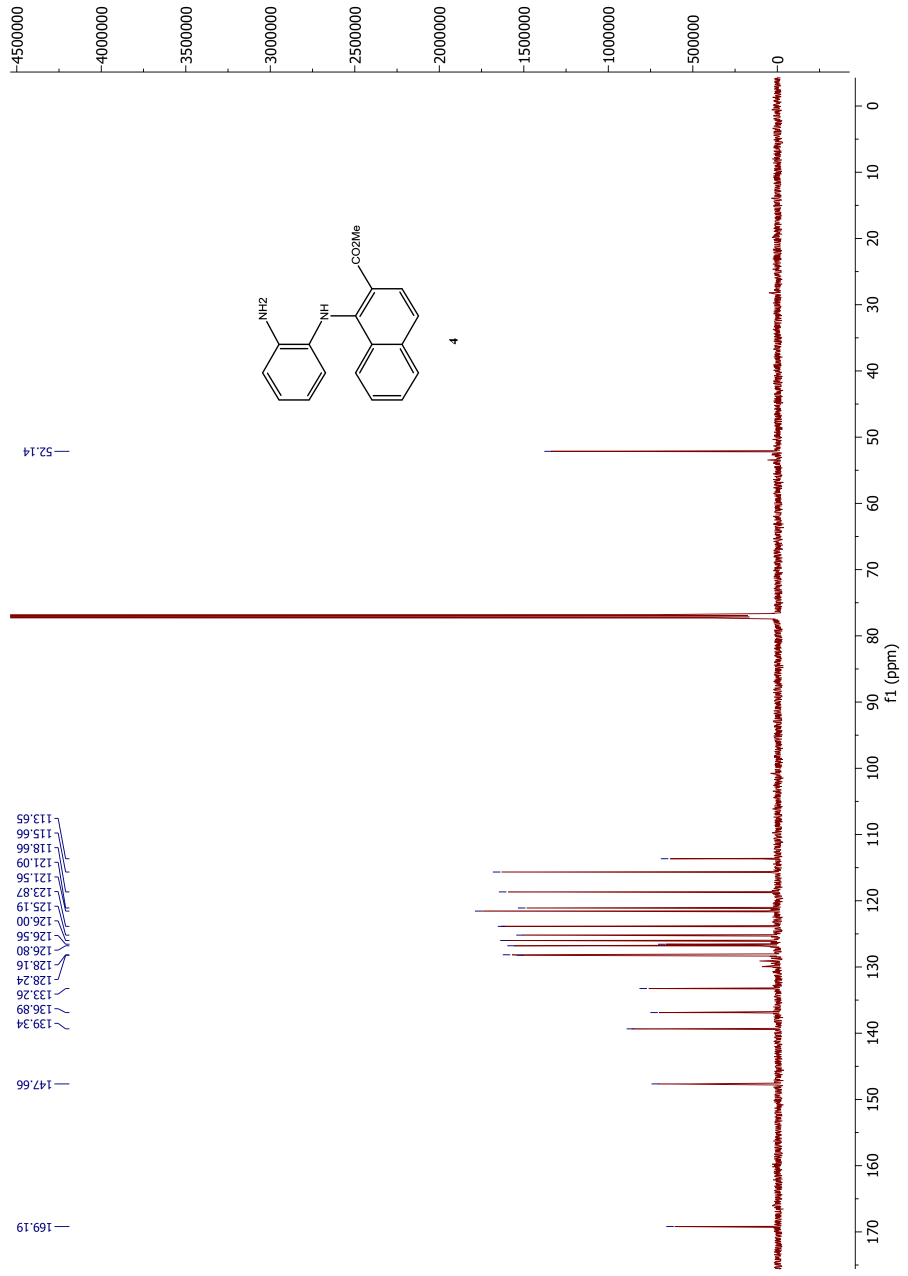

Figure D.4: ^{13}C NMR spectrum of compound **4**

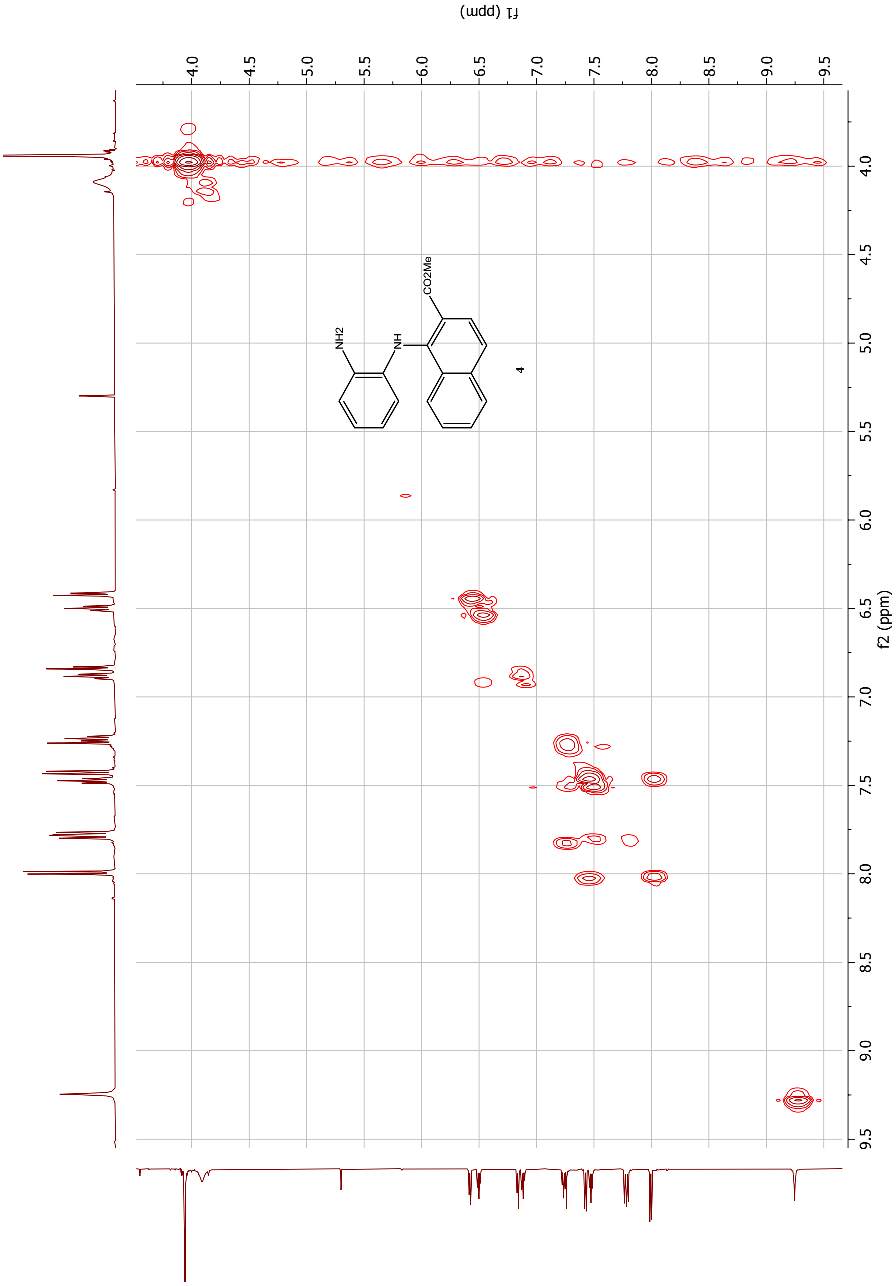

Figure D.5: COSY NMR spectrum of compound **4**

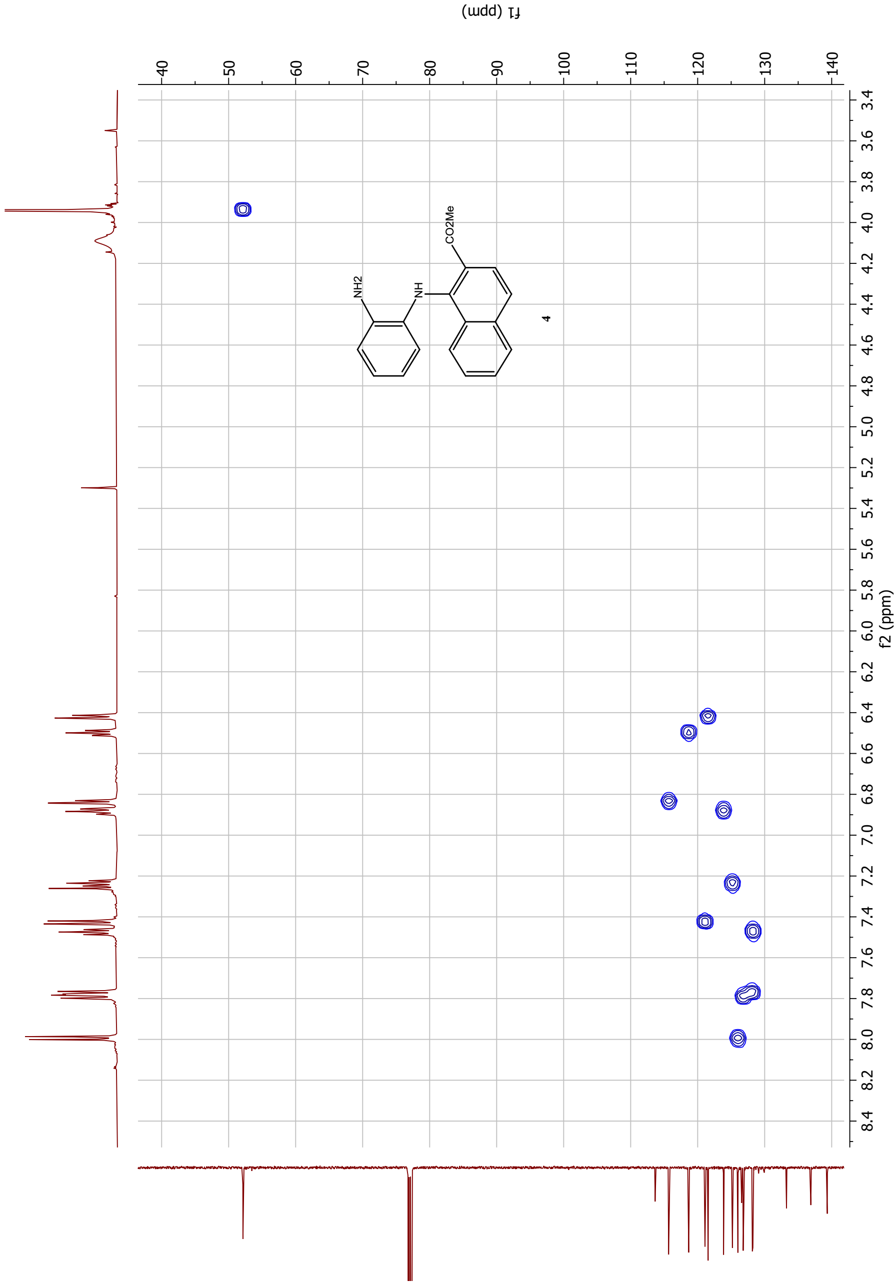

Figure D.6: HSQC NMR spectrum of compound **4**

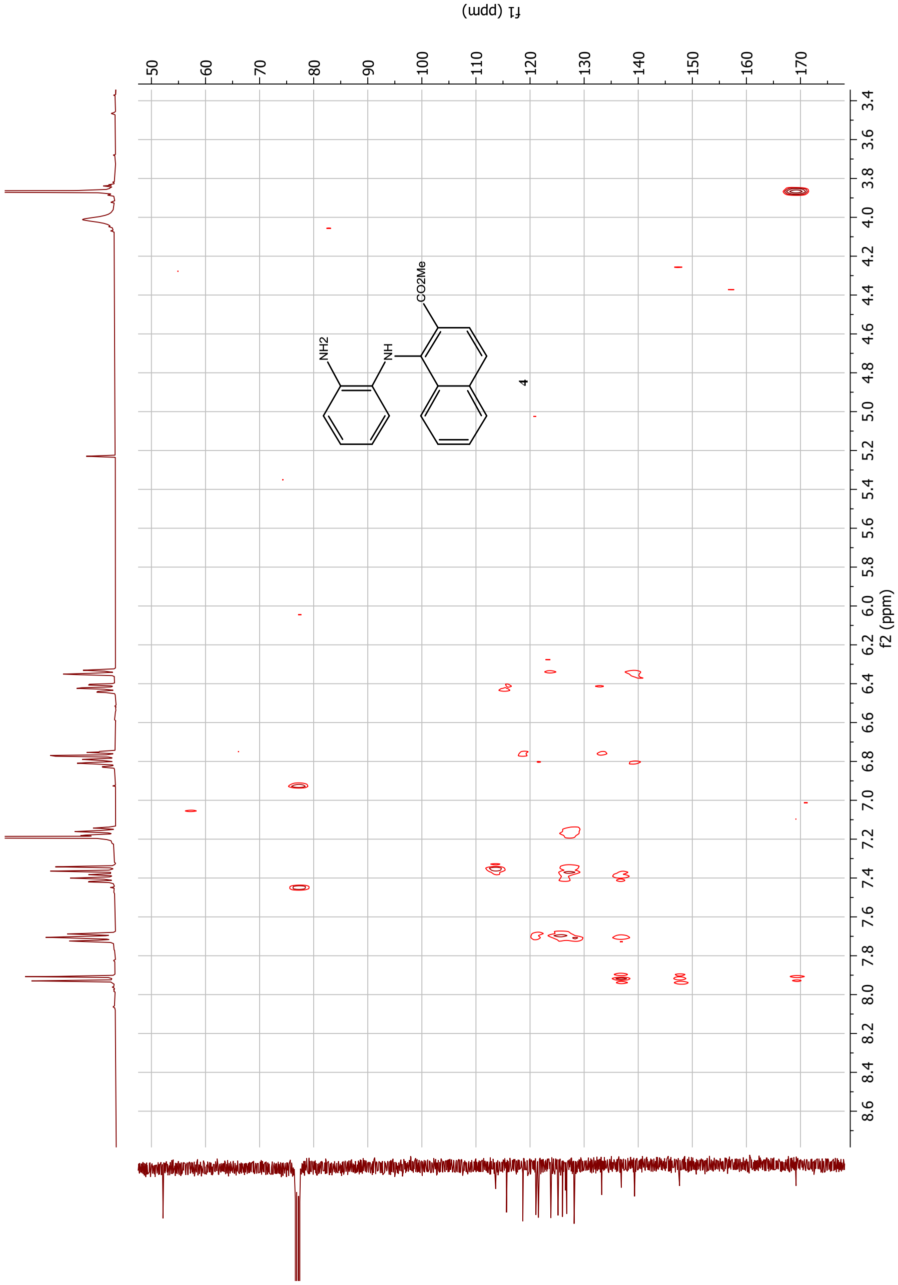

Figure D.7: HMBC NMR spectrum of compound **4**

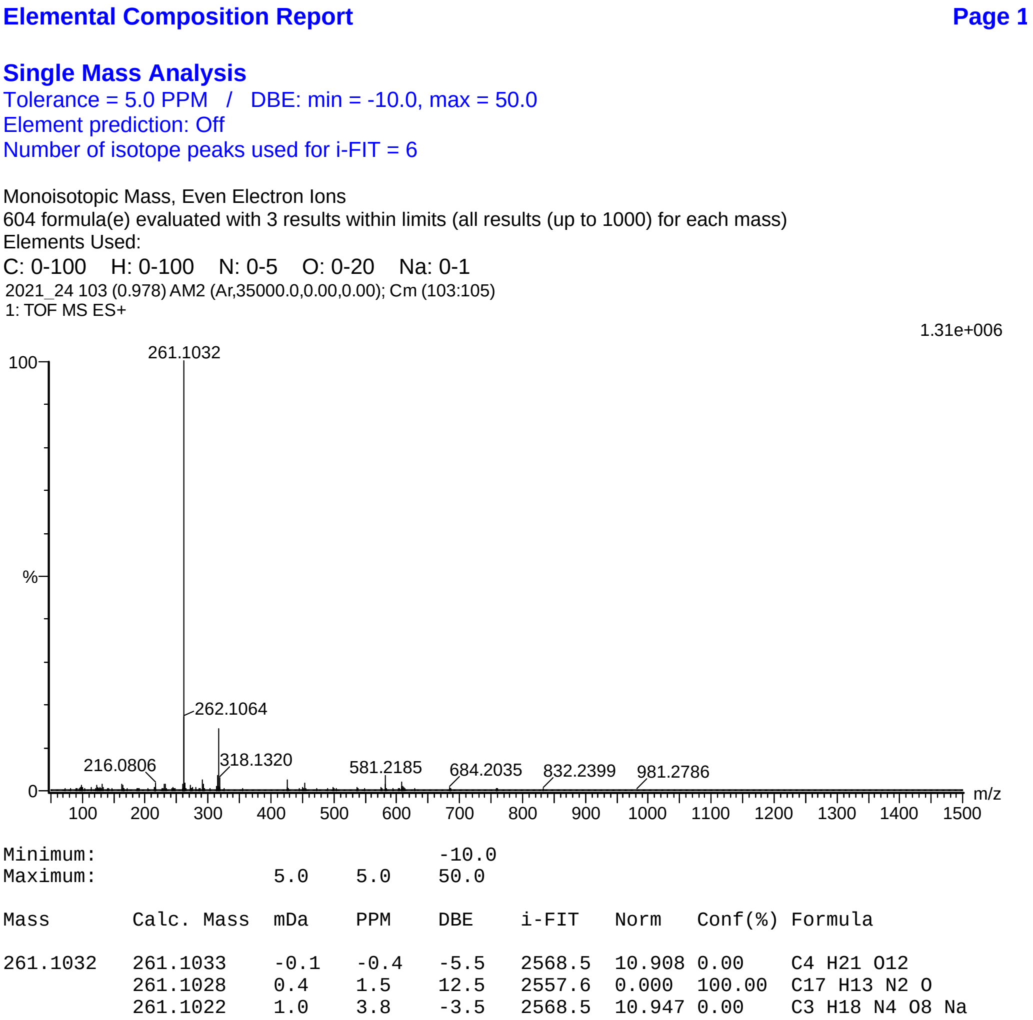

Elemental Composition Report **Page 1**

Single Mass Analysis
Tolerance = 5.0 PPM / DBE: min = -10.0, max = 50.0
Element prediction: Off
Number of isotope peaks used for i-FIT = 6

Monoisotopic Mass, Even Electron Ions
604 formula(e) evaluated with 3 results within limits (all results (up to 1000) for each mass)
Elements Used:
C: 0-100 H: 0-100 N: 0-5 O: 0-20 Na: 0-1
2021_24 103 (0.978) AM2 (Ar,35000.0,0.00,0.00); Cm (103:105)
1: TOF MS ES+

```
Minimum:                                 -10.0
Maximum:                5.0      5.0     50.0

Mass        Calc. Mass  mDa      PPM     DBE     i-FIT    Norm   Conf(%) Formula

261.1032    261.1033    -0.1     -0.4    -5.5    2568.5   10.908 0.00    C4 H21 O12
            261.1028    0.4      1.5     12.5    2557.6   0.000  100.00  C17 H13 N2 O
            261.1022    1.0      3.8     -3.5    2568.5   10.947 0.00    C3 H18 N4 O8 Na
```

Figure D.8: MS spectrum of compound **4**

E Spectroscopic data for compound 5

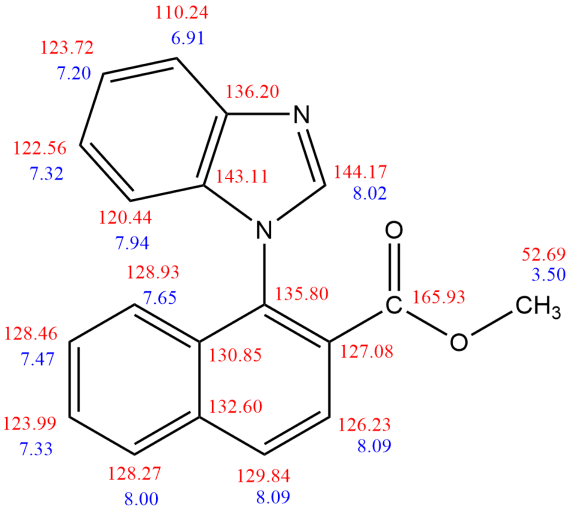

Figure E.1: Assigned ^{1}H and ^{13}C NMR signals of compound **5**

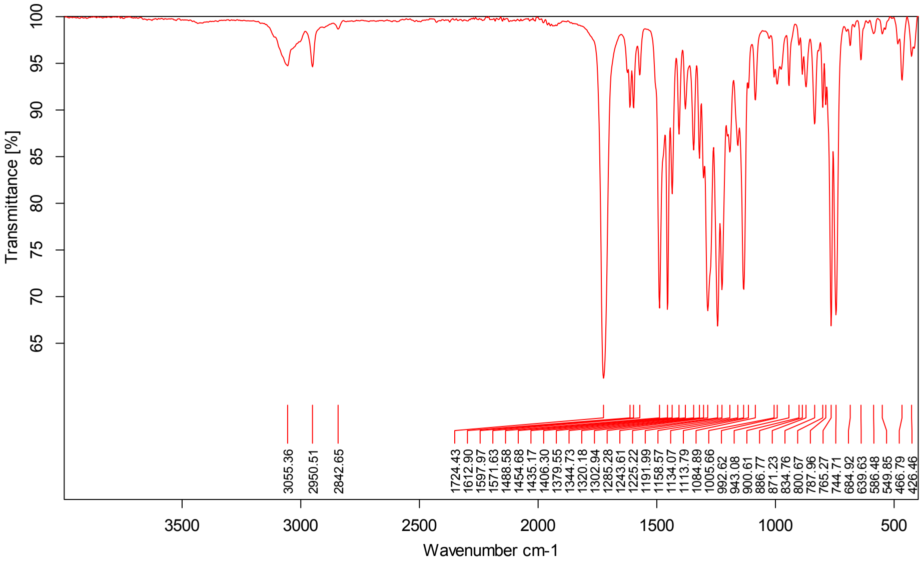

Figure E.2: IR spectrum of compound **5**

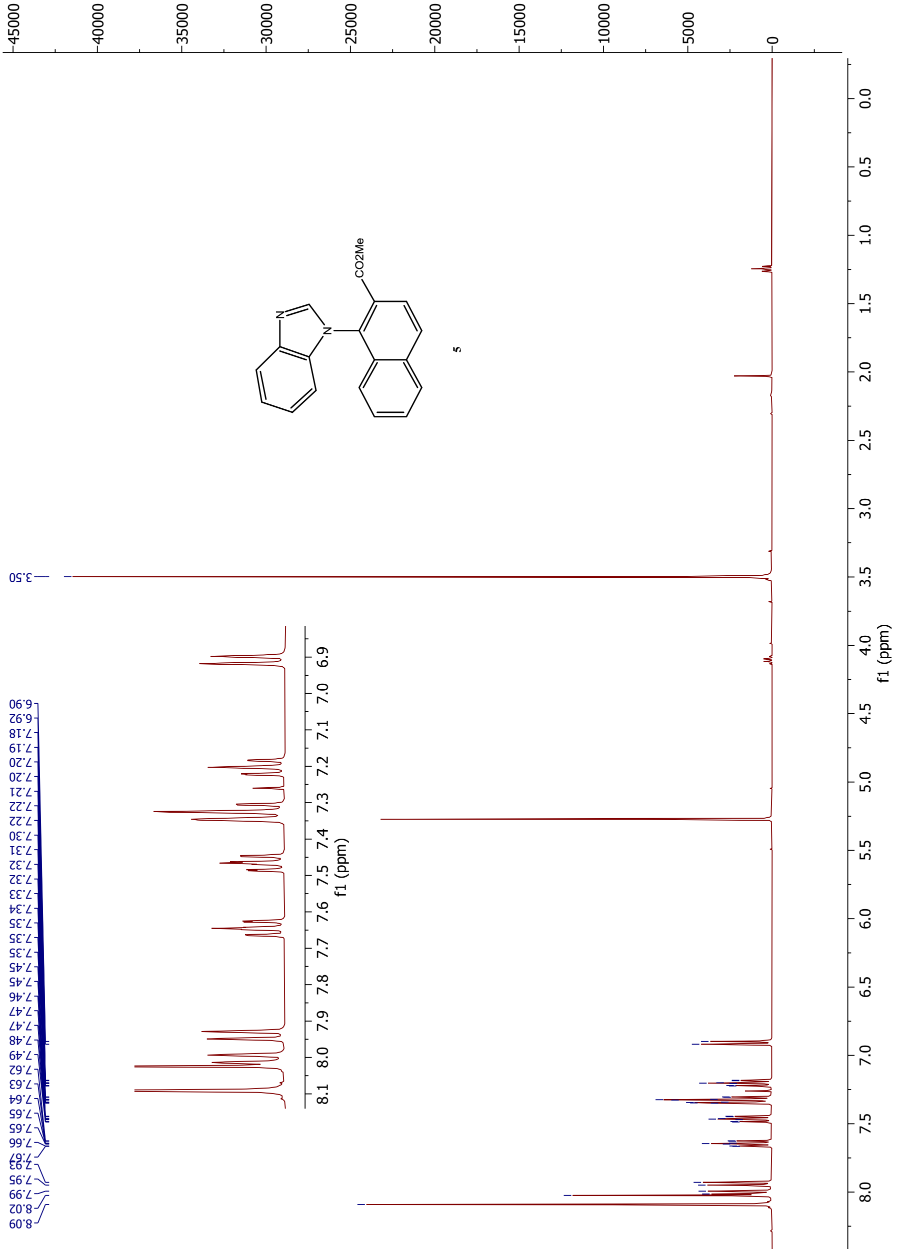

Figure E.3: ^{1}H NMR spectrum of compound **5**

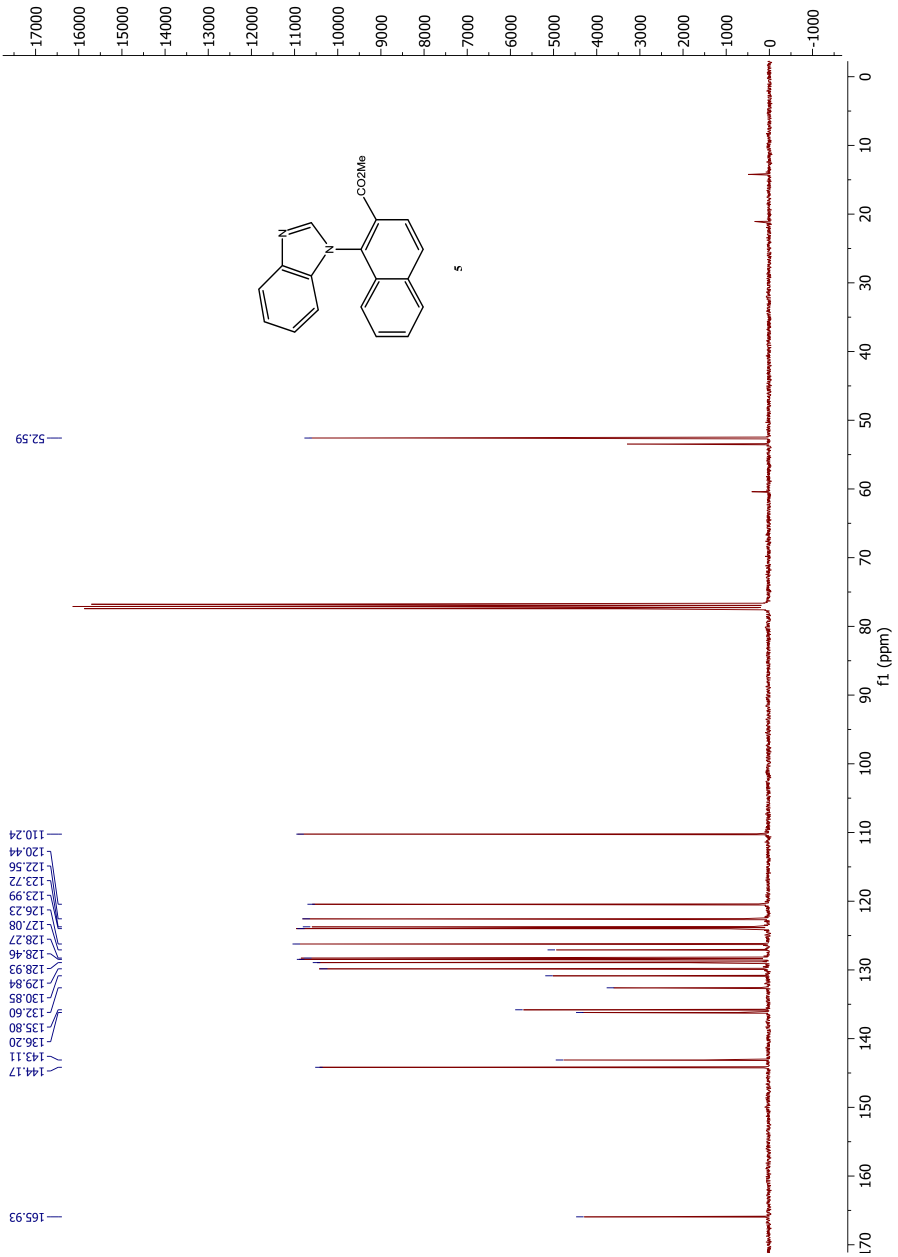

Figure E.4: ^{13}C NMR spectrum of compound **5**

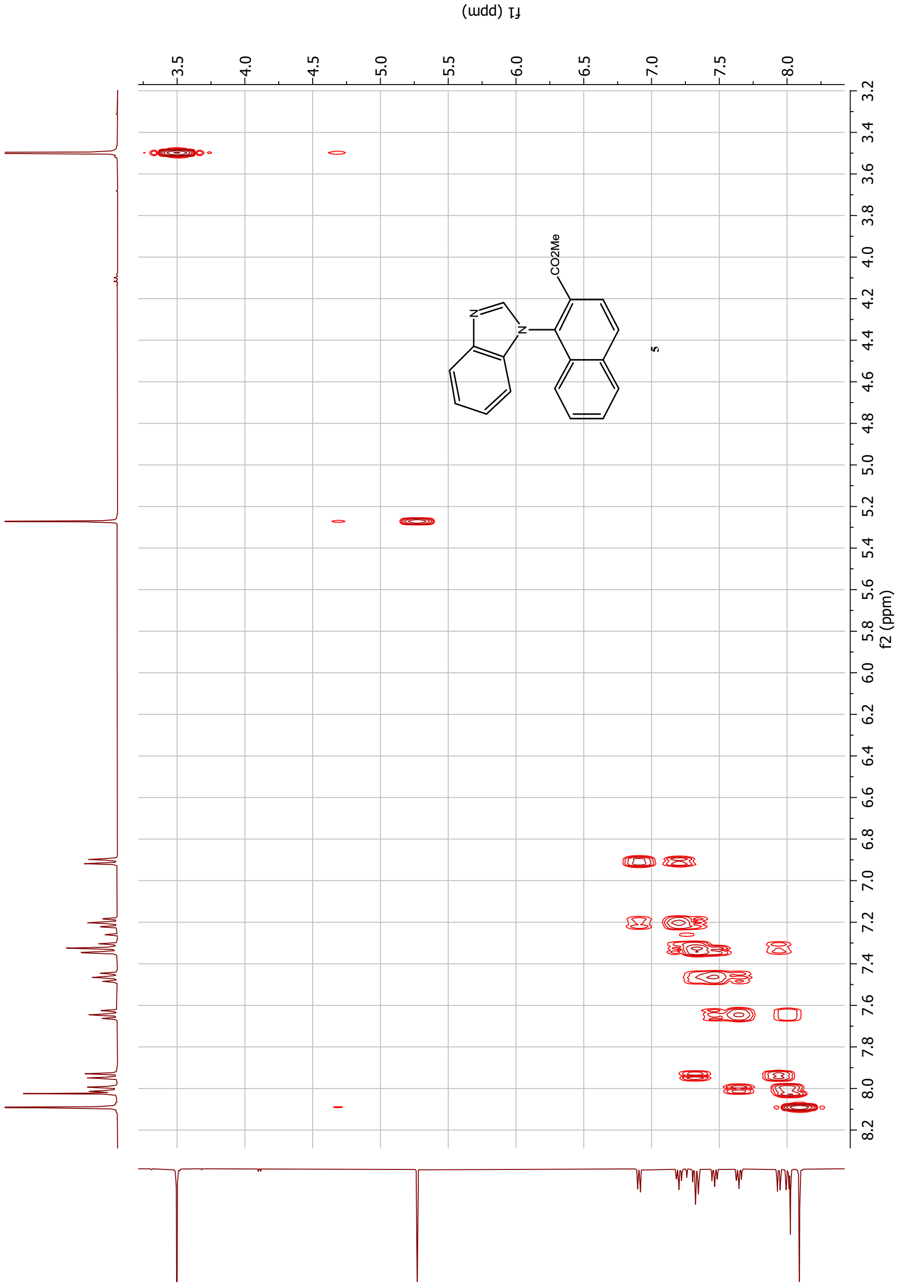

Figure E.5: COSY NMR spectrum of compound **5**

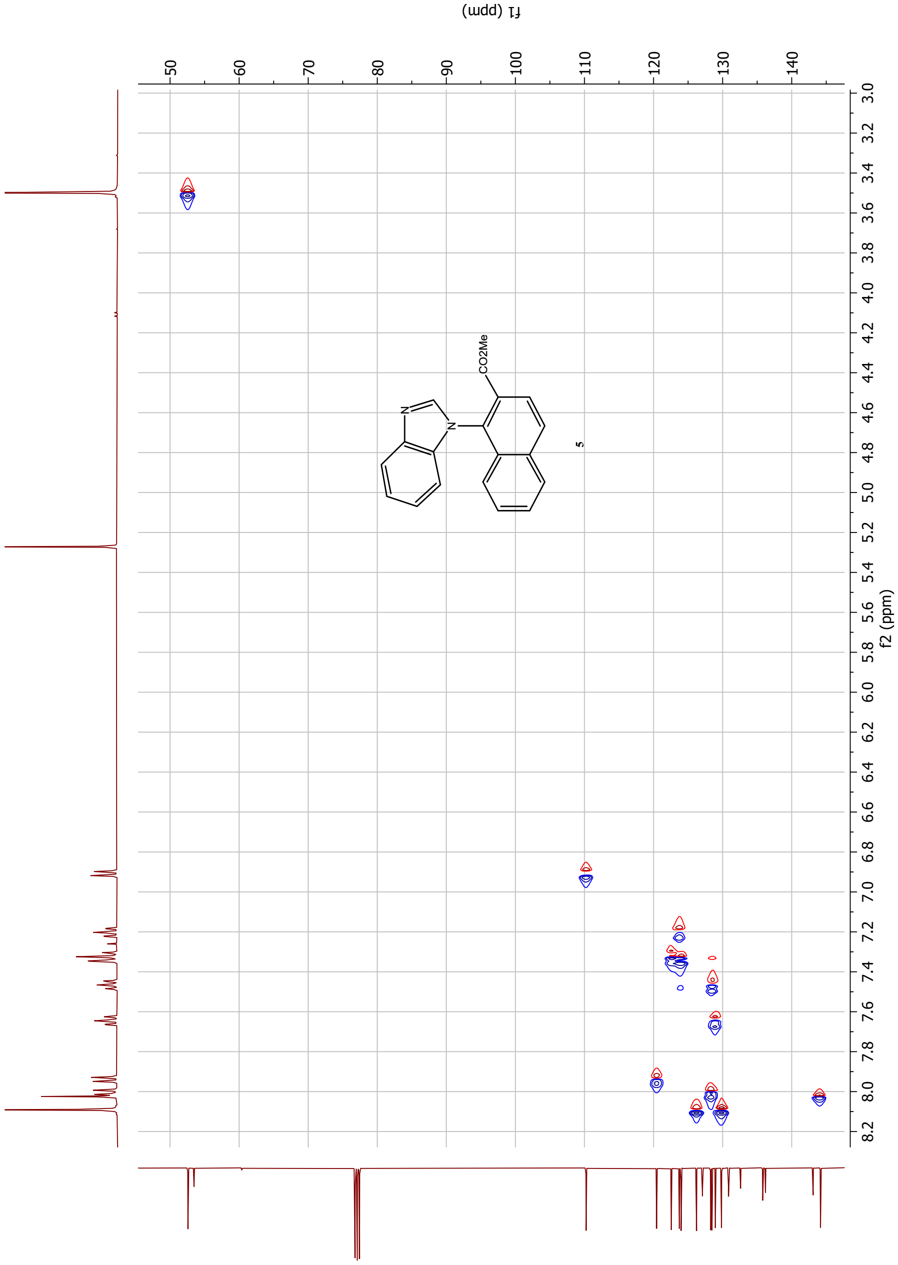

Figure E.6: HSQC NMR spectrum of compound **5**

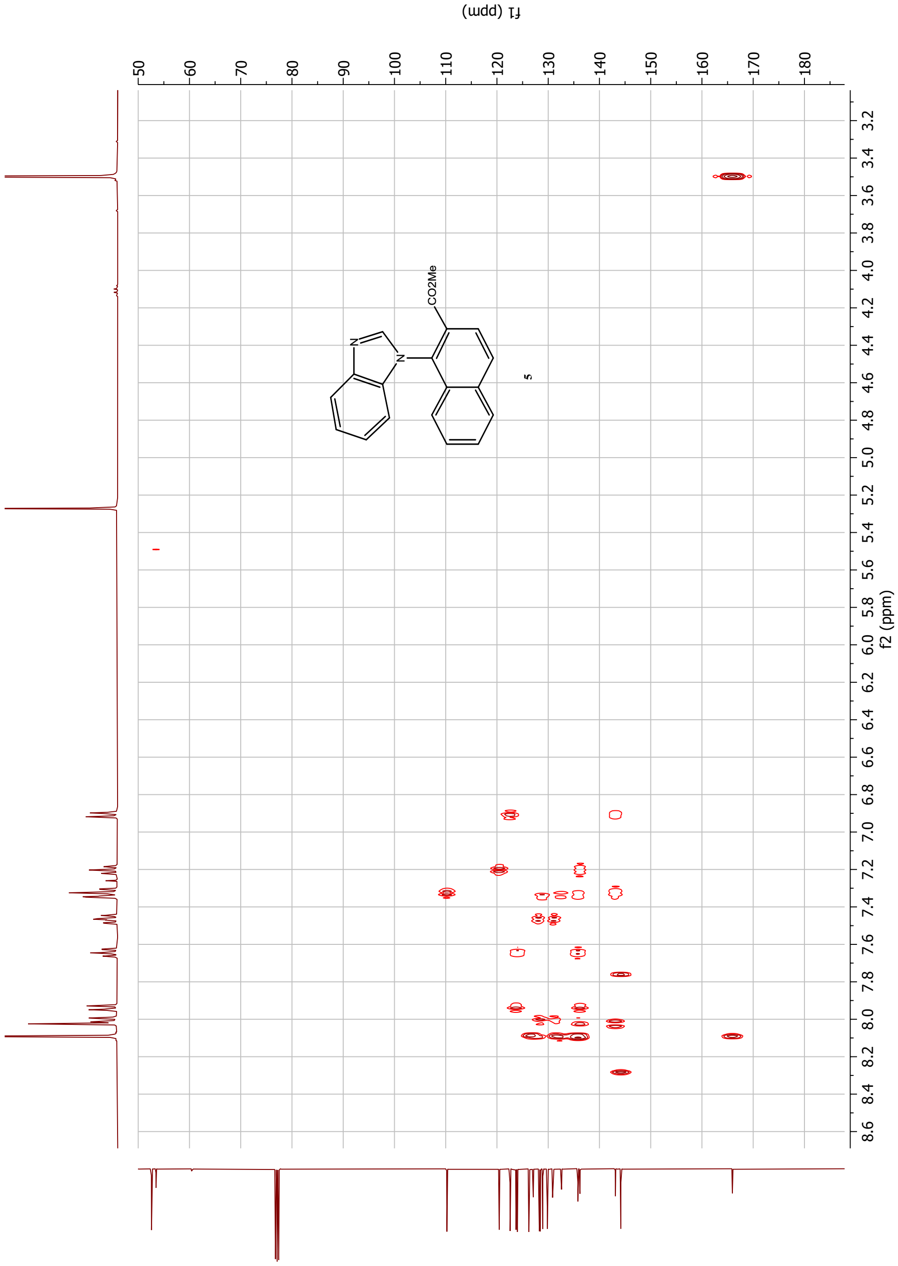

Figure E.7: HMBC NMR spectrum of compound **5**

Elemental Composition Report

Page 1

Single Mass Analysis

Tolerance = 2.5 PPM / DBE: min = -10.0, max = 50.0
Element prediction: Off
Number of isotope peaks used for i-FIT = 6

Monoisotopic Mass, Even Electron Ions
490 formula(e) evaluated with 1 results within limits (all results (up to 1000) for each mass)
Elements Used:
C: 0-100 H: 0-100 N: 0-5 O: 0-10 Sb: 0-1
2021_31 178 (1.676) AM2 (Ar,35000.0,0.00,0.00); Cm (178:181)
1: TOF MS ES+

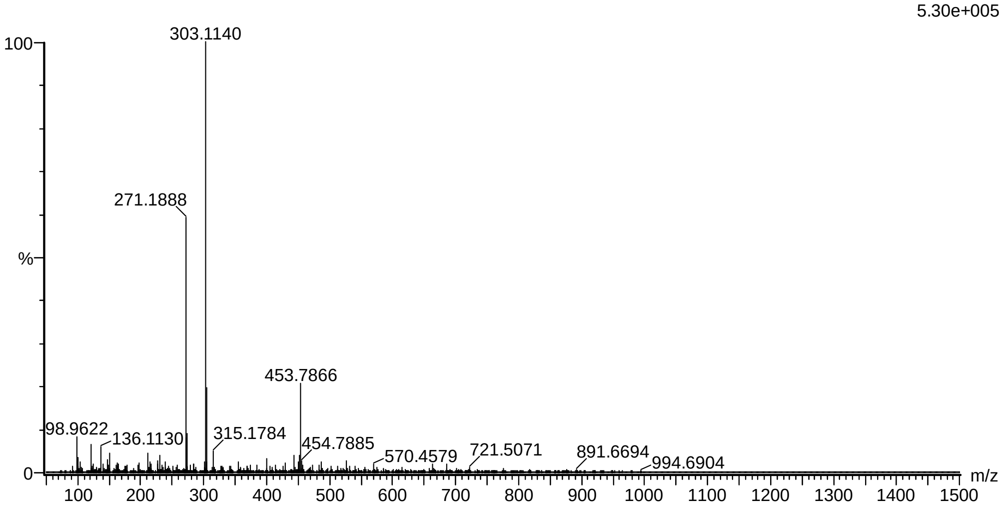

```
Minimum:                              -10.0
Maximum:                5.0     2.5     50.0

Mass        Calc. Mass  mDa     PPM     DBE     i-FIT    Norm    Conf(%) Formula

303.1140    303.1134    0.6     2.0     13.5    2408.4   n/a     n/a     C19 H15 N2 O2
```

Figure E.8: MS spectrum of compound **5**

F Spectroscopic data for compound 7

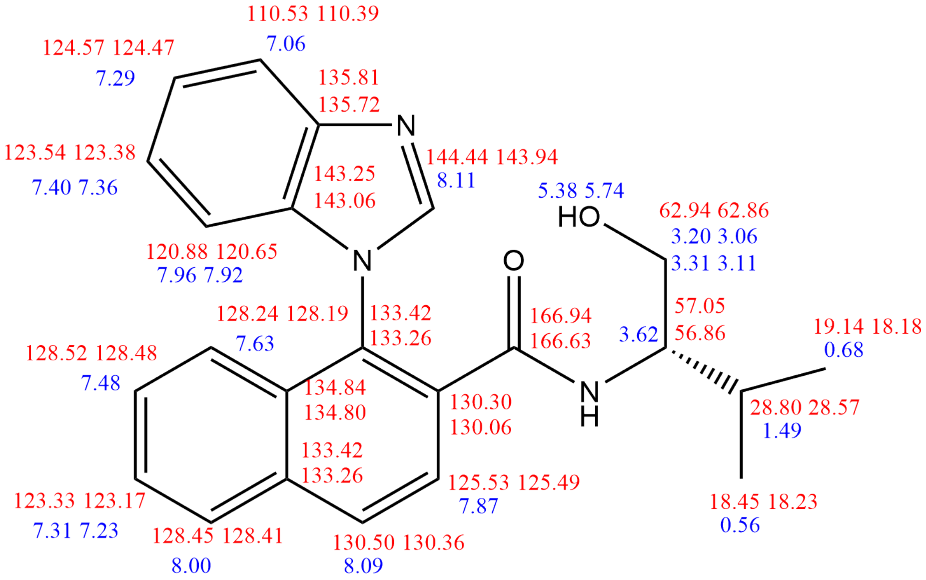

Figure F.1: Assigned ^{1}H and ^{13}C NMR signals of compound **7**

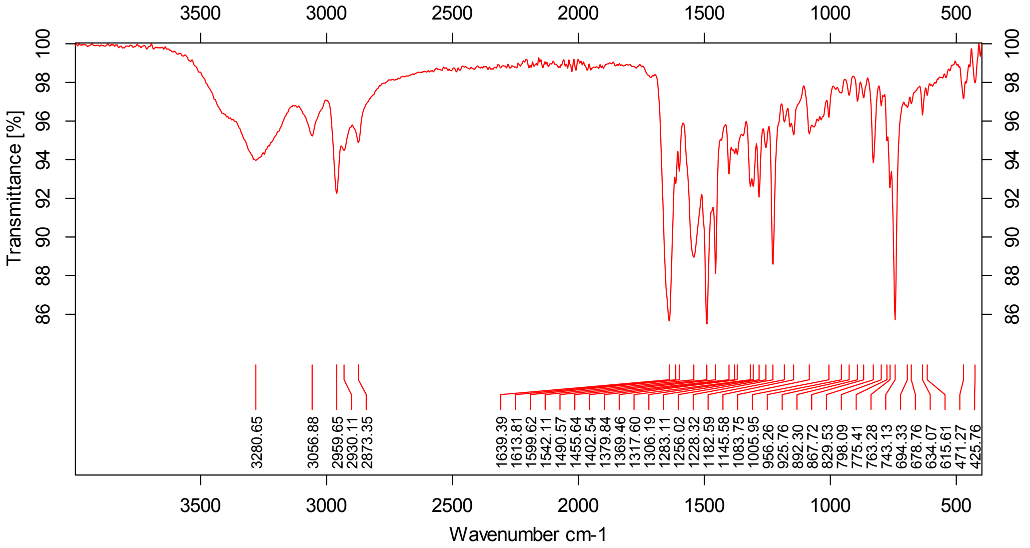

Figure F.2: IR spectrum of compound **7**

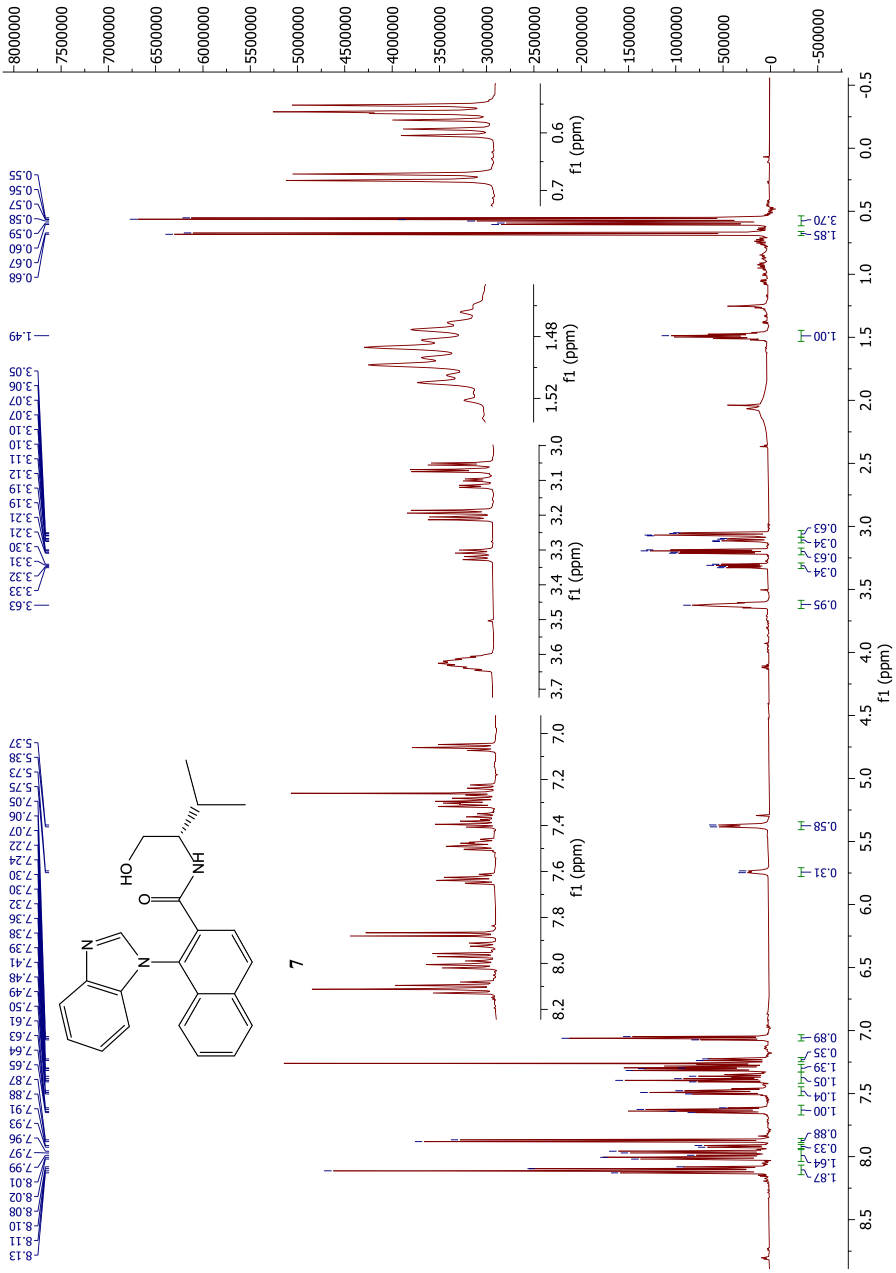

Figure F.3: ^{1}H NMR spectrum of compound **7**

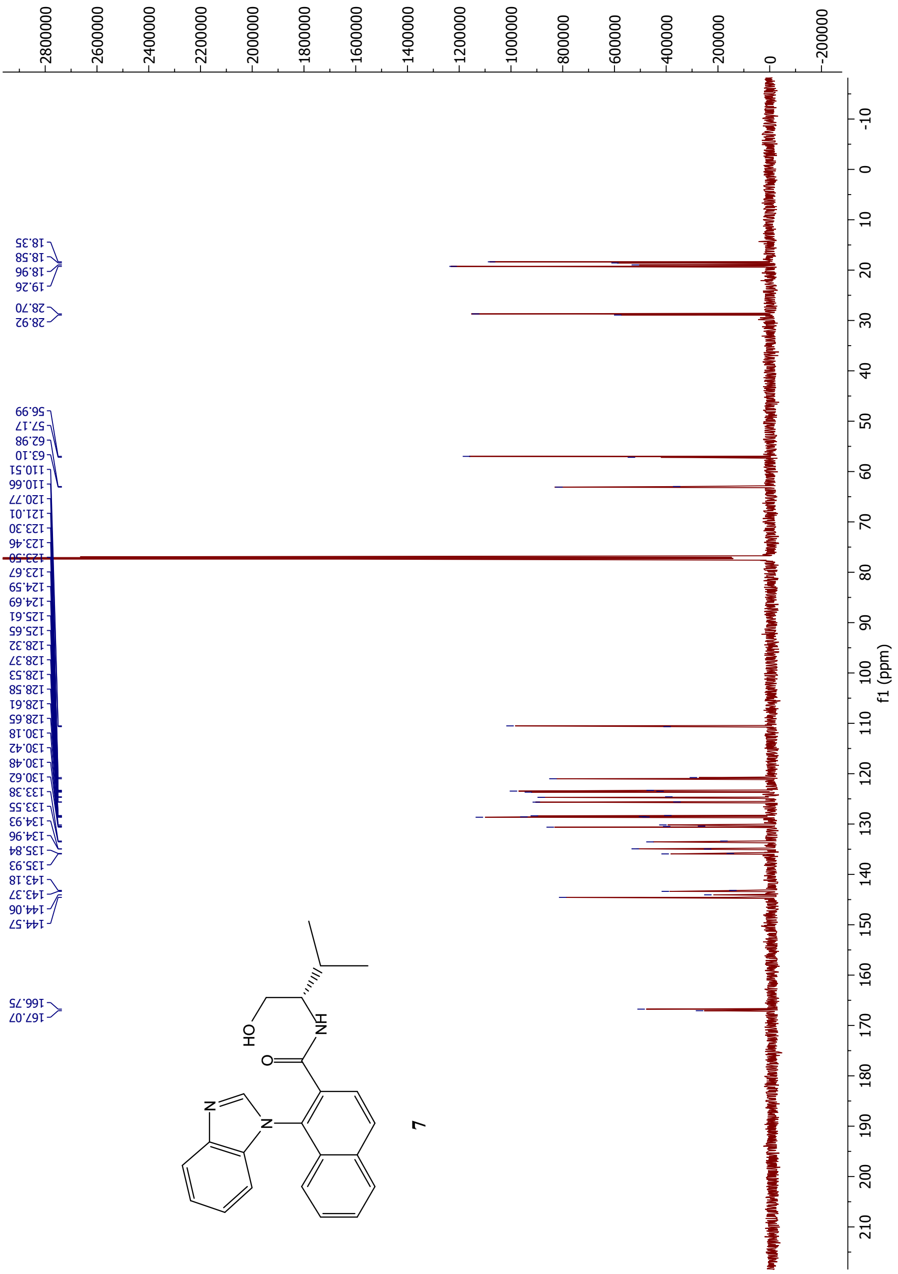

Figure F.4: ^{13}C NMR spectrum of compound **7**

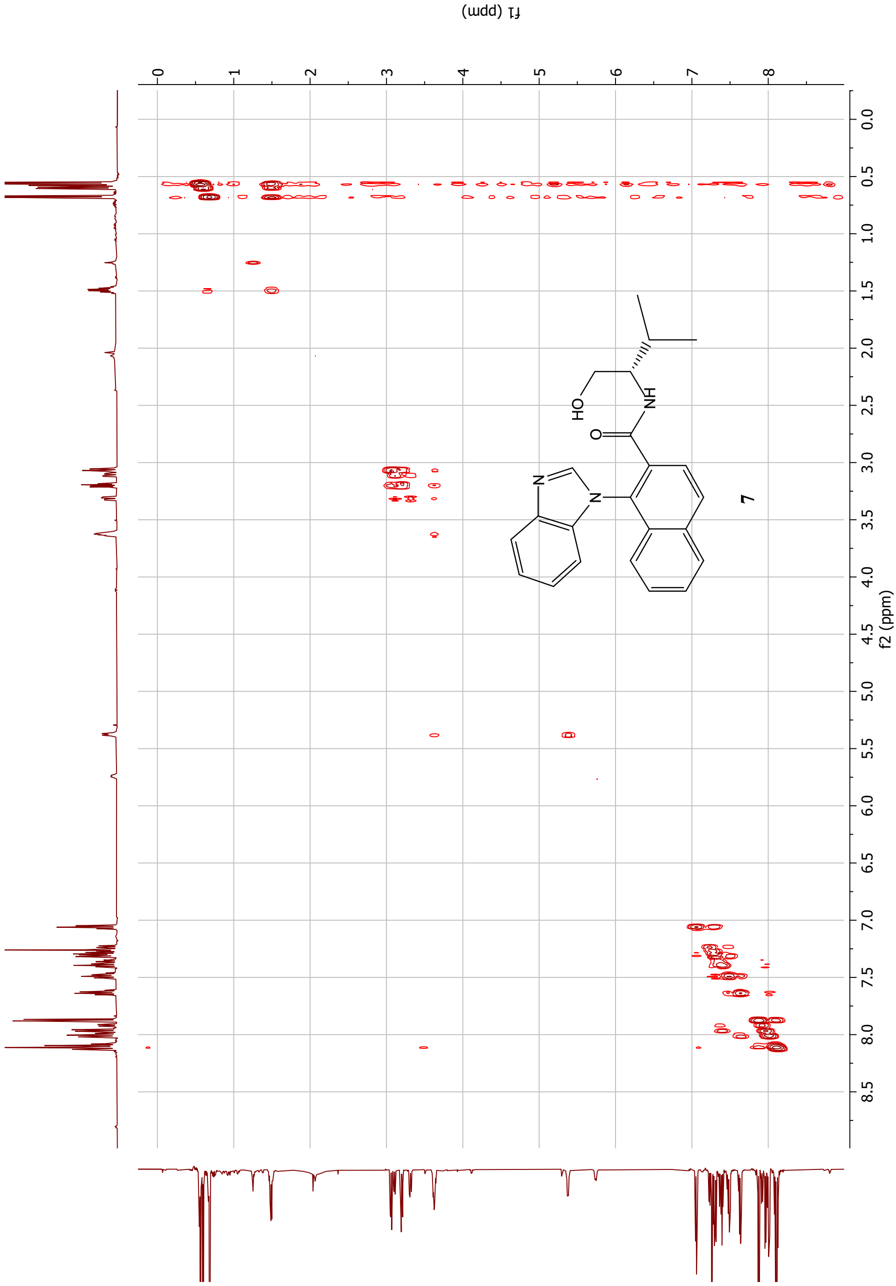

Figure F.5: COSY NMR spectrum of compound **7**

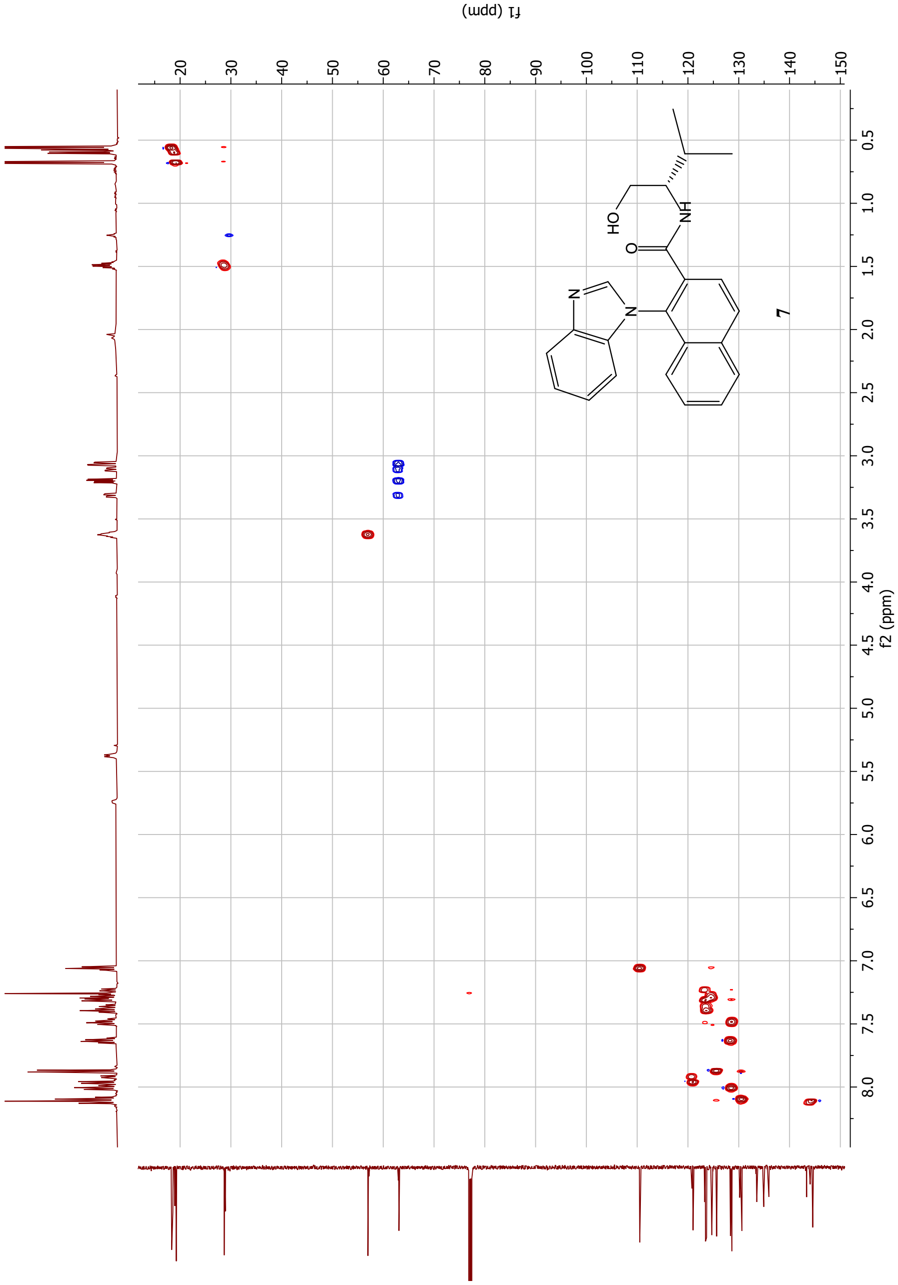

Figure F.6: HSQC NMR spectrum of compound **7**

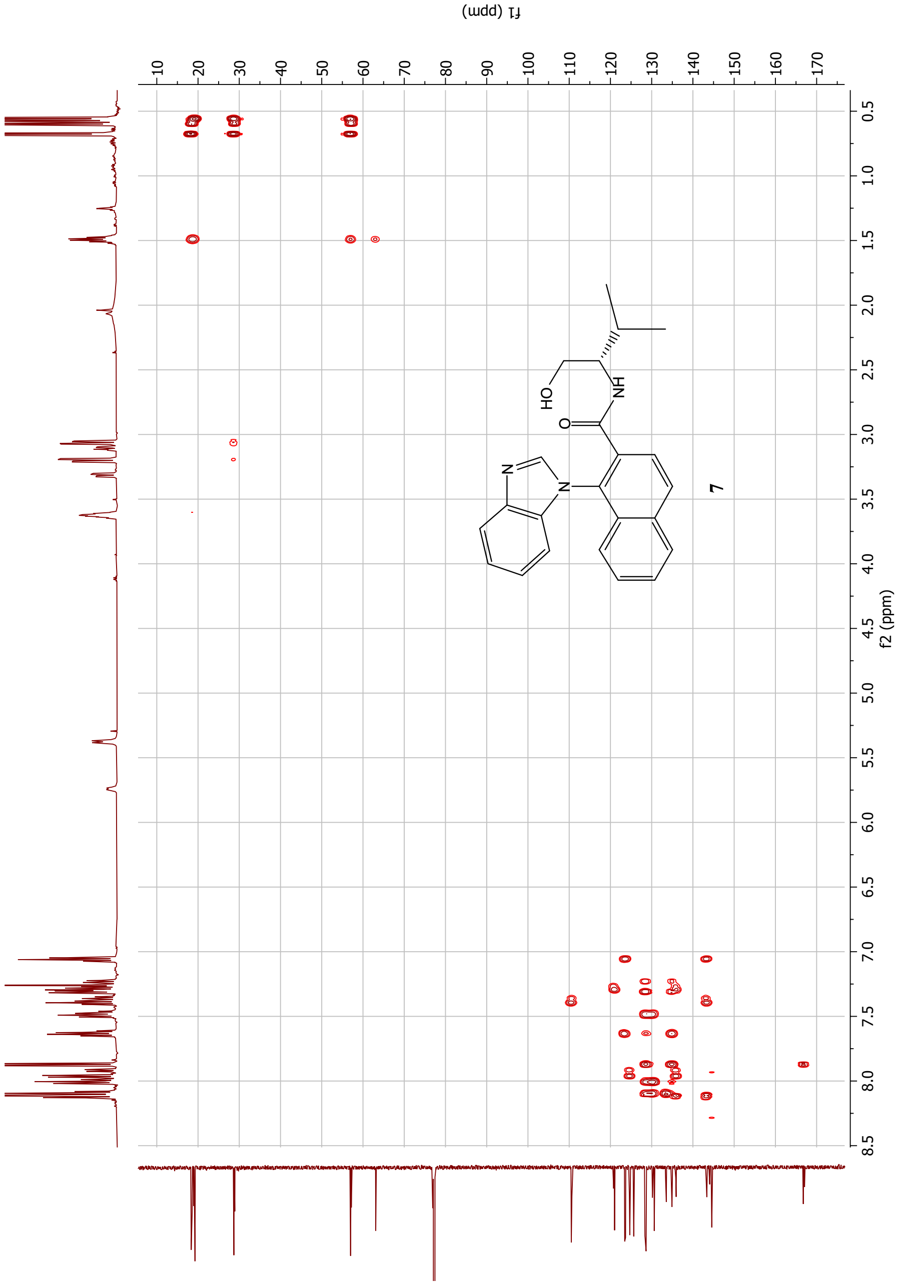

Figure F.7: HMBC NMR spectrum of compound **7**

Elemental Composition Report

Page 1

Single Mass Analysis

Tolerance = 3.0 PPM / DBE: min = -10.0, max = 50.0
Element prediction: Off
Number of isotope peaks used for i-FIT = 6

Monoisotopic Mass, Even Electron Ions
1273 formula(e) evaluated with 2 results within limits (all results (up to 1000) for each mass)
Elements Used:
C: 0-100 H: 0-100 N: 0-3 O: 0-20 S: 0-3
2021_49 156 (1.468) AM2 (Ar,35000.0,0.00,0.00); Cm (153:156)
1: TOF MS ES+

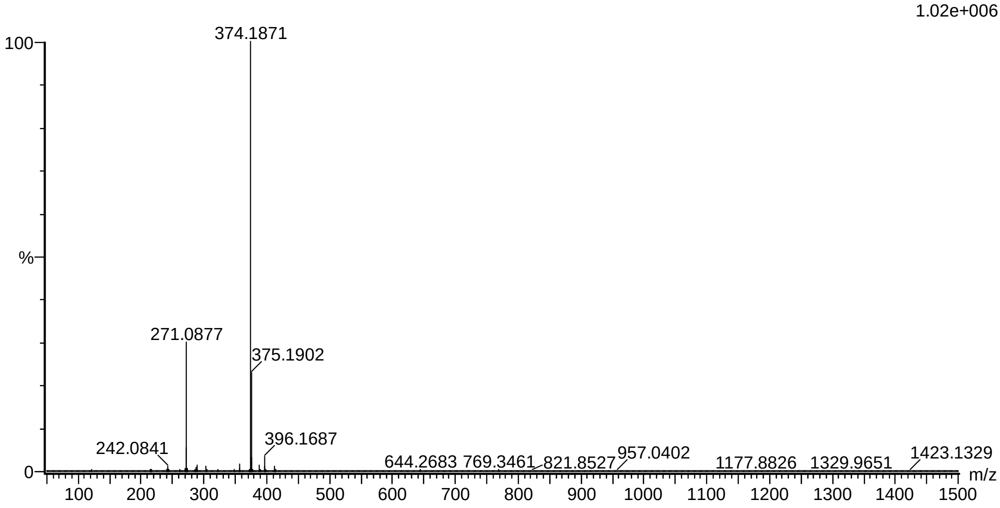

```
Minimum:                               -10.0
Maximum:                5.0     3.0    50.0

Mass        Calc. Mass  mDa     PPM    DBE    i-FIT   Norm   Conf(%) Formula

374.1871    374.1869    0.2     0.5    13.5   1805.1  0.001  99.93   C23 H24 N3 O2
            374.1874    -0.3    -0.8   -4.5   1812.3  7.229  0.07    C10 H32 N O13
```

Figure F.8: MS spectrum of compound **7**

G Spectroscopic data for compound 8a

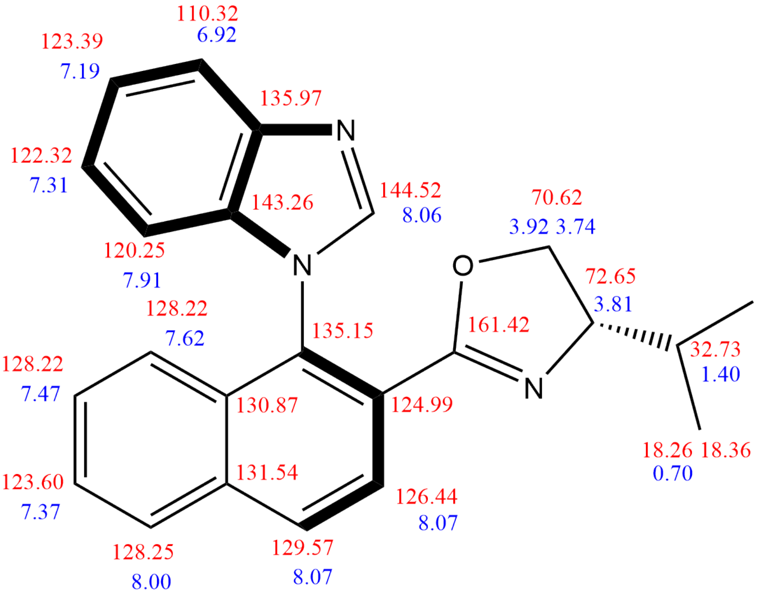

Figure G.1: Assigned ^{1}H and ^{13}C NMR signals of compound **8a**

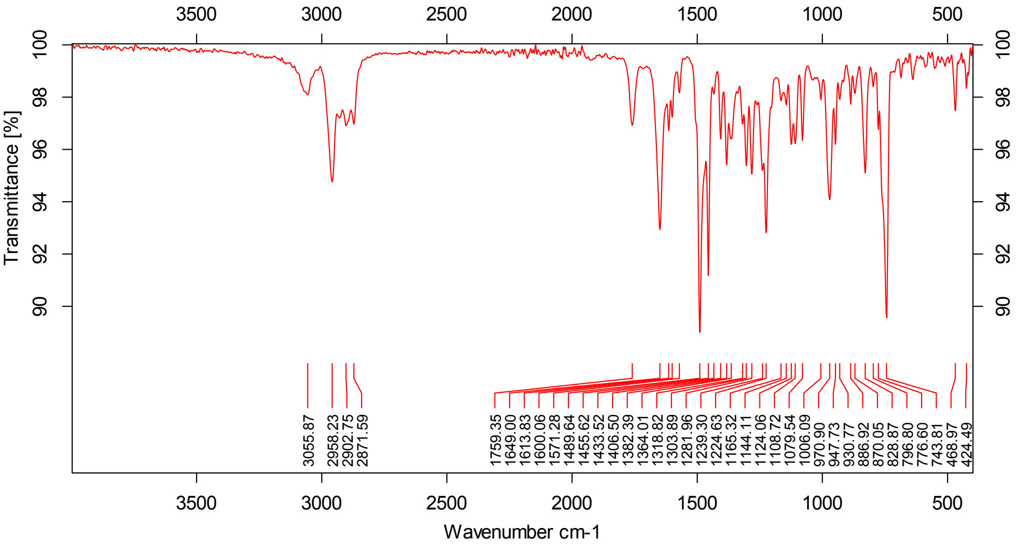

Figure G.2: IR spectrum of compound **8a**

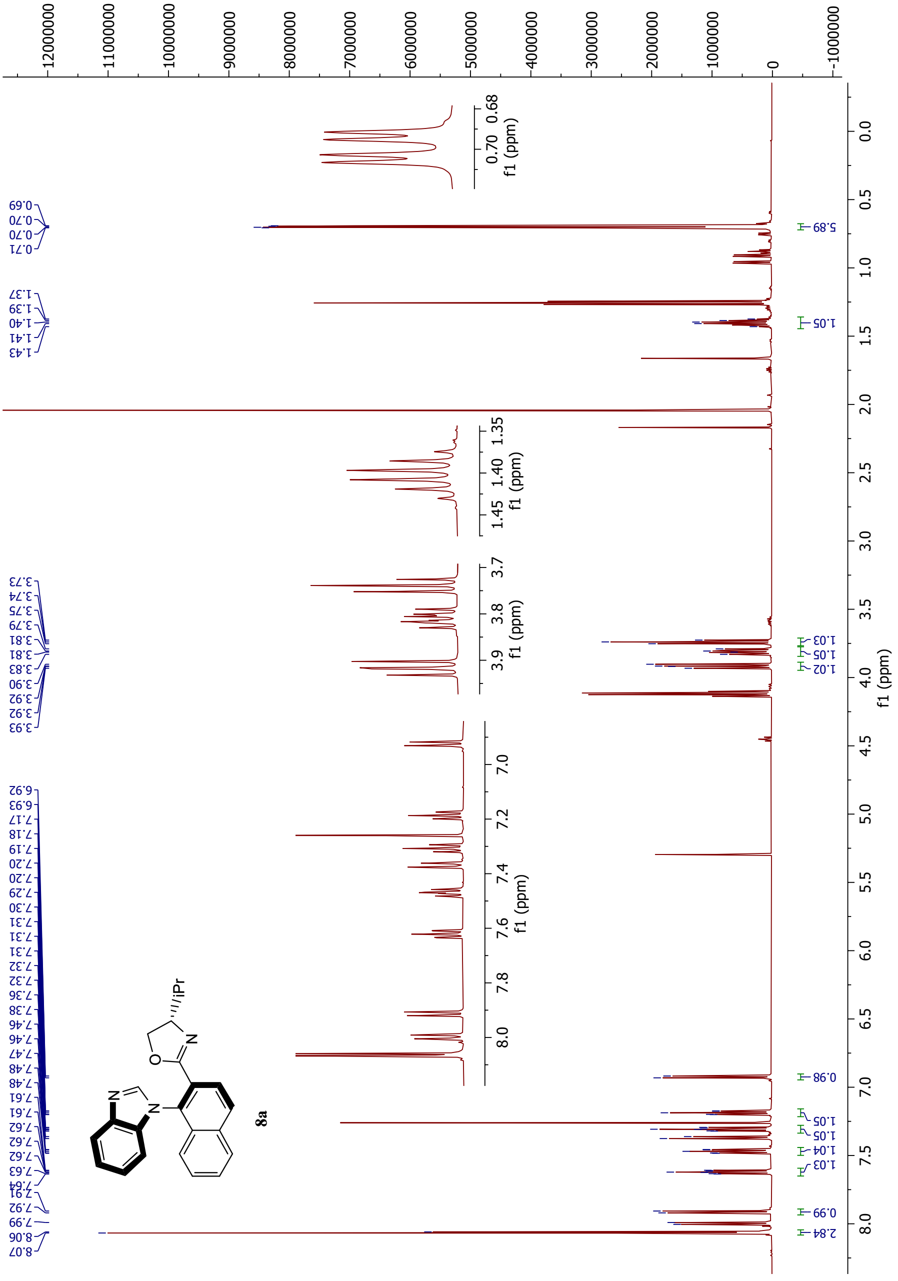

Figure G.3: ¹H NMR spectrum of compound **8a**

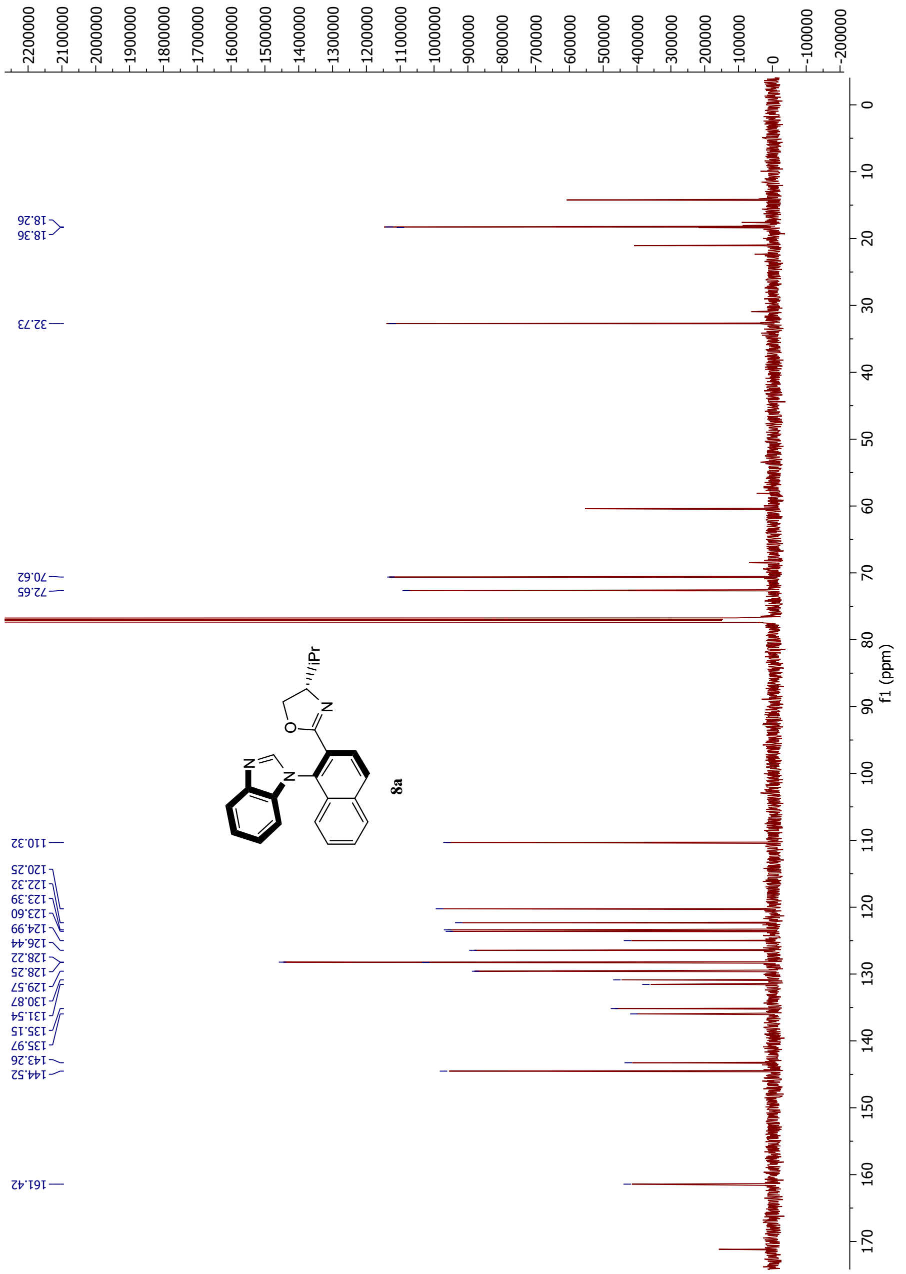

Figure G.4: ^{13}C NMR spectrum of compound **8a**

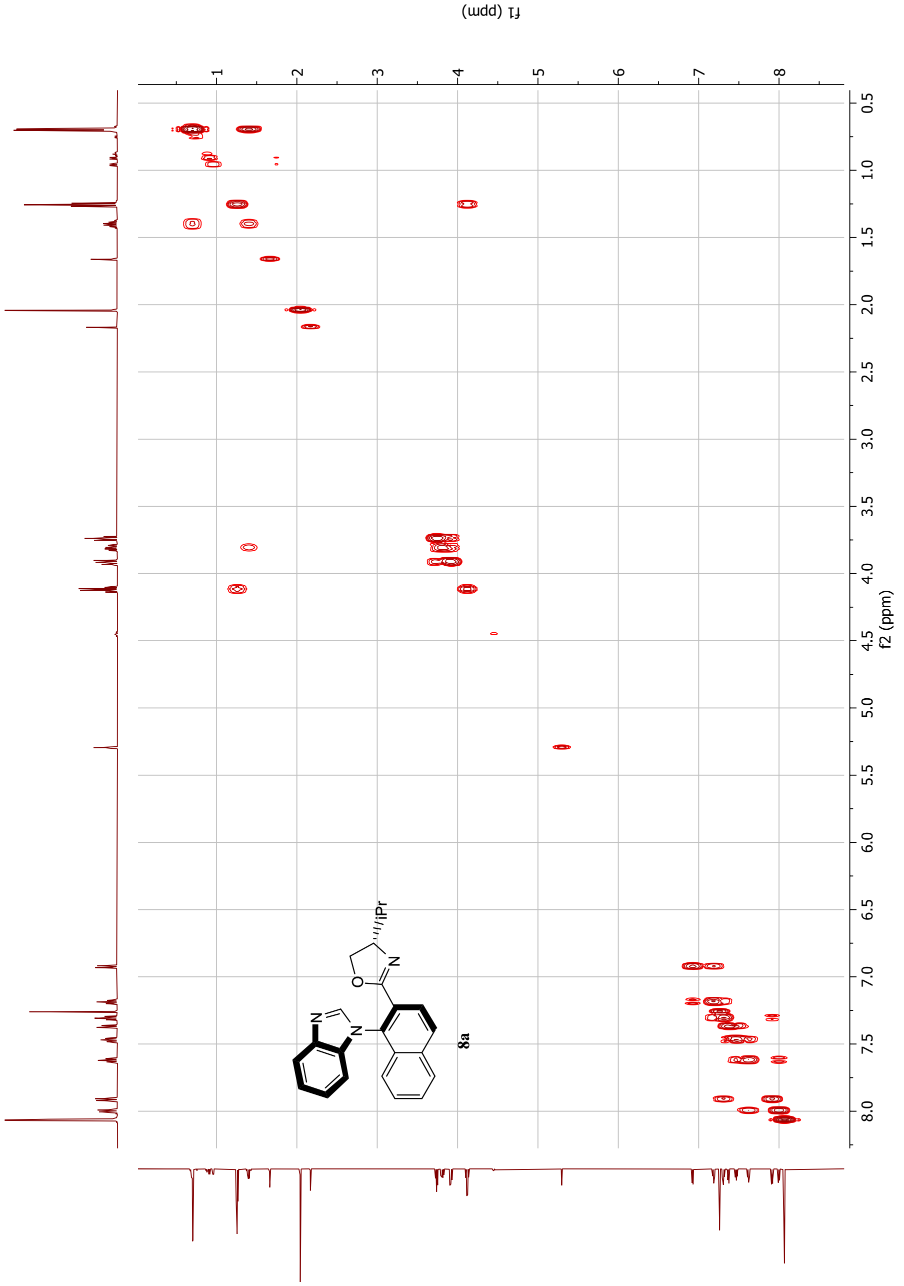

Figure G.5: COSY NMR spectrum of compound **8a**

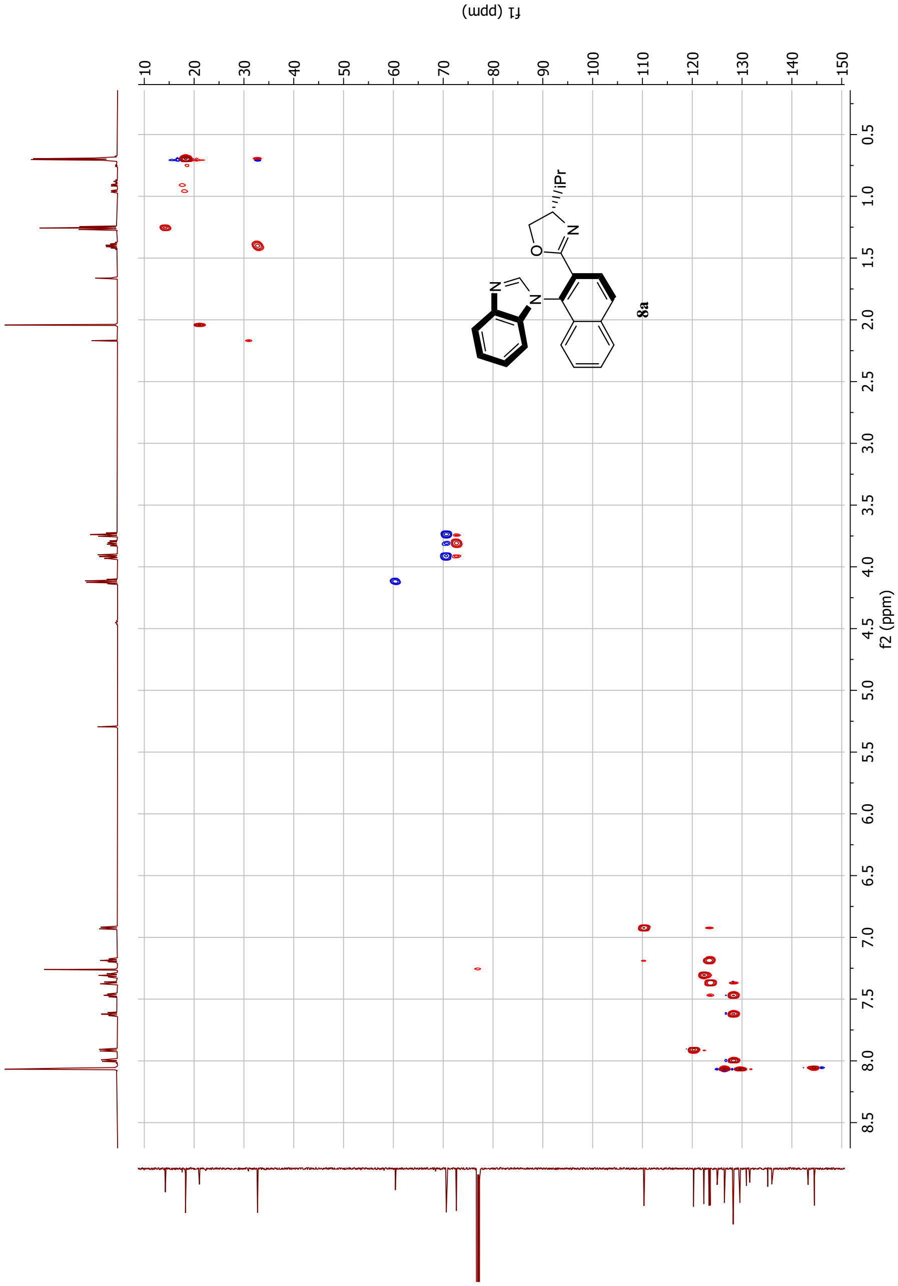

Figure G.6: HSQC NMR spectrum of compound **8a**

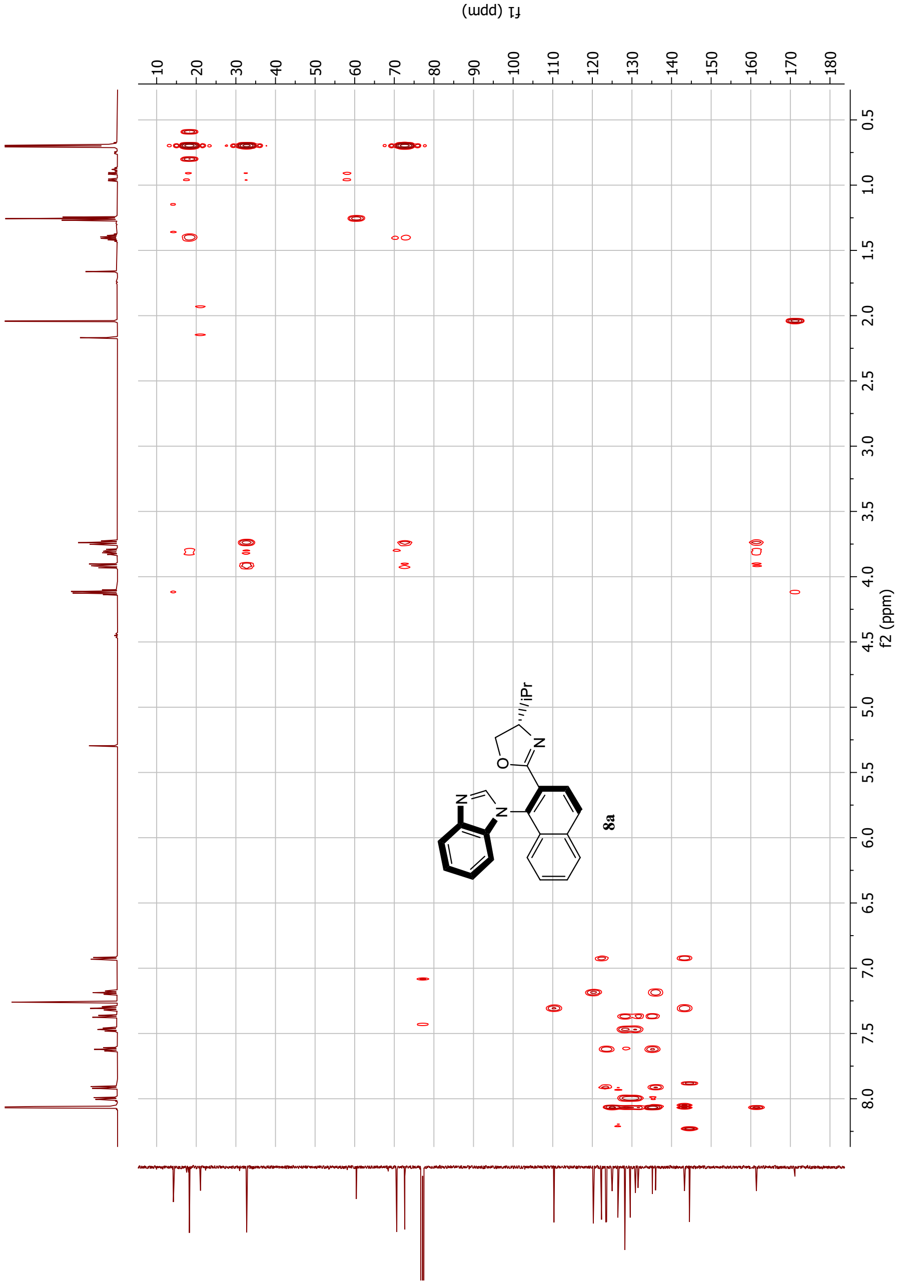

Figure G.7: HMBC NMR spectrum of compound **8a**

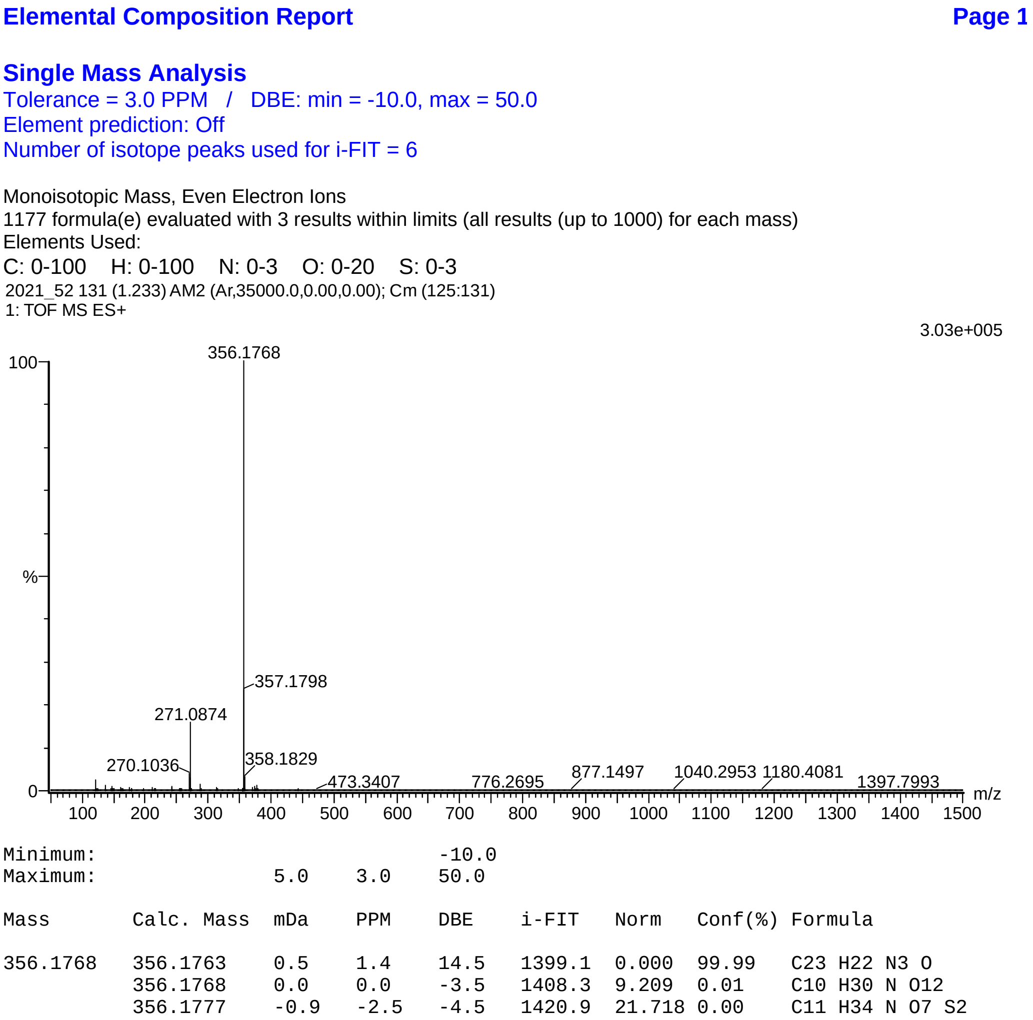

Elemental Composition Report **Page 1**

Single Mass Analysis
Tolerance = 3.0 PPM / DBE: min = -10.0, max = 50.0
Element prediction: Off
Number of isotope peaks used for i-FIT = 6

Monoisotopic Mass, Even Electron Ions
1177 formula(e) evaluated with 3 results within limits (all results (up to 1000) for each mass)
Elements Used:
C: 0-100 H: 0-100 N: 0-3 O: 0-20 S: 0-3
2021_52 131 (1.233) AM2 (Ar,35000.0,0.00,0.00); Cm (125:131)
1: TOF MS ES+

```
Minimum:                         -10.0
Maximum:              5.0   3.0   50.0

Mass      Calc. Mass  mDa   PPM   DBE   i-FIT  Norm   Conf(%) Formula

356.1768  356.1763    0.5   1.4   14.5  1399.1 0.000  99.99   C23 H22 N3 O
          356.1768    0.0   0.0   -3.5  1408.3 9.209  0.01    C10 H30 N O12
          356.1777    -0.9  -2.5  -4.5  1420.9 21.718 0.00    C11 H34 N O7 S2
```

Figure G.8: MS spectrum of compound **8a**

H Spectroscopic data for compound 8b

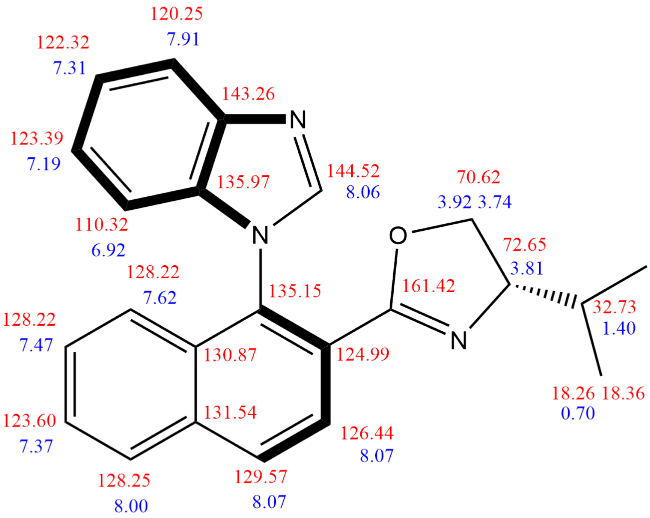

Figure H.1: Assigned ^{1}H and ^{13}C NMR signals of compound **8b**

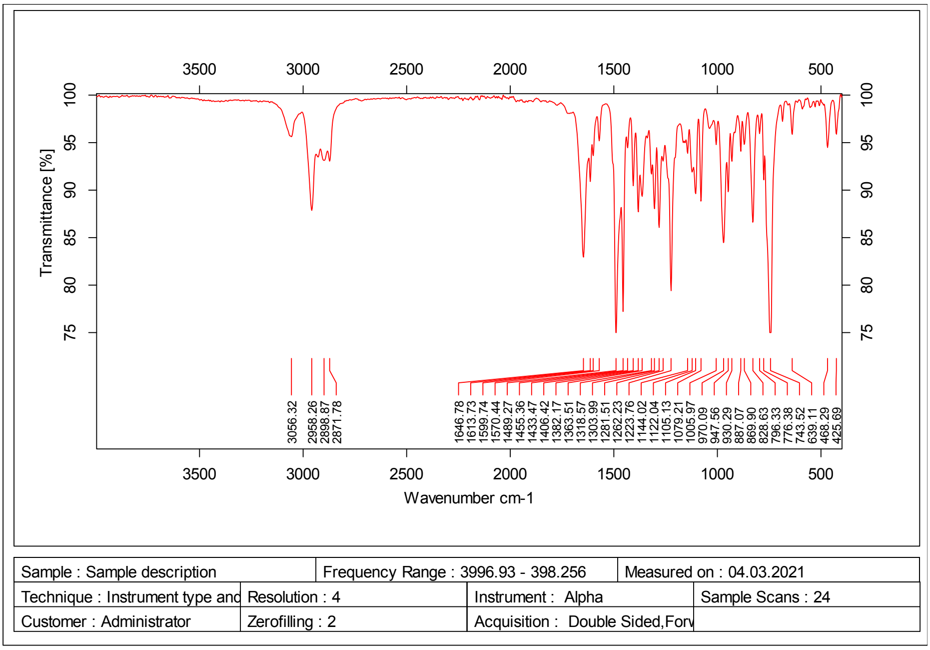

Sample : Sample description
Frequency Range : 3996.93 - 398.256
Measured on : 04.03.2021
Technique : Instrument type and
Resolution : 4
Instrument : Alpha
Sample Scans : 24
Customer : Administrator
Zerofilling : 2
Acquisition : Double Sided,Forv

Figure H.2: IR spectrum of compound **8b**

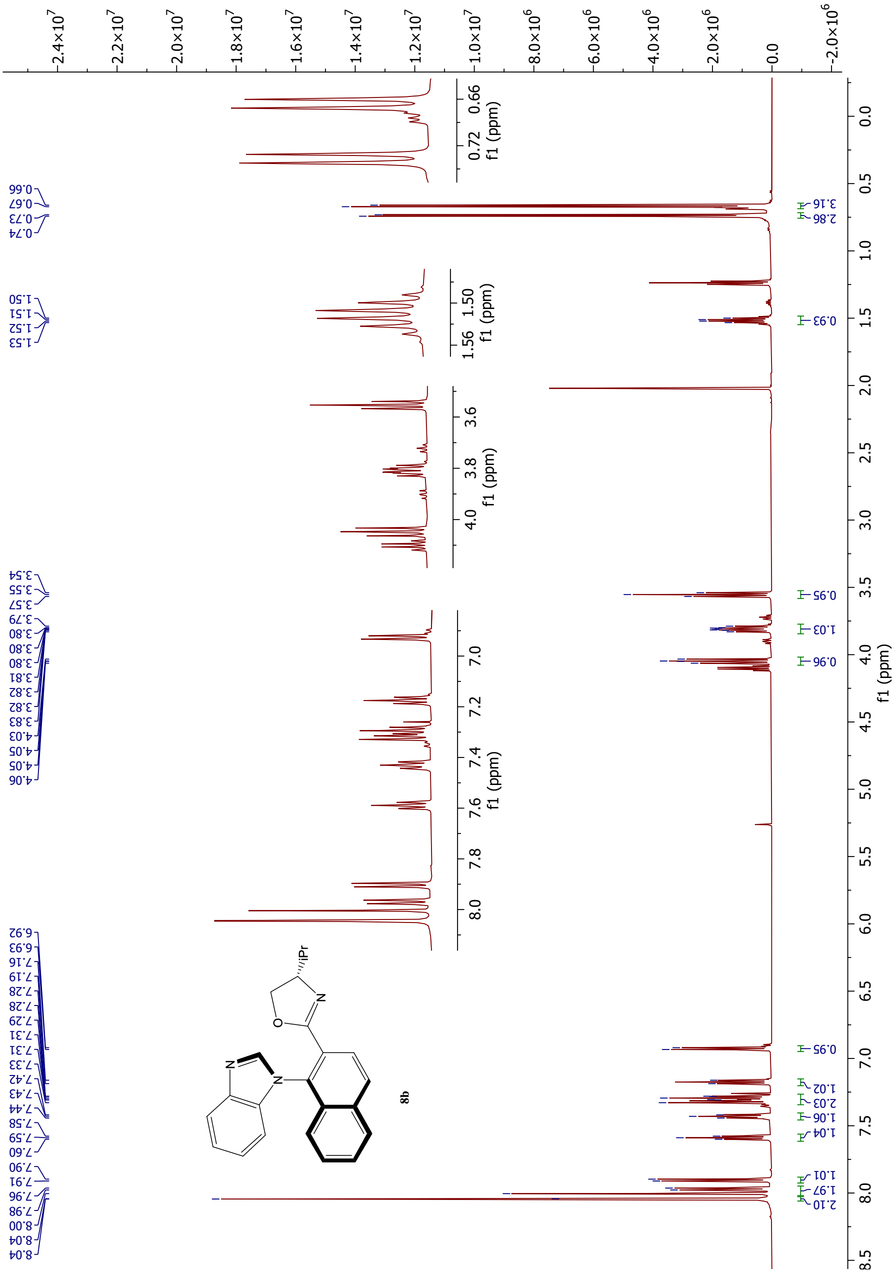

Figure H.3: ^{1}H NMR spectrum of compound **8b**

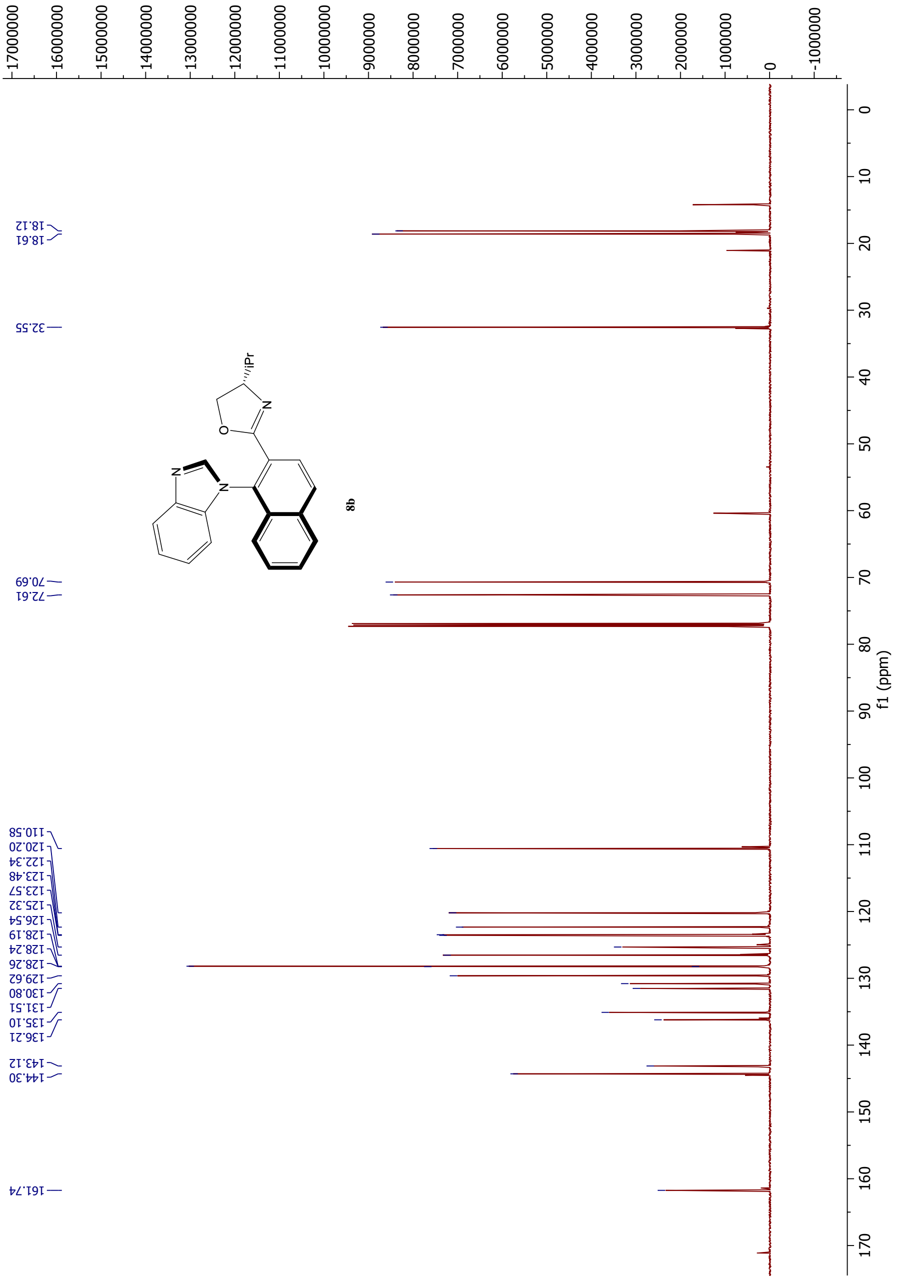

Figure H.4: ^{13}C NMR spectrum of compound **8b**

Figure H.5: COSY NMR spectrum of compound **8b**

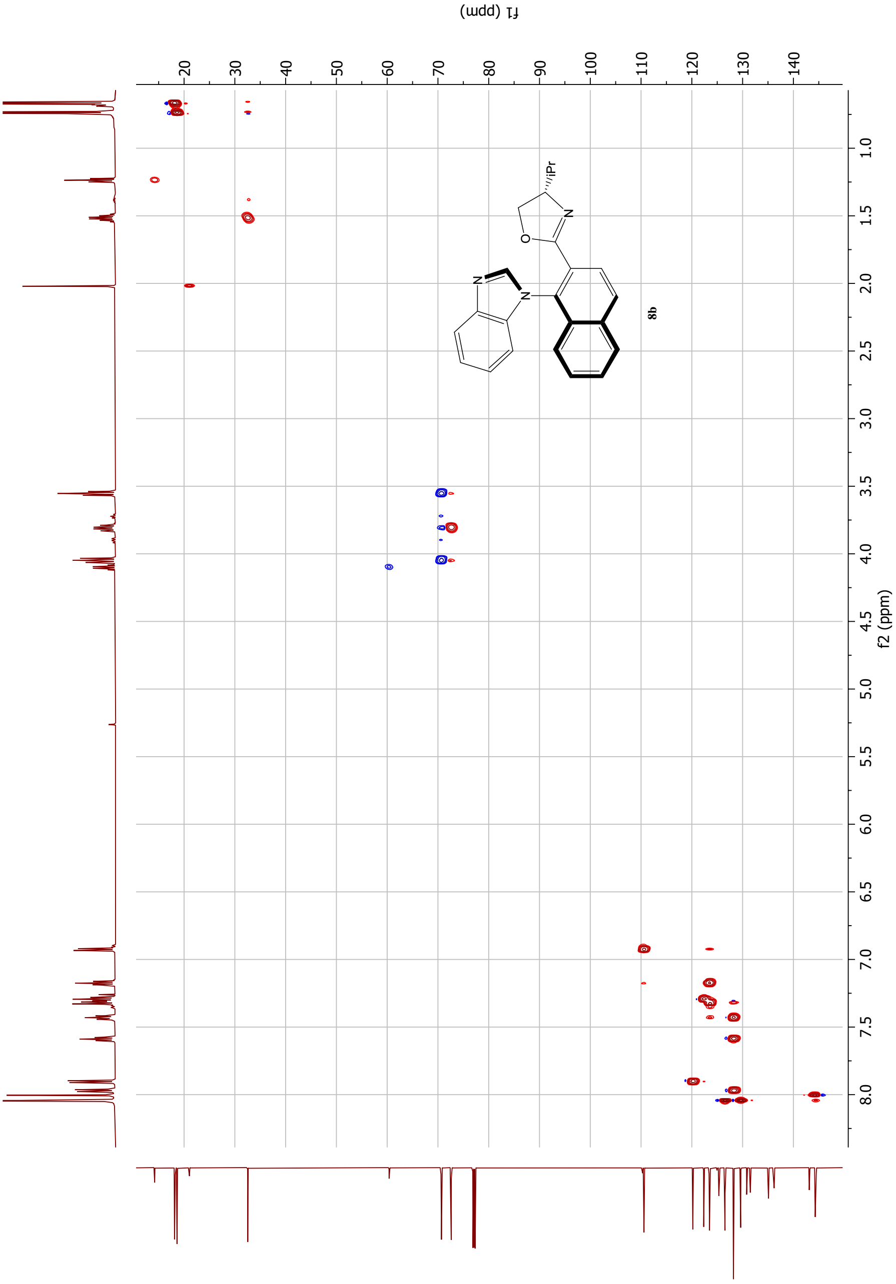

Figure H.6: HSQC NMR spectrum of compound **8b**

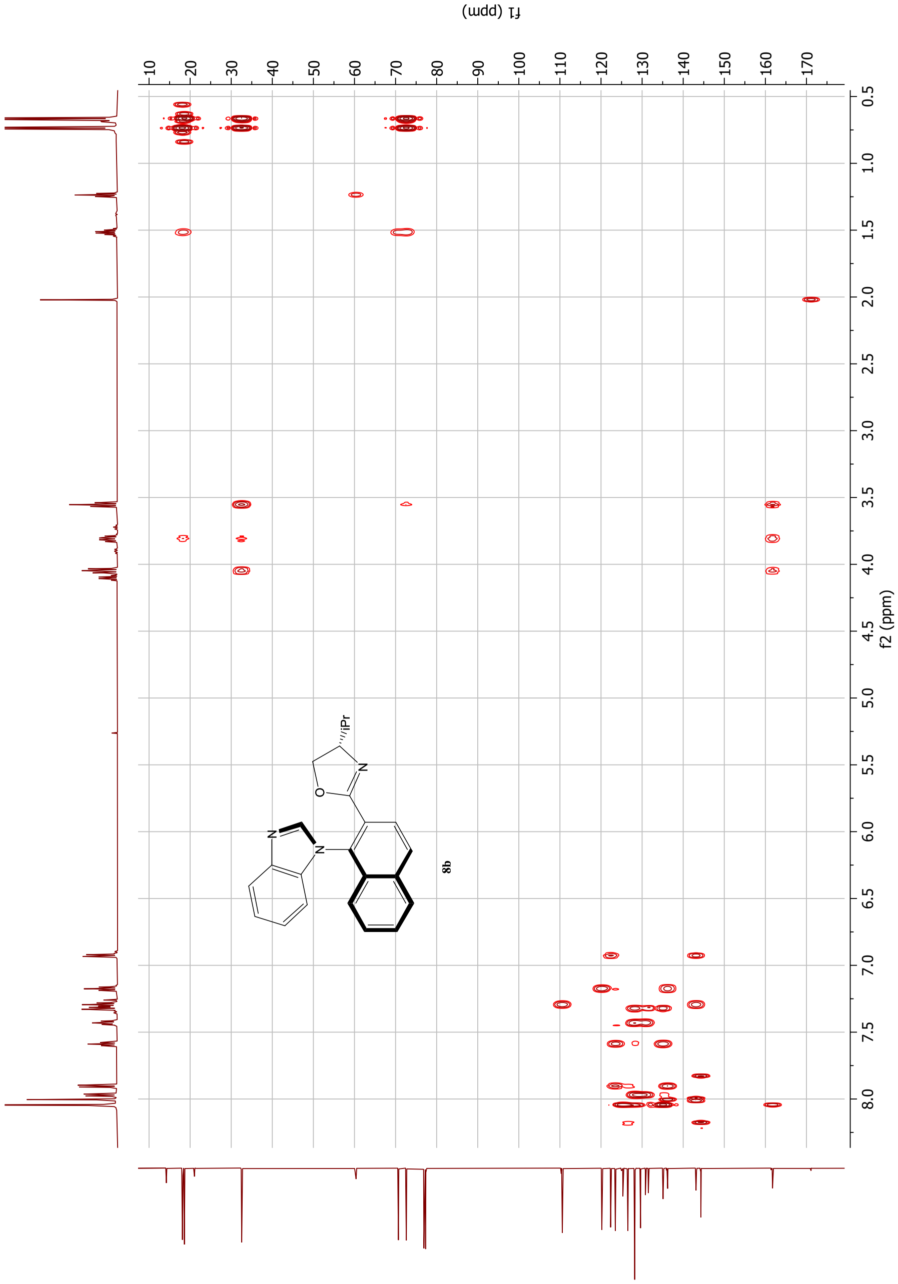

Figure H.7: HMBC NMR spectrum of compound **8b**

I Spectroscopic data for compound 9a

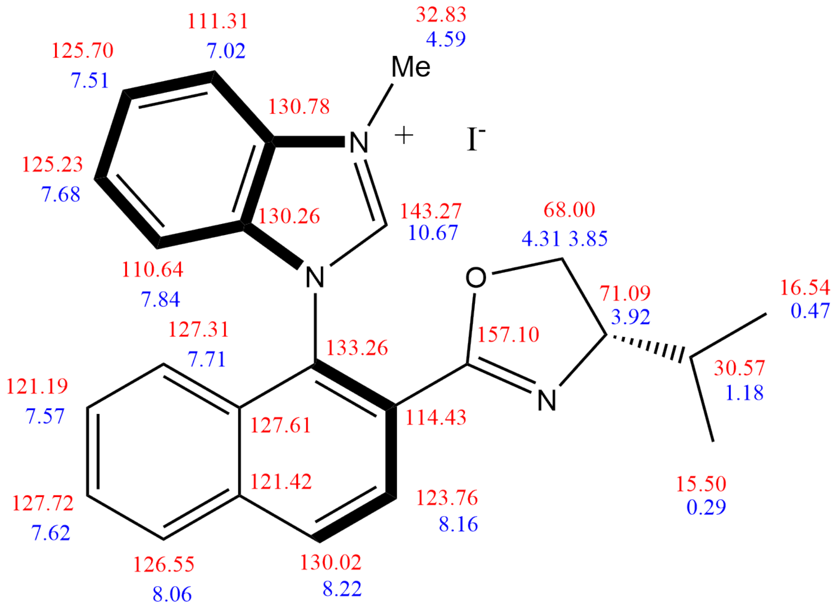

Figure I.1: Assigned ^{1}H and ^{13}C NMR signals of compound **9a**

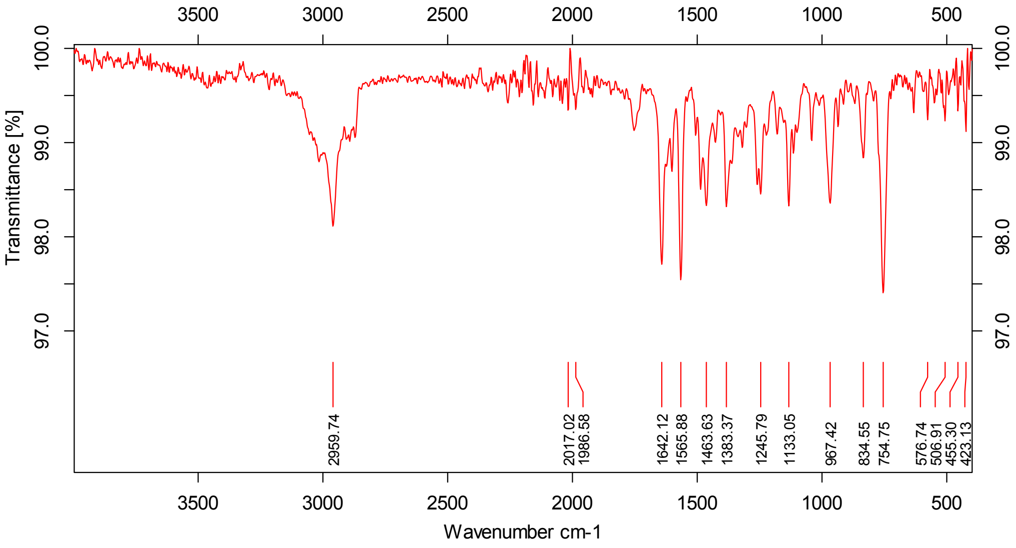

Figure I.2: IR spectrum of compound **9a**

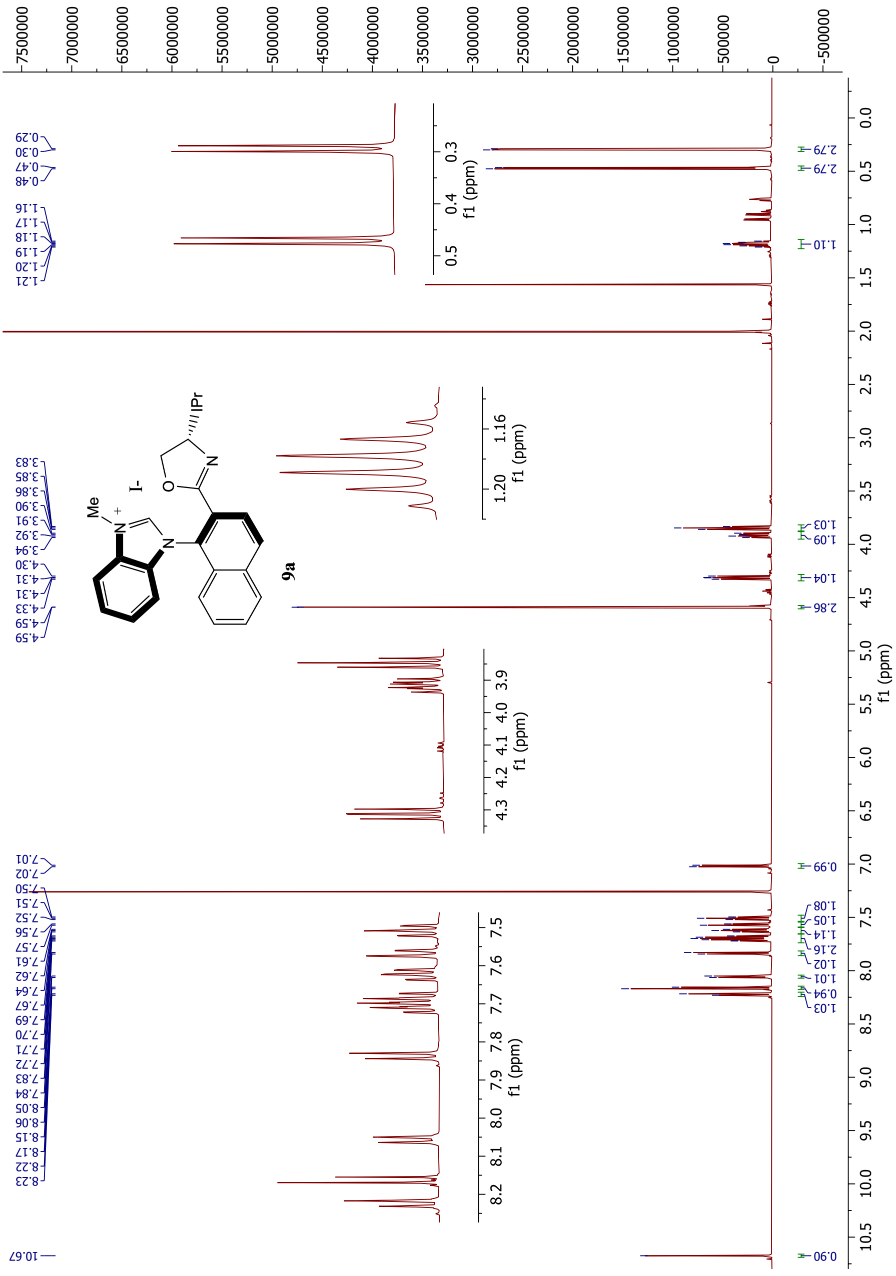

Figure I.3: ^{1}H NMR spectrum of compound **9a**

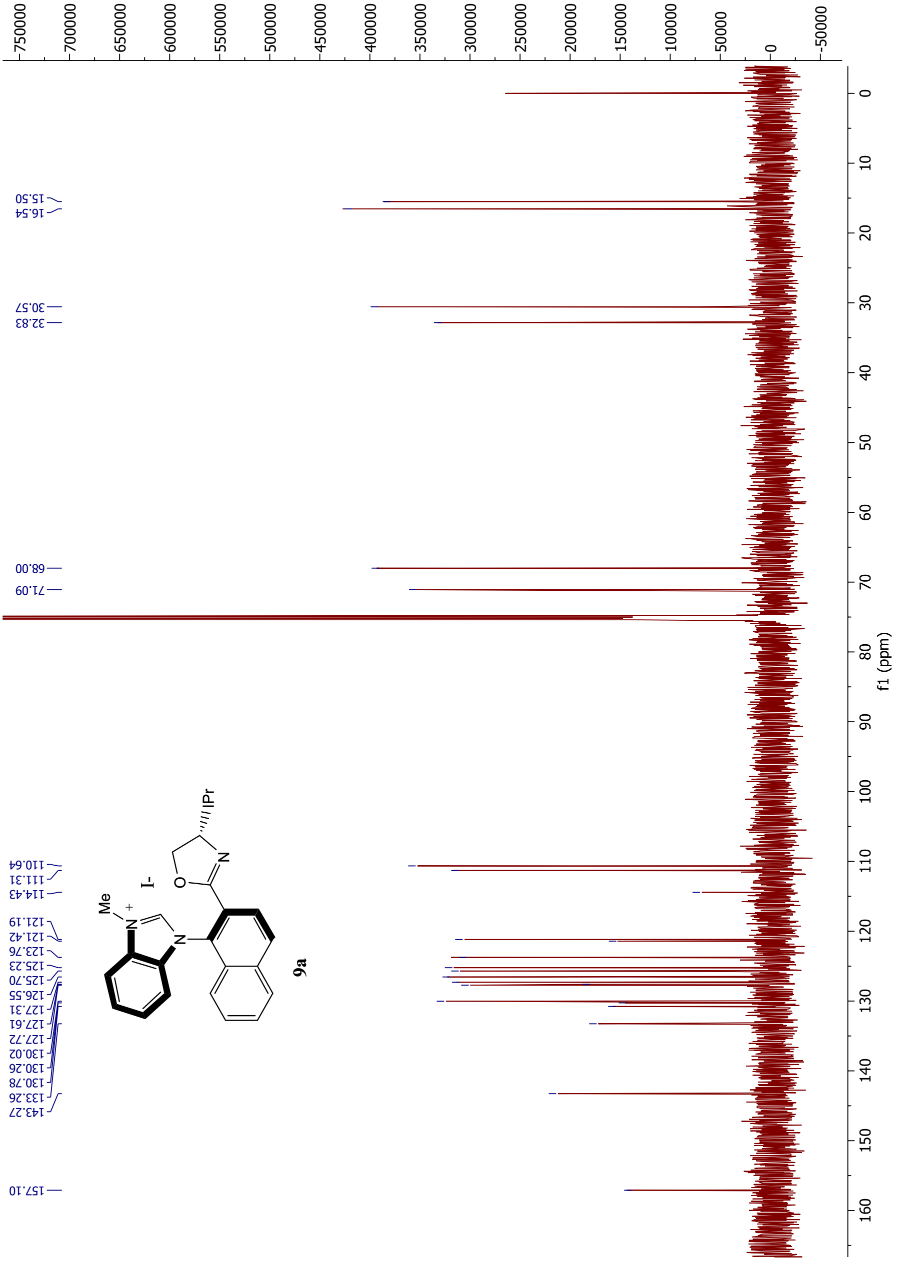

Figure I.4: ^{13}C NMR spectrum of compound **9a**

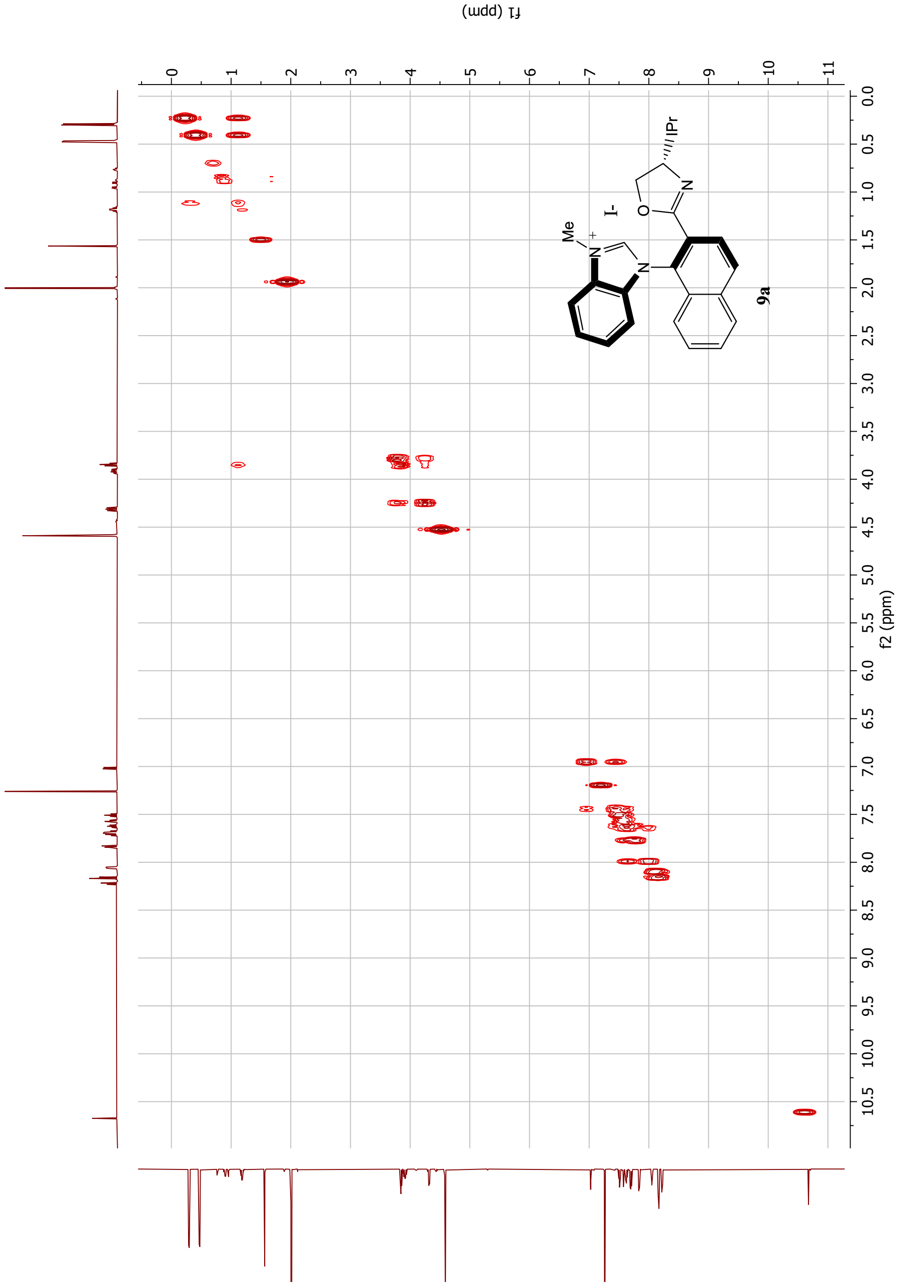

Figure I.5: COSY NMR spectrum of compound **9a**

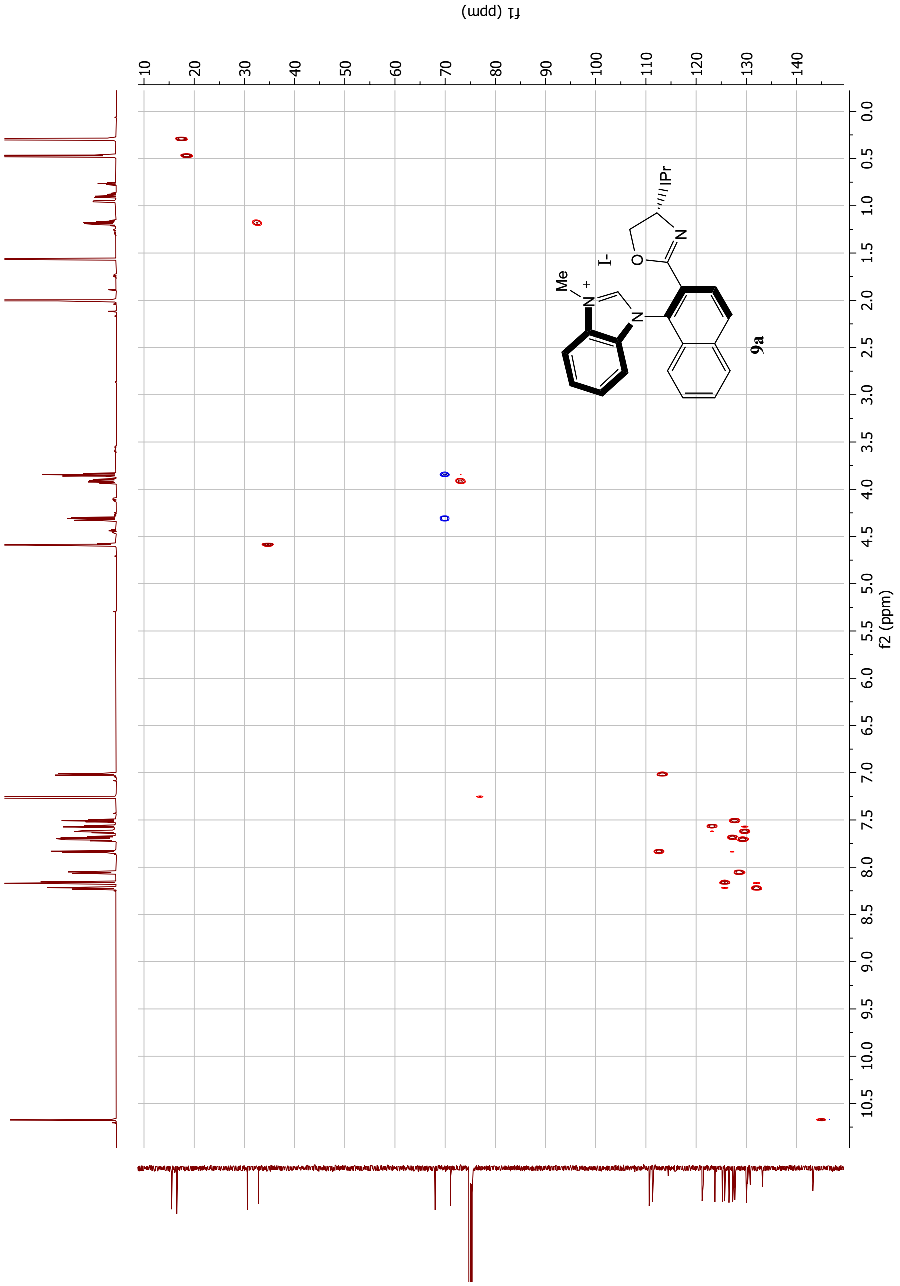

Figure I.6: HSQC NMR spectrum of compound **9a**

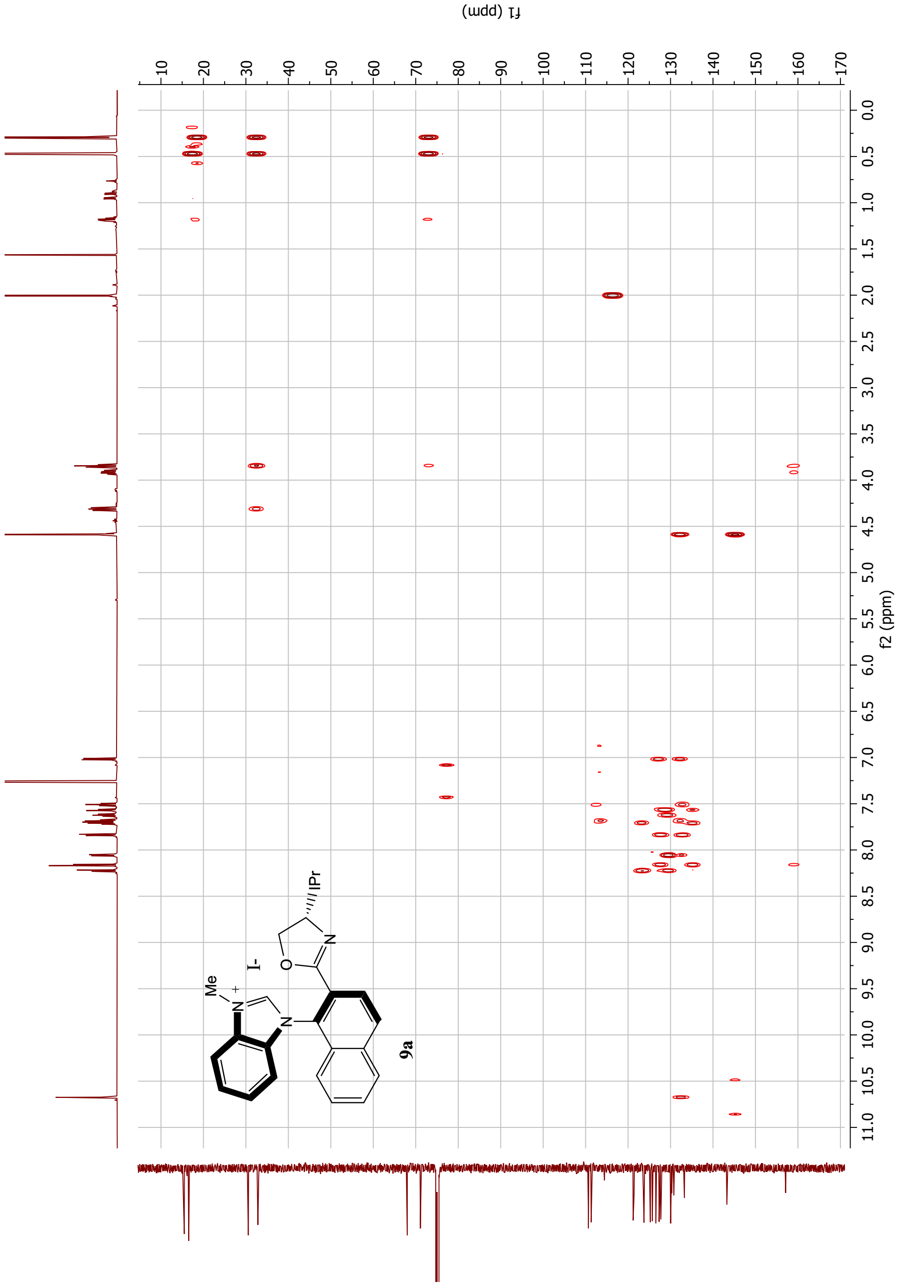

Figure I.7: HMBC NMR spectrum of compound **9a**

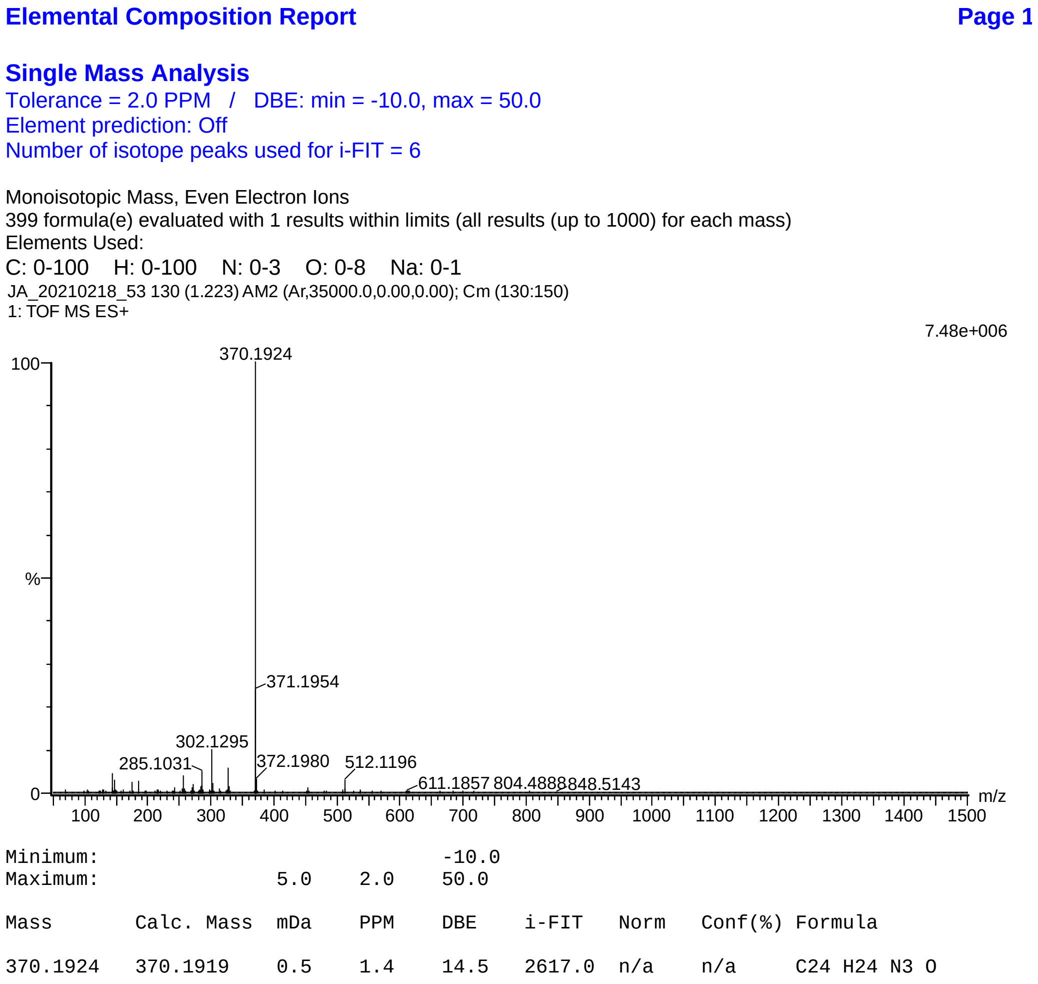

Elemental Composition Report

Page 1

Single Mass Analysis

Tolerance = 2.0 PPM / DBE: min = -10.0, max = 50.0
Element prediction: Off
Number of isotope peaks used for i-FIT = 6

Monoisotopic Mass, Even Electron Ions
399 formula(e) evaluated with 1 results within limits (all results (up to 1000) for each mass)
Elements Used:
C: 0-100 H: 0-100 N: 0-3 O: 0-8 Na: 0-1
JA_20210218_53 130 (1.223) AM2 (Ar,35000.0,0.00,0.00); Cm (130:150)
1: TOF MS ES+

```
Minimum:                                  -10.0
Maximum:                 5.0      2.0     50.0

Mass       Calc. Mass    mDa      PPM     DBE      i-FIT    Norm     Conf(%)  Formula

370.1924   370.1919      0.5      1.4     14.5     2617.0   n/a      n/a      C24 H24 N3 O
```

Figure I.8: MS spectrum of compound **9a**

J Spectroscopic data for compound 9b

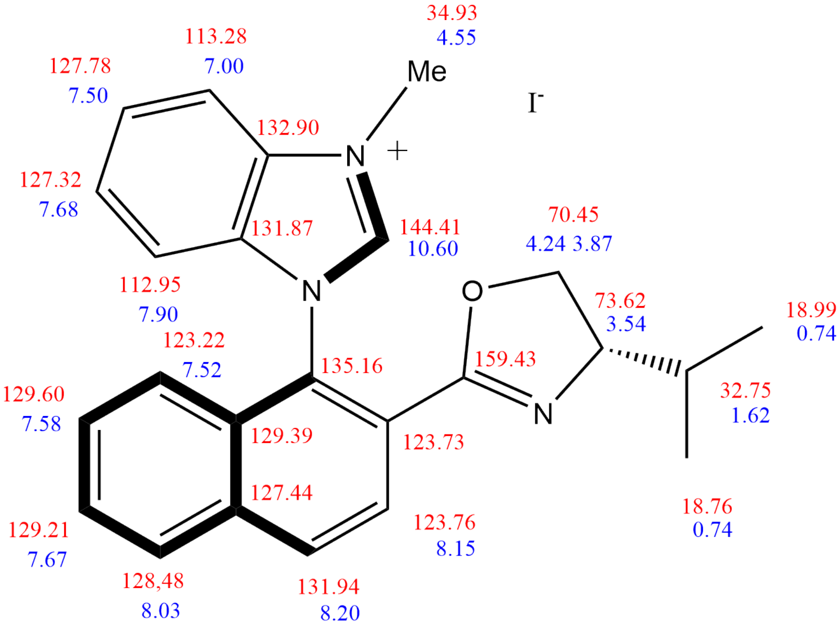

Figure J.1: Assigned ^{1}H and ^{13}C NMR signals of compound **9b**

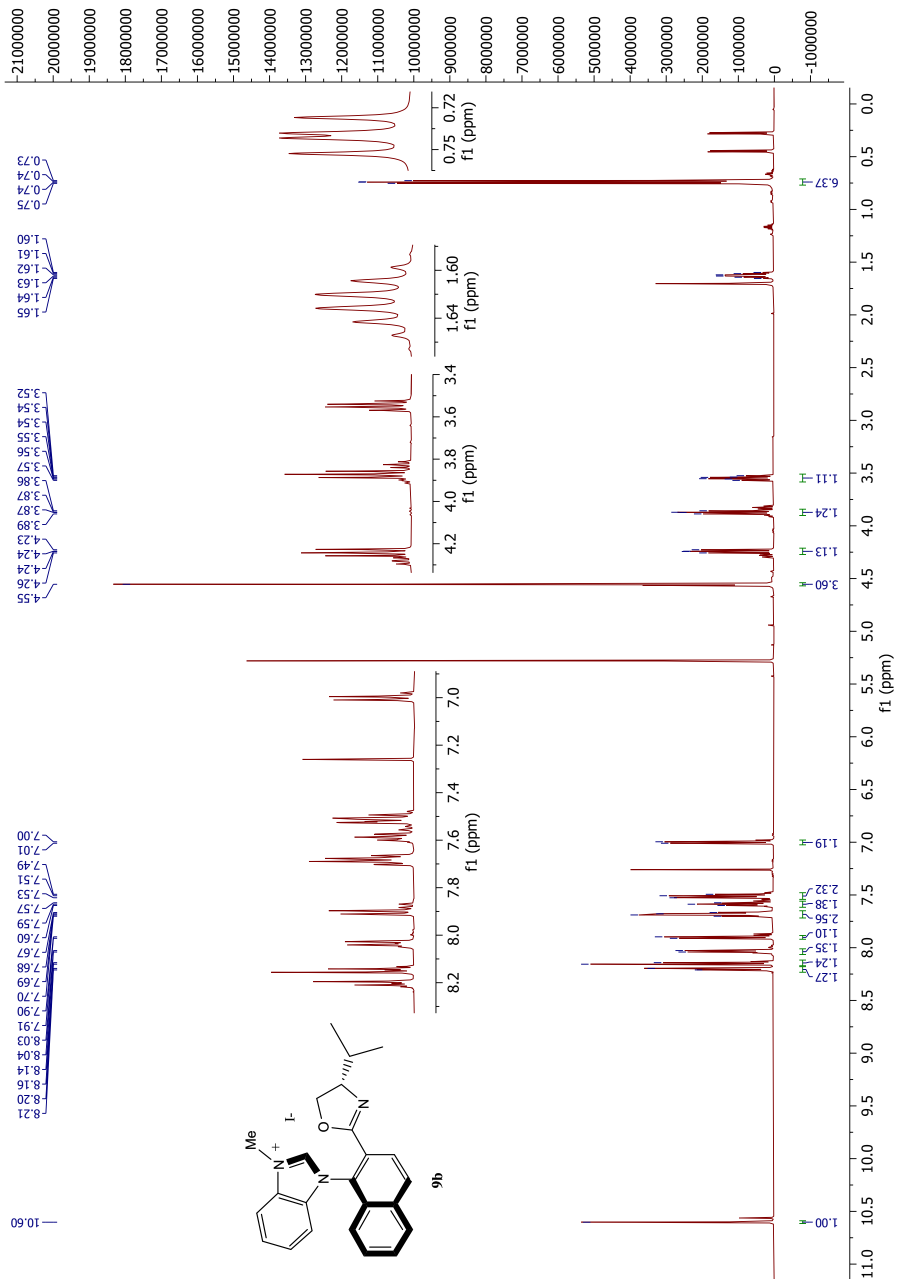

Figure J.2: ^{1}H NMR spectrum of compound **9b**

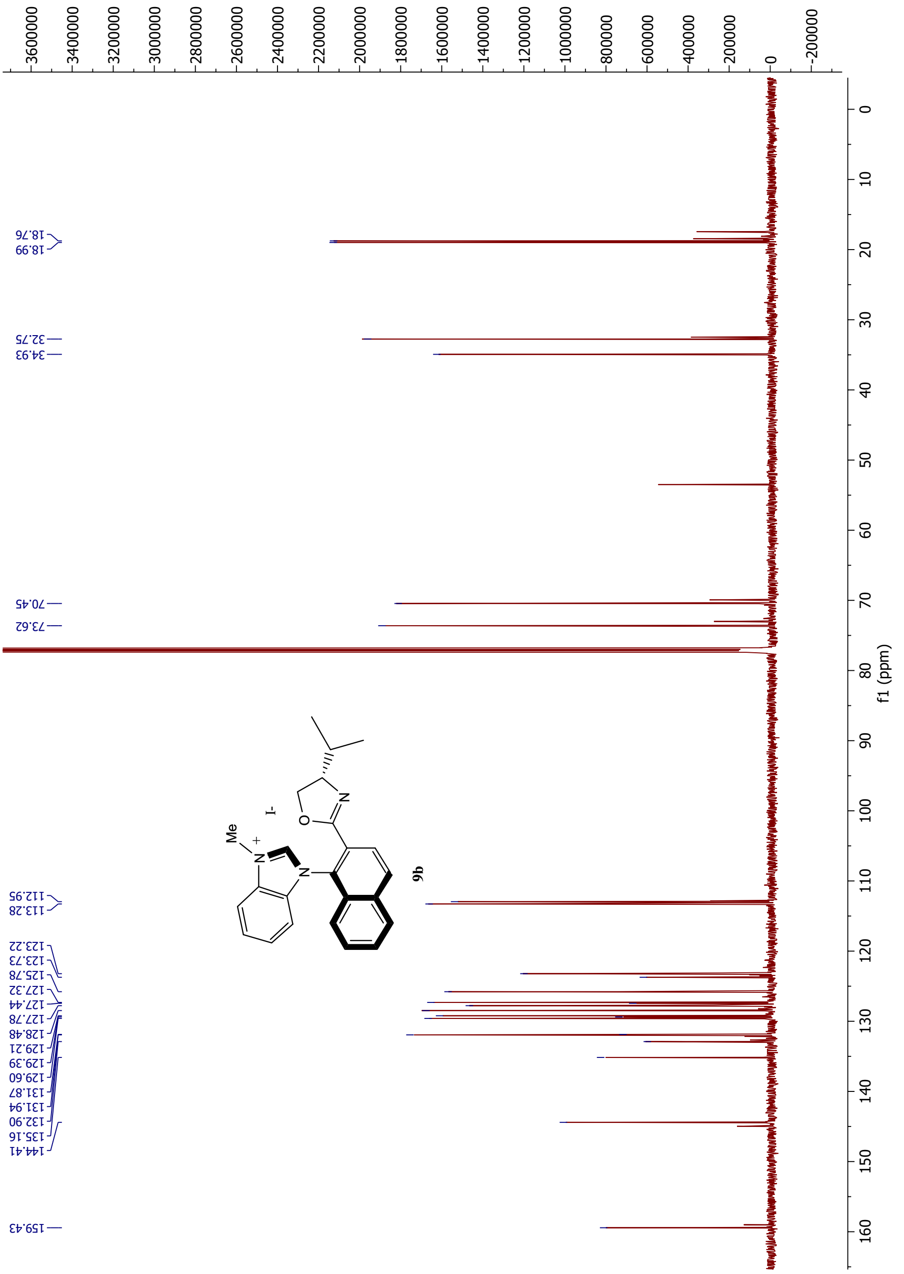

Figure J.3: ^{13}C NMR spectrum of compound **9b**

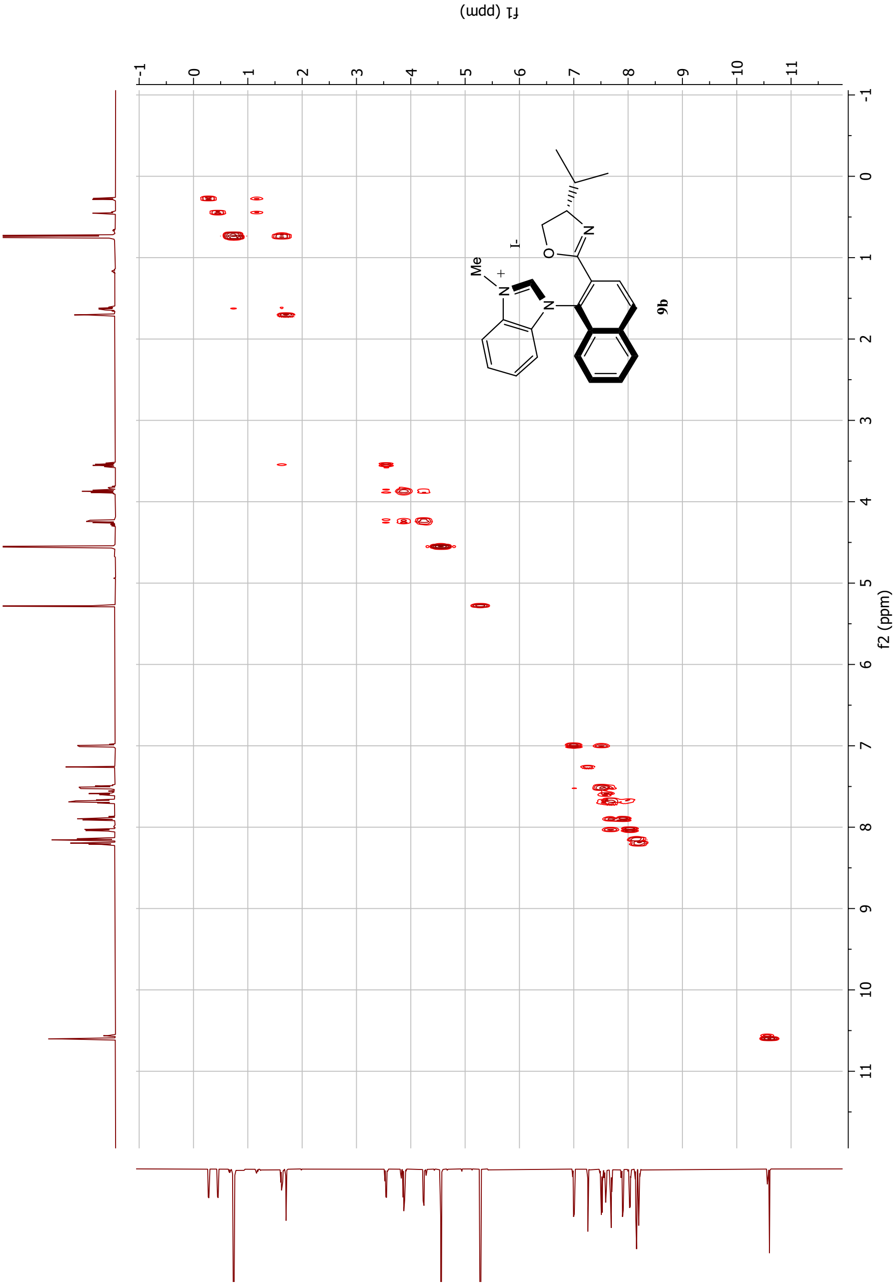

Figure J.4: COSY NMR spectrum of compound **9b**

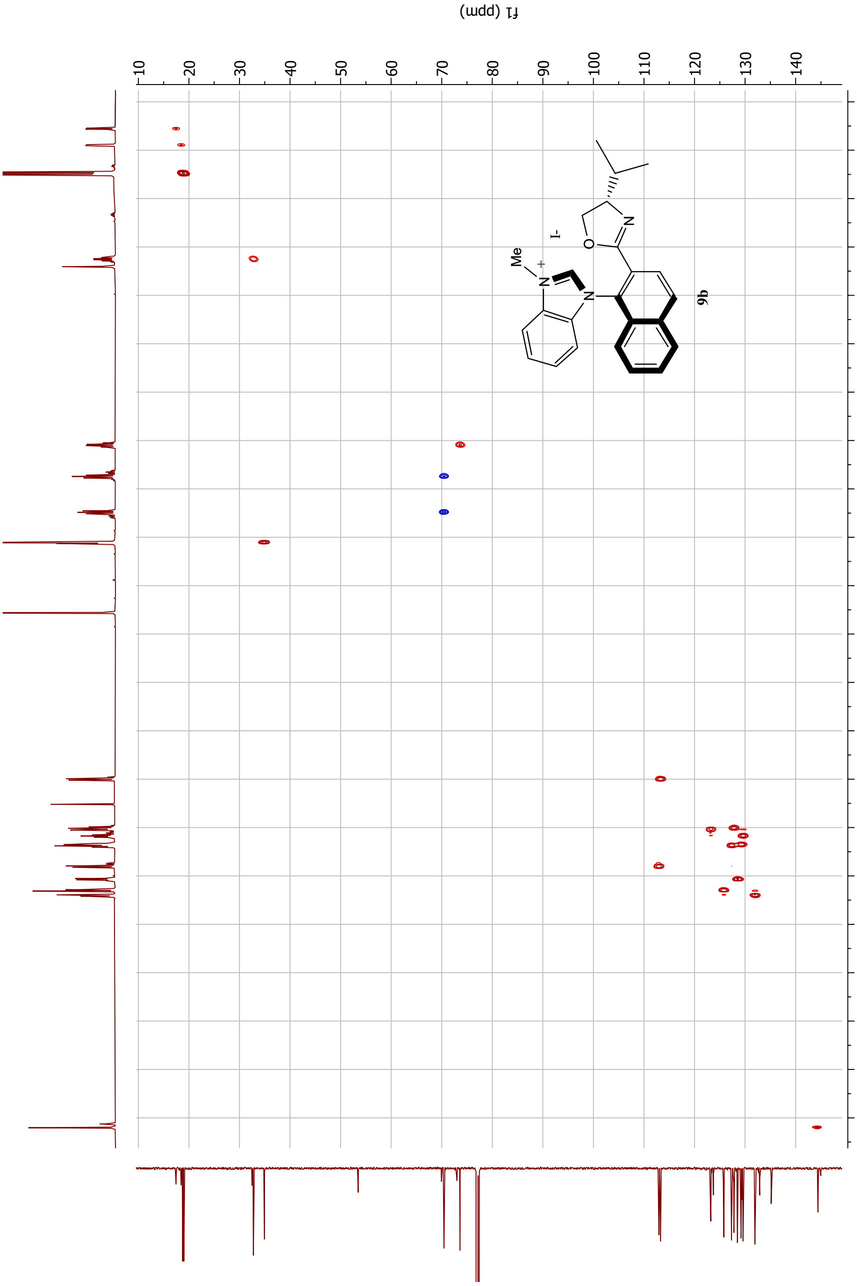

Figure J.5: HSQC NMR spectrum of compound **9b**

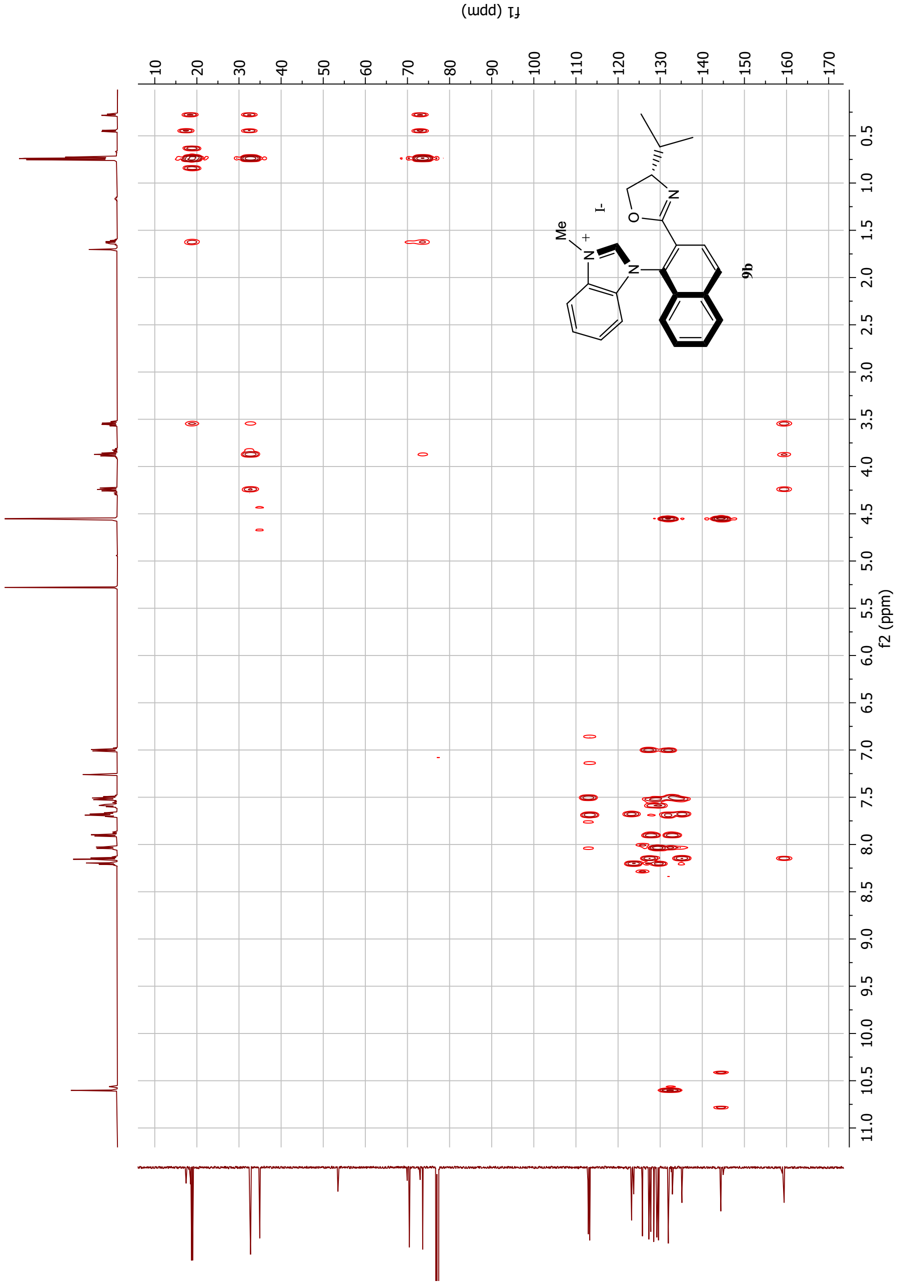

Figure J.6: HMBC NMR spectrum of compound **9b**

K Spectroscopic data for compound 10a

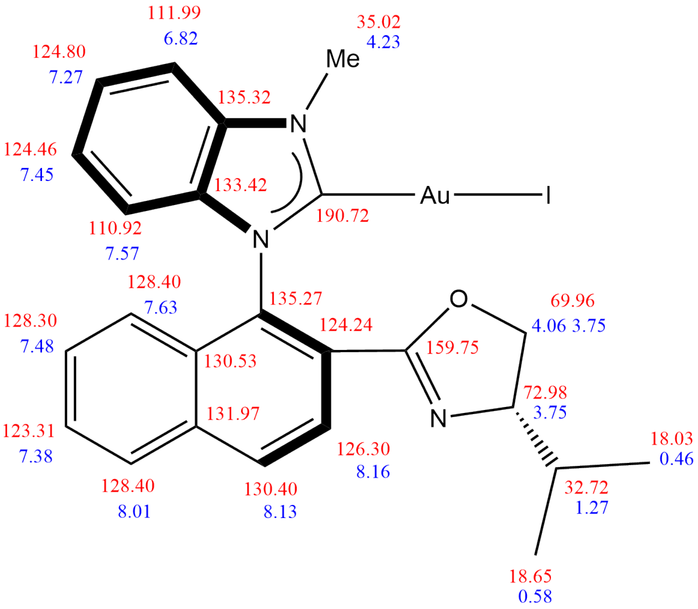

Figure K.1: Assigned ^{1}H and ^{13}C NMR signals of compound **10a**

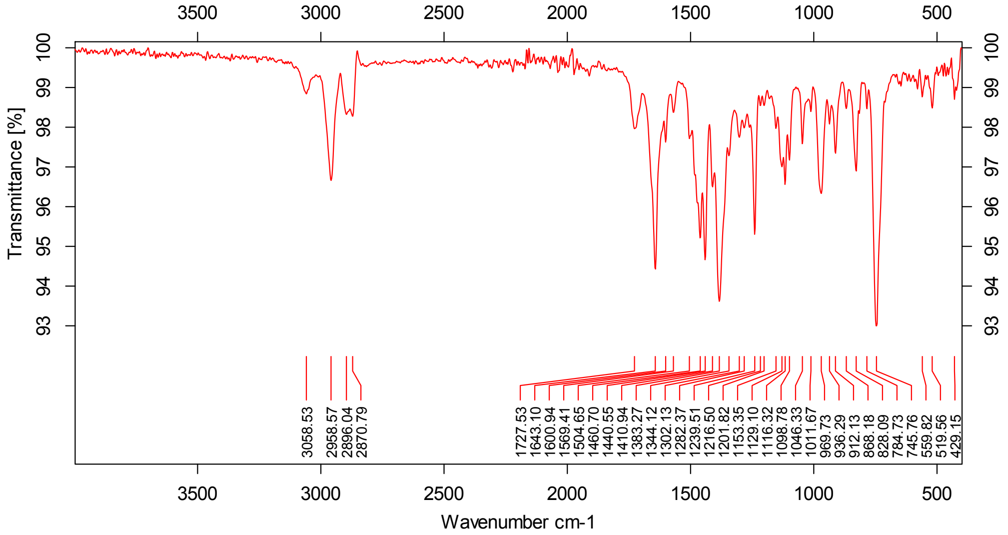

Figure K.2: IR spectrum of compound **10a**

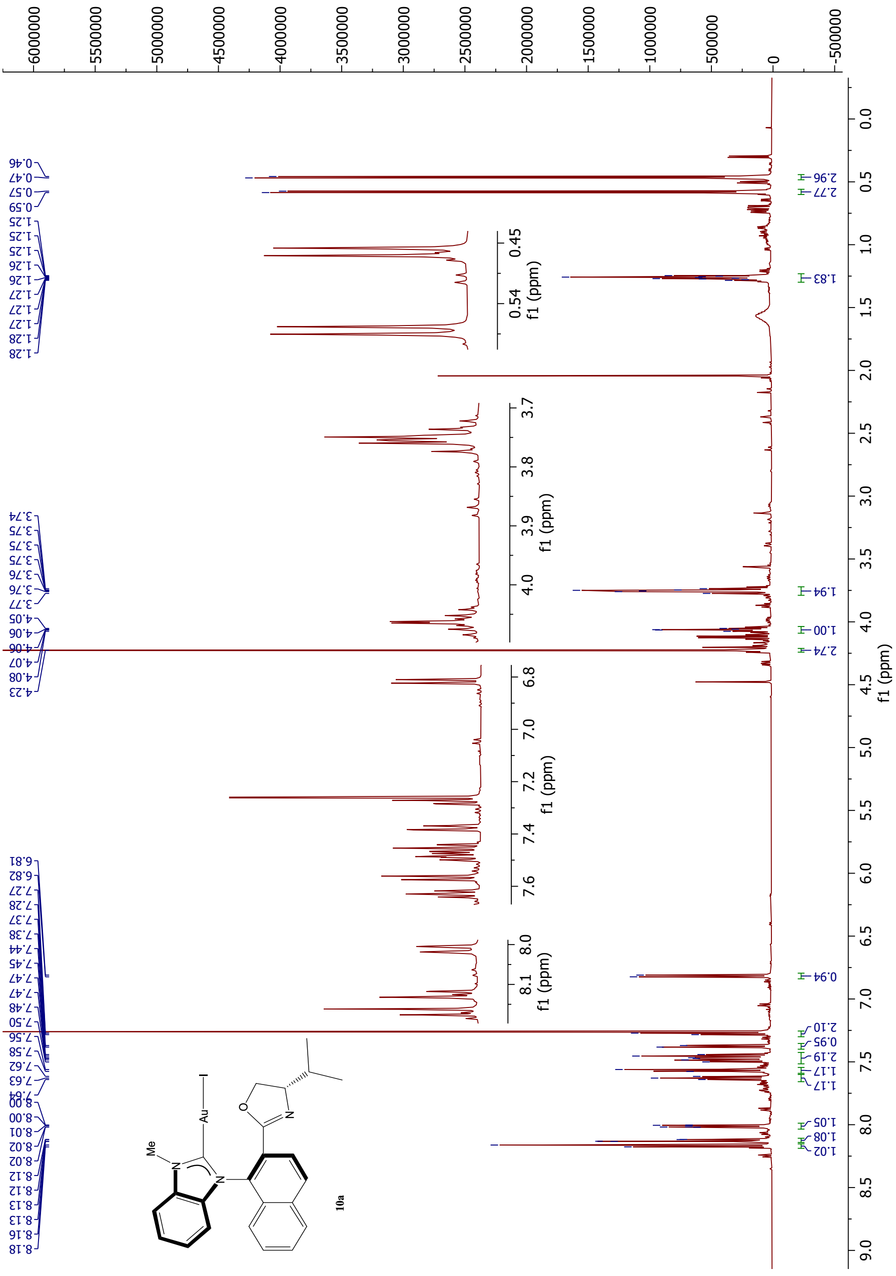

Figure K.3: ^{1}H NMR spectrum of compound **10a**

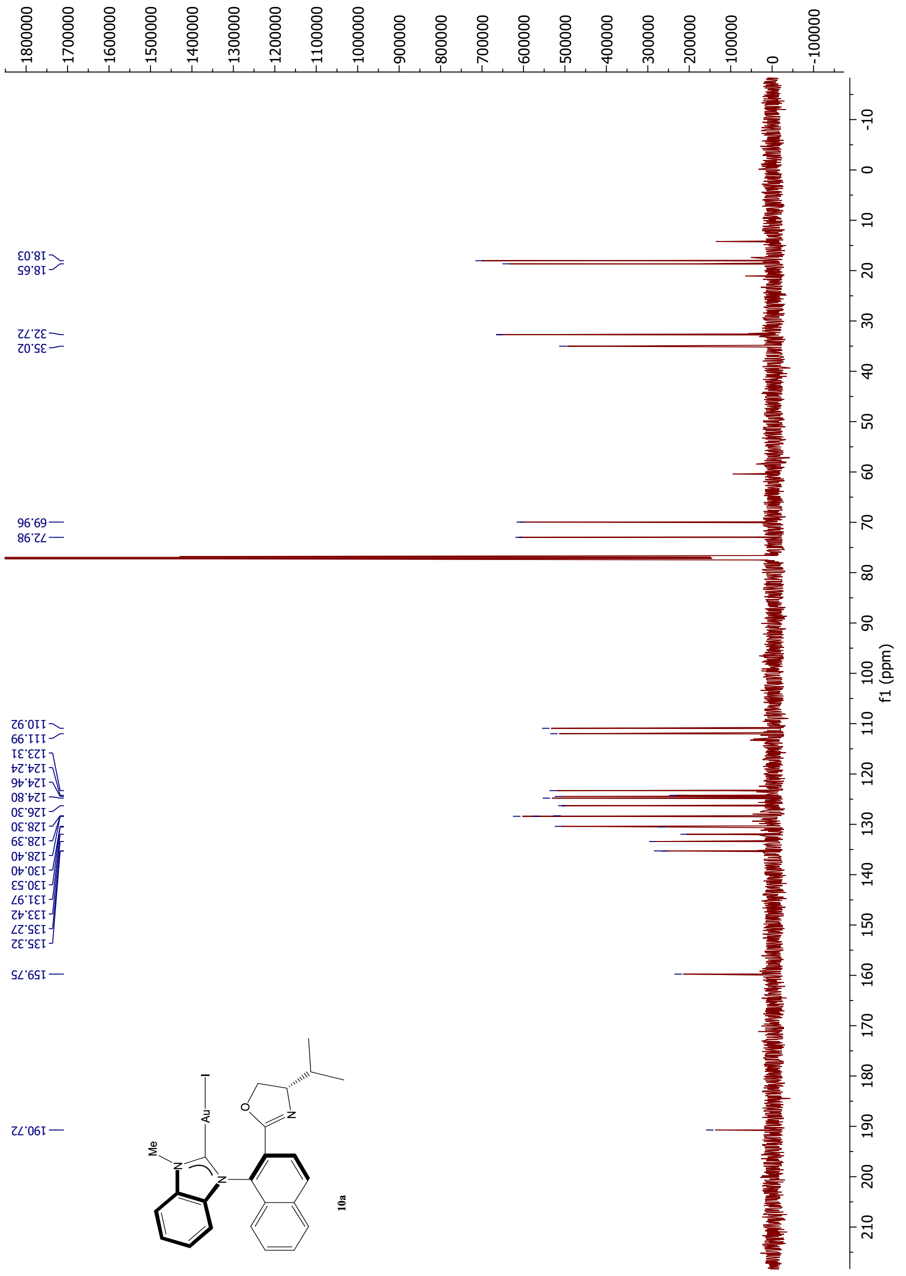

10a

Figure K.4: ^{13}C NMR spectrum of compound **10a**

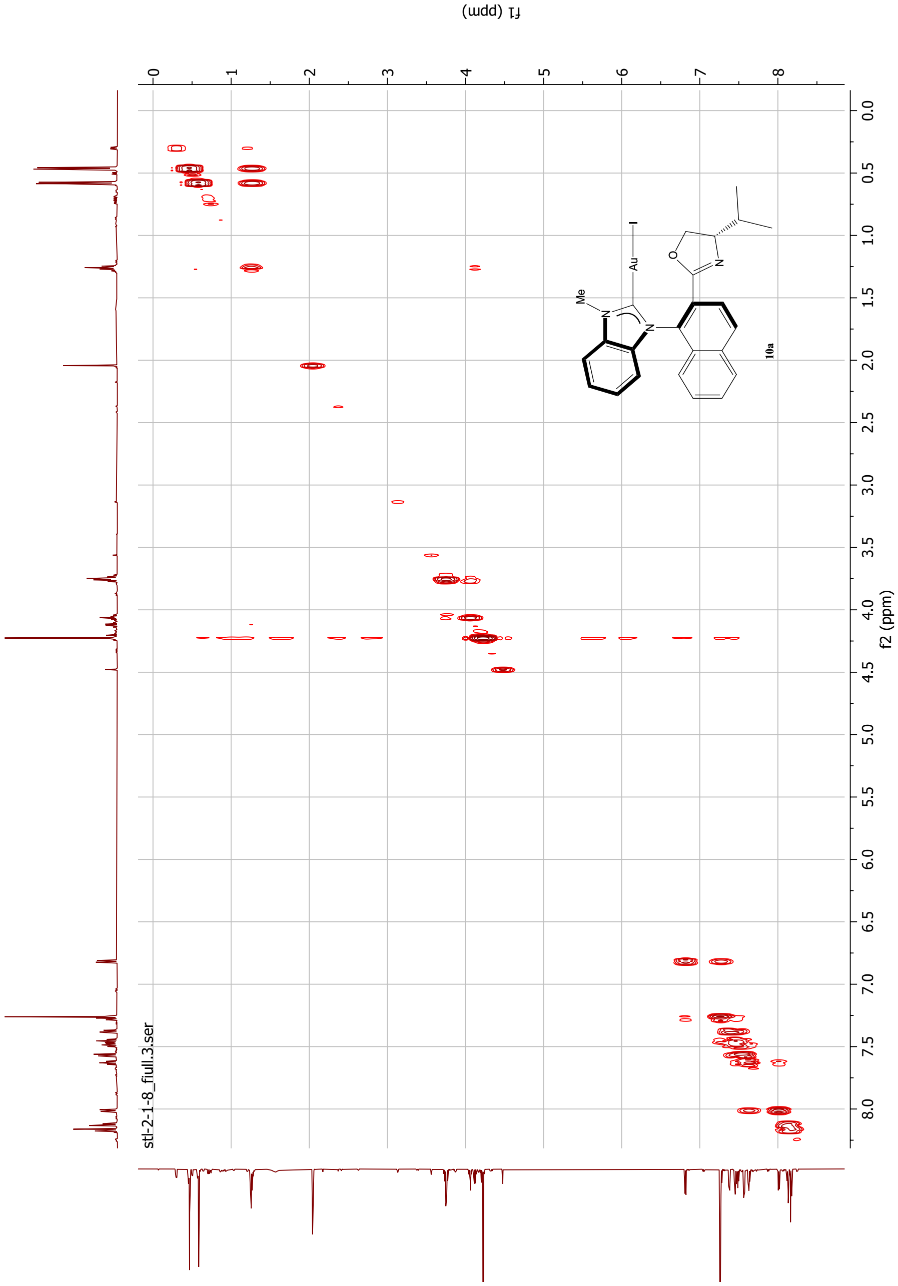

Figure K.5: COSY NMR spectrum of compound **10a**

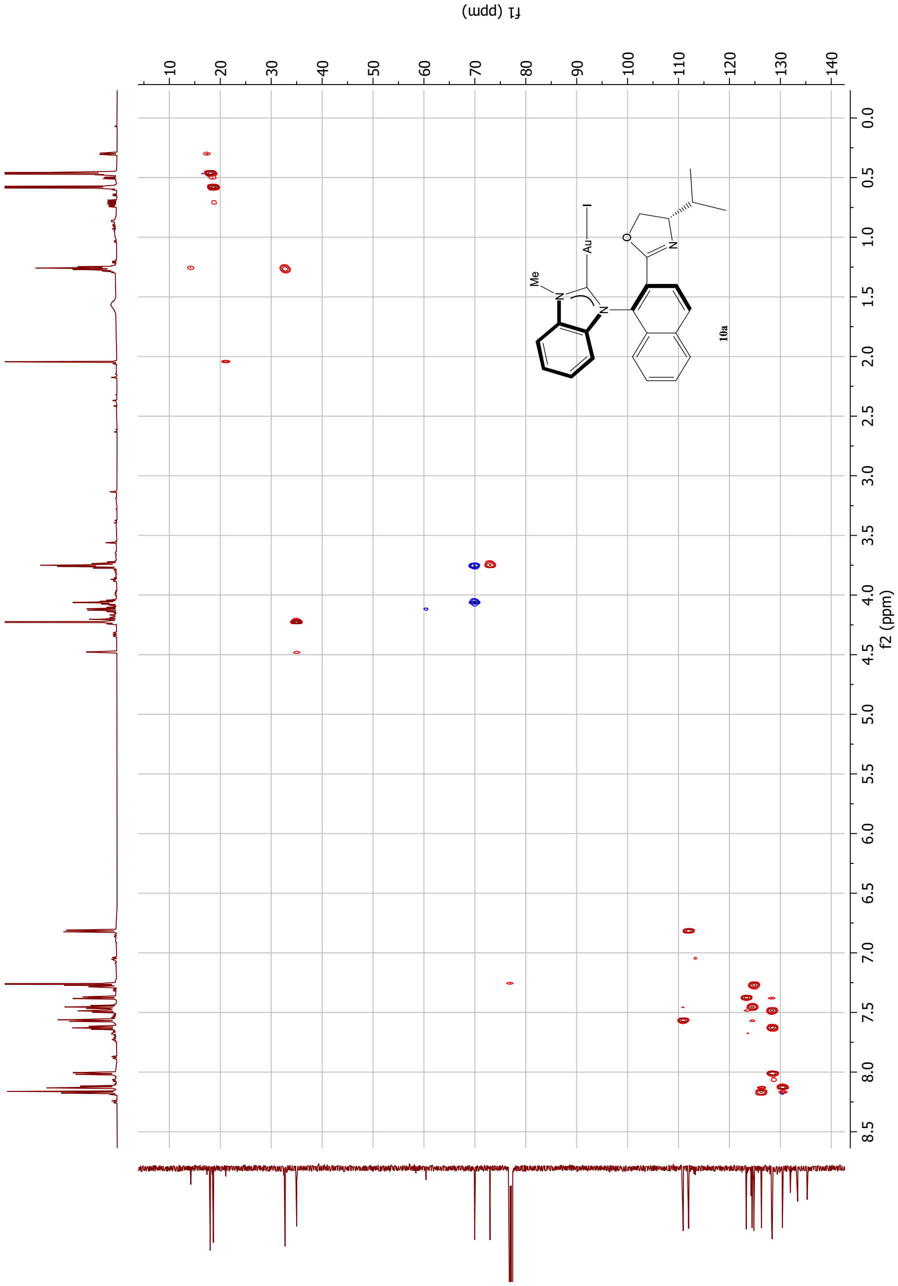

Figure K.6: HSQC NMR spectrum of compound **10a**

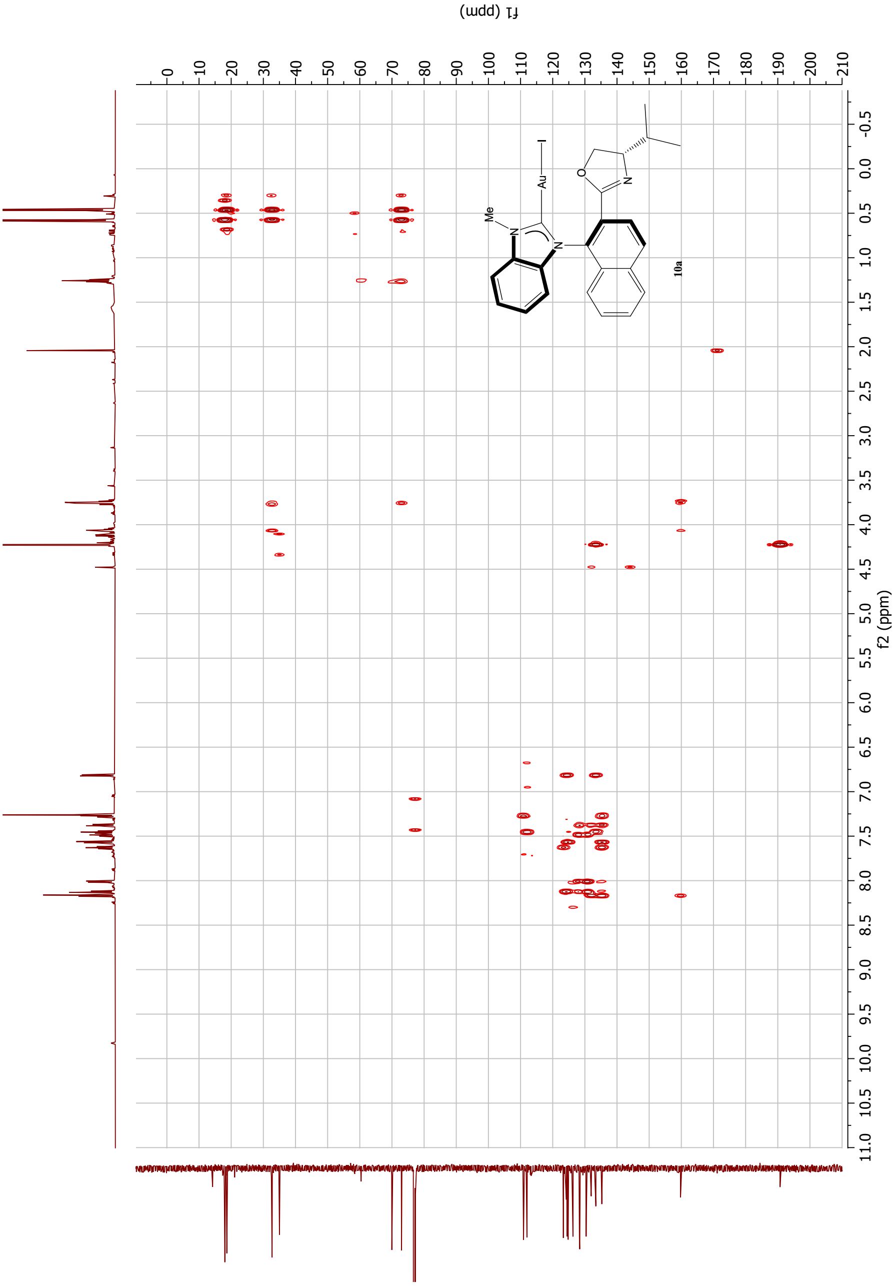

Figure K.7: HMBC NMR spectrum of compound **10a**

Elemental Composition Report

Single Mass Analysis

Tolerance = 2.0 PPM / DBE: min = -10.0, max = 50.0
Element prediction: Off
Number of isotope peaks used for i-FIT = 6

Monoisotopic Mass, Even Electron Ions
13449 formula(e) evaluated with 24 results within limits (all results (up to 1000) for each mass)
Elements Used:
C: 0-100 H: 0-100 N: 0-6 O: 0-6 Na: 0-1 Si: 0-2 I: 0-2 Au: 0-2

2021-218 97 (0.918) AM2 (Ar,35000.0,0.00,0.00); Cm (97:111)
1: TOF MS ES+

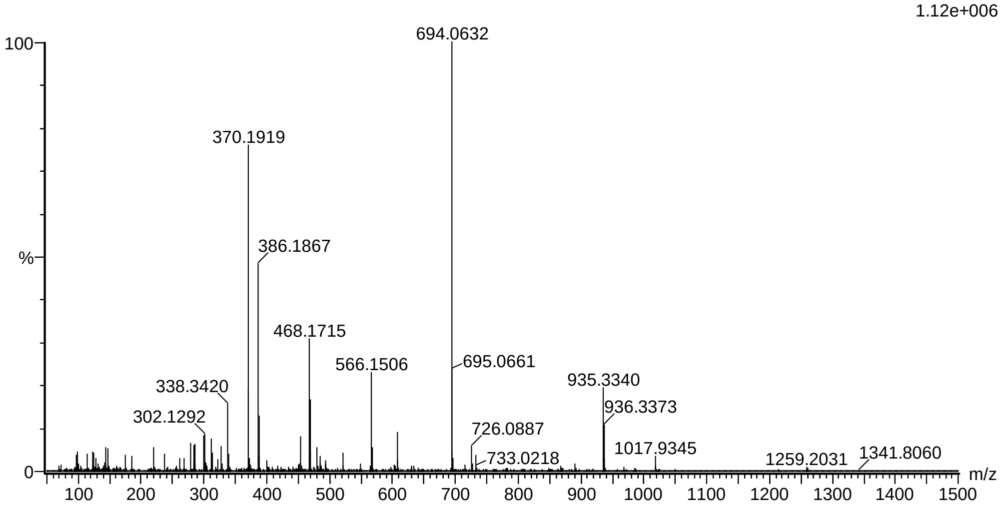

```
Minimum:                         -10.0
Maximum:              5.0   2.0  50.0

Mass      Calc. Mass  mDa   PPM   DBE    i-FIT   Norm   Conf(%) Formula

694.0632  694.0630    0.2   0.3   14.5   1313.1  0.050  95.10   C24 H24 N3 O I
                                                                Au
          694.0639    -0.7  -1.0  9.5    1316.4  3.319  3.62    C25 H34 N3 O4
                                                                I2
          694.0639    -0.7  -1.0  6.5    1317.7  4.612  0.99    C11 H18 N5 O5
                                                                Au2
          694.0641    -0.9  -1.3  -5.5   1319.0  5.929  0.27    C11 H37 N3 O2 I2
                                                                Au
          694.0637    -0.5  -0.7  6.5    1322.5  9.472  0.01    C18 H29 N3 O2 Na
                                                                Si I Au
          694.0621    1.1   1.6   5.5    1323.0  9.905  0.00    C15 H28 N5 O4 Si
                                                                I Au
          694.0618    1.4   2.0   34.5   1323.8  10.747 0.00    C37 H11 N3 Au
          694.0628    0.4   0.6   29.5   1324.3  11.208 0.00    C38 H21 N3 O3 I
          694.0639    -0.7  -1.0  -8.5   1324.8  11.766 0.00    C4 H32 N3 Na Si
                                                                I Au2
          694.0644    -1.2  -1.7  30.5   1325.7  12.653 0.00    C41 H22 N O Na
                                                                I
          694.0626    0.6   0.9   26.5   1326.1  13.072 0.00    C31 H16 N3 O Na
                                                                Si Au
          694.0635    -0.3  -0.4  21.5   1326.2  13.145 0.00    C32 H26 N3 O4 Na
                                                                Si I
          694.0623    0.9   1.3   -9.5   1326.5  13.463 0.00    C H31 N5 O2 Si I
                                                                Au2
```

Figure K.8: MS spectrum of compound **10a**

L Spectroscopic data mixture of compounds 11 and 15

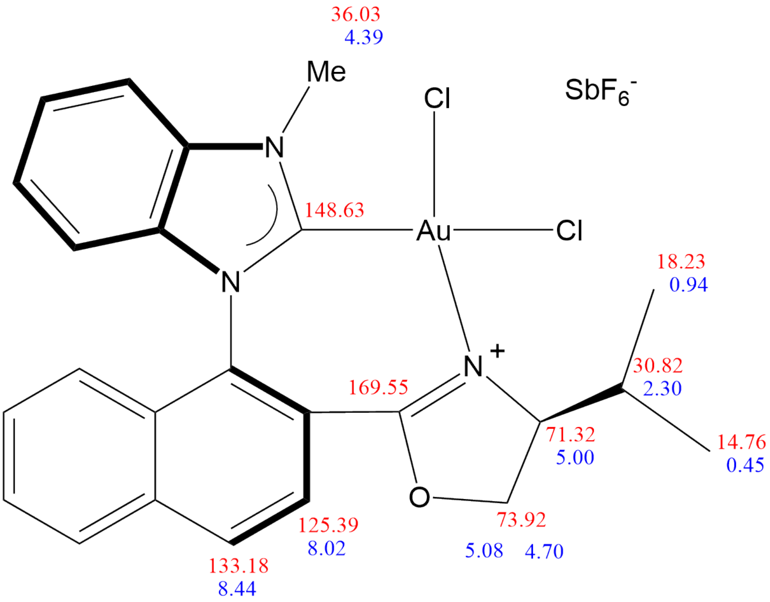

Figure L.1: Assigned ^{1}H and ^{13}C NMR signals of compound **11**

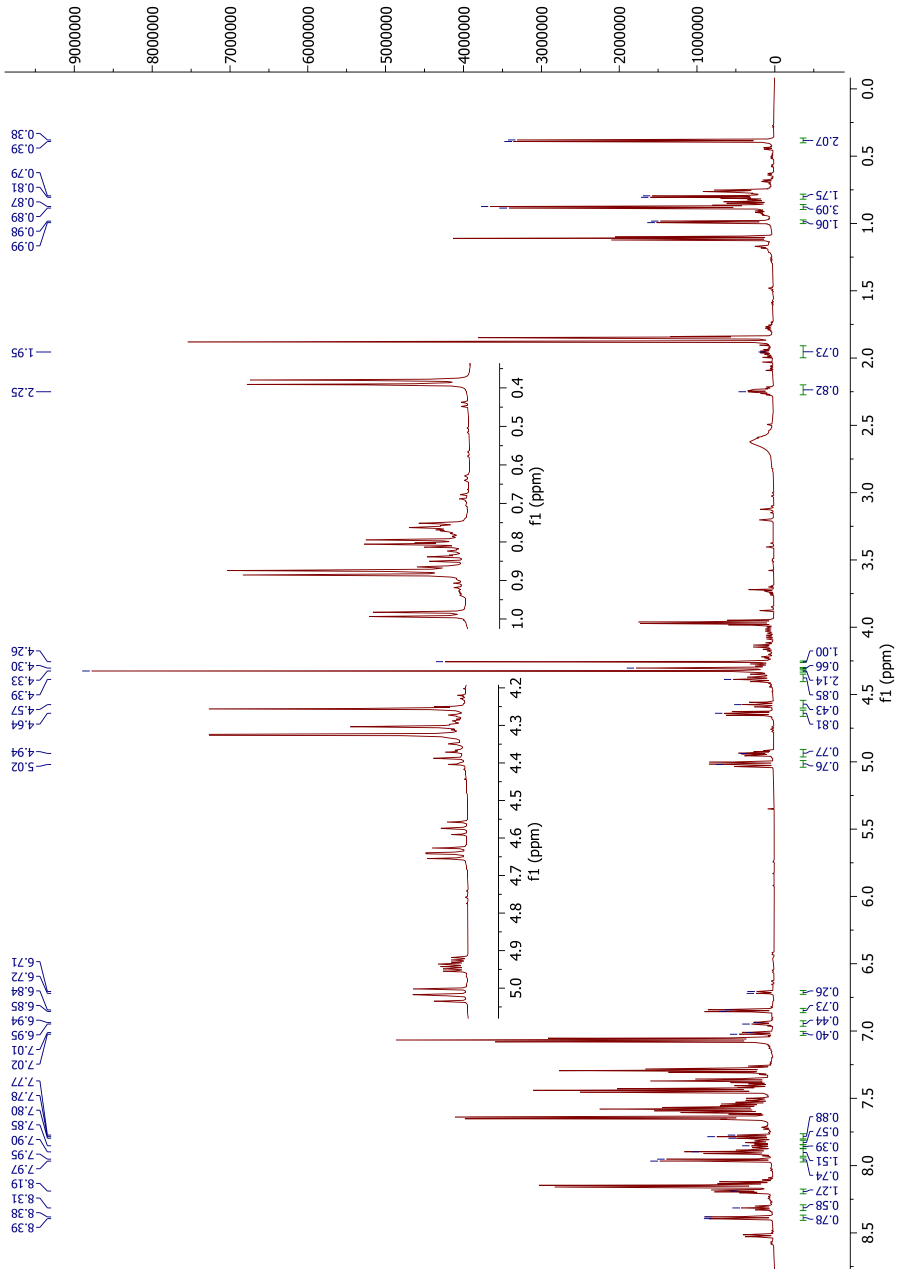

Figure L.2: ^{1}H NMR spectrum of compounds **11** and **15**

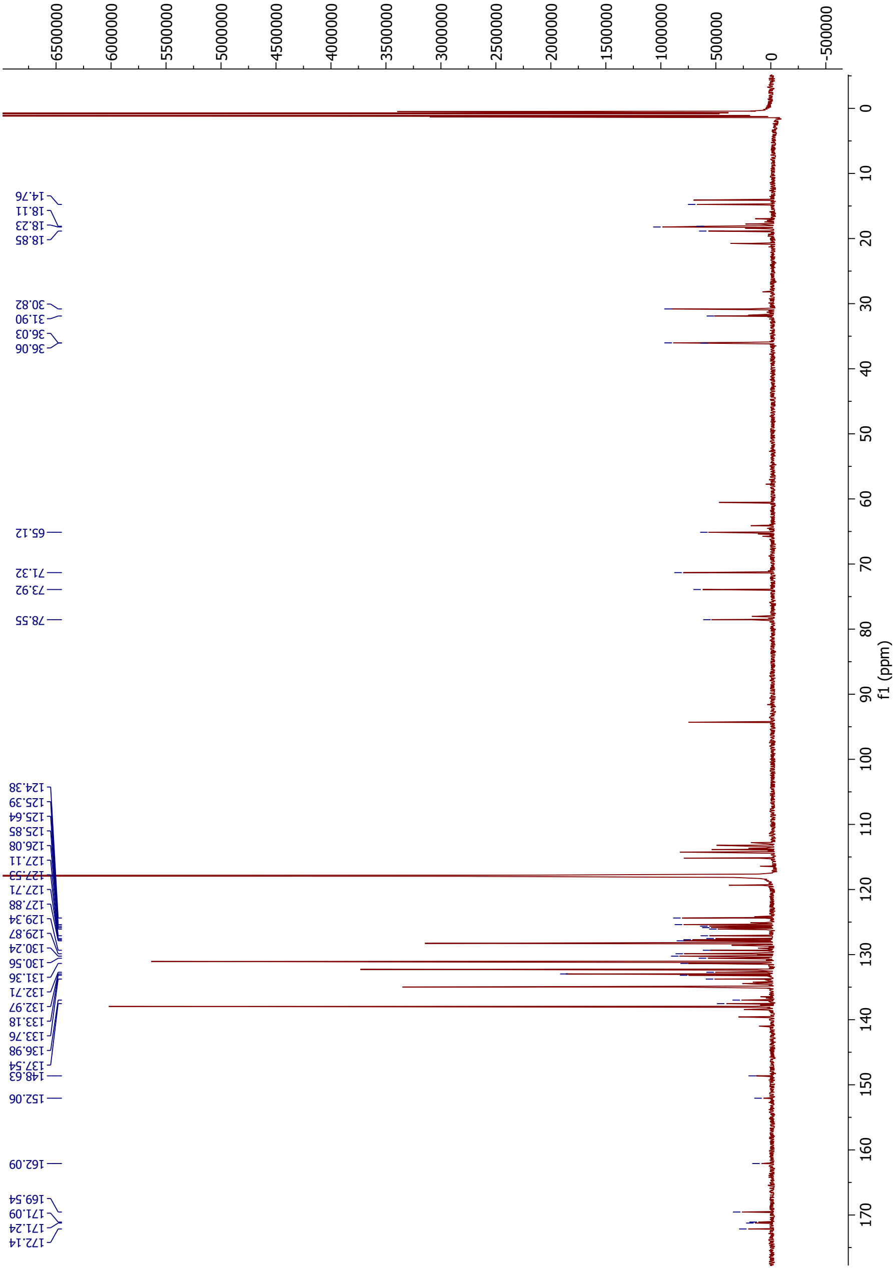

Figure L.3: ^{13}C NMR spectrum of compounds **11** and **15**

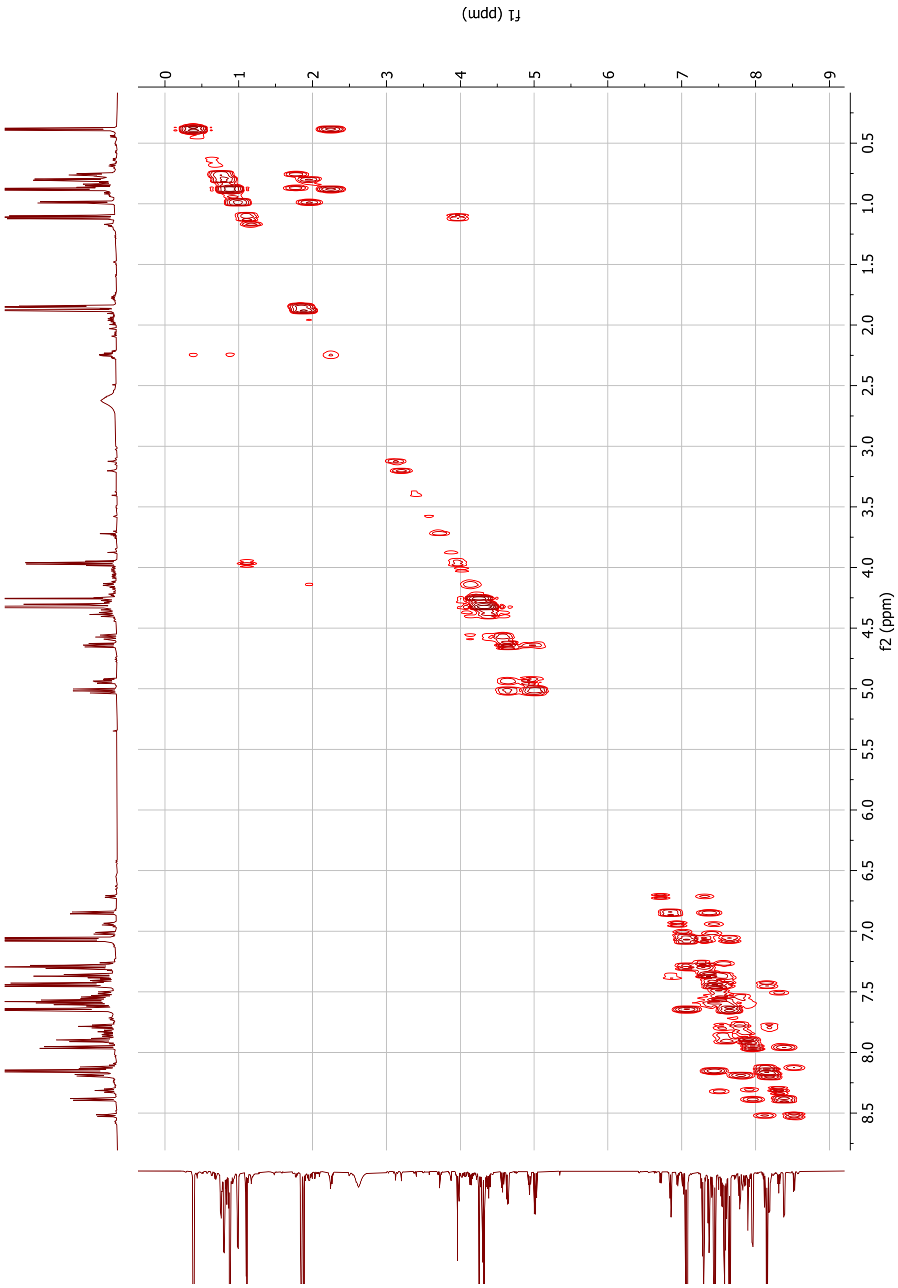

Figure L.4: COSY NMR spectrum of compounds **11** and **15**

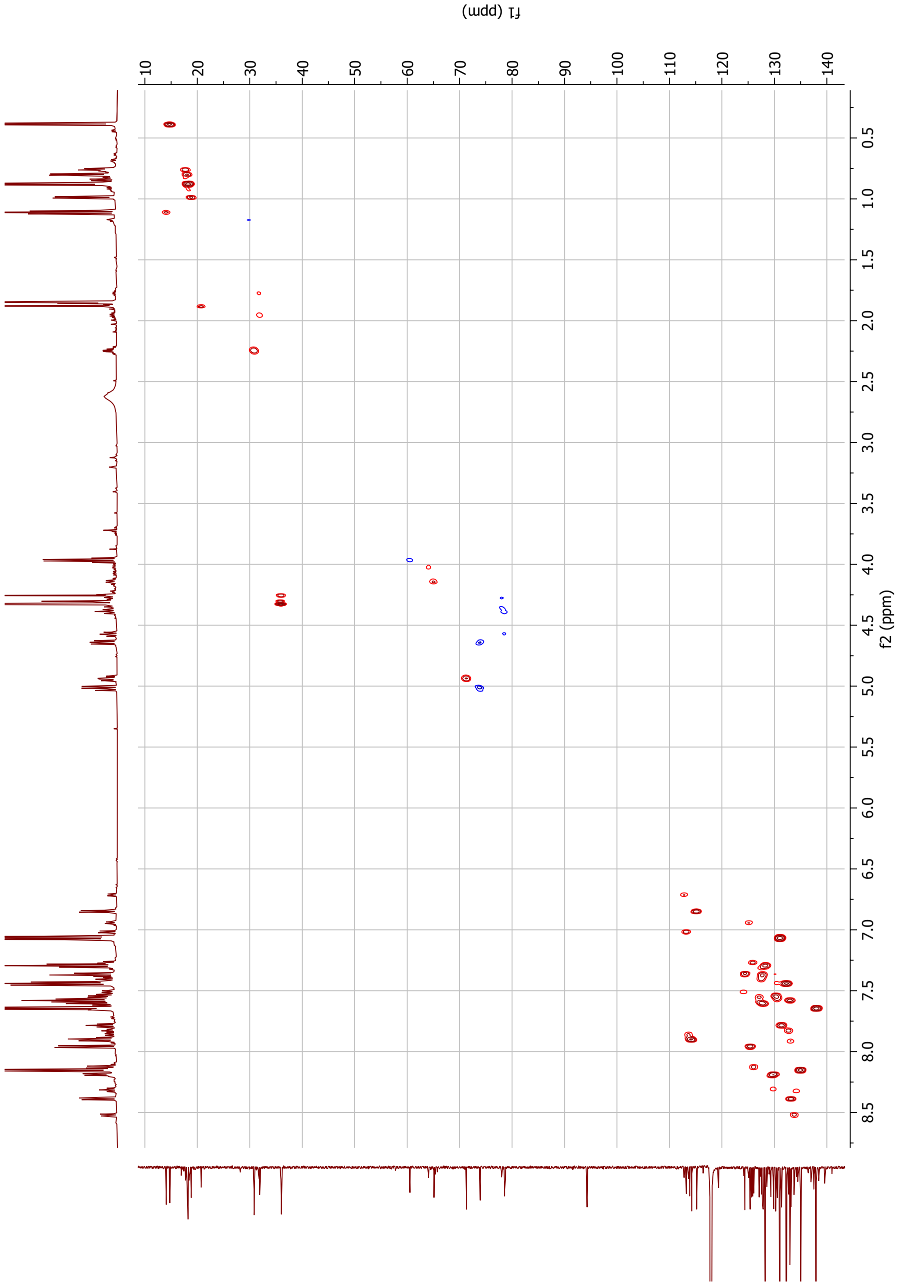

Figure L.5: HSQC NMR spectrum of compounds **11** and **15**

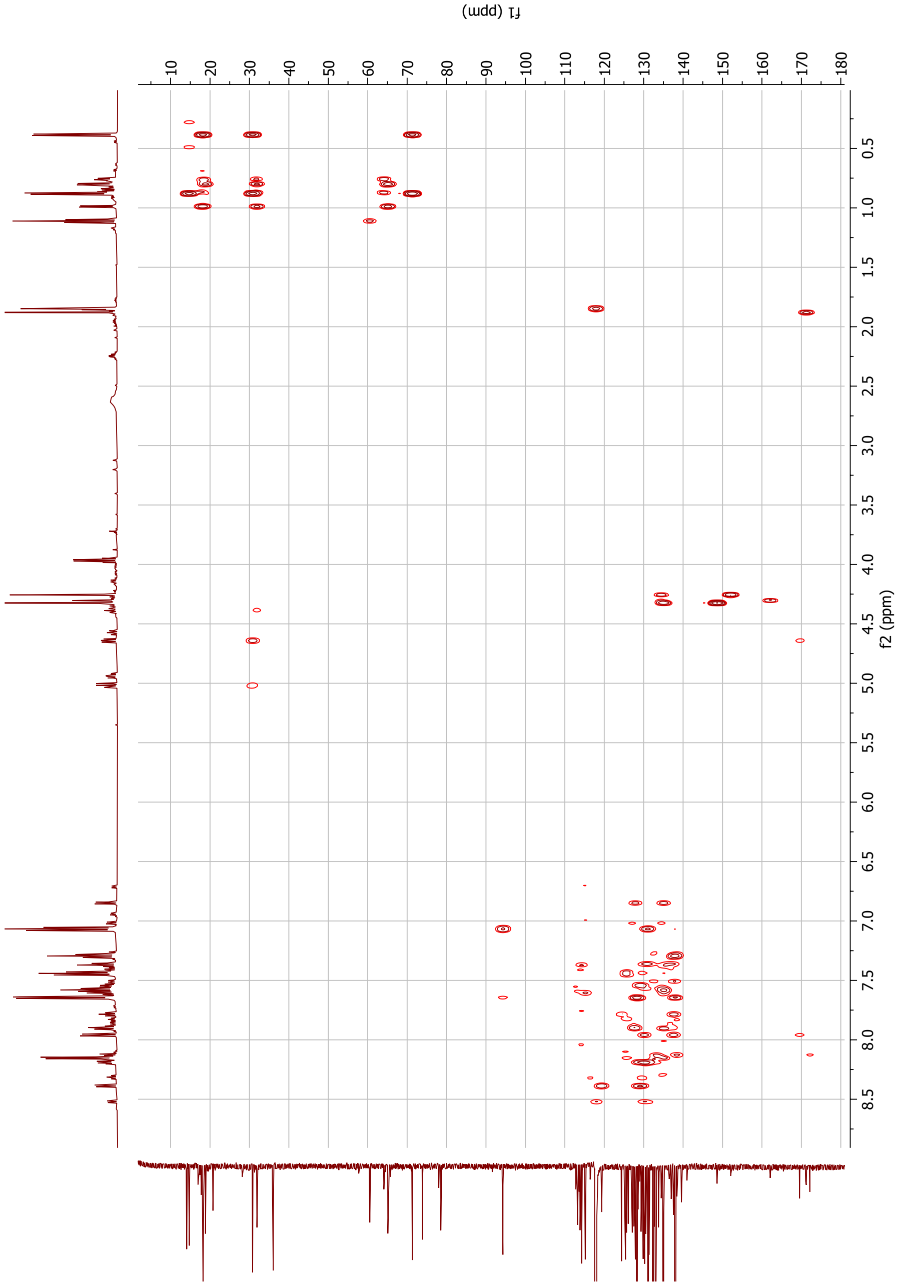

Figure L.6: HMBC NMR spectrum of compounds **11** and **15**

M Spectroscopic data of compound 25

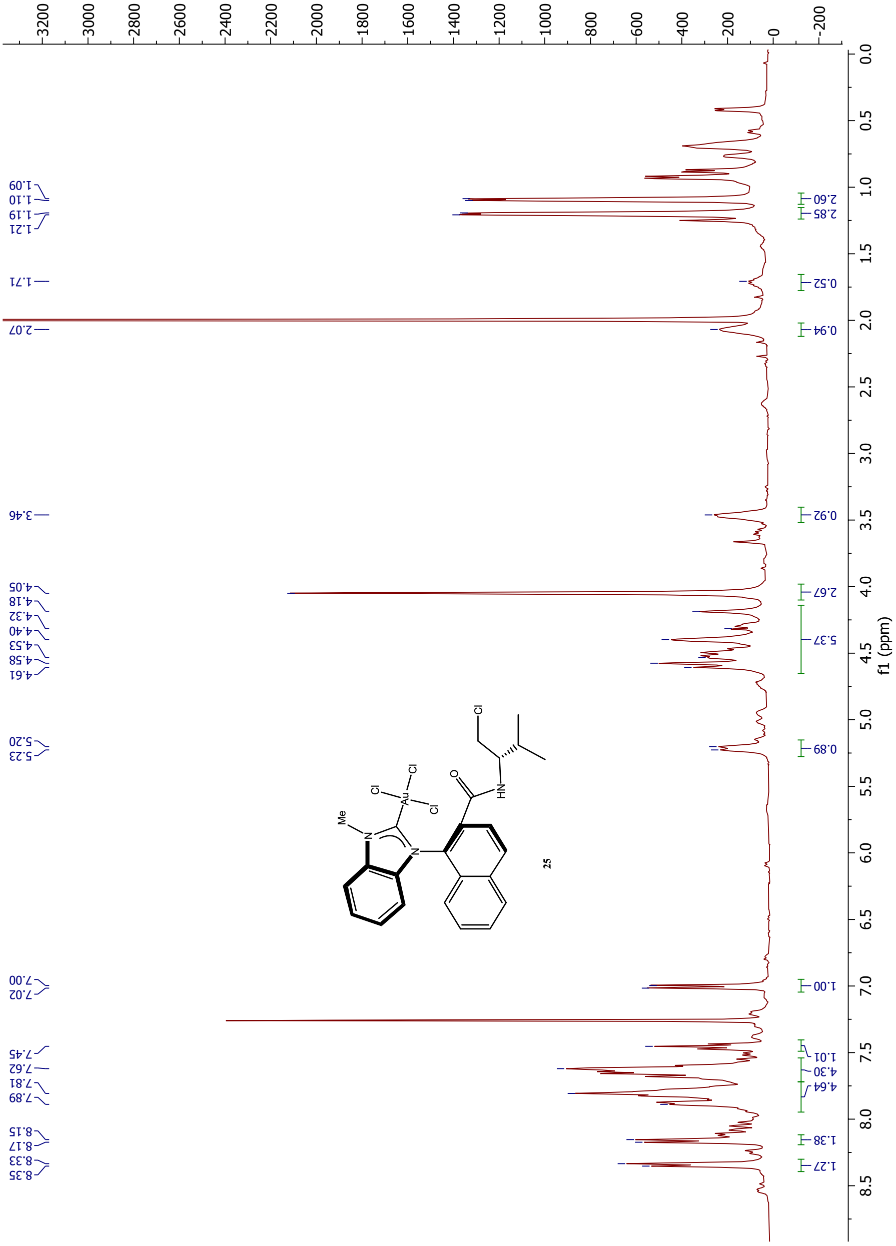

Figure M.1: ^{1}H NMR spectrum of compound **25**

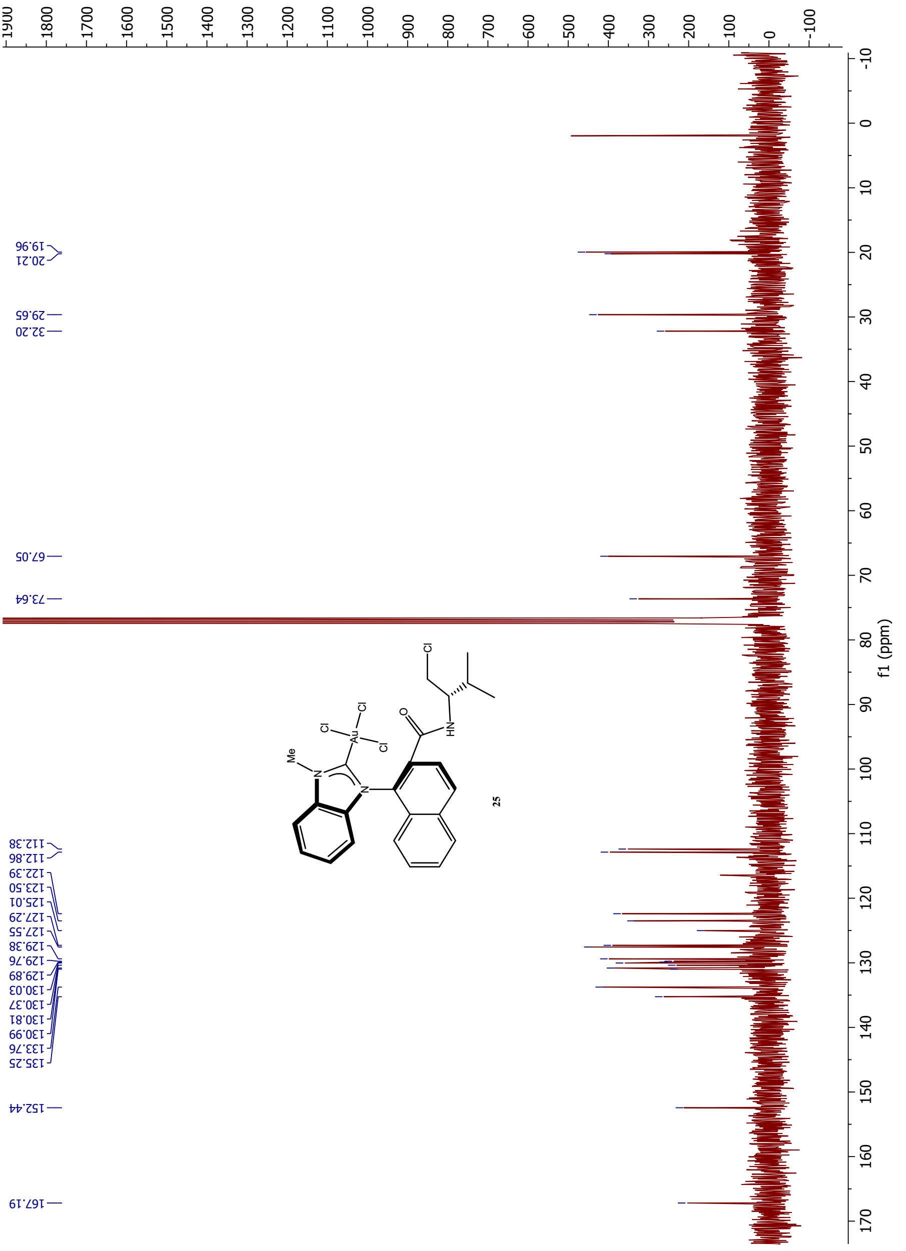

Figure M.2: ^{13}C NMR spectrum of compound **25**

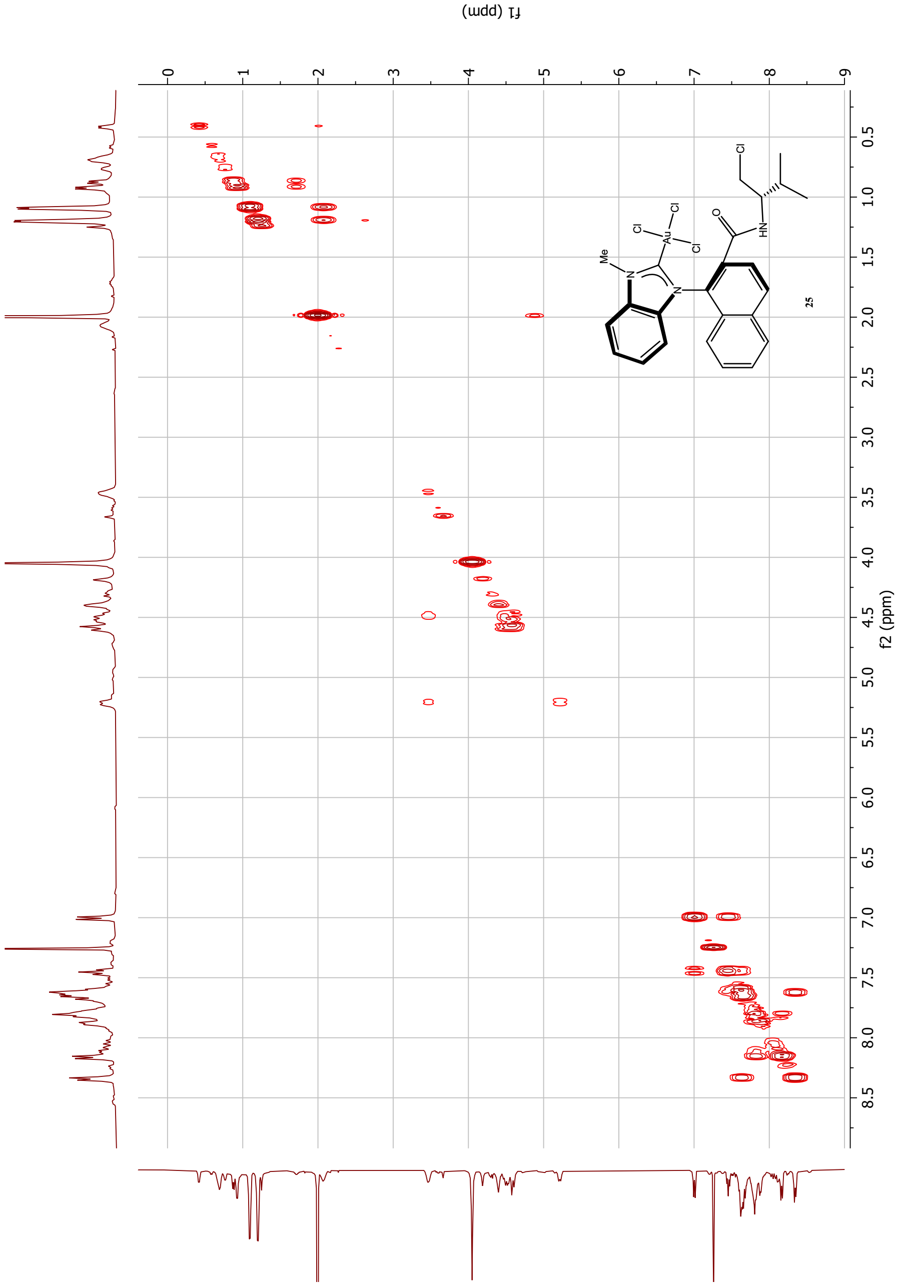

Figure M.3: COSY NMR spectrum of compound **25**

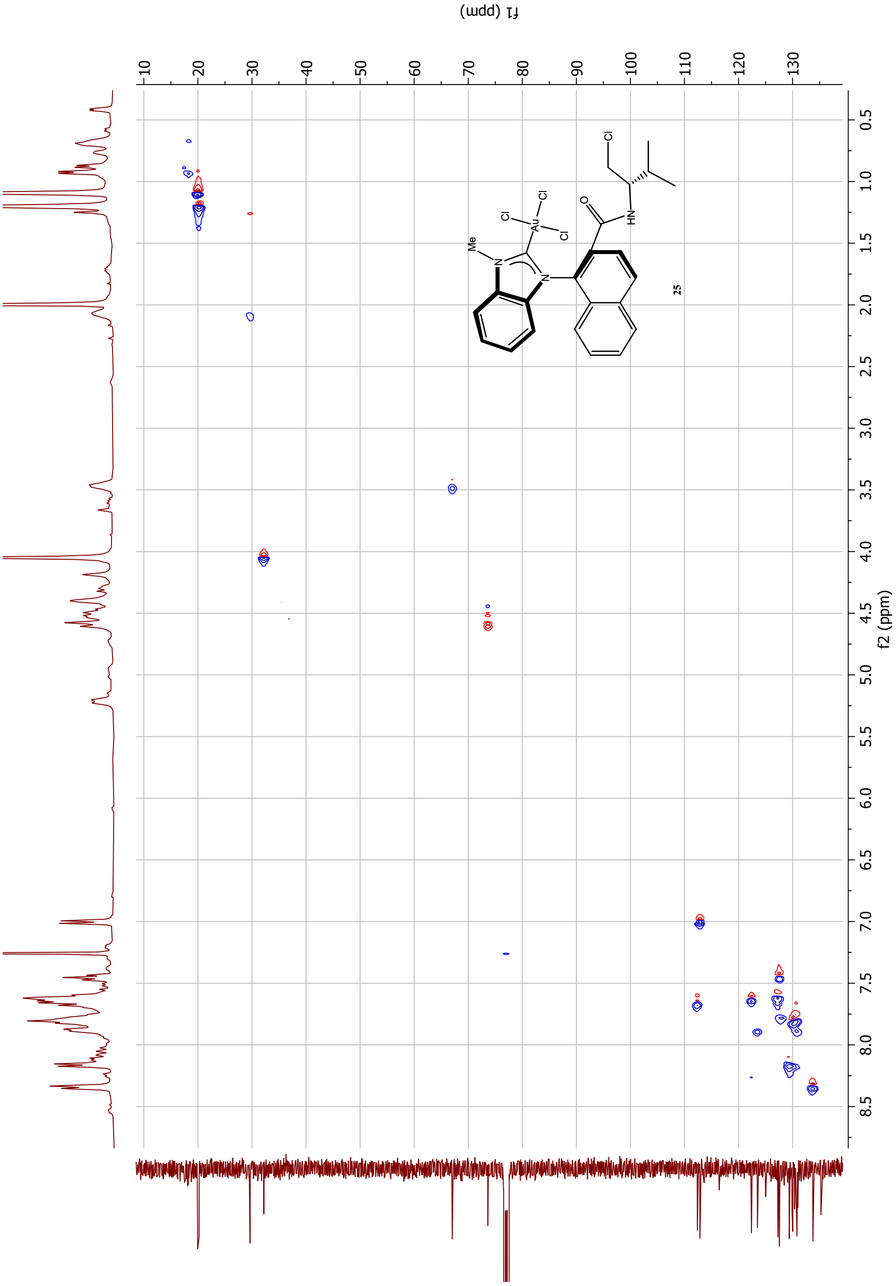

Figure M.4: HSQC NMR spectrum of compound **25**

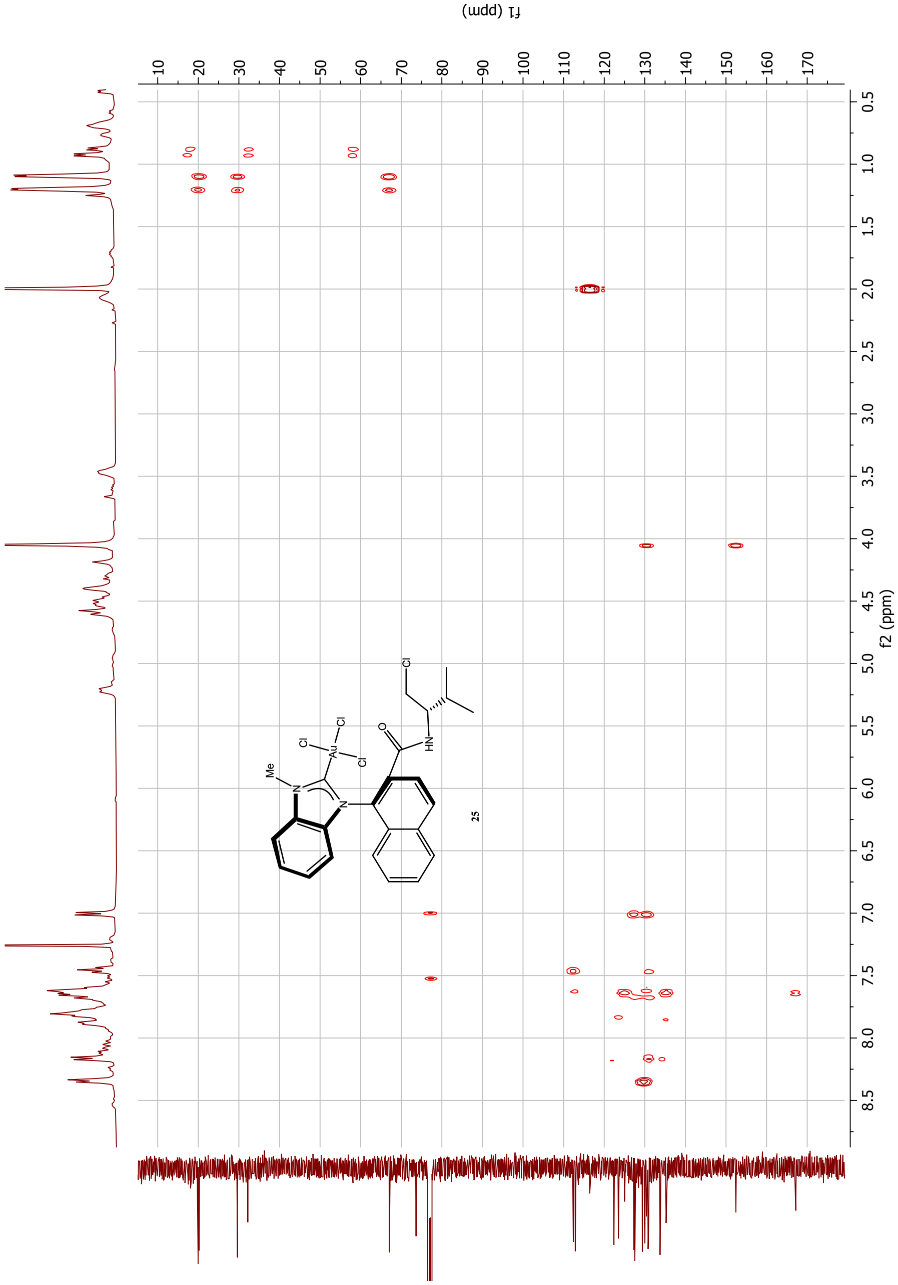

Figure M.5: HMBC NMR spectrum of compound **25**

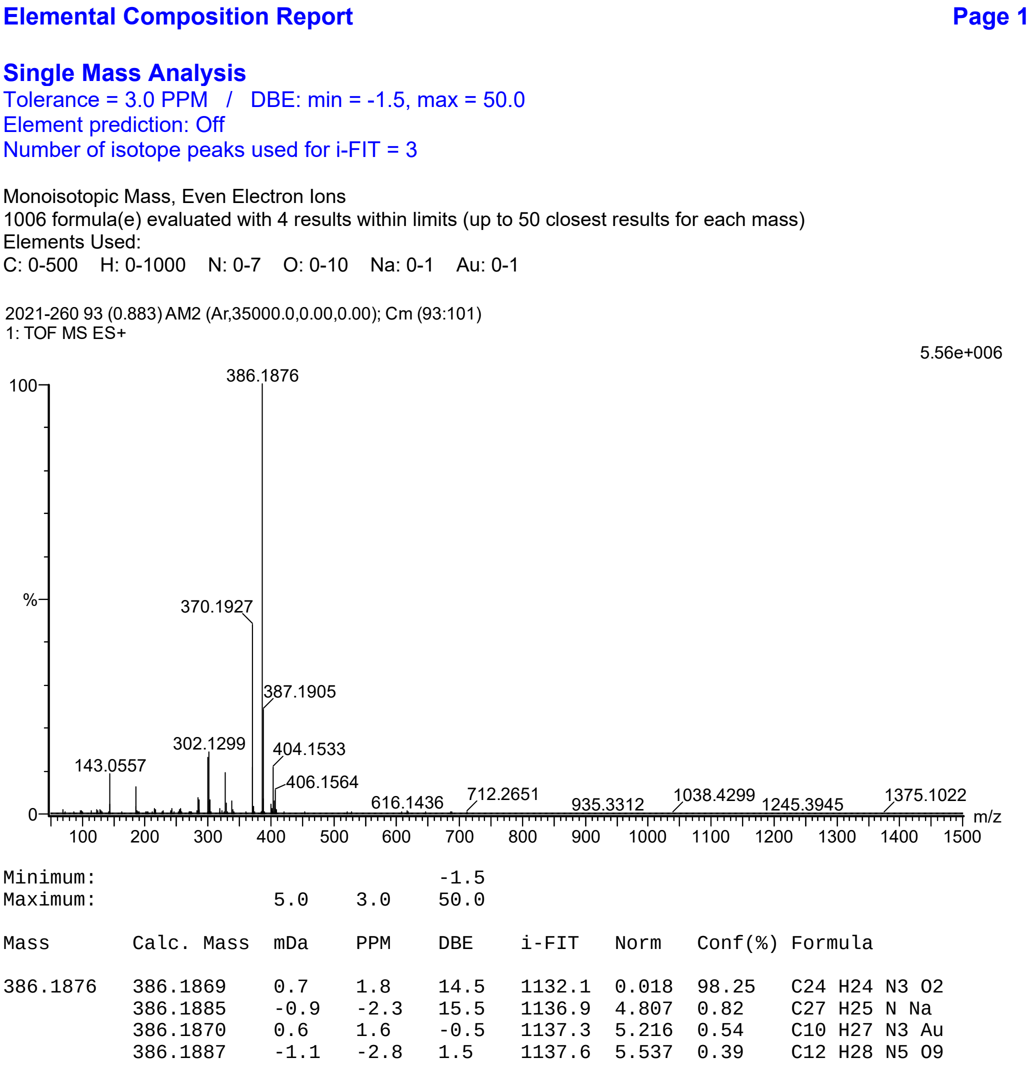

Elemental Composition Report **Page 1**

Single Mass Analysis
Tolerance = 3.0 PPM / DBE: min = -1.5, max = 50.0
Element prediction: Off
Number of isotope peaks used for i-FIT = 3

Monoisotopic Mass, Even Electron Ions
1006 formula(e) evaluated with 4 results within limits (up to 50 closest results for each mass)
Elements Used:
C: 0-500 H: 0-1000 N: 0-7 O: 0-10 Na: 0-1 Au: 0-1

2021-260 93 (0.883) AM2 (Ar,35000.0,0.00,0.00); Cm (93:101)
1: TOF MS ES+

```
Minimum:                              -1.5
Maximum:                5.0     3.0   50.0

Mass       Calc. Mass  mDa     PPM    DBE    i-FIT   Norm   Conf(%) Formula

386.1876   386.1869    0.7     1.8    14.5   1132.1  0.018  98.25   C24 H24 N3 O2
           386.1885    -0.9    -2.3   15.5   1136.9  4.807  0.82    C27 H25 N Na
           386.1870    0.6     1.6    -0.5   1137.3  5.216  0.54    C10 H27 N3 Au
           386.1887    -1.1    -2.8   1.5    1137.6  5.537  0.39    C12 H28 N5 O9
```

Figure M.6: MS spectrum of the uncoordinated compound of decomposed **25**

N Spectroscopic data for compound 19a

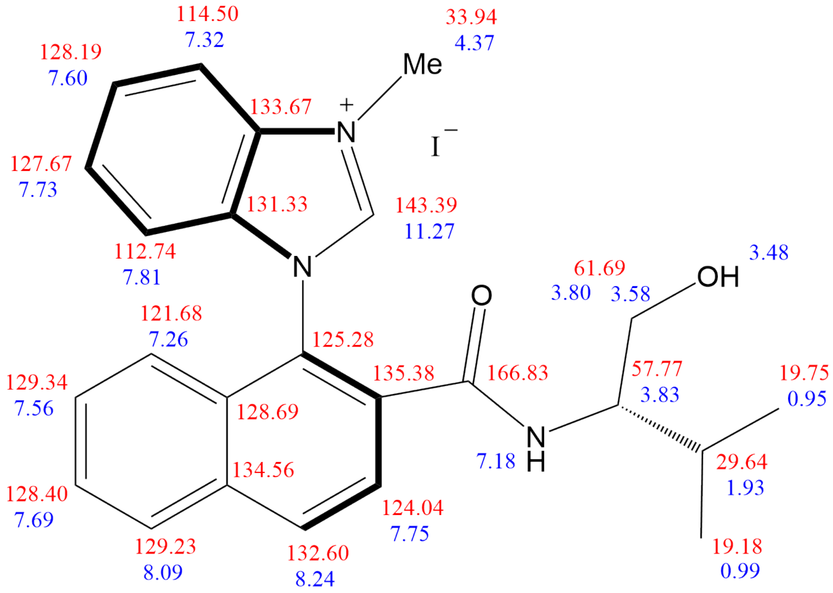

Figure N.1: Assigned ^{1}H and ^{13}C NMR signals of compound **19a**

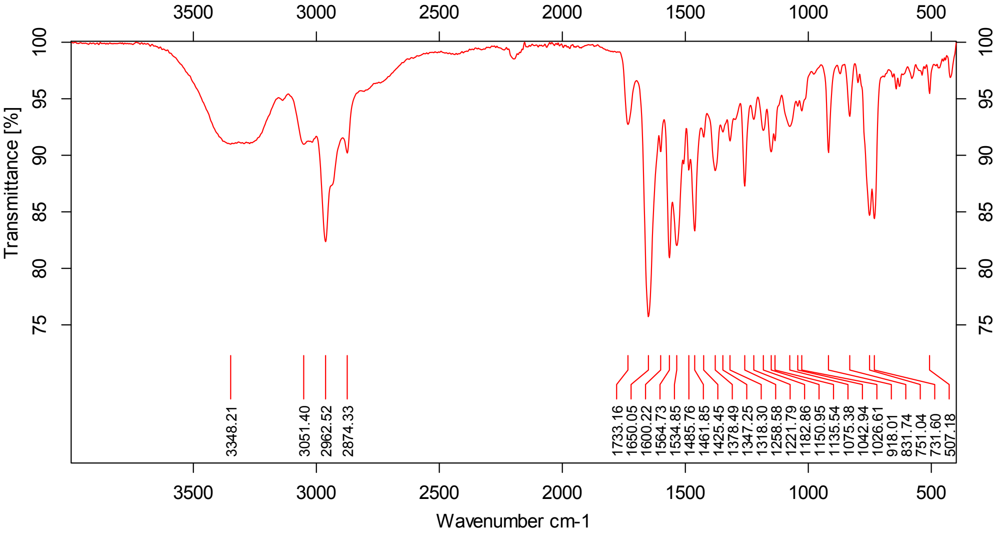

Figure N.2: IR spectrum of compound **19a**

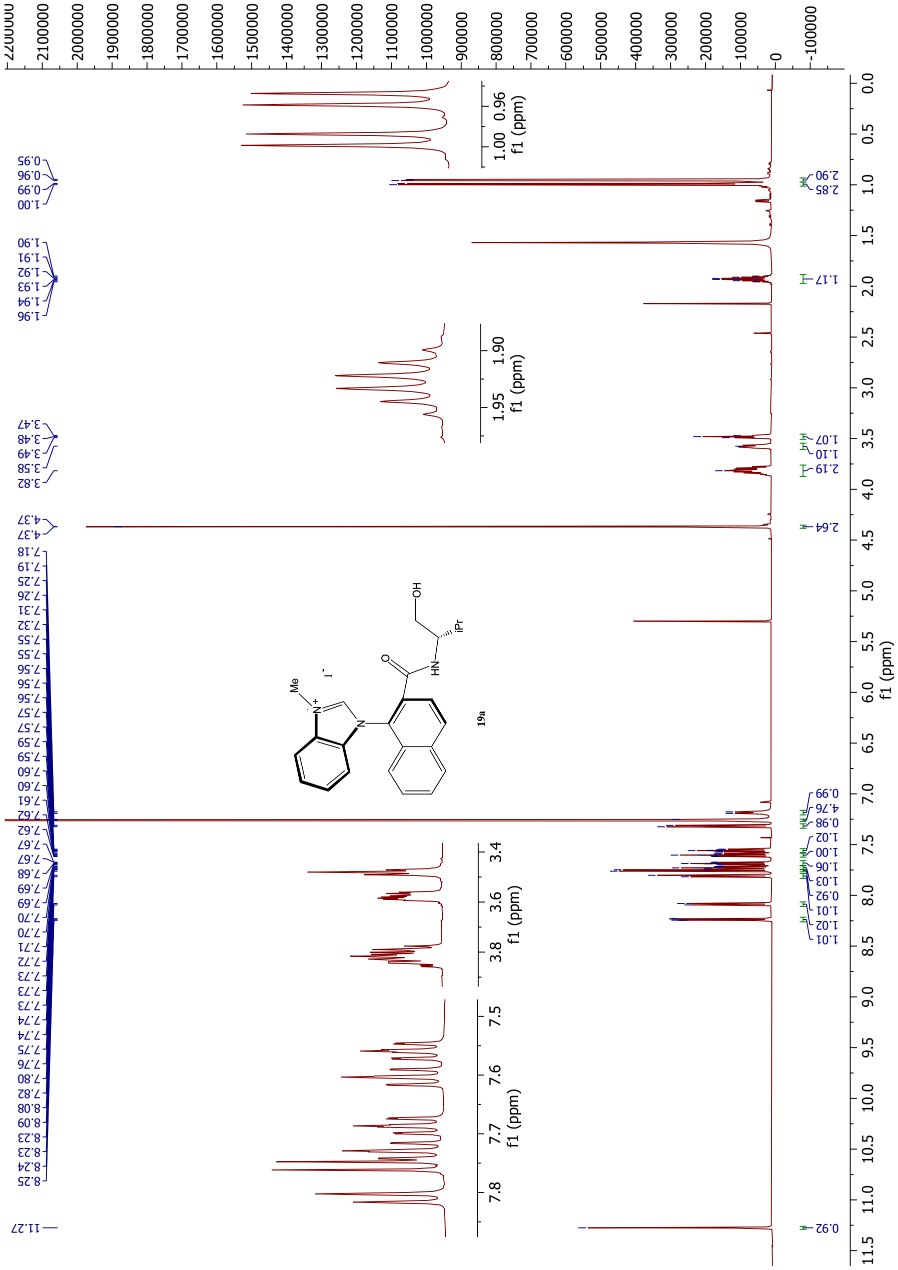

Figure N.3: ^{1}H NMR spectrum of compound **19a**

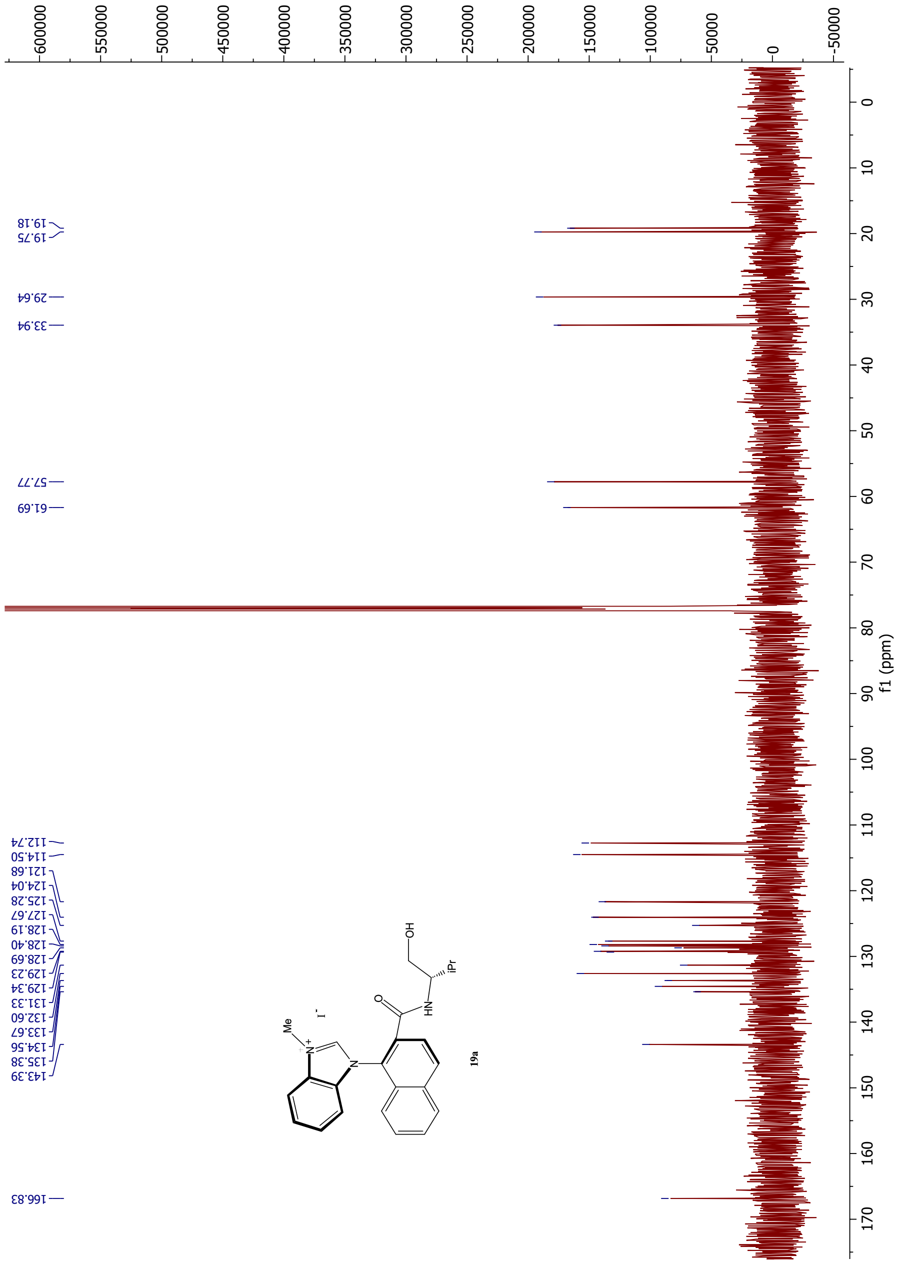

Figure N.4: ^{13}C NMR spectrum of compound **19a**

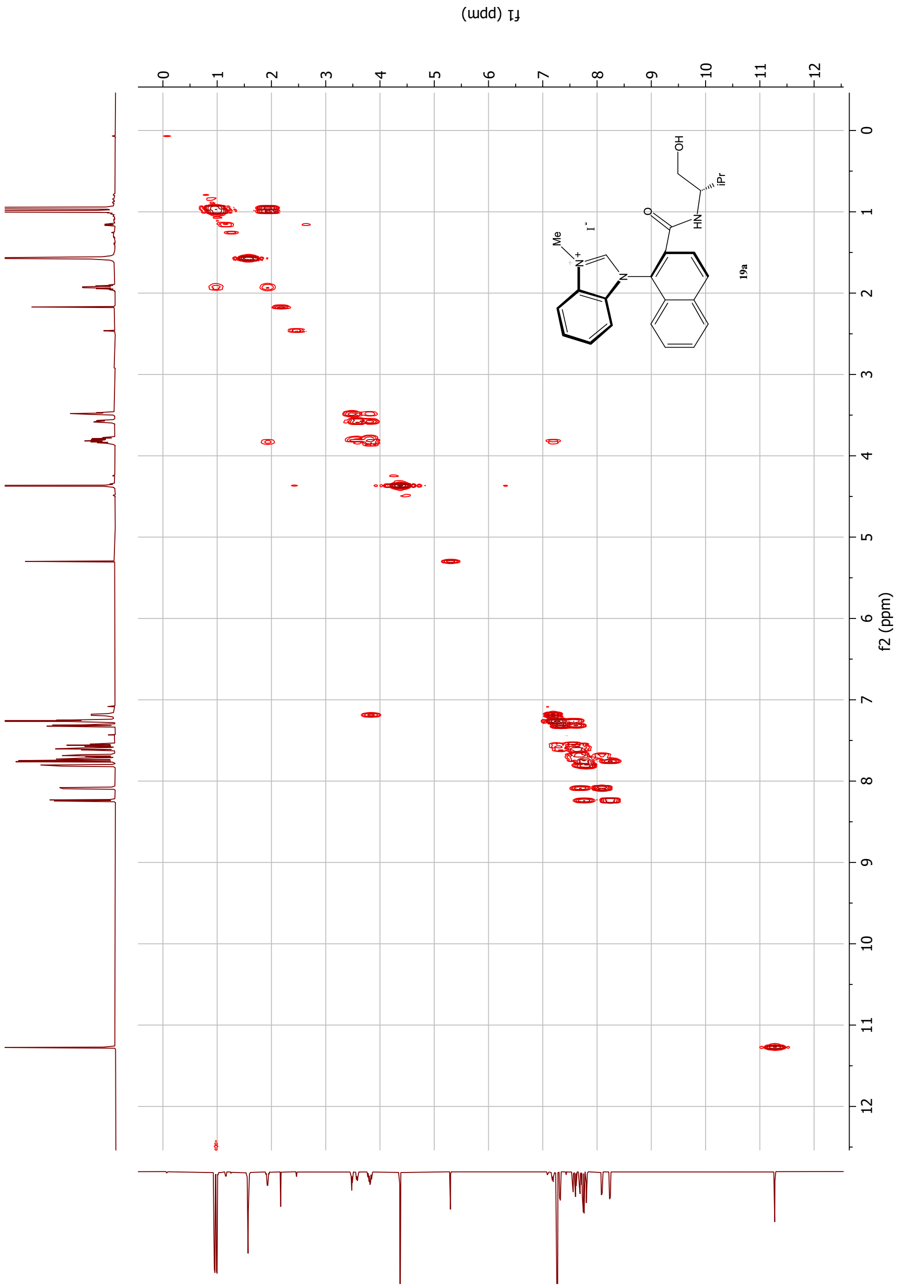

Figure N.5: COSY NMR spectrum of compound **19a**

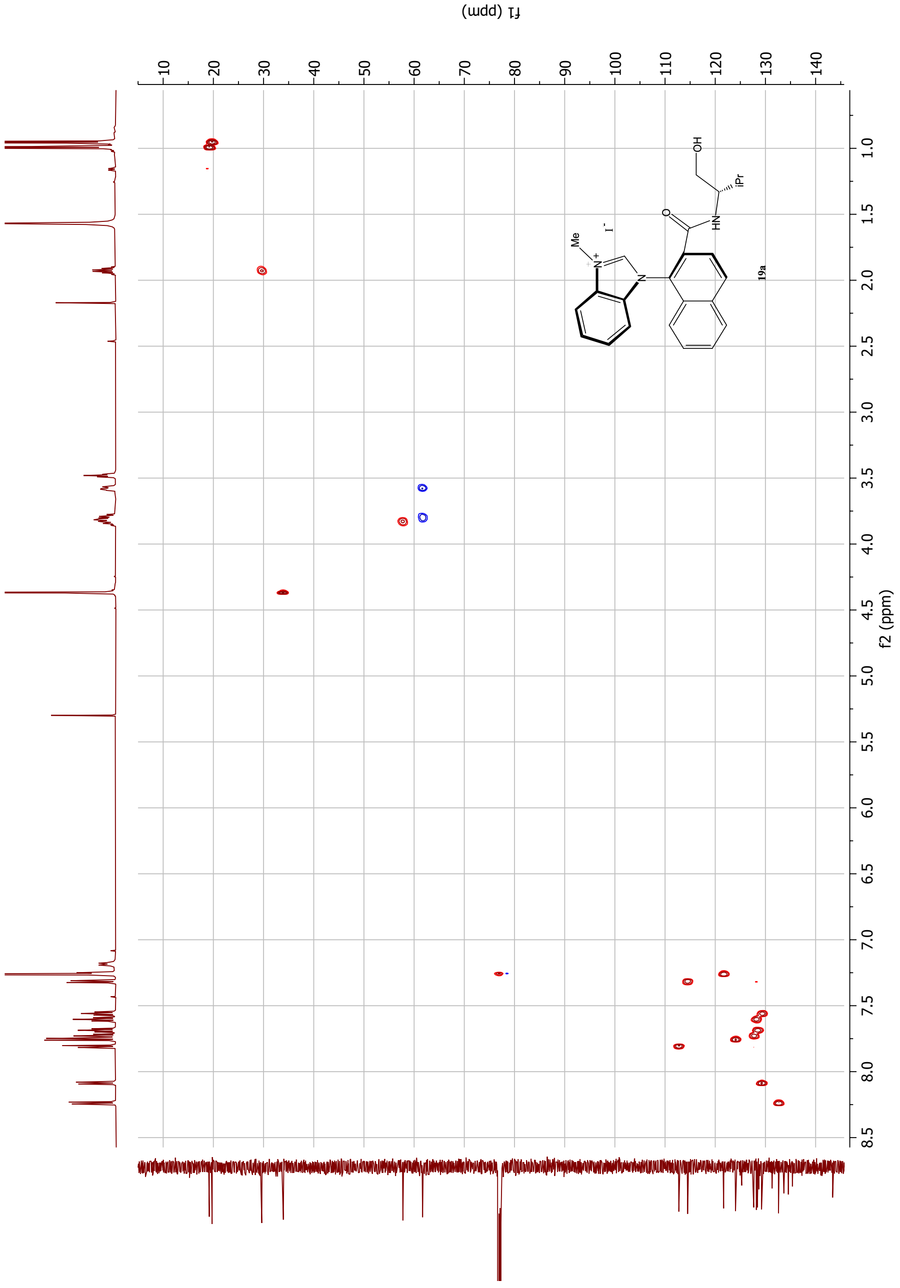

Figure N.6: HSQC NMR spectrum of compound **19a**

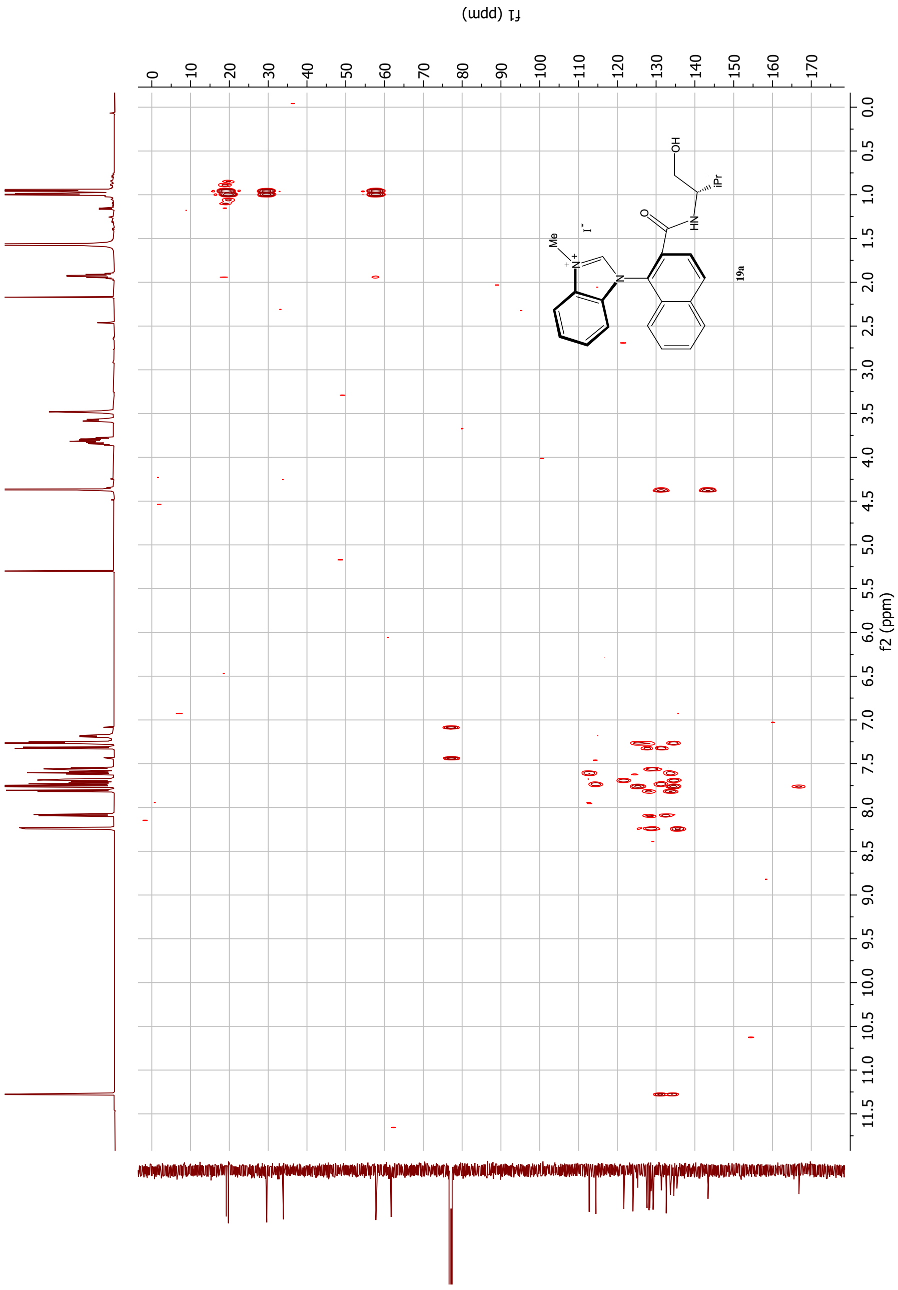

Figure N.7: HMBC NMR spectrum of compound **19a**

Elemental Composition Report

Page 1

Single Mass Analysis

Tolerance = 2.0 PPM / DBE: min = -10.0, max = 50.0
Element prediction: Off
Number of isotope peaks used for i-FIT = 6

Monoisotopic Mass, Even Electron Ions
757 formula(e) evaluated with 1 results within limits (all results (up to 1000) for each mass)
Elements Used:
C: 0-100 H: 0-100 N: 0-12 O: 0-10

2021-152 117 (1.301) AM2 (Ar,35000.0,0.00,0.00); Cm (108:120)
1: TOF MS ES+

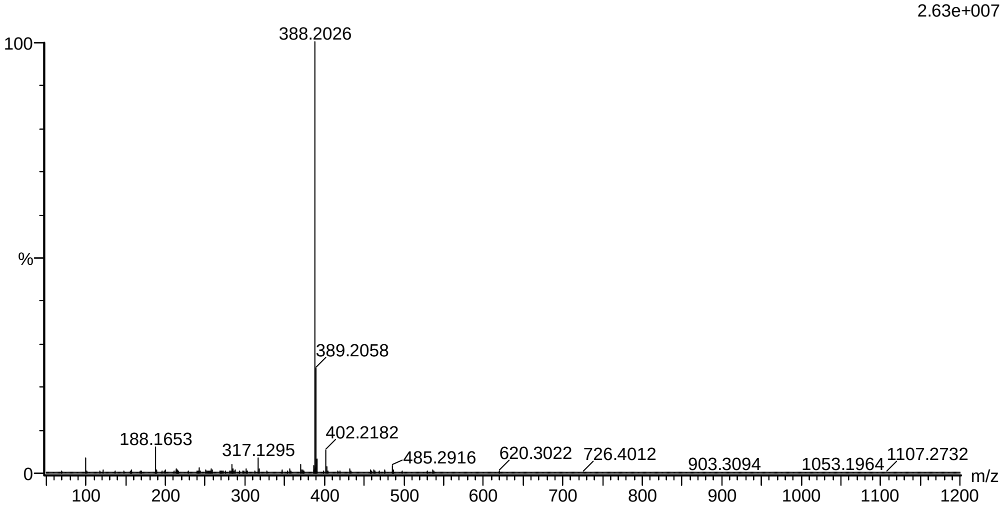

```
Minimum:                                -10.0
Maximum:                 5.0     2.0    50.0

Mass        Calc. Mass   mDa     PPM    DBE     i-FIT    Norm    Conf(%) Formula

388.2026    388.2025     0.1     0.3    13.5    2803.1   n/a     n/a     C24 H26 N3 O2
```

Figure N.8: MS spectrum of compound **19a**

O Spectroscopic data for compound 19b

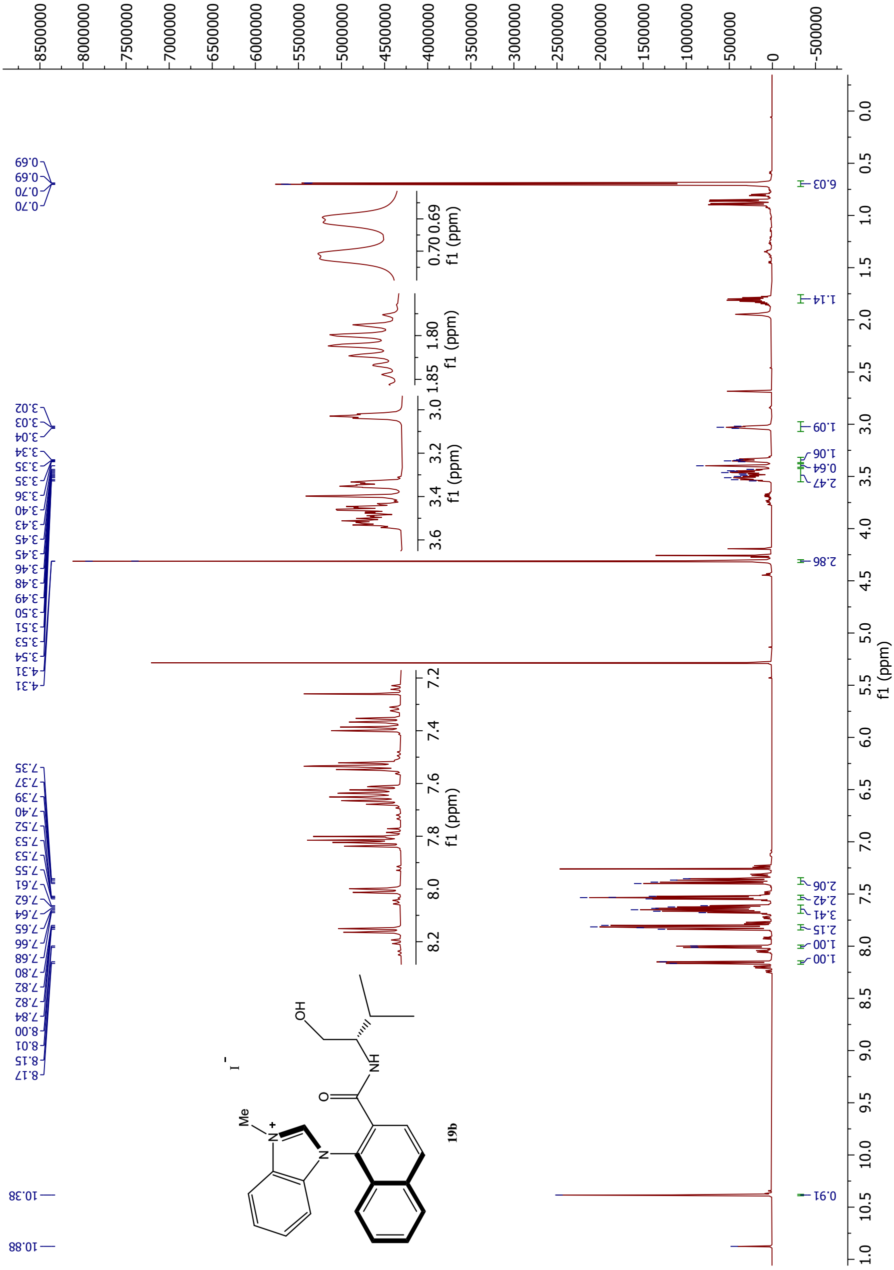

Figure O.1: ^{1}H NMR spectrum of compound **19b**

P Spectroscopic data for compound 20a

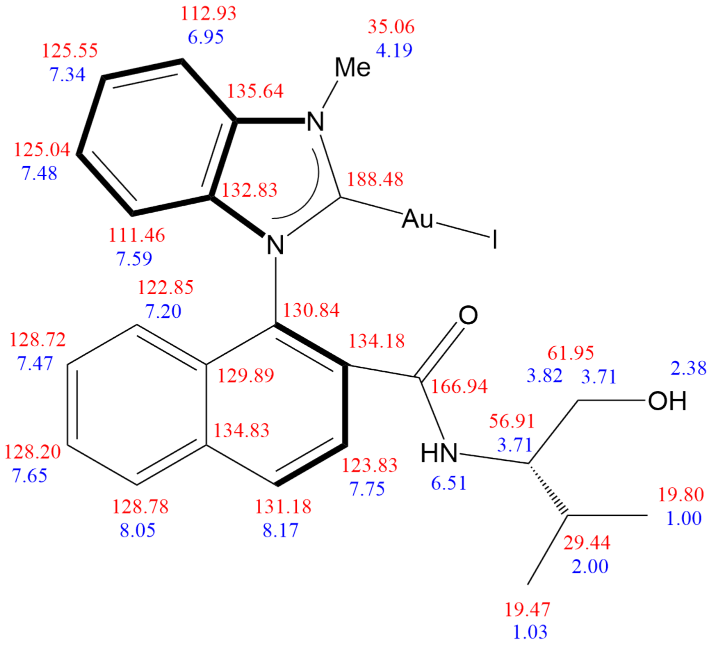

Figure P.1: Assigned ^{1}H and ^{13}C NMR signals of compound **20a**

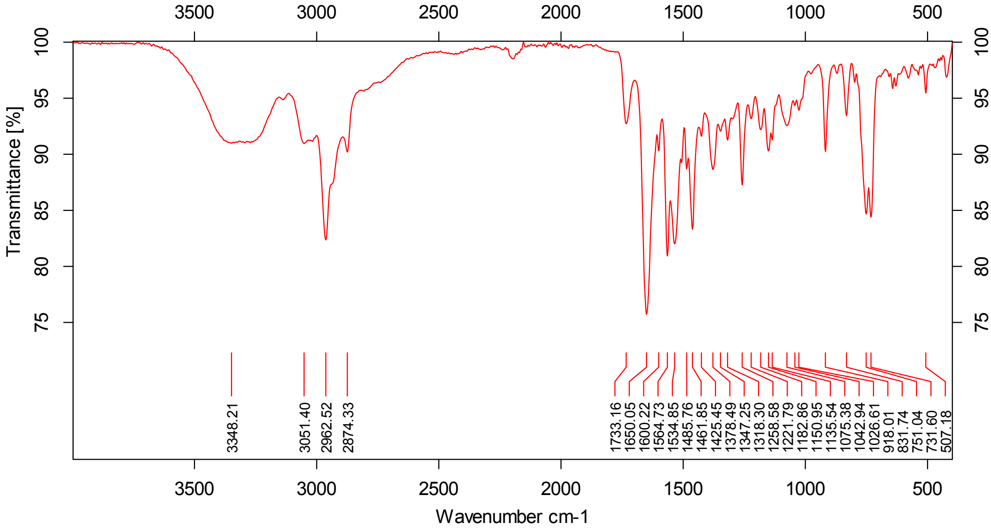

Figure P.2: IR spectrum of compound **20a**

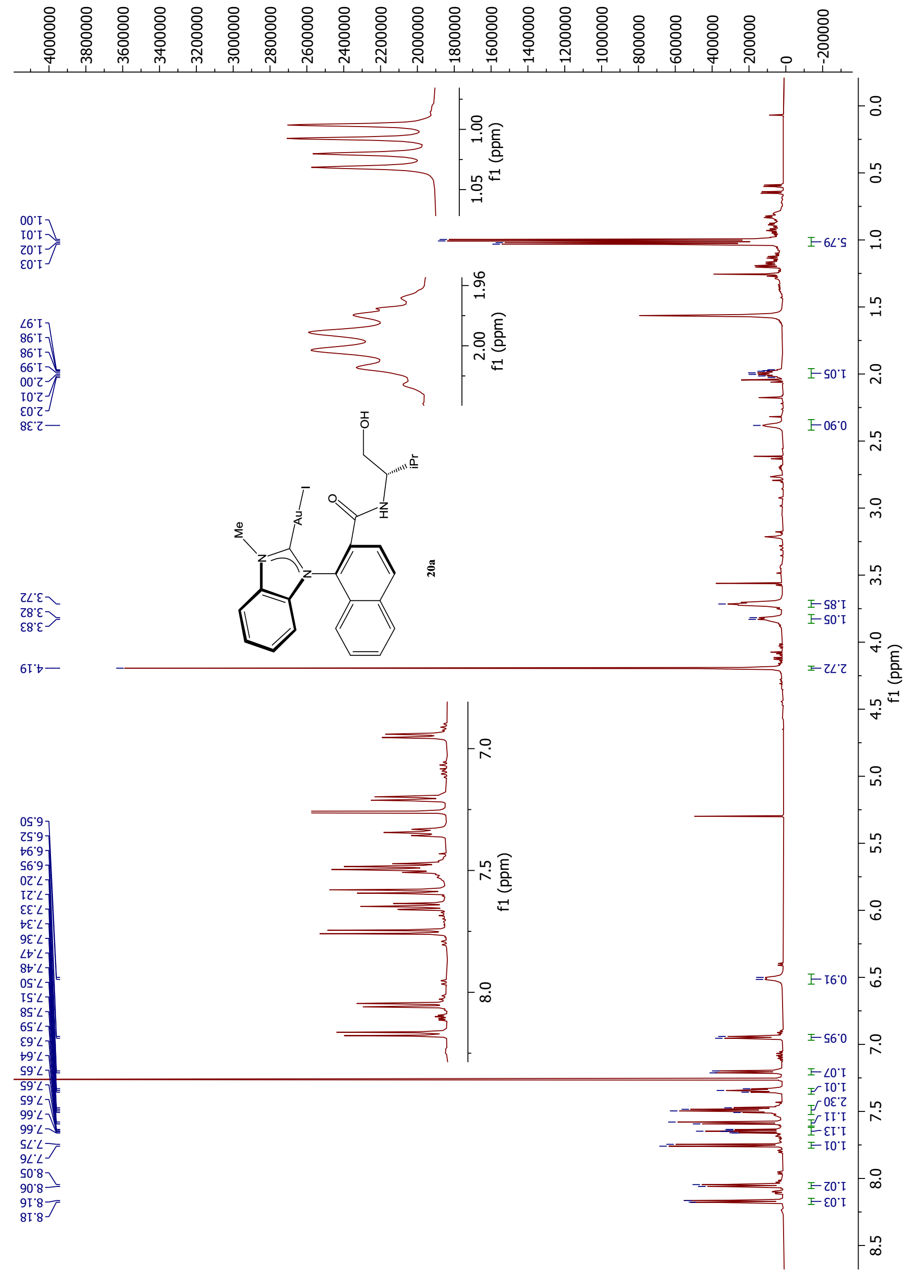

Figure P.3: ^{1}H NMR spectrum of compound **20a**

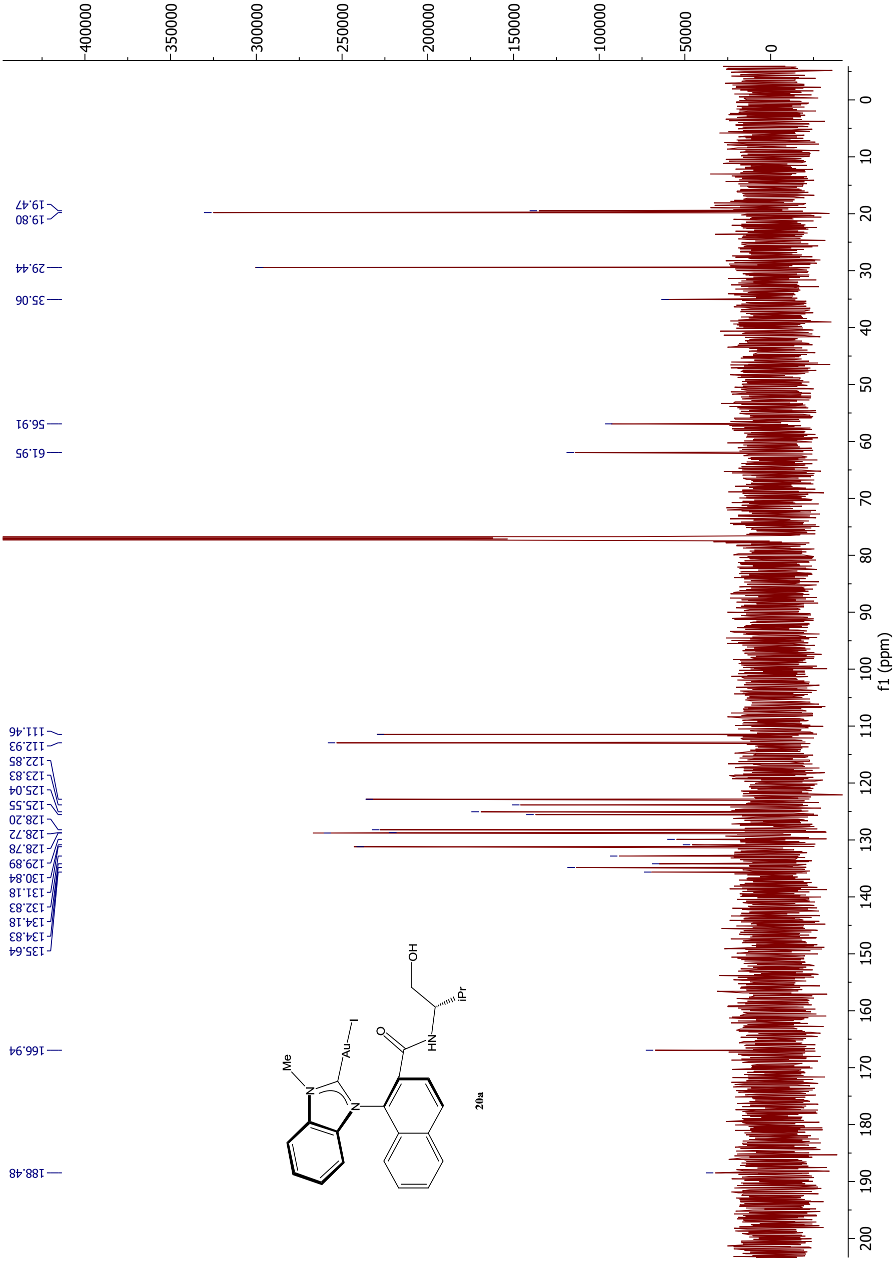

Figure P.4: ^{13}C NMR spectrum of compound **20a**

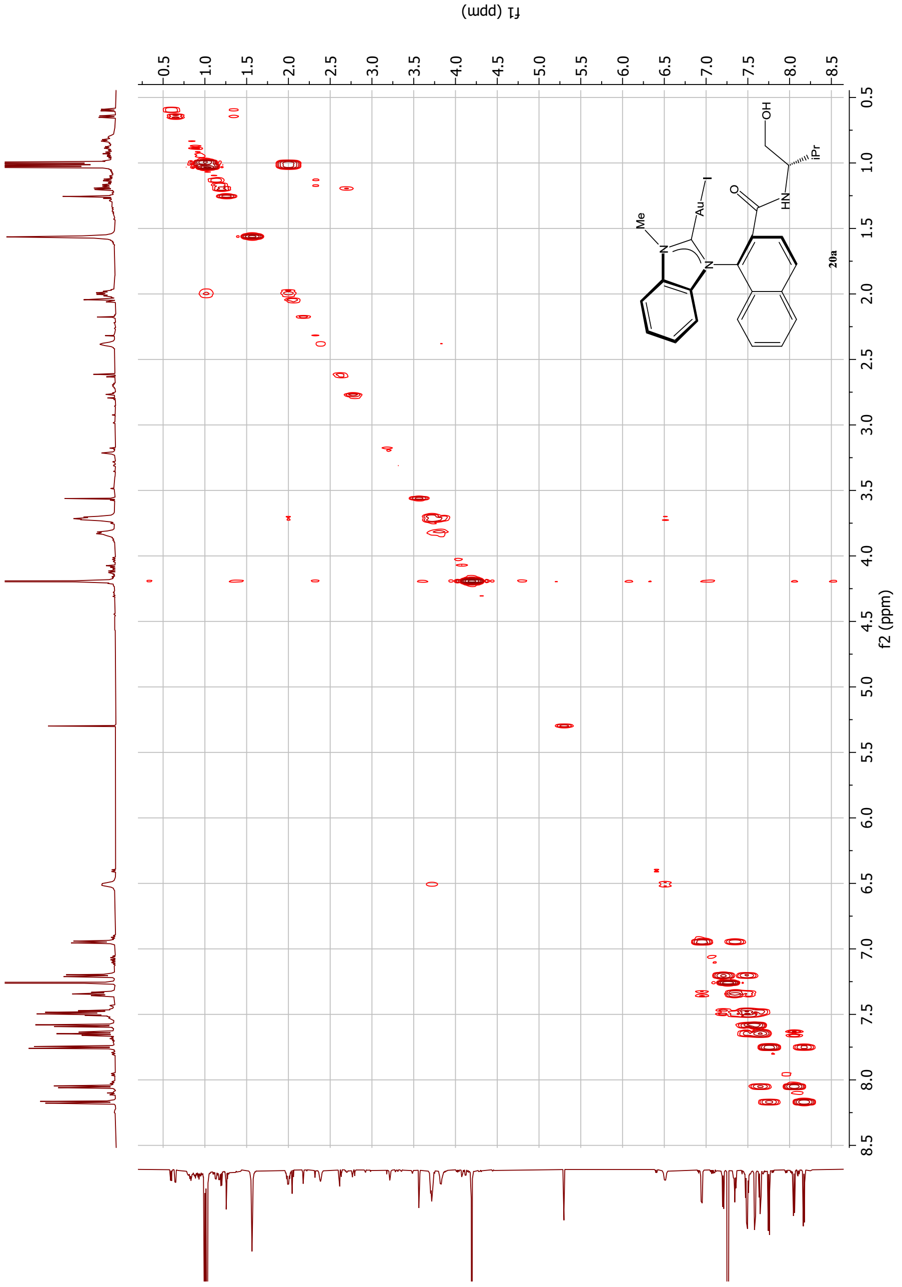

Figure P.5: COSY NMR spectrum of compound **20a**

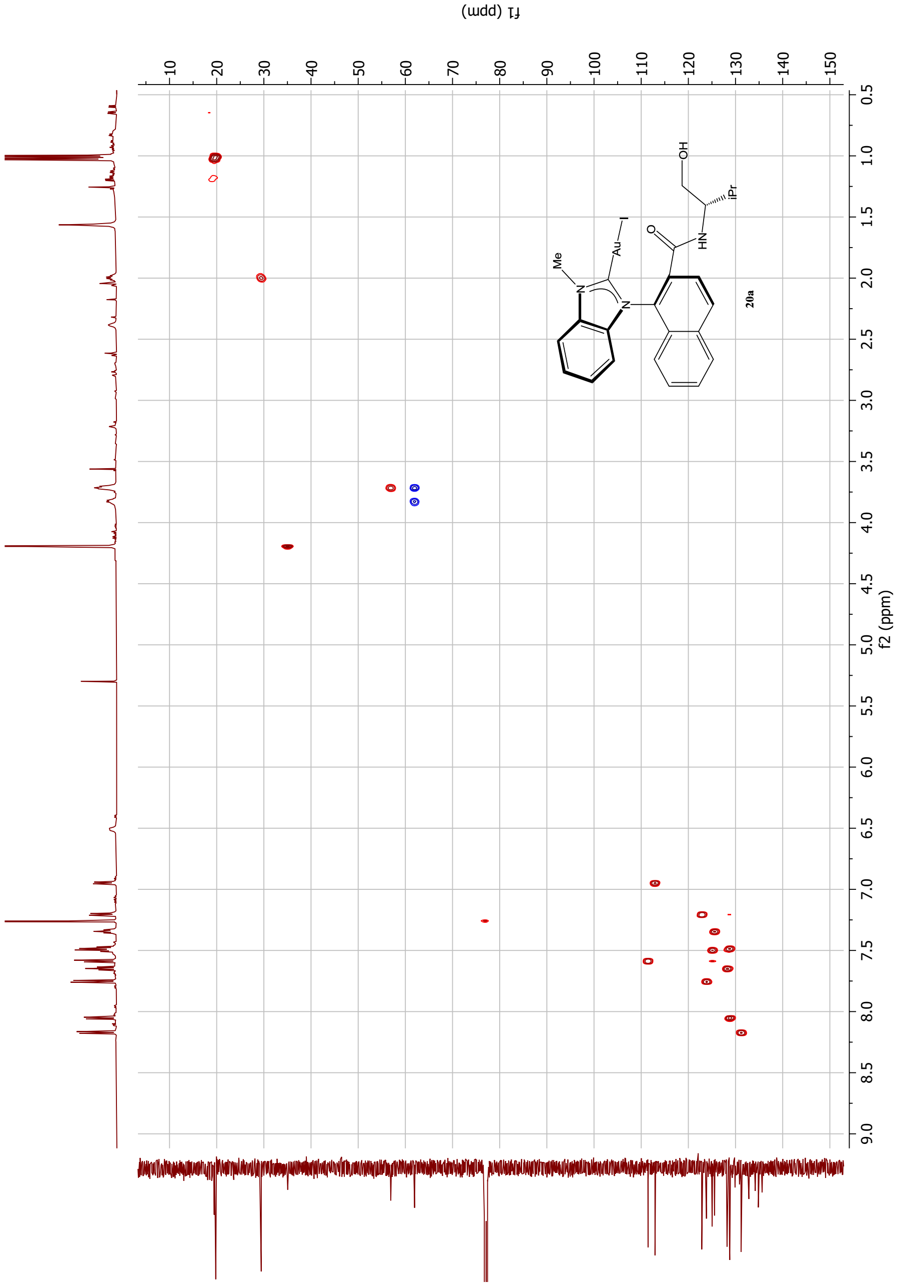

Figure P.6: HSQC NMR spectrum of compound **20a**

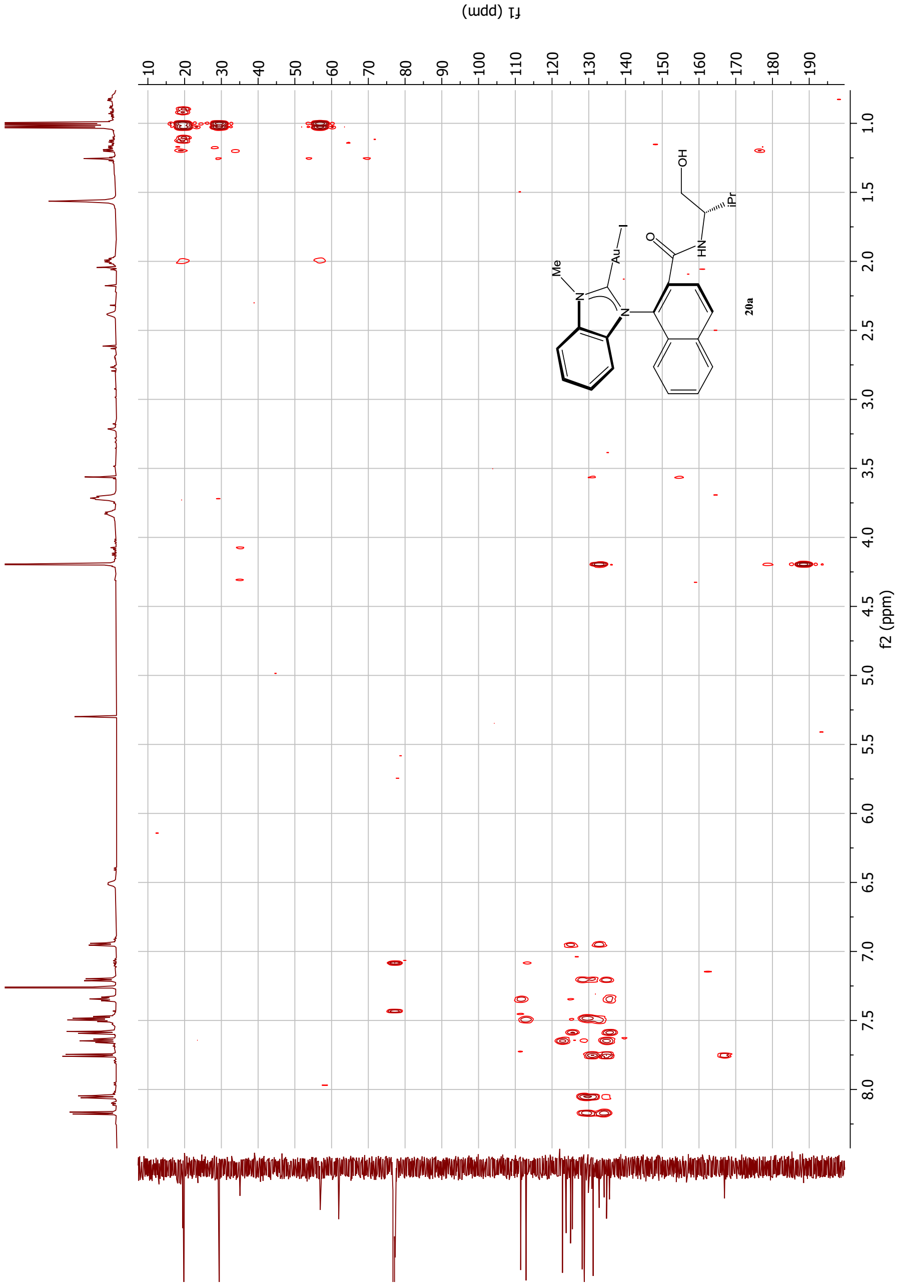

Figure P.7: HMBC NMR spectrum of compound **20a**

Elemental Composition Report

Page 1

Single Mass Analysis

Tolerance = 2.0 PPM / DBE: min = -10.0, max = 50.0
Element prediction: Off
Number of isotope peaks used for i-FIT = 6

Monoisotopic Mass, Even Electron Ions
3717 formula(e) evaluated with 6 results within limits (all results (up to 1000) for each mass)
Elements Used:
C: 0-100 H: 0-100 N: 0-4 O: 0-8 Na: 0-1 Au: 0-1 I: 0-2

2021-162 55 (0.619) AM2 (Ar,35000.0,0.00,0.00); Cm (55:60)
1: TOF MS ES+

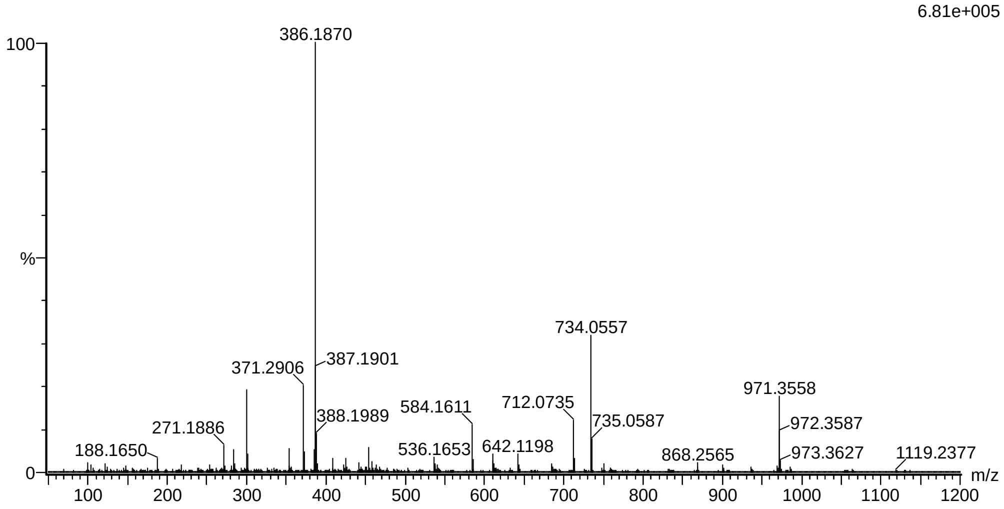

```
Minimum:                                       -10.0
Maximum:                      5.0      2.0     50.0

Mass        Calc. Mass    mDa      PPM      DBE      i-FIT     Norm     Conf(%)  Formula

734.0557    734.0555      0.2      0.3      13.5     1054.7    0.058    94.37    C24 H25 N3 O2 Na
                                                                                 Au I
            734.0553      0.4      0.5      28.5     1066.4    11.729   0.00     C38 H22 N3 O4 Na
                                                                                 I
            734.0564      -0.7     -1.0     8.5      1057.6    2.879    5.62     C25 H35 N3 O5 Na
                                                                                 I2
            734.0566      -0.9     -1.2     -6.5     1063.9    9.259    0.01     C11 H38 N3 O3 Na
                                                                                 Au I2
            734.0568      -1.1     -1.5     36.5     1066.3    11.603   0.00     C39 H11 N3 O Au
            734.0544      1.3      1.8      33.5     1065.5    10.841   0.00     C37 H12 N3 O Na
                                                                                 Au
```

Figure P.8: MS spectrum of compound **20a**

Q Spectroscopic data for compound 20b

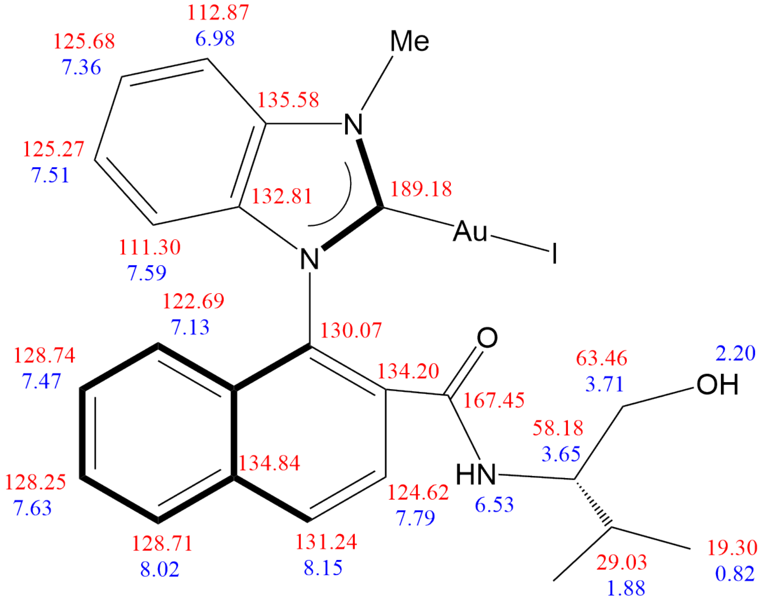

Figure Q.1: Assigned ^{1}H and ^{13}C NMR signals of compound **20b**

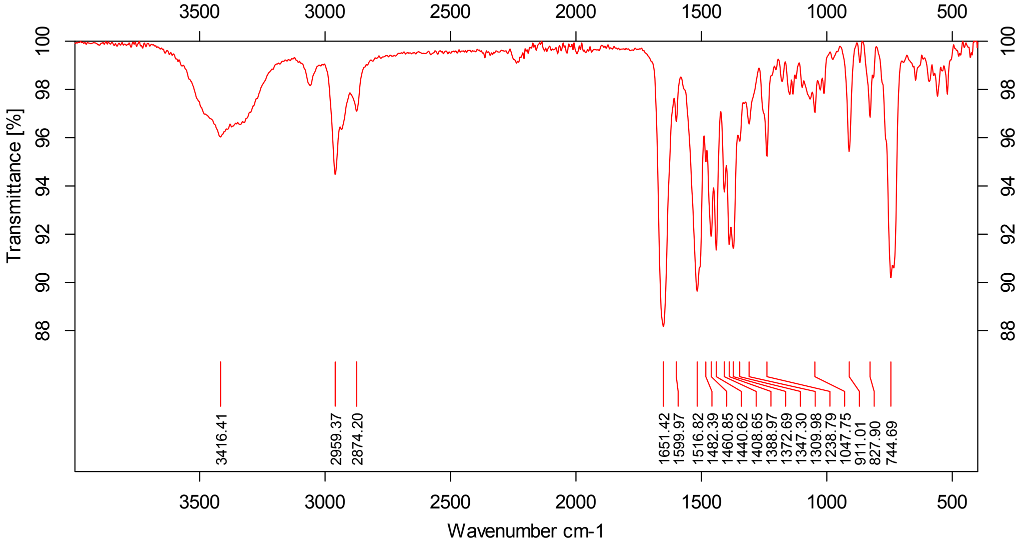

Figure Q.2: IR spectrum of compound **20b**

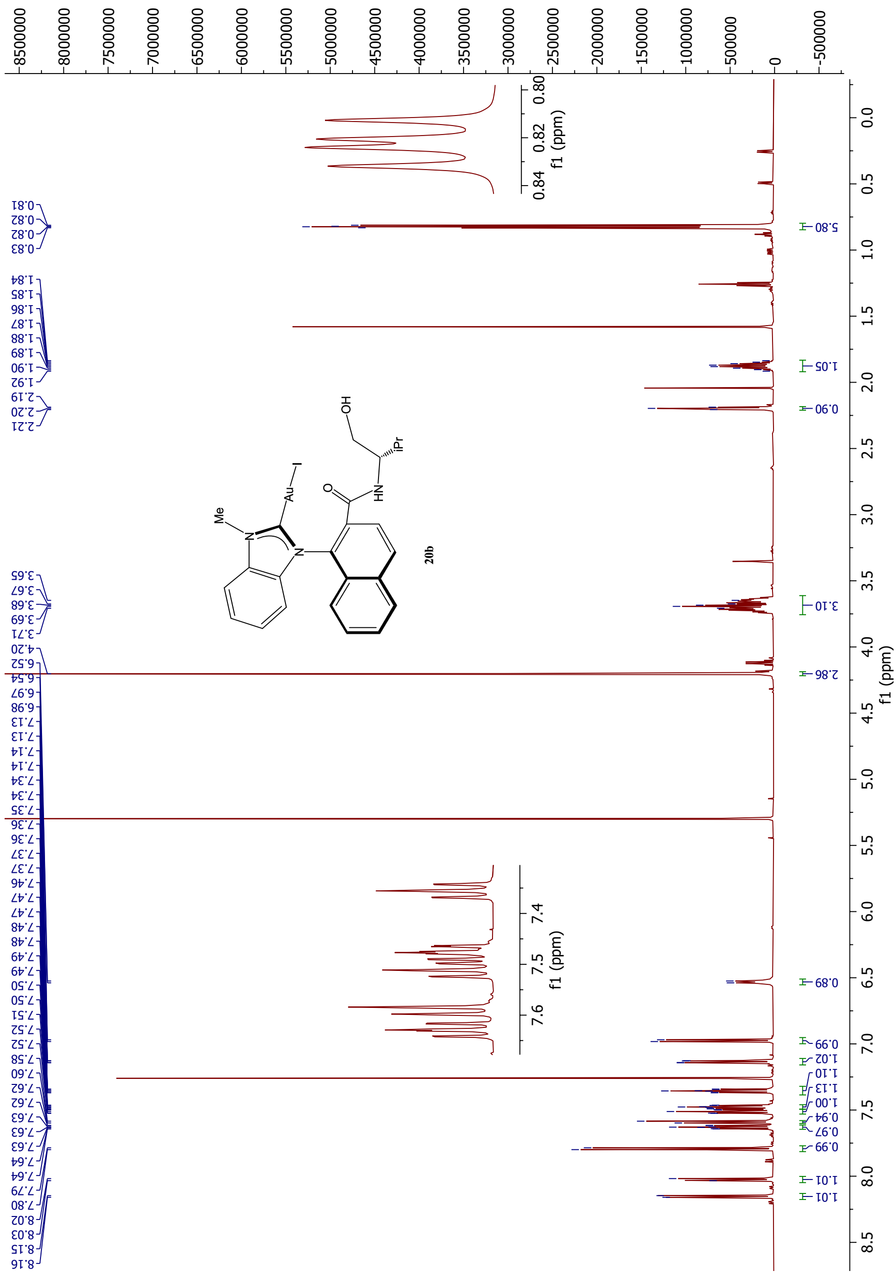

Figure Q.3: ^{1}H NMR spectrum of compound **20b**

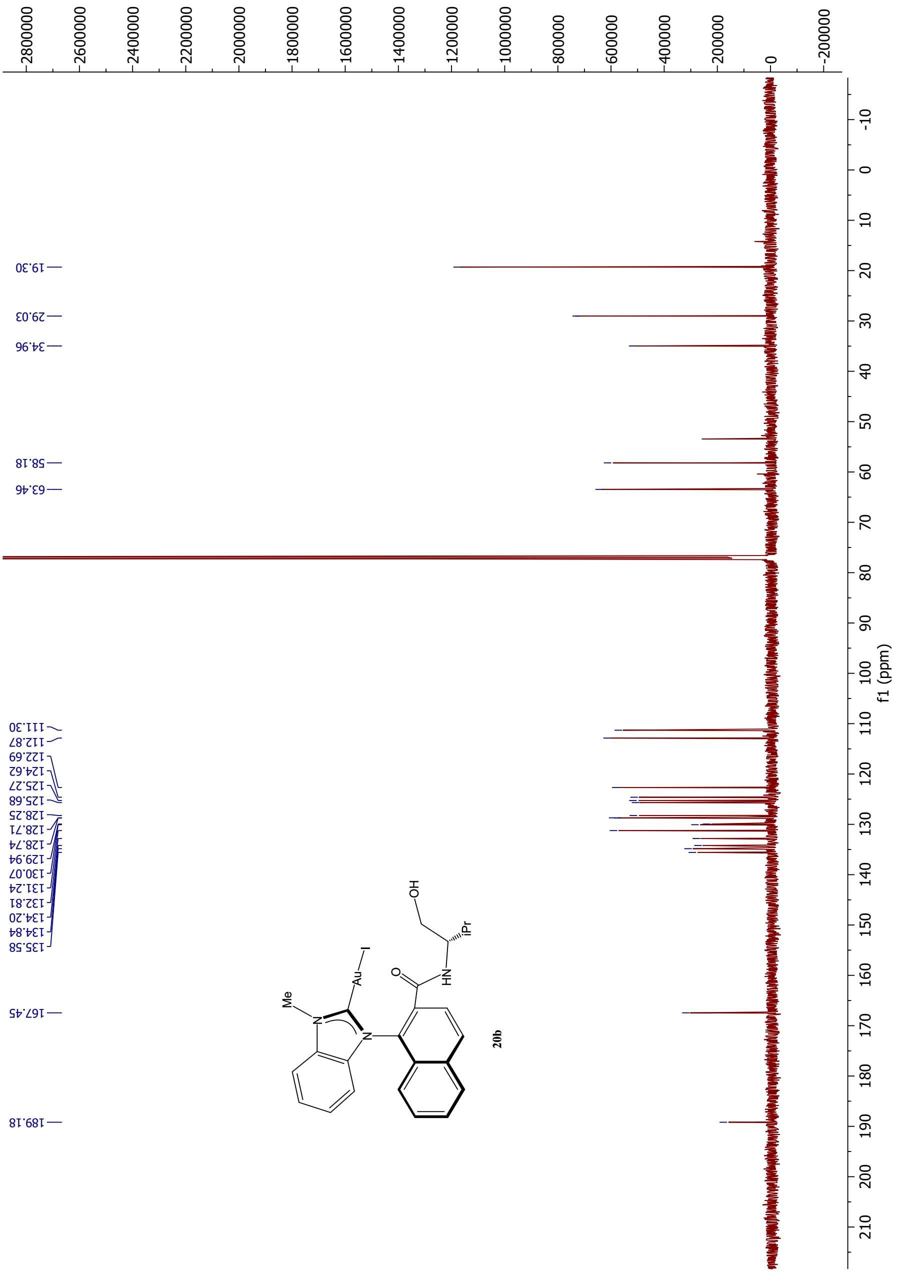

Figure Q.4: ^{13}C NMR spectrum of compound **20b**

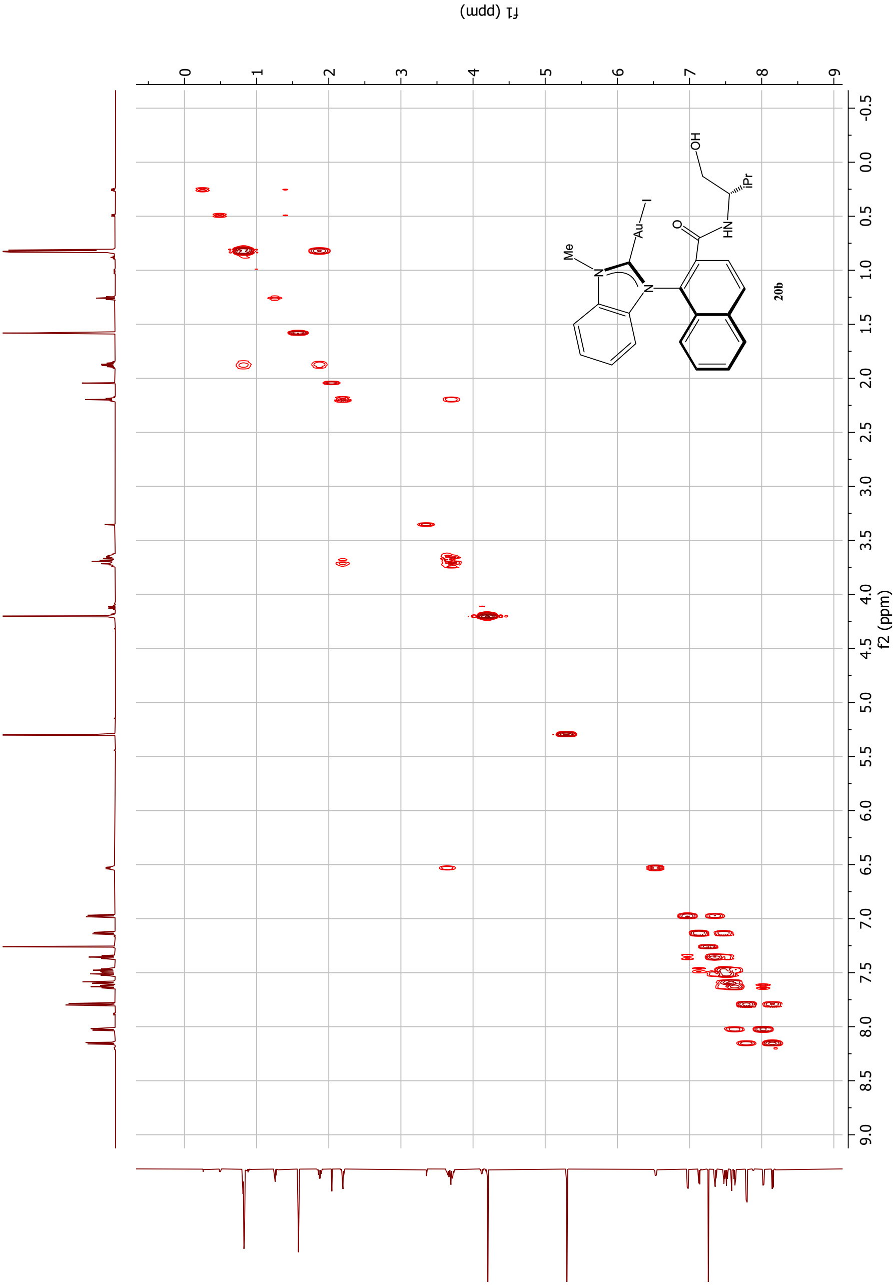

Figure Q.5: COSY NMR spectrum of compound **20b**

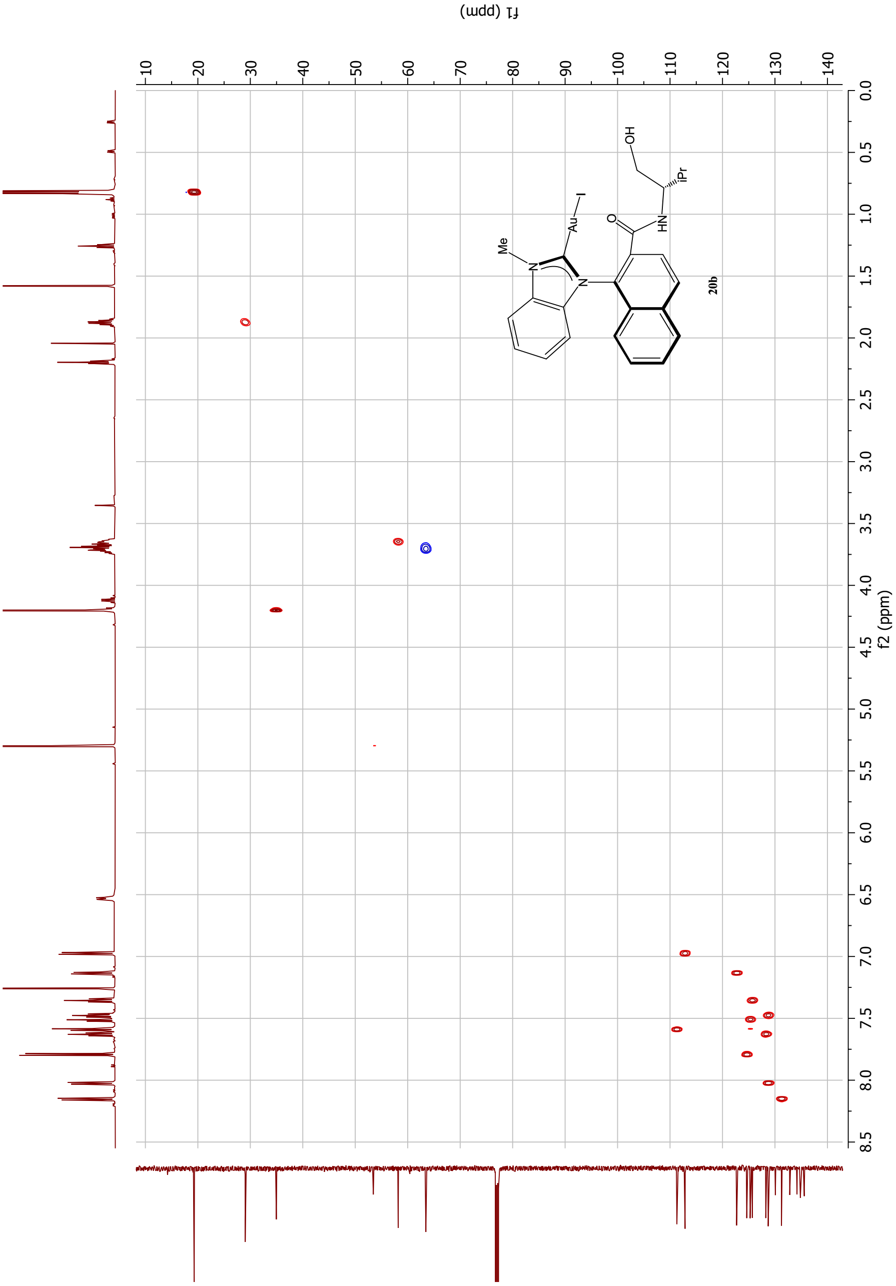

Figure Q.6: HSQC NMR spectrum of compound **20b**

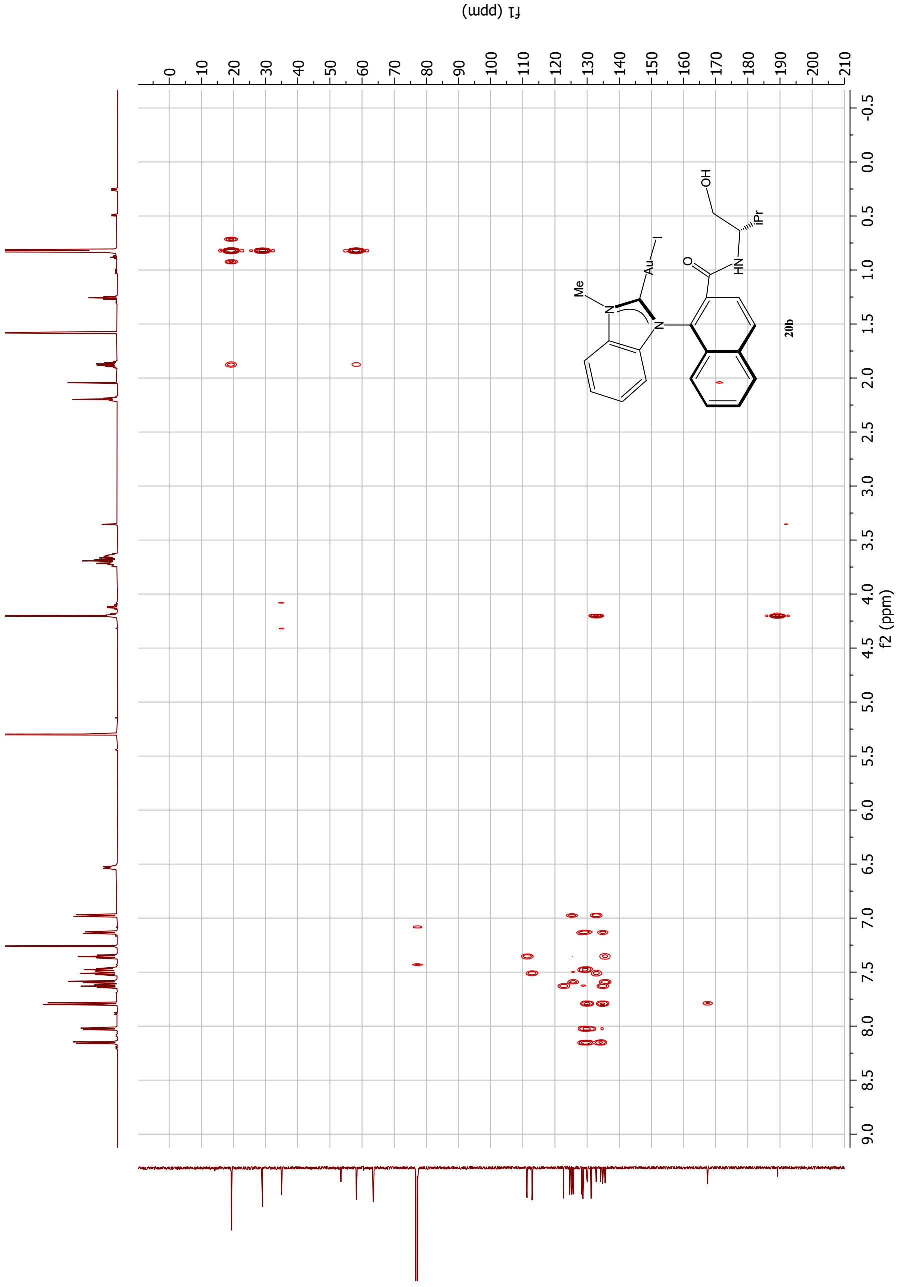

Figure Q.7: HMBC NMR spectrum of compound **20b**

Elemental Composition Report

Page 1

Single Mass Analysis

Tolerance = 2.0 PPM / DBE: min = -10.0, max = 50.0
Element prediction: Off
Number of isotope peaks used for i-FIT = 6

Monoisotopic Mass, Even Electron Ions
3717 formula(e) evaluated with 6 results within limits (all results (up to 1000) for each mass)
Elements Used:
C: 0-100 H: 0-100 N: 0-4 O: 0-8 Na: 0-1 Au: 0-1 I: 0-2

2021-163 69 (0.774) AM2 (Ar,35000.0,0.00,0.00); Cm (69:73)
1: TOF MS ES+

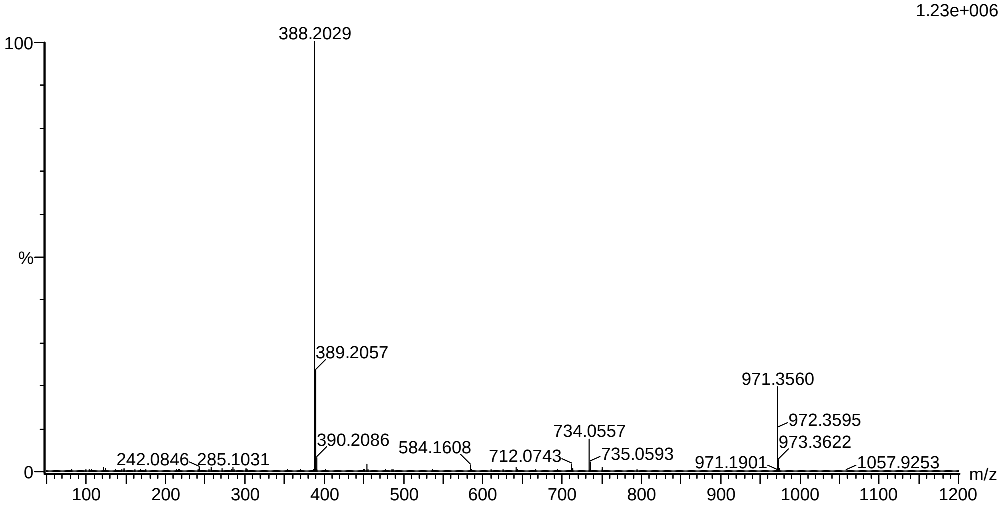

```
Minimum:                                -10.0
Maximum:                  5.0     2.0   50.0

Mass         Calc. Mass   mDa     PPM     DBE     i-FIT    Norm    Conf(%)  Formula

734.0557     734.0555     0.2     0.3     13.5    861.2    0.006   99.40    C24 H25 N3 O2 Na
                                                                            Au I
             734.0553     0.4     0.5     28.5    876.6    15.460  0.00     C38 H22 N3 O4 Na
                                                                            I
             734.0564     -0.7    -1.0    8.5     866.3    5.110   0.60     C25 H35 N3 O5 Na
                                                                            I2
             734.0566     -0.9    -1.2    -6.5    875.5    14.358  0.00     C11 H38 N3 O3 Na
                                                                            Au I2
             734.0568     -1.1    -1.5    36.5    876.5    15.322  0.00     C39 H11 N3 O Au
             734.0544     1.3     1.8     33.5    875.6    14.400  0.00     C37 H12 N3 O Na
                                                                            Au
```

Figure Q.8: MS spectrum of compound **20b**

R Spectroscopic data for compound 22a

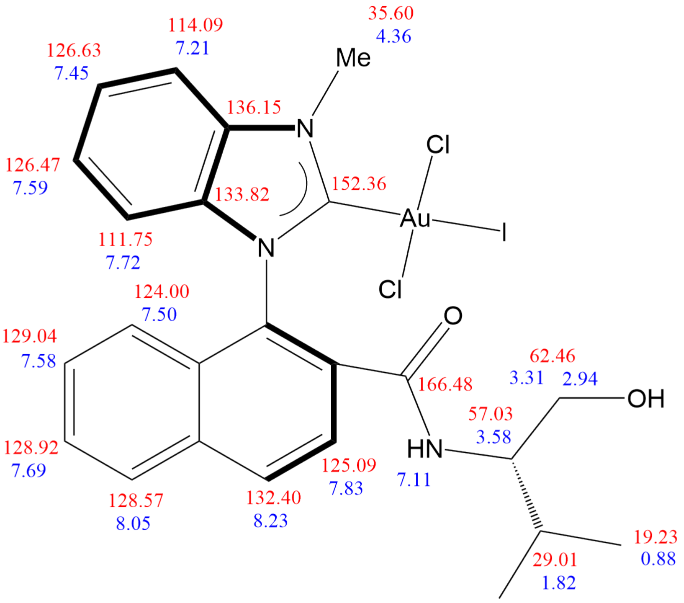

Figure R.1: Assigned ^{1}H and ^{13}C NMR signals of compound **22a**

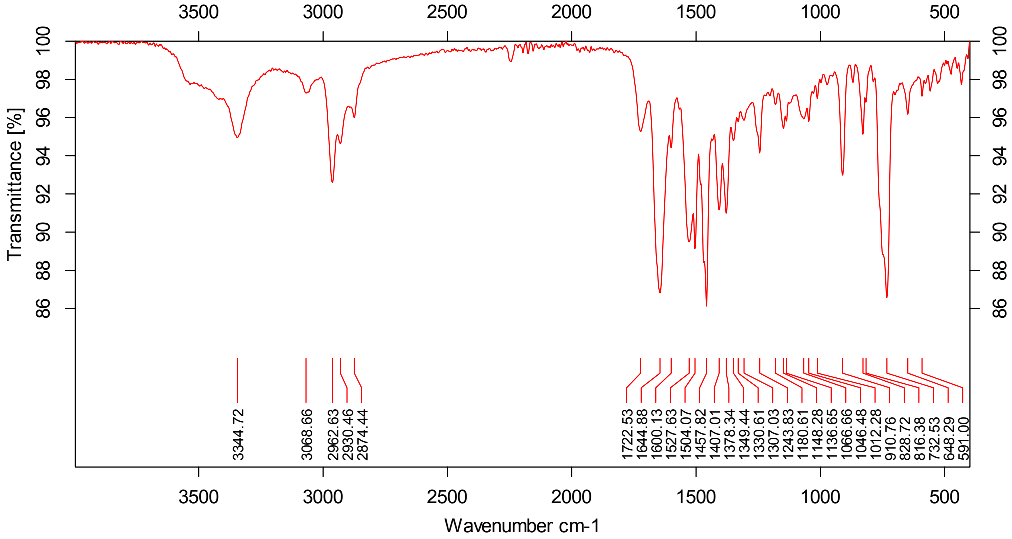

Figure R.2: IR spectrum of compound **22a**

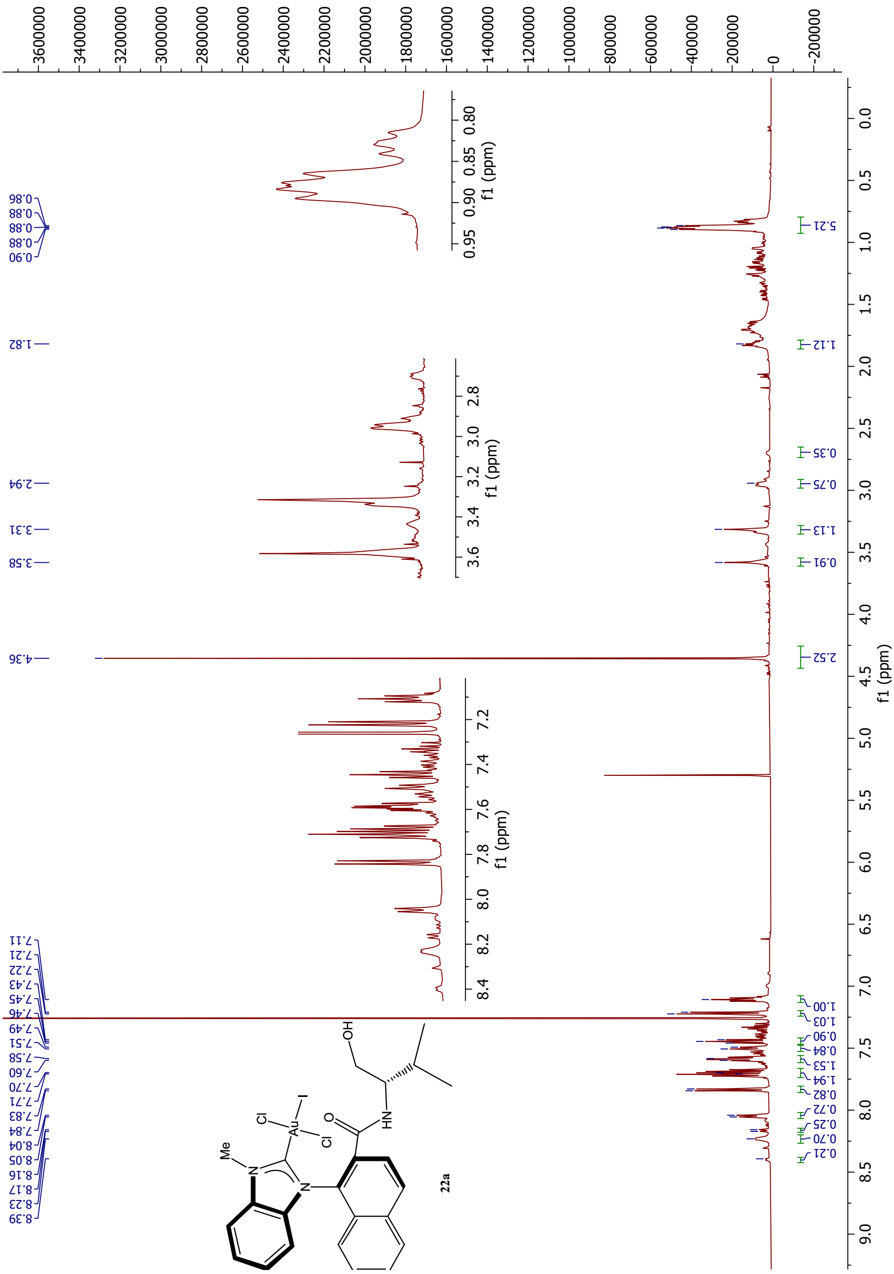

Figure R.3: ^{1}H NMR spectrum of compound **22a**

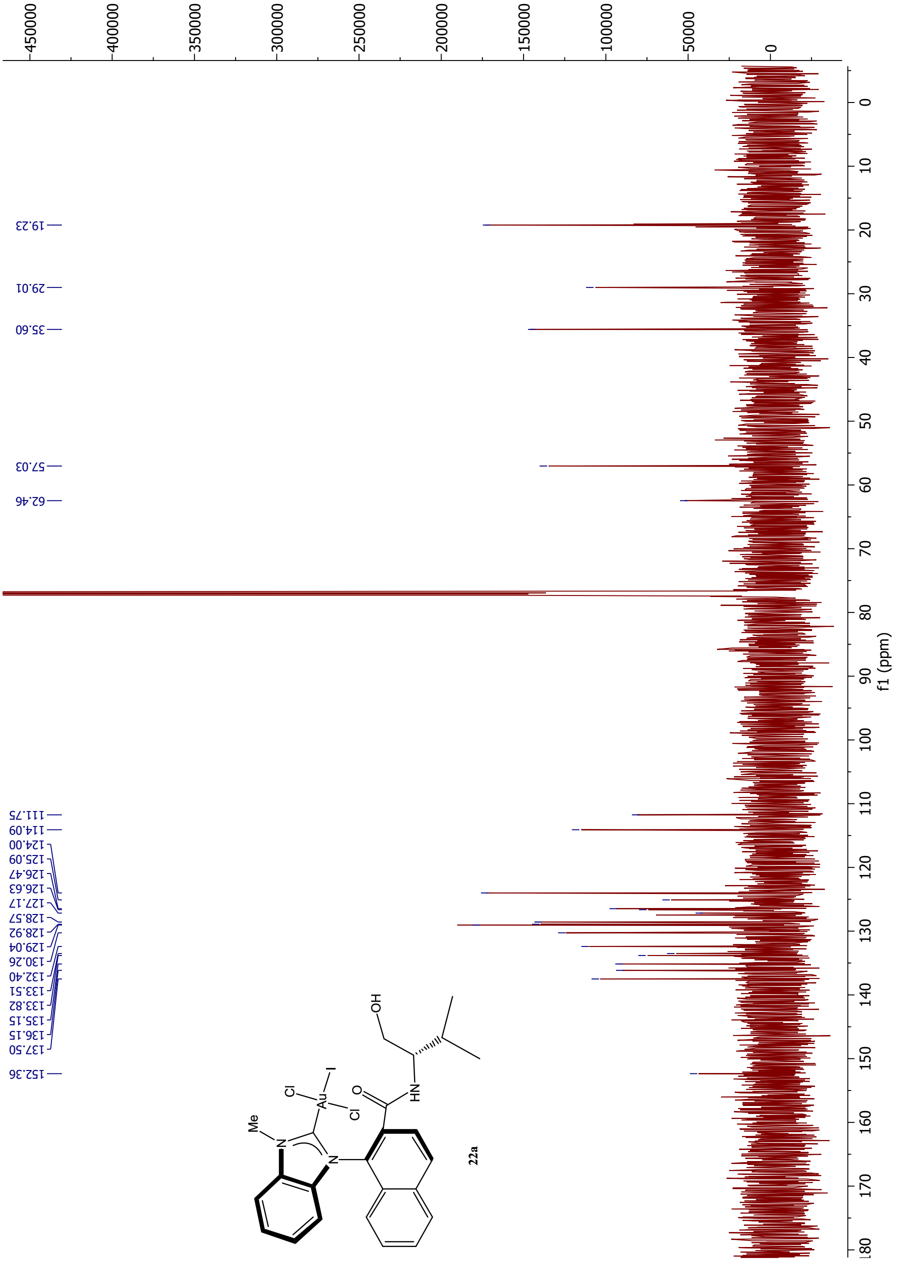

Figure R.4: ^{13}C NMR spectrum of compound **22a**

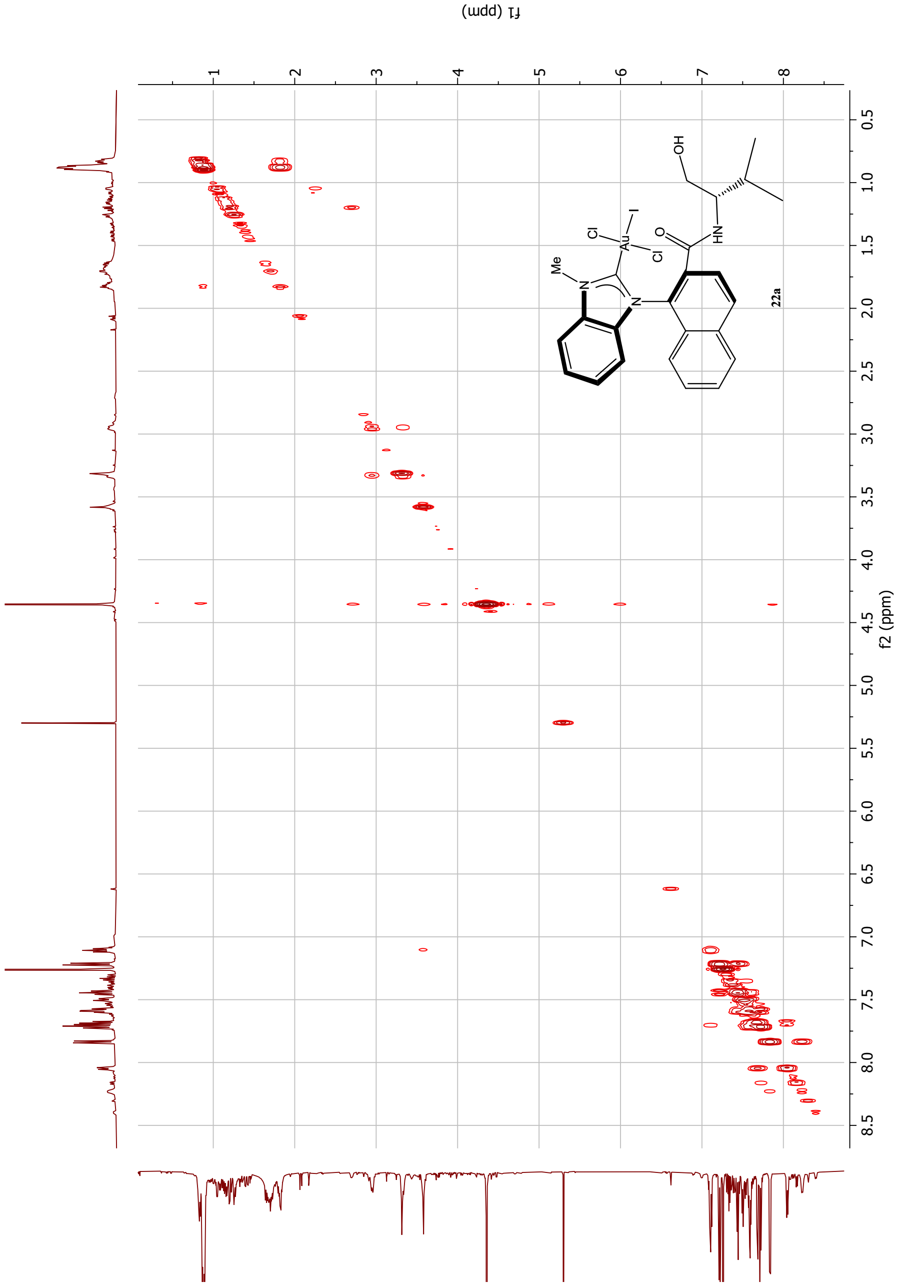

Figure R.5: COSY NMR spectrum of compound **22a**

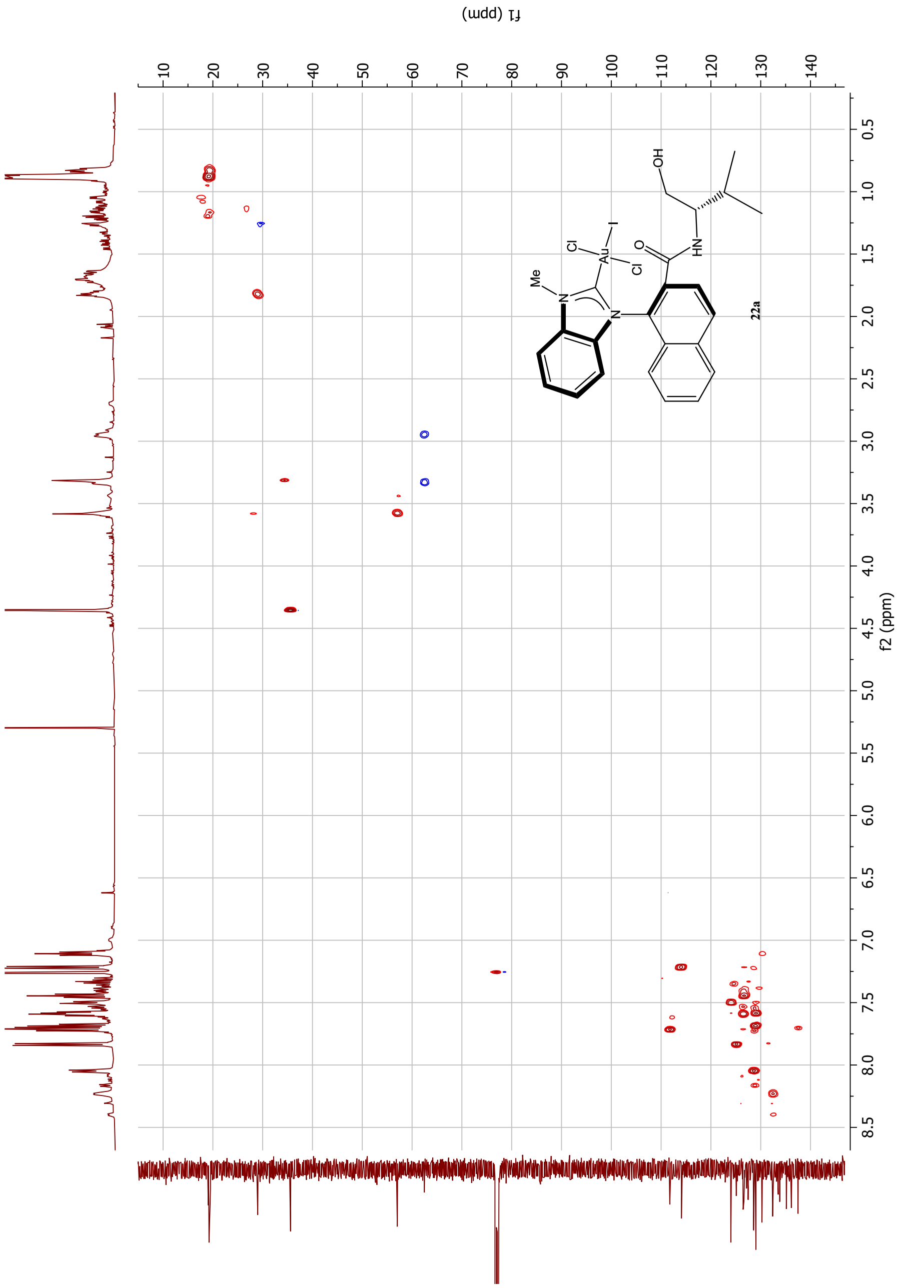

Figure R.6: HSQC NMR spectrum of compound **22a**

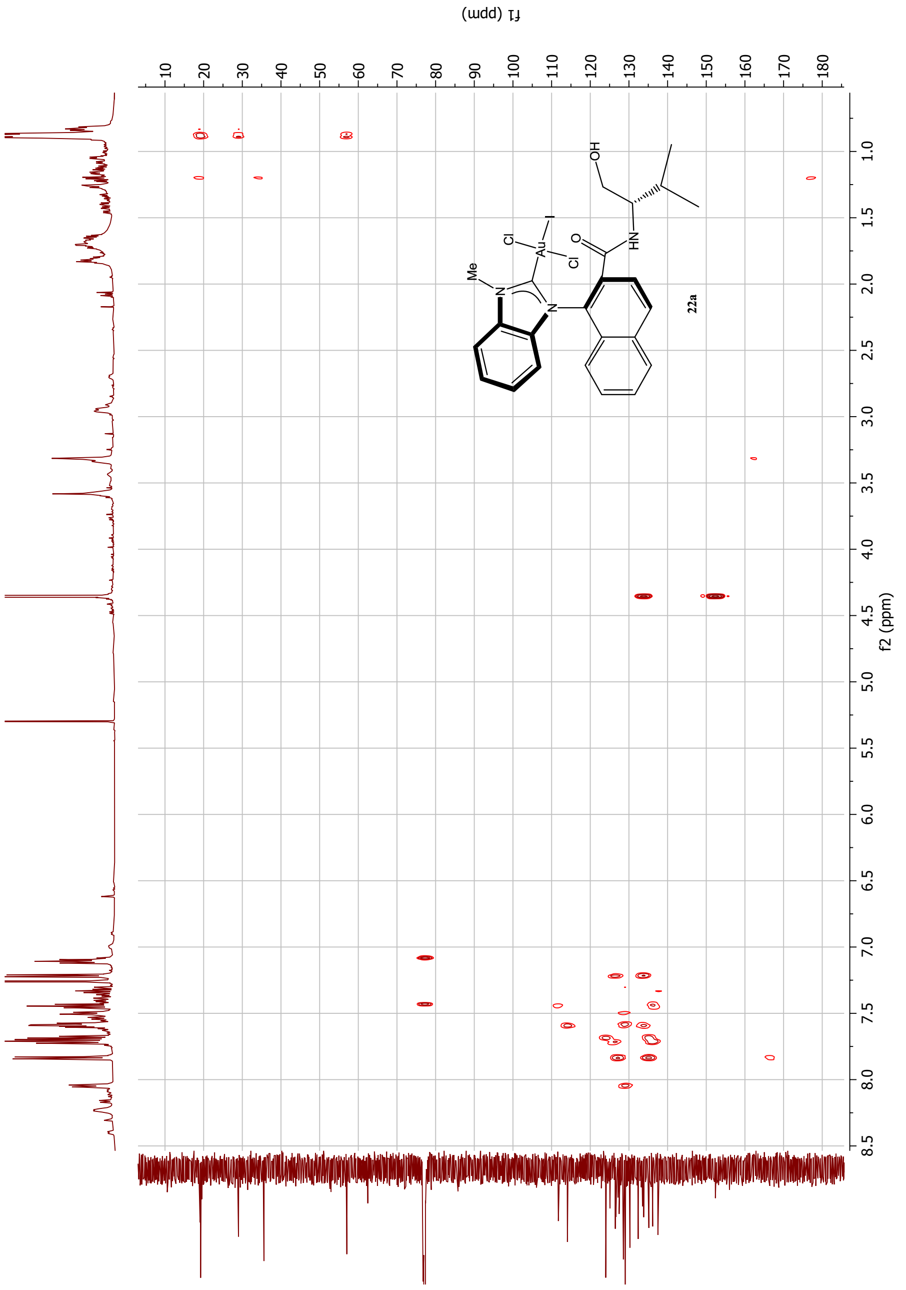

Figure R.7: HMBC NMR spectrum of compound **22a**

Elemental Composition Report Page 1

Single Mass Analysis
Tolerance = 3.0 PPM / DBE: min = -1.5, max = 50.0
Element prediction: Off
Number of isotope peaks used for i-FIT = 3

Monoisotopic Mass, Even Electron Ions
5105 formula(e) evaluated with 15 results within limits (up to 50 closest results for each mass)
Elements Used:
C: 0-500 H: 0-1000 N: 0-7 O: 0-10 Cl: 0-2 Au: 0-1

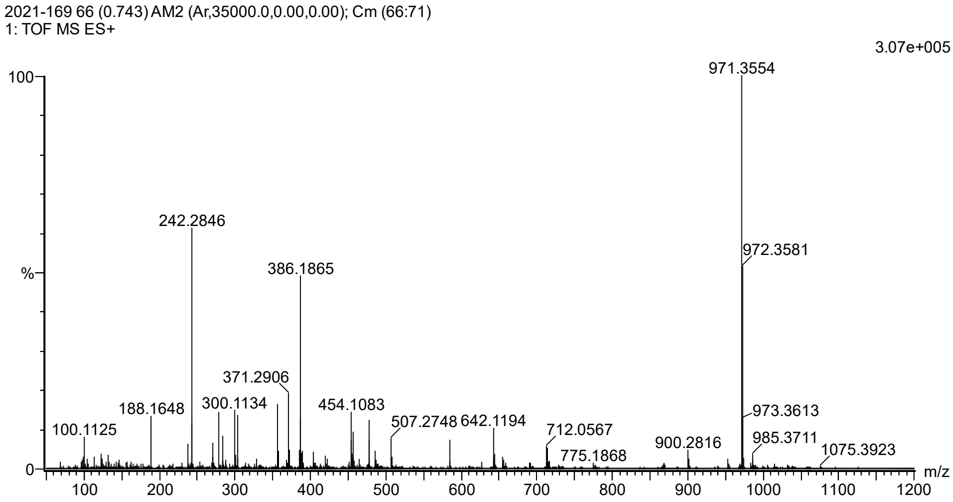

```
Minimum:                              -1.5
Maximum:                5.0     3.0   50.0

Mass        Calc. Mass  mDa     PPM   DBE     i-FIT   Norm    Conf(%) Formula

971.3554    971.3546    0.8     0.8   22.5    384.7   0.368   69.20   C47 H54 N2 O8 Au
            971.3559    -0.5    -0.5  27.5    385.6   1.190   30.43   C48 H50 N6 O4 Au
```

Figure R.8: MS spectrum of compound **22a**

S Spectroscopic data for compound 22b

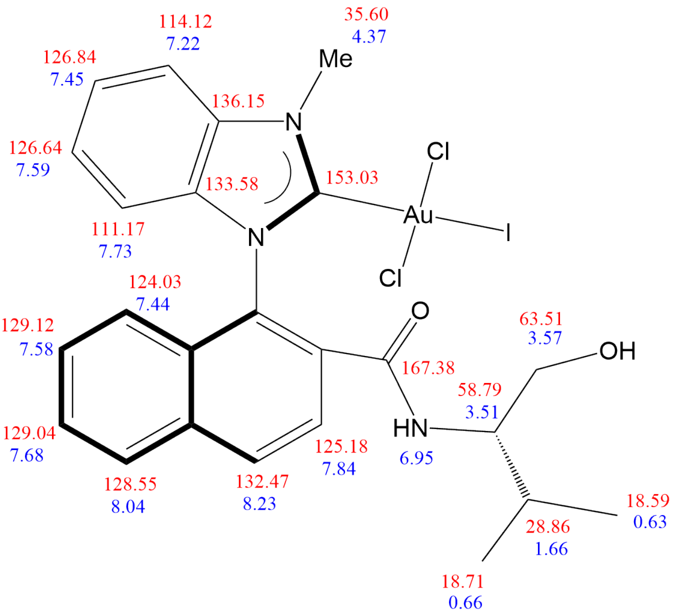

Figure S.1: Assigned ^{1}H and ^{13}C NMR signals of compound **22b**

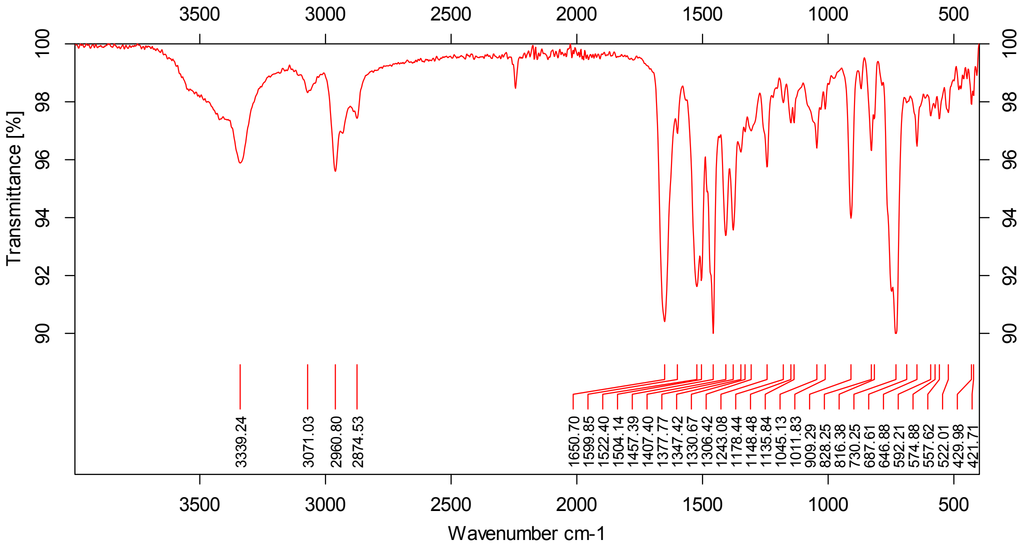

Figure S.2: IR spectrum of compound **22b**

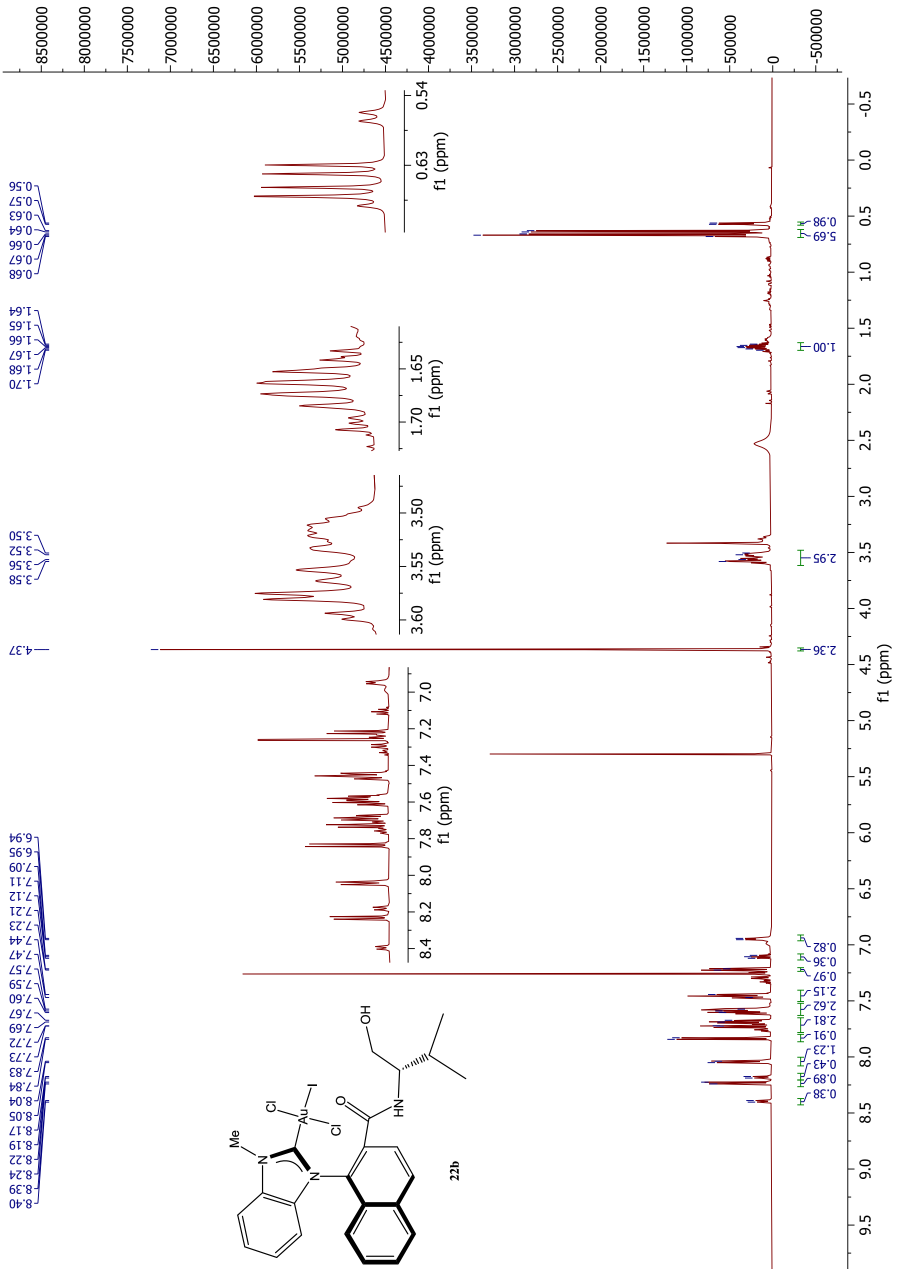

Figure S.3: ^{1}H NMR spectrum of compound **22b**

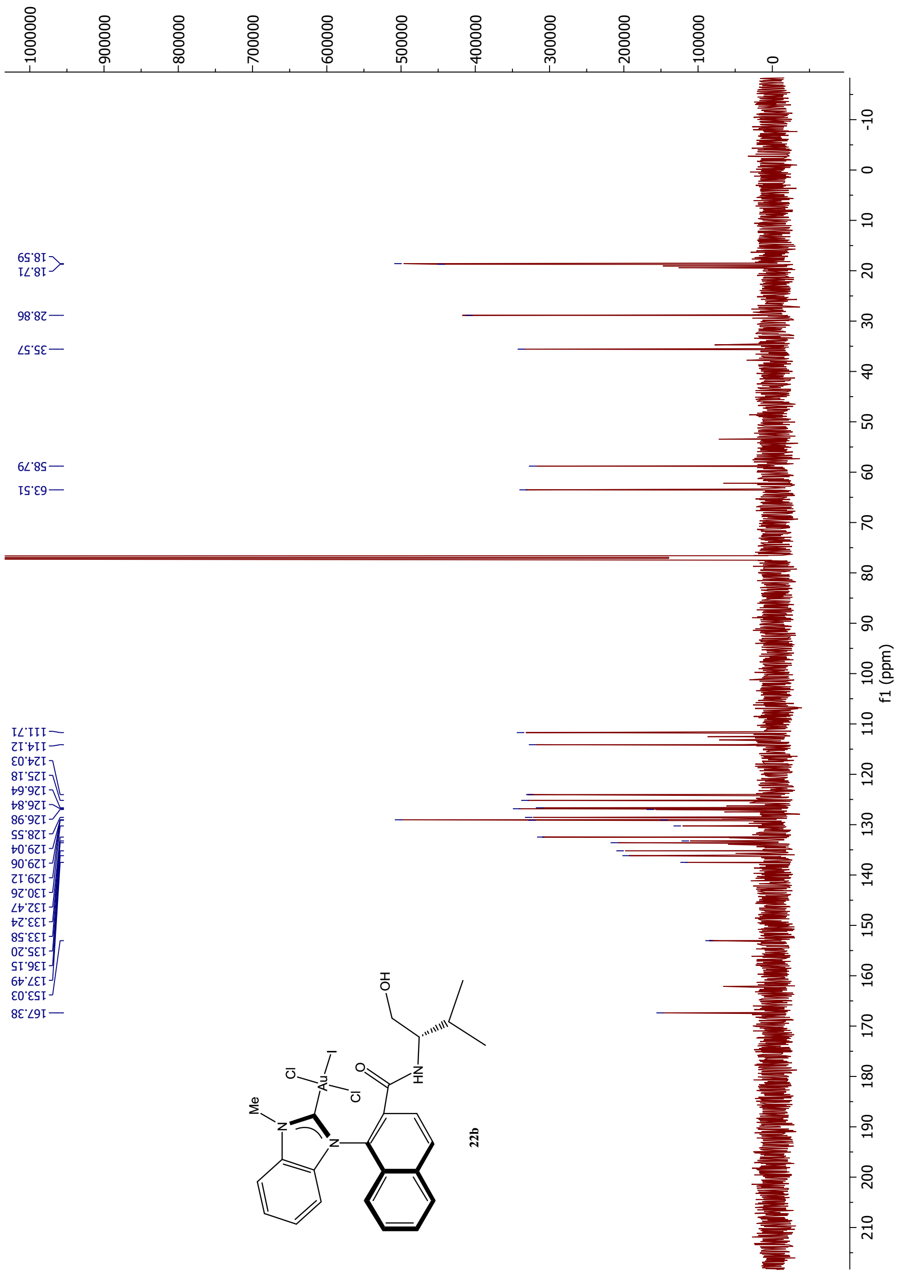

Figure S.4: ^{13}C NMR spectrum of compound **22b**

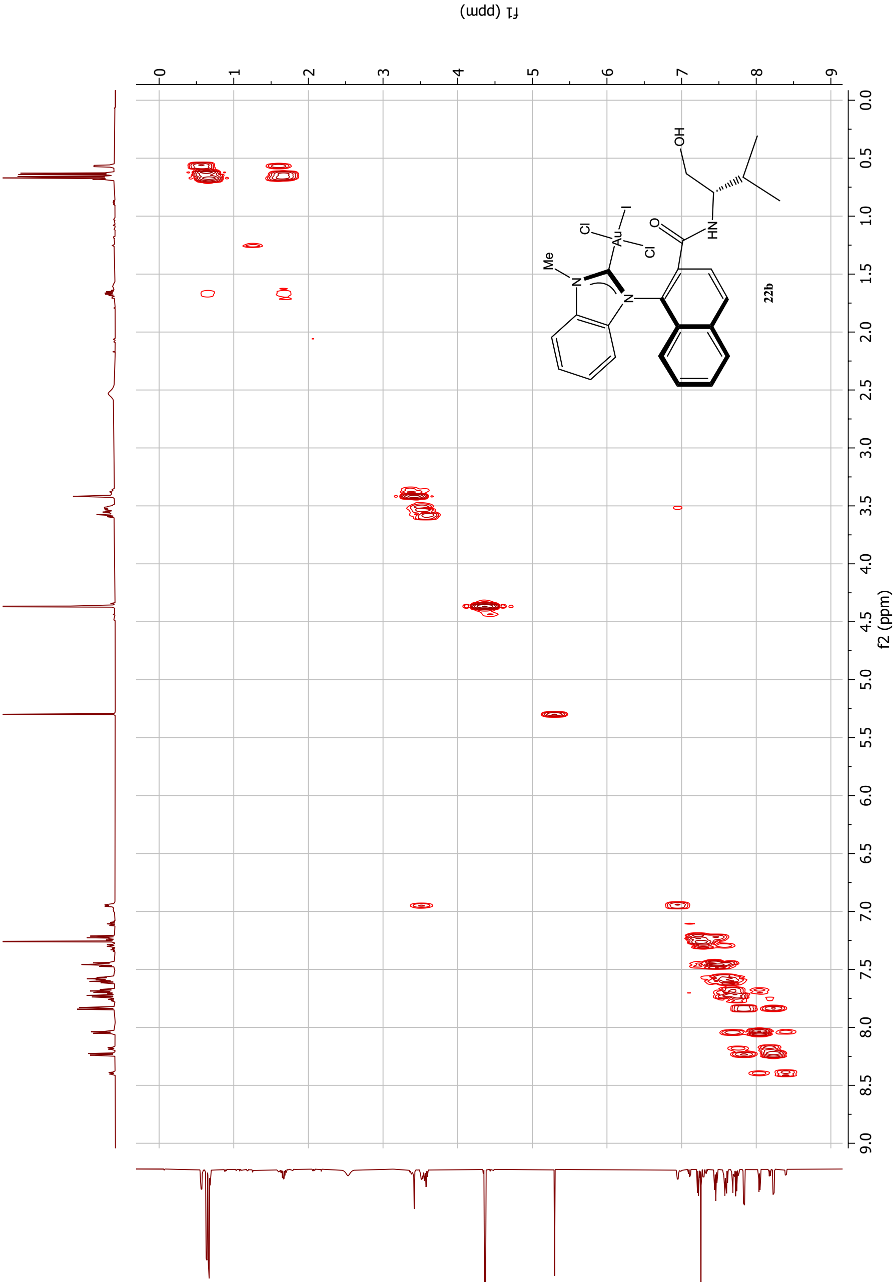

Figure S.5: COSY NMR spectrum of compound **22b**

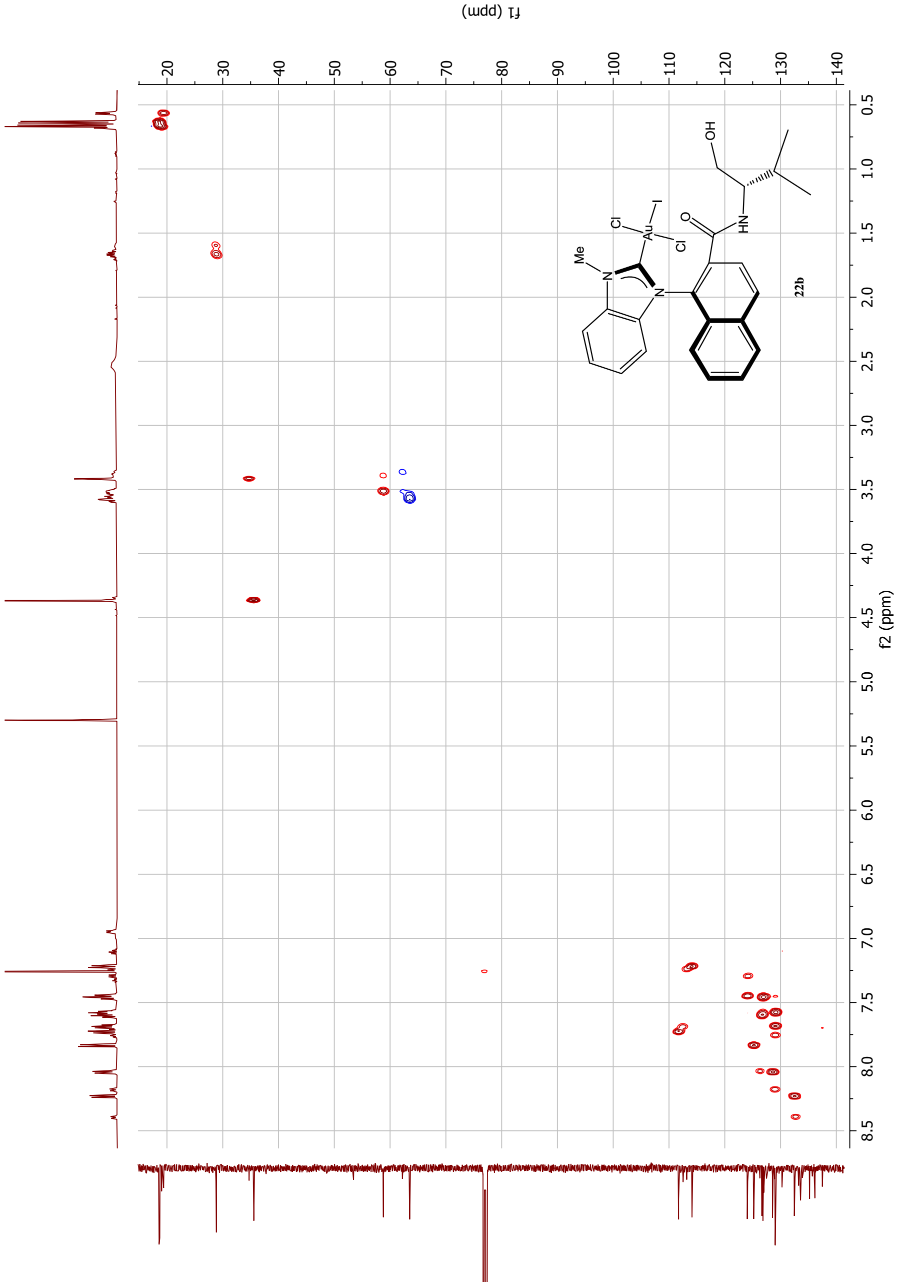

Figure S.6: HSQC NMR spectrum of compound **22b**

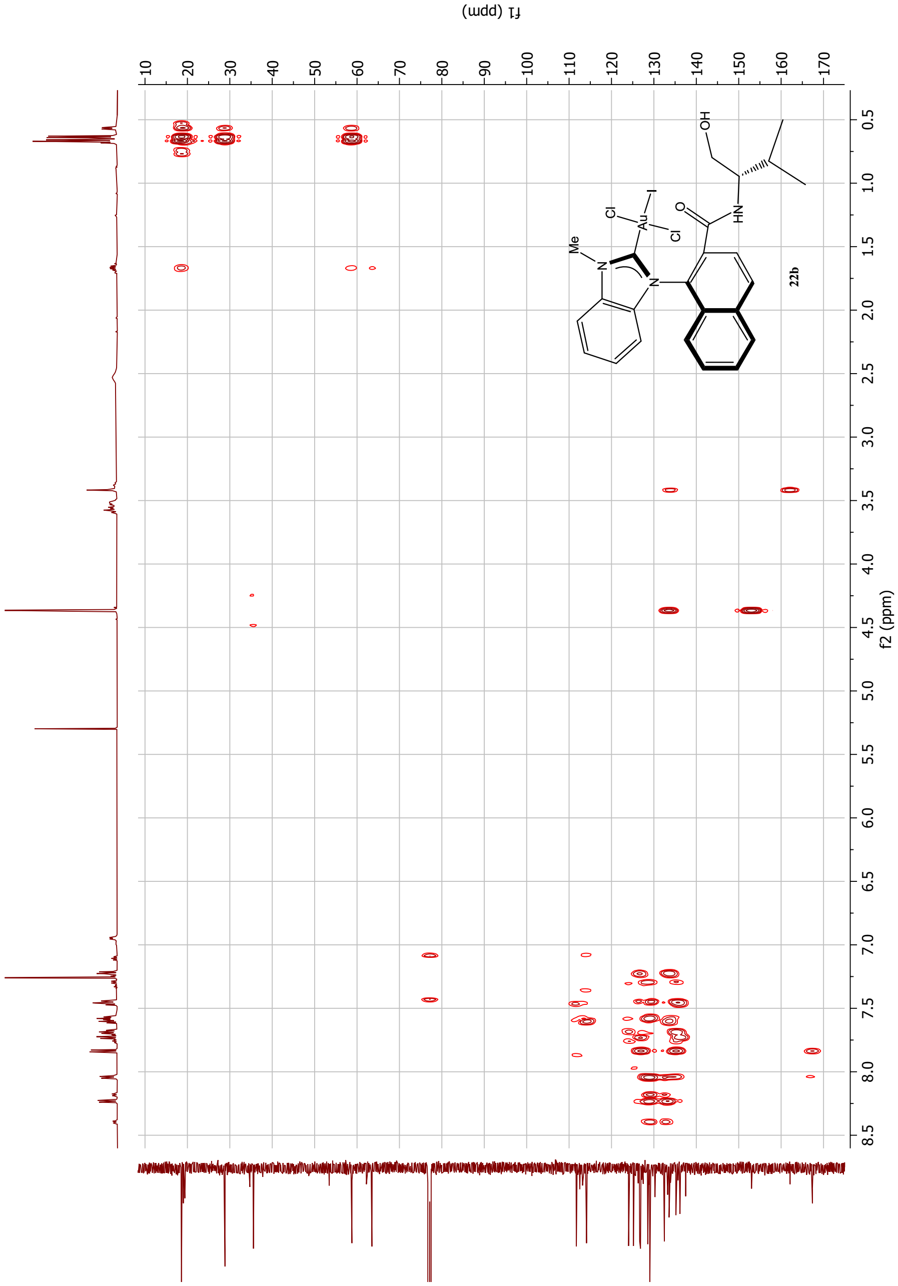

Figure S.7: HMBC NMR spectrum of compound **22b**

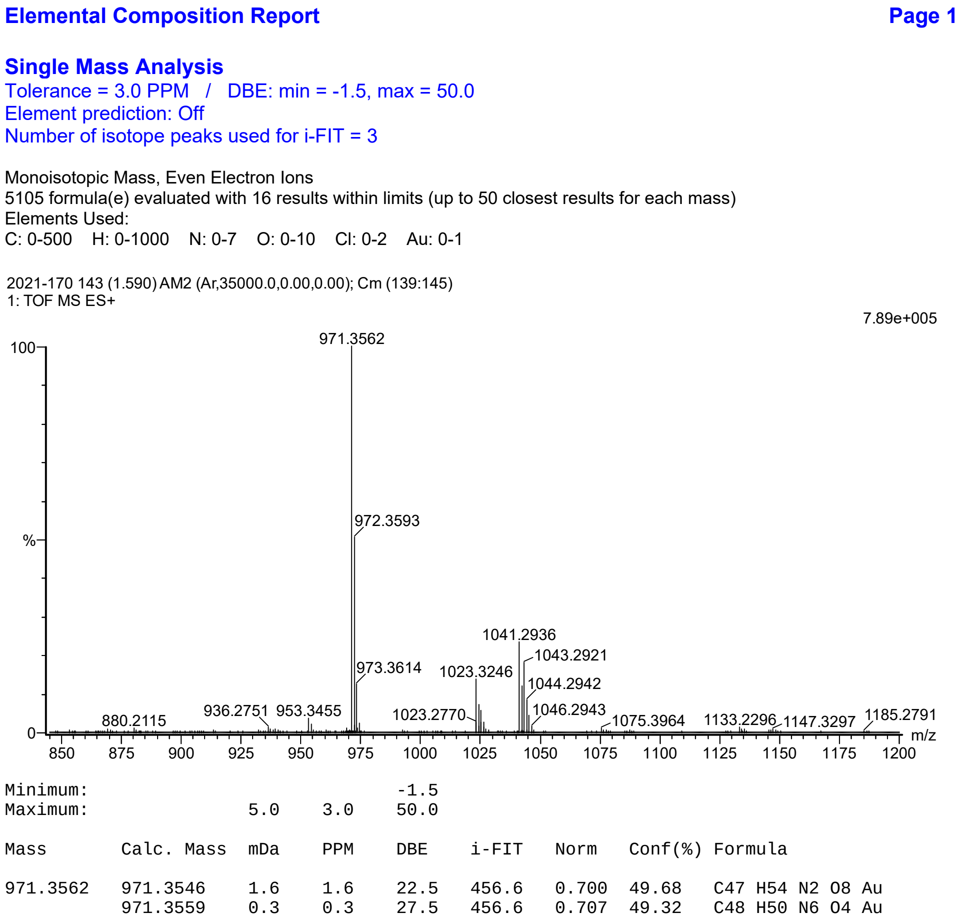

Elemental Composition Report **Page 1**

Single Mass Analysis
Tolerance = 3.0 PPM / DBE: min = -1.5, max = 50.0
Element prediction: Off
Number of isotope peaks used for i-FIT = 3

Monoisotopic Mass, Even Electron Ions
5105 formula(e) evaluated with 16 results within limits (up to 50 closest results for each mass)
Elements Used:
C: 0-500 H: 0-1000 N: 0-7 O: 0-10 Cl: 0-2 Au: 0-1

2021-170 143 (1.590) AM2 (Ar,35000.0,0.00,0.00); Cm (139:145)
1: TOF MS ES+

```
Minimum:                                  -1.5
Maximum:                 5.0     3.0      50.0

Mass        Calc. Mass   mDa     PPM      DBE     i-FIT    Norm   Conf(%) Formula

971.3562    971.3546     1.6     1.6      22.5    456.6    0.700  49.68   C47 H54 N2 O8 Au
            971.3559     0.3     0.3      27.5    456.6    0.707  49.32   C48 H50 N6 O4 Au
```

Figure S.8: MS spectrum of compound **22b**

T Spectroscopic data for compound 17b

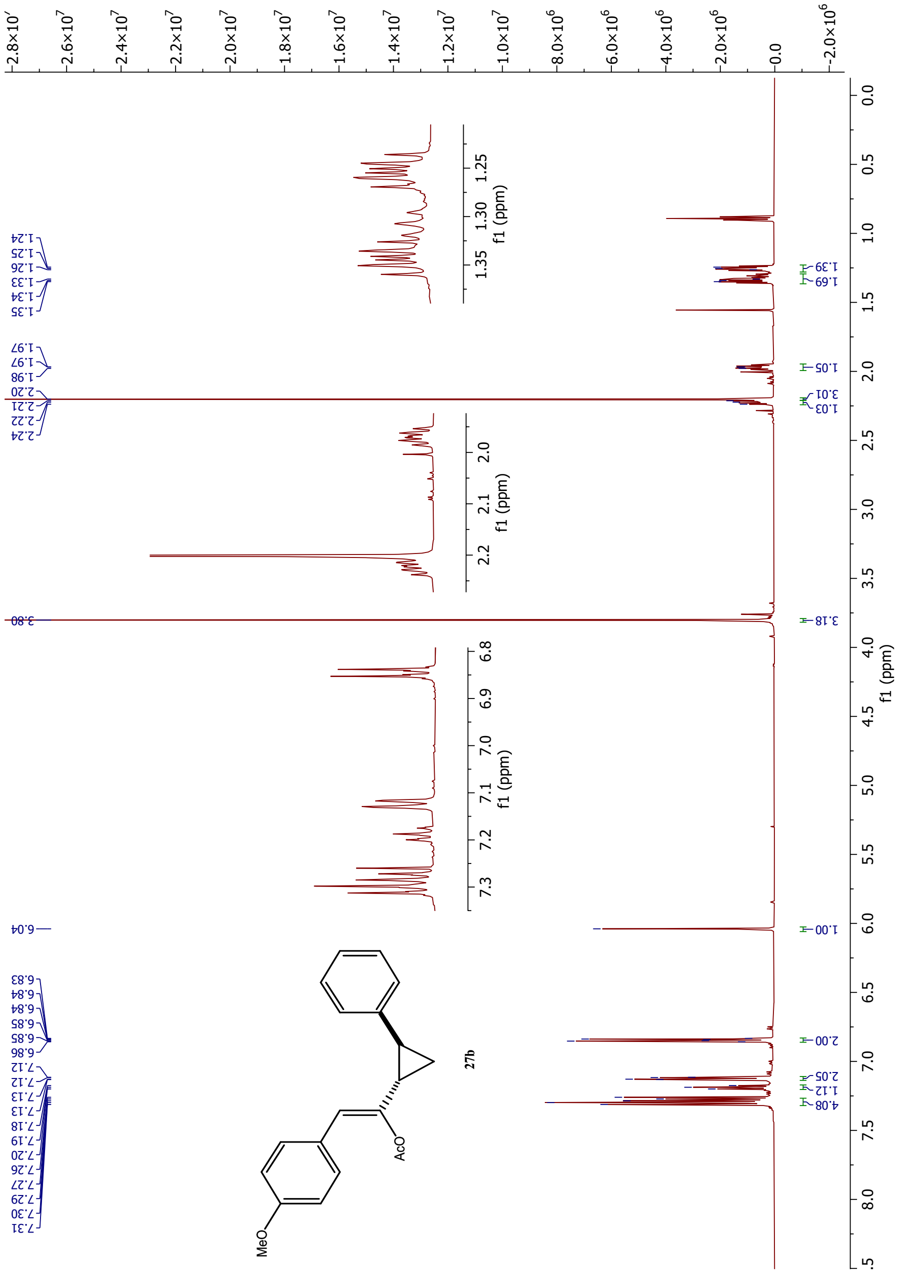

Figure T.1: HMBC NMR spectrum of compound **27b**

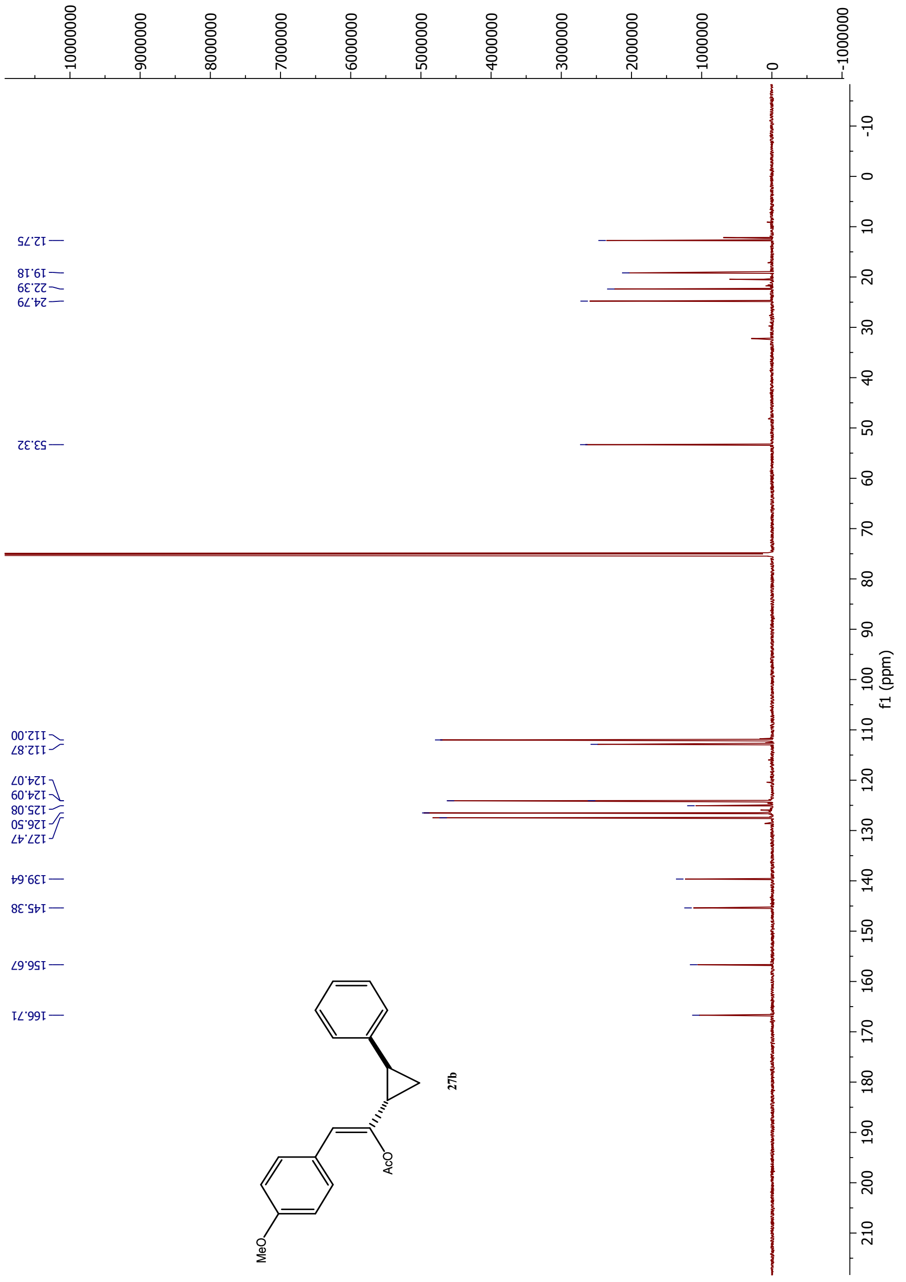

Figure T.2: ^{13}C NMR spectrum of compound **27b**

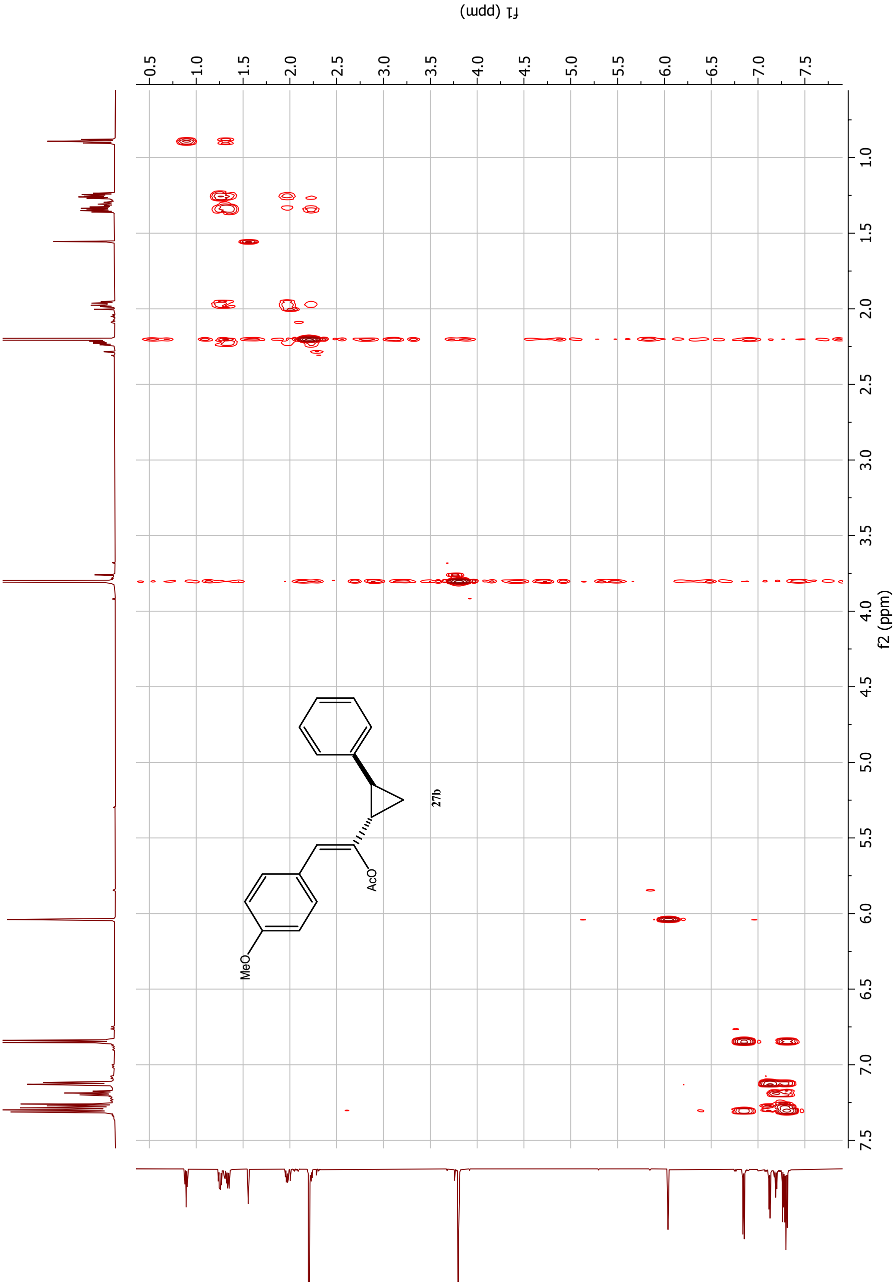

Figure T.3: COSY NMR spectrum of compound **27b**

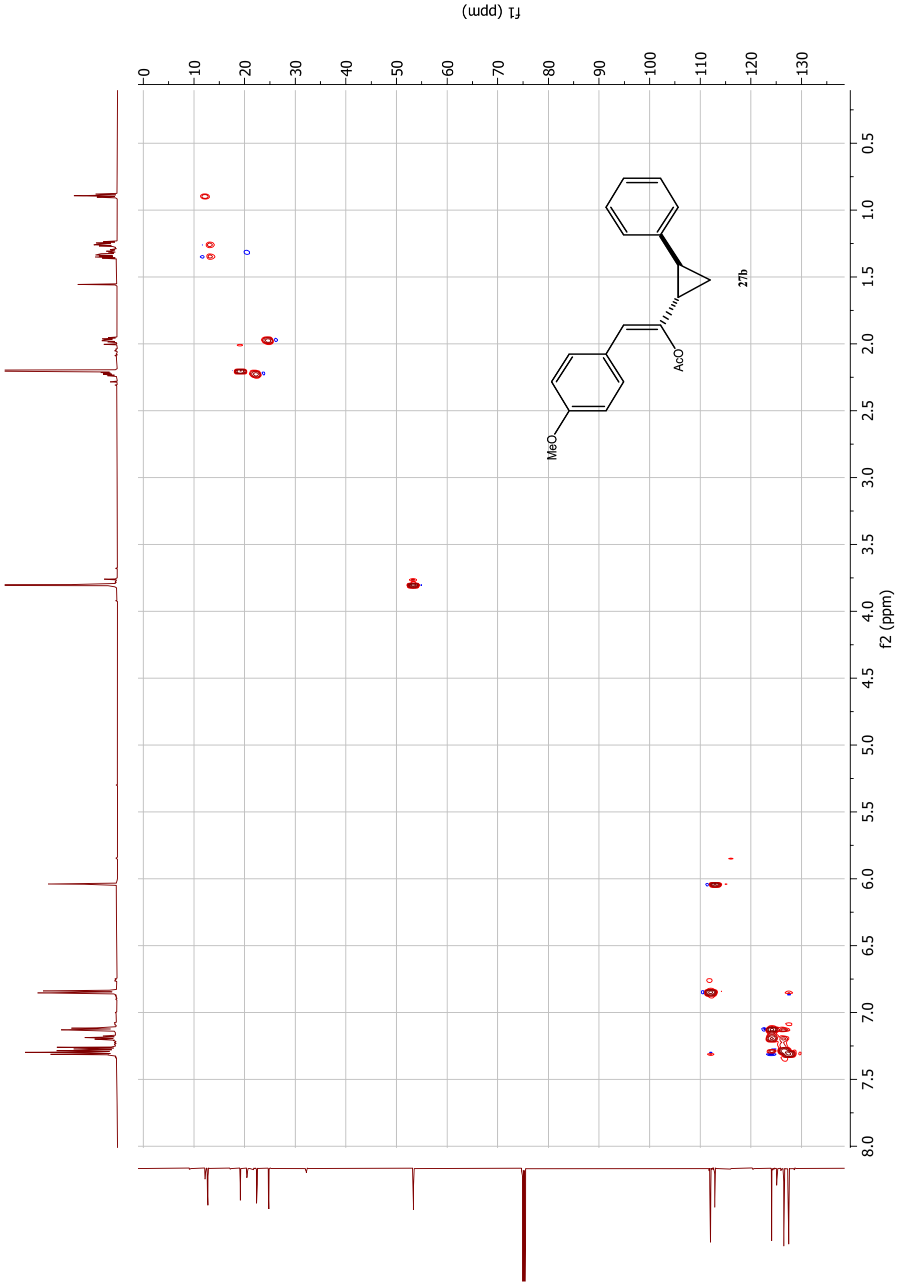

Figure T.4: HSQC NMR spectrum of compound **27b**

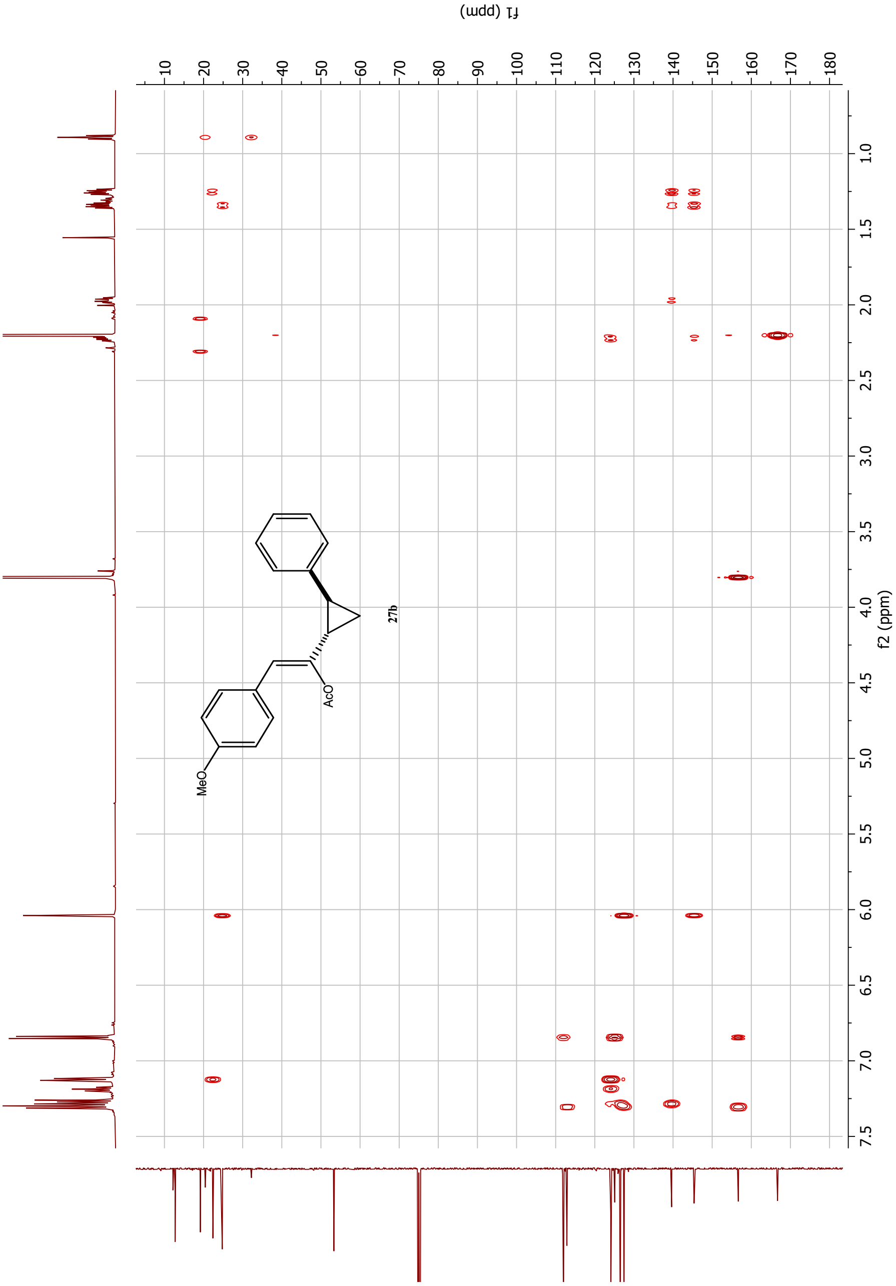

Figure T.5: HMBC NMR spectrum of compound **27b**

```
Data File C:\CHEM32\1\DATA\SONDRETL\STL-2-4-3_(2-5-2_D1).D
Sample Name: stl-2-4-3_(2-5-2_d1)

    =====================================================================
    Acq. Operator   : Sondre Lomeland
    Acq. Instrument : Instrument 1                   Location :   -
    Injection Date  : 3/26/2021 11:45:59 AM
    Acq. Method     : C:\CHEM32\1\METHODS\THOMAS NORDBØ SOLVI\TNS_CYCLOPROP.M
    Last changed    : 3/26/2021 11:44:34 AM by Sondre Lomeland
    Analysis Method : C:\CHEM32\1\METHODS\CECILIE\YIN_SYRE.M
    Last changed    : 3/20/2021 8:27:19 PM by Mari Rødseth
                      (modified after loading)
    Sample Info     : AD-H, Isocratic, n-Hexane:iPrOH (95:5), 0.8 mL/min
```

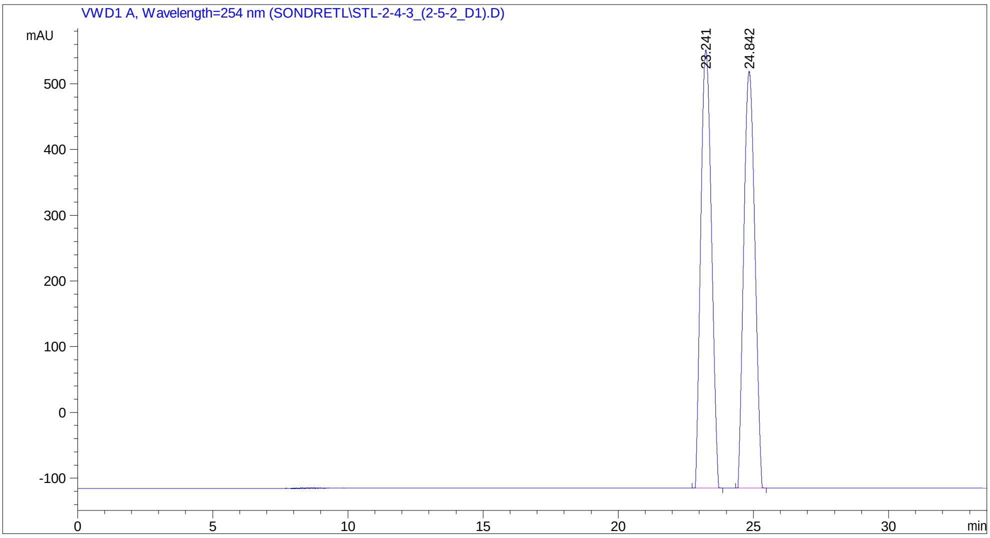

```
    =====================================================================
                    Area Percent Report with Performance
    =====================================================================

    Multiplier:                    :      1.0000
    Dilution:                      :      1.0000
    Use Multiplier & Dilution Factor with ISTDs


    Signal 1: VWD1 A, Wavelength=254 nm


    RetTime    k'     Area      Height   Symm.  Width   Plates Resol Select
     [min]         mAU   *s   [mAU   ]          [min]          ution ivity
    -------|------|----------|----------|-----|-------|-------|-----|------
     23.241    -   1.82725e4   666.76074  0.87  0.4514   14689   -      -
     24.842    -   1.80423e4   634.09821  0.90  0.4696   15506  2.04   1.07


    =====================================================================
                              *** End of Report ***

Instrument 1 3/26/2021 1:07:47 PM Mari Rødseth                    Page    1 of 1
```

Figure T.6: HPLC chromatogram of compound **27b**, catalyzed by **20a**

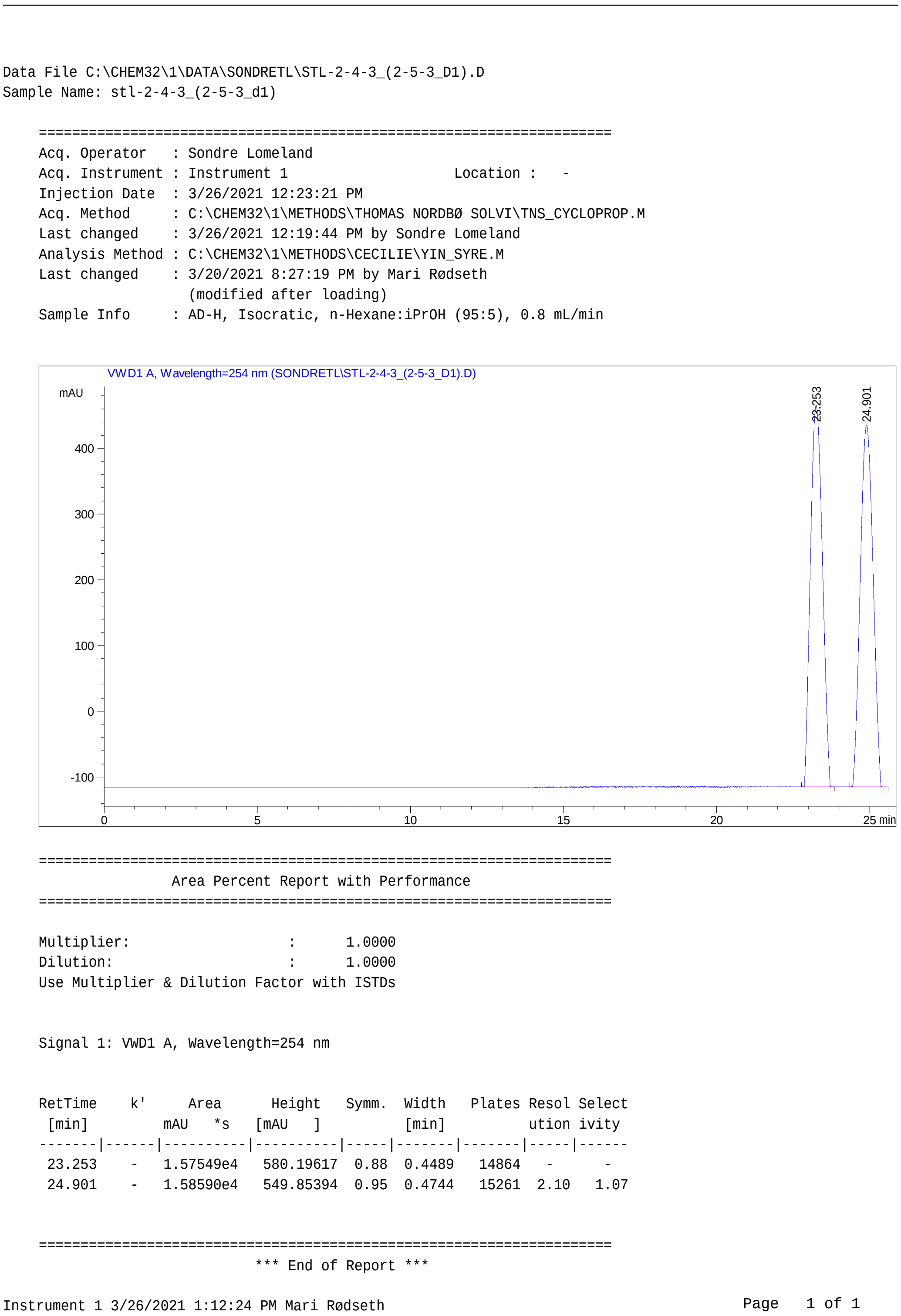

```
Data File C:\CHEM32\1\DATA\SONDRETL\STL-2-4-3_(2-5-3_D1).D
Sample Name: stl-2-4-3_(2-5-3_d1)

    =====================================================================
    Acq. Operator   : Sondre Lomeland
    Acq. Instrument : Instrument 1                   Location :   -
    Injection Date  : 3/26/2021 12:23:21 PM
    Acq. Method     : C:\CHEM32\1\METHODS\THOMAS NORDBØ SOLVI\TNS_CYCLOPROP.M
    Last changed    : 3/26/2021 12:19:44 PM by Sondre Lomeland
    Analysis Method : C:\CHEM32\1\METHODS\CECILIE\YIN_SYRE.M
    Last changed    : 3/20/2021 8:27:19 PM by Mari Rødseth
                      (modified after loading)
    Sample Info     : AD-H, Isocratic, n-Hexane:iPrOH (95:5), 0.8 mL/min
```

```
    =====================================================================
                    Area Percent Report with Performance
    =====================================================================

    Multiplier:                   :      1.0000
    Dilution:                     :      1.0000
    Use Multiplier & Dilution Factor with ISTDs


    Signal 1: VWD1 A, Wavelength=254 nm


    RetTime    k'     Area      Height   Symm.  Width   Plates Resol Select
     [min]         mAU   *s   [mAU   ]          [min]          ution ivity
    -------|------|----------|----------|-----|-------|-------|-----|------
     23.253    -   1.57549e4   580.19617  0.88  0.4489   14864   -      -
     24.901    -   1.58590e4   549.85394  0.95  0.4744   15261  2.10   1.07


    =====================================================================
                              *** End of Report ***

Instrument 1 3/26/2021 1:12:24 PM Mari Rødseth                        Page    1 of 1
```

Figure T.7: HPLC chromatogram of compound **27b**, catalyzed by **22a**

```
Data File C:\CHEM32\1\DATA\SONDRETL\STL-2-4-3_(2-5-3_D2).D
Sample Name: stl-2-4-3_(2-5-3_d2)

    =====================================================================
    Acq. Operator   : Sondre Lomeland
    Acq. Instrument : Instrument 1                   Location :   -
    Injection Date  : 3/26/2021 12:52:11 PM
    Acq. Method     : C:\CHEM32\1\METHODS\THOMAS NORDBØ SOLVI\TNS_CYCLOPROP.M
    Last changed    : 3/26/2021 12:49:14 PM by Sondre Lomeland
    Analysis Method : C:\CHEM32\1\METHODS\CECILIE\YIN_SYRE.M
    Last changed    : 3/20/2021 8:27:19 PM by Mari Rødseth
                      (modified after loading)
    Sample Info     : AD-H, Isocratic, n-Hexane:iPrOH (95:5), 0.8 mL/min
```

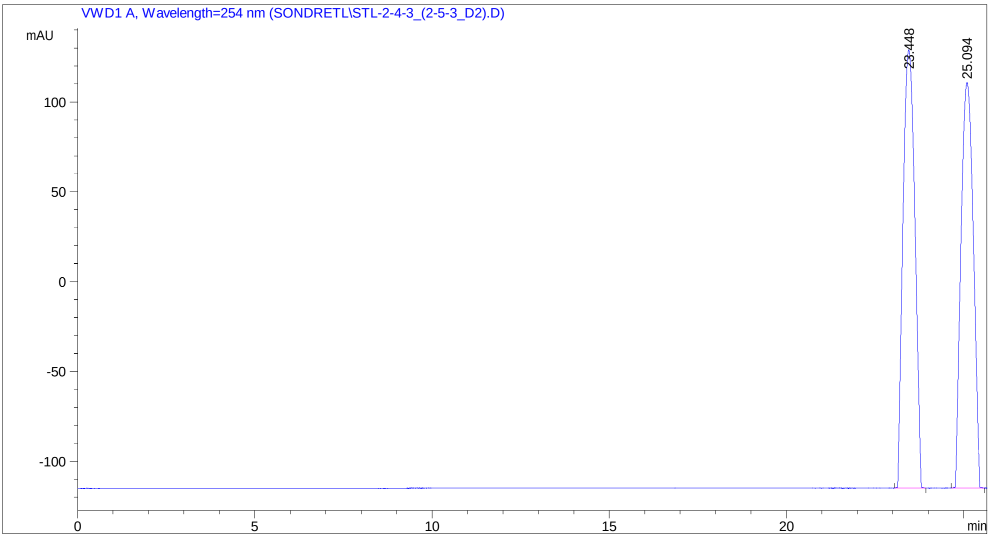

```
    =====================================================================
                    Area Percent Report with Performance
    =====================================================================

    Multiplier:                   :      1.0000
    Dilution:                     :      1.0000
    Use Multiplier & Dilution Factor with ISTDs


    Signal 1: VWD1 A, Wavelength=254 nm


    RetTime    k'     Area      Height   Symm.  Width   Plates Resol Select
     [min]         mAU   *s   [mAU   ]         [min]          ution ivity
    -------|------|----------|----------|-----|-------|-------|-----|------
     23.448    -   5667.70313  243.94595  0.91  0.3931   19709   -      -
     25.094    -   5436.98975  225.77769  0.94  0.4077   20988  2.41   1.07


    =====================================================================
                              *** End of Report ***

Instrument 1 3/26/2021 1:18:32 PM Mari Rødseth                         Page    1 of 1
```

Figure T.8: HPLC chromatogram of compound **27b**, catalyzed by **22b**

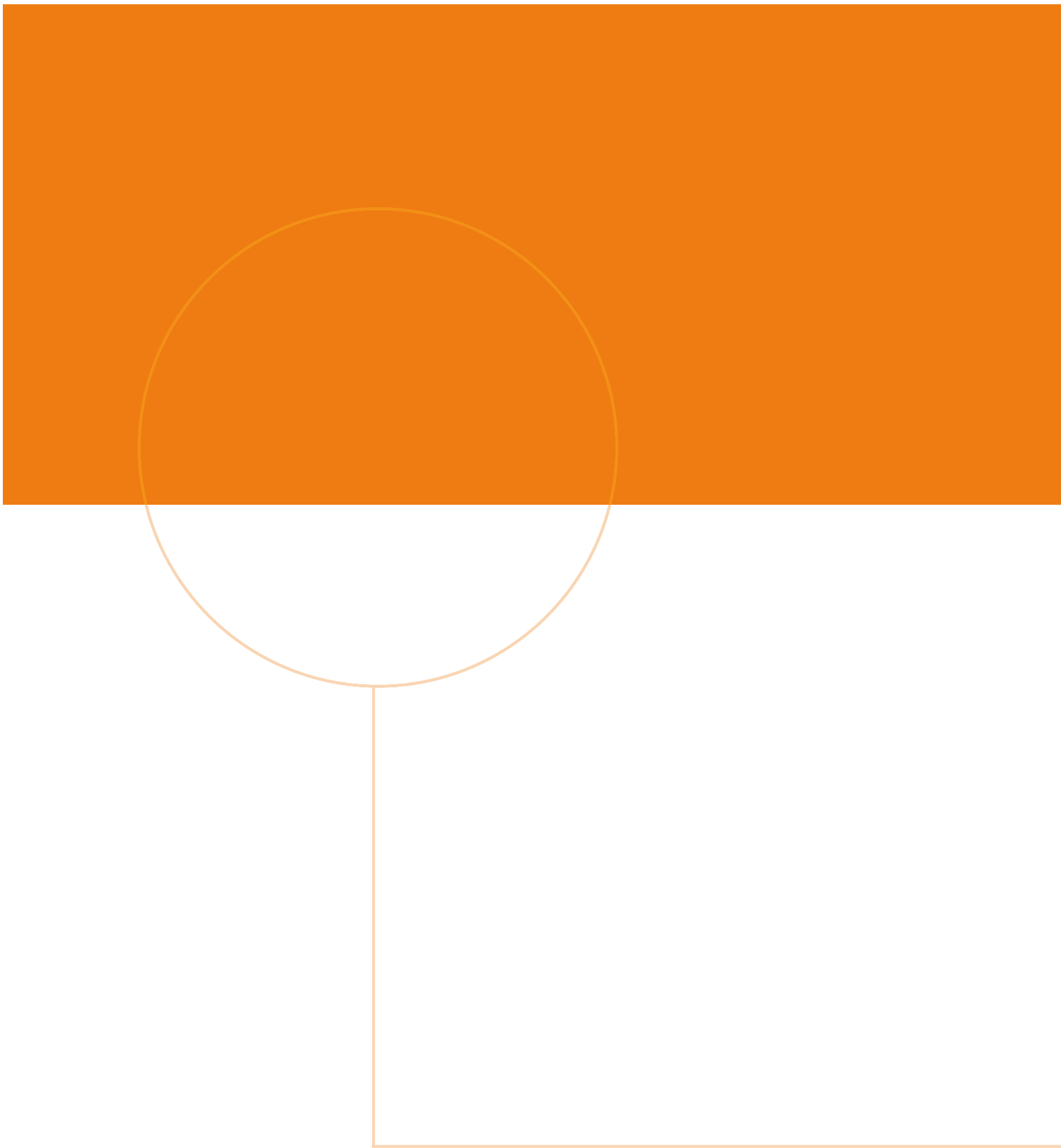

NTNU

Norwegian University of
Science and Technology